ROBFREE 98

Free-Space Holographic Optical Interconnects in Dichromated Gelatin

Brian Robertson

Submitted for the degree of Doctor of Philosophy

Heriot-Watt University

Department of Physics

August 1993

Contents

Abstract

An investigation into the fabrication of volume phase holographic optical interconnects in dichromated gelatin is presented. Two main classes of components are discussed; space-invariant fan-out holograms and multi-facet space-variant interconnects.

The applications and requirements of free-space holographic optical interconnection elements are outlined. The main diffractive properties of a volume phase transmission hologram are then analysed using coupled wave theory. This is followed by a review of dichromated gelatin holography and a description of the processing techniques used throughout the course of this work.

The central part of the thesis presents the results of an experimental investigation into the fabrication of volume phase fan-out holograms. Initially both binary-phase and binary-amplitude Dammann gratings are used to produce the object wavefront in an interferometric recording set-up, thereby allowing a series of compact array generators to be realised. An interferometric recording technique for fabricating off-axis continuous-phase fan-out elements is then described. The field generated by a specially designed binary-amplitude computer generated hologram is spatially filtered to produce a continuous phase object wavefront. As this approach combines the high efficiency of a kinoform with the flexibility of a volume phase hologram the resulting components are referred to as hybrid kinoforms. A 1×8 array generator with a diffraction efficiency of 96% and a uniformity of ±3.2% was recorded using this technique.

An experimental and theoretical investigation into the optical damage threshold of a sealed dichromated gelatin hologram is described. A model predicting the temperature profile induced by a Gaussian laser beam is developed. This allows the optical damage threshold of dichromated gelatin holograms to be estimated. Finally an experimental technique for recording multi-facet space-variant optical interconnects is described.

Acknowledgements

I would like to thank my supervisor, Mohammad Taghizadeh for all his help and guidance over the past few years. Cheers Mo. Thanks to Ian Redmond for teaching me the joys of DCG holography, Jari Turunen and Antti Vasara whose work made so much of this thesis possible, Chris Godsalve for developing the theoretical model used in chapter 7, and Ed Restall for his collaboration on chapter 8. I would also like to acknowledge the Science and Engineering Research Council and Pilkington plc for their financial support. A big thank you goes to Mike, Dave, Jo, Arlene, Dom, Newfy, Hiroyuki, Rebbie, my friends from home, my guitar, Alan, Ashley, Frank, Andy, Sue, Ross, Doug, Paul, Paul, Paul, Paul and everyone else at Heriot-Watt University for their advice and encouragement. Finally, I would like to thank my Father and my family for their love and support when I needed it most.

Associated Publications

1) B. Robertson, M. R. Taghizadeh, J. Turunen and A. Vasara, "Fabrication of space-invariant interconnects in dichromated gelatin", Applied Optics **29**, 1134-1141 (1990).

2) B. Robertson, M. R. Taghizadeh, J. Turunen and A. Vasara, "High efficiency, wide bandwidth optical fan-out elements in dichromated", Optics Letters, **16**, 694-696 (1990).

3) B. Robertson, E. J. Restall, M. R. Taghizadeh and A. C. Walker, "Space-variant holographic optical elements in dichromated gelatin", Applied Optics, **30**, 2368-2374 (1991).

4) B. Robertson, J. Turunen, H. Ichikawa, J. M. Miller, M. R. Taghizadeh and A. Vasara, "Hybrid kinoform fan-out holograms in dichromated gelatin", Applied Optics, **30**, 3711-3720 (1991).

5) B. Robertson, C. Godsalve and M. R. Taghizadeh, "Dichromated gelatin: An investigation into laser induced damage", to be published in Applied Optics.

In memory of my Mother

Chapter 1

Free-Space Optical Interconnection Technology

1.1 Introduction

The idea of using optics to perform image and signal processing operations was first proposed in the early 1960s. Initial research concentrated on the development of coherent analogue optical computers, which, in general, made use of the Fourier-transforming properties of a lens to process data, and discrete optical processors, which took advantage of optics parallel information processing capabilities [1]. The relatively recent advent of low power optical logic devices has, however, revolutionised the field of optical computing as it is now possible to process arrays of optical data digitally [2,3]. Processors based on two-dimensional arrays of optical logic gates and interconnected by free-space optics have a number of fundamental advantages over conventional electronic systems. As free-space optical data links have a higher transmission bandwidth than their electronic counterparts, information can be transferred at faster data rates, and, perhaps more importantly, the free-space topology is ideal for architectures which require some form of global, or non-local communications [4,5]. This can allow a very high degree of parallelism to be built into the circuit.

In order to implement these circuits, optical components capable of efficiently generating and routing two-dimensional arrays of optical data must be developed. This has given rise to a new field of optical device research which is commonly referred to as free-space optical interconnection technology. Already a number of successful prototype schemes based on bulk optics, micro-optics, planar optics and diffractive optics have been realised (see, for example, references [1] and [4]). In general, however, currently available

interconnection technology tends to be inefficient and limited in the types of connection topolgies it can achieve. Thus, if the full potential of digital optical processing is to be realised, new and better ways of interconnecting optical data must be perfected.

The following thesis presents the results of an experimental investigation into the design and fabrication of free-space holographic optical interconnects. These components have several features which would make them appear ideal for applications within the field of digital optical computing and photonic switching. Due to the flexibility of the recording process, highly complex connection patterns can be implemented which may be impossible to realise using conventional bulk optics. In addition, they are lightweight, cheap to reproduce, and may be easily integrated into an optical system.

The primary aim of the research described in this thesis was to develop new techniques for recording efficient interconnects in dichromated gelatin (DCG). Over the past two decades, DCG has proven itself to be one of the best materials available for fabricating holographic optical elements. This success can be attributed to the fact that it is an almost ideal medium for recording both transmission and reflection volume phase gratings [6]. In particular, due to the large refractive index modulations which can be obtained, diffraction efficiencies approaching 100% are possible. DCG can be processed in relatively thick layers ($\approx$ 100 μm) for operation in both the visible and the near infra-red [7] and, when properly developed, it has a low absorption and a high signal to noise ratio.

The rest of this chapter is intended to outline the requirements and applications of free-space optical interconnects. It is hoped that this will set a basis for developing practical device specifications, and allow the performance of the DCG interconnects which were produced during the course of this thesis to be evaluated. The limitations of current electronic interconnection technology and the advantages of optical interconnections are described. This is followed by a brief introduction to free-space optical interconnection technology. Finally the outline of the thesis will be given.

1.2 Motivation

Over the past few decades, significant advances have been made in microelectronic design and fabrication techniques. Current integrated circuit technology, however, has reached

the point where difficulties in data communication are beginning to limit the performance of these systems. The problems associated with electronic timing and layout constraints, for example, are now seen as one of the main issues facing microelectronic circuit designers, a situation which is becoming further complicated by the increasing use of parallel computer architectures.

A large proportion of any integrated circuit, as much as 70% in certain cases, can be devoted to internal wiring. This limits the number of gates which may be used when specifying the circuit. In addition, although it is possible to pass wires over or under each other using a multi-level structure, only a small number of layers may be used before fabrication problems start to occur. This can cause severe design problems, and make the implementation of certain global interconnection schemes impractical. A further area of difficulty is related to the limited number of chip pin-outs that an integrated circuit (IC) can support. Although many thousands of components can be assembled on a typical IC, the number of pin-puts is typically only in the hundreds. This has become a major bottleneck in communications flow [8].

Propagation delays due to the resistivity and parasitic capacitance associated with any wire can also cause severe difficulties in circuit design and operation, particularly in the case of clock signal distribution. Any relative difference between these signals reaching different parts of a circuit will lead to non-synchronous operation, a problem which is commonly referred to as clock skew. Although propagation delays can be reduced by packing circuit components closer together, this inevitably introduces heat dissipation problems. Very high performance computers such as the Cray 2, for example, must use complex and expensive cooling technology to prevent overheating. Parasitic capacitance and inductance can also lead to the appearance of crosstalk between neighbouring electrical connections.

Free-space optical interconnects offer one possible method of avoiding many of these communication difficulties [8-10]. As their name implies, free-space optical interconnects route the optical data via free-space. Thus, as no physical link between the source and detector is required, total freedom exists in deciding upon the form of the interconnection pattern. Due to their higher transmission bandwidth, signals can be propagated at far faster data rates. Commercially available fibre optic communication links, for example, are

capable of transmission rates of several Giga bits/s. Moreover, unlike their electronic counterparts, optical interconnects are free from capacitive loading and mutual interference effects and, perhaps more importantly, they do not suffer from the restrictions of electronics quasi-planar geometry. This will permit the use of non-local interconnections which are difficult to implement electrically and allow greater parallelism to be employed within the circuit architecture. In addition, as the size of an optical pin-out can be much smaller than the corresponding electrical pin-out, interconnection densities can be increased [8]. Finally, by using this approach it may be possible to implement reconfigurable interconnection schemes. This would add an extra degree of flexibility to the circuit design, and permit a number of novel architectures, such as those based on neural networks to be implemented.

A number of theoretical models calculating the relative power consumption of electrical and optical interconnection links have been developed [11]. These studies have shown that over communication distances of less than a few cm (i.e. across an integrated circuit), electrical connections are more efficient. Over longer distances, however, optical interconnects have a lower power consumption. From a pure power argument, therefore, optical interconnections would appear suited only for board-to-board and processor-to-processor communications. The advantages of a faster data communication rate, greater flexibility and potentially higher interconnection densities may, under certain circumstances, make optics the better choice at all communication hierarchy levels.

1.3 Guided wave optical interconnects

Optical interconnection links may also be implemented using guided wave optical systems. In some respects guided wave interconnects suffer from some of the same restrictions which affect electronic wiring in that a physical link must exist between the source and detector. This tends to limit the interconnection densities which can be achieved, and restrict the interconnection paths which may be implemented. However, several successful guided wave interconnects have been demonstrated. These include a number of high bandwidth fibre optic communication links designed to transmit data between

processors [12,13]. In addition, a variety of guided wave schemes have been developed to provide backplane interconnections [14] and for use in very high speed photonic switching systems [15].

1.4 Applications of optics in electronic computing systems

Already optics based sub-systems are beginning to find applications within conventional electronic computers. Optical data storage, for example, is expected to start replacing magnetic disk memories in the near future [4]. This is due to the higher data storage capacity, faster access time and the potential for parallel memory addressing which such systems offer. In addition, a number of optical interconnection schemes designed to alleviate some of the communication problems which affect current electronic computers are also being developed. Examples of such systems include high speed processor-to-processor data links [11,12], optical buses [16] and optical clock signal distribution systems [17].

1.5 Free-space holographic optical interconnects

As mentioned in the introduction, this thesis will be primarily concerned with the development of interconnects for use in free-space digital optical processors. Typically these systems are based on two-dimensional planar arrays of optical logic elements (see, for example, references [2] and [3]). The functionality of these devices may range from simple all optical logic gates to programmable 'smart pixels' which contain local memory and are capable of more involved processing routines [18]. At each device plane there may exist a limited number of electrical connections supplying control signals and providing local communications between processing elements (e.g., nearest neighbour connections). Data transfer between successive device planes, however, is achieved using some form of free-space optical interconnect, as shown in figure 1.1. In theory this allows for essentially unlimited freedom in deciding upon the circuit architecture, thus, by taking advantage of the parallelism and interconnectivity of optics, many communication intensive architectures which inherently require global communications may be implemented [4]. These include, for example, data sorting systems, matrix-matrix multiplication, the fast Fourier

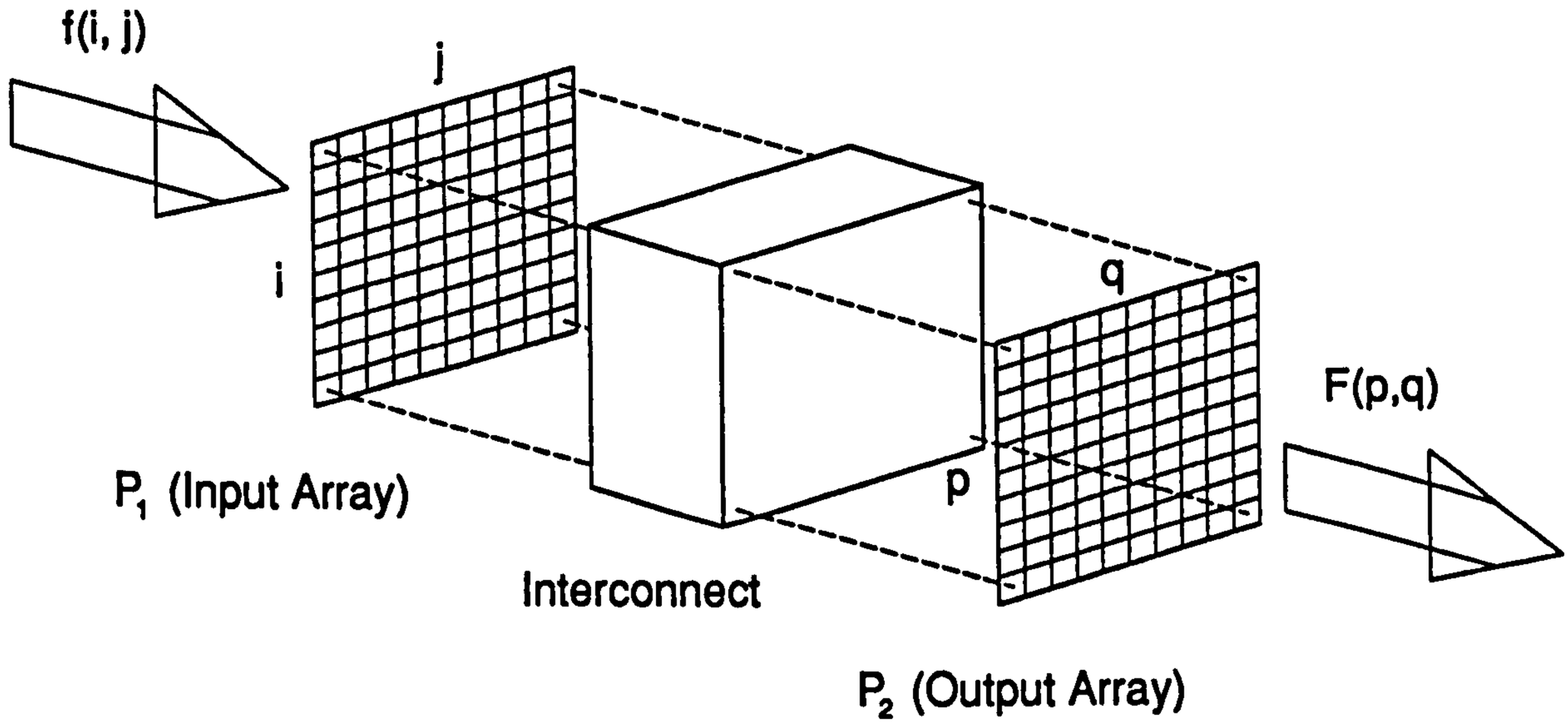

Figure 1.1 - Schematic of a free-space optical interconnect.

transform (FFT) and a variety of image processing problems, all of which are ideally suited to an optical implementation. In addition, a number of free-space photonic switching fabrics have been developed which utilise this type of interconnection topology. These circuits range from single stage optical crossbars [19,20] to multi-stage networks [21,22]. A full review of this subject is contained in references [8] and [15].

In its most general form, a free-space optical interconnect must be capable of transferring a two dimensional array of optical data between two successive device planes whilst rearranging the order of the data according to some desired interconnection topology. The data may be encoded either in terms of intensity or polarisation and have either a digital or analog format. The basic outline of such a system is shown in figure 1.1. An array of optical processing elements in the input plane, P_1, is connected via a free-space optical interconnect to an array of devices in the output plane, P_2. Each of the processing elements in the input plane P_1 may be defined with respect to its co-ordinate position within the array, (i,j). Similarly, each of the processing elements in the output plane may be represented by the co-ordinates (p,q). Using these two co-ordinate systems it is possible to mathematically describe any interconnection pattern using the following matrix relation [4]:

$$G(p,q)=\sum_{i=1}^{I}\sum_{j=1}^{J} g(i,j)\,K(i,j,p,q) \qquad (1.1)$$

where g(i, j) describes the output from device (i, j), G(p,q) the subsequent input to device (p,q) and K(i,j,p,q) represents the normalised weighting of the connection from (i,j) to (p,q). Note that this notation makes no restriction on the actual weightings of the interconnection pathways, and may be used to define the interconnection pattern between two arrays of different dimensions.

The set-up shown in figure 1.1 permits communication between nearest neighbour gates as easily as those furthest away. In addition, to a first approximation, all interconnection distances will be the same. This will ease the problem of providing synchronous data transfer, particularly for clock and control signals.

1.6 Optical array generation

As mentioned in the previous section, many of the optical computing circuits currently under development are based on two-dimensional planar arrays of optical logic elements. Thus, in order to address and control these circuits, some method of efficiently generating an equally spaced array of uniform amplitude beams is required. This has led to the development of a variety of optical systems which are capable of producing arrays of beams from a single source, including set-ups utilising lenslet arrays, fractional Talbot imaging systems and periodic diffraction gratings. A full review of this topic is presented in reference [23].

At present periodic binary surface-relief gratings offer the most practical method of generating large arrays of beams. These were first investigated by Dammann and Görtler in 1971, and are commonly referred to as Dammann gratings [24]. The optical arrangement used for array generation is shown in figure 1.2. When illuminated with a single collimated input beam, the binary-phase grating, *BPG*, generates a discrete angular spectrum of plane waves. If a Fourier transform lens, L_1, is placed after the grating, these waves are focussed down to produce an array of uniformly spaced diffraction orders. As the grating is operating in a Fourier transform mode, the power spectrum of the array is essentially independent of the input beam profile and depends only on the grating structure. The input beam does,

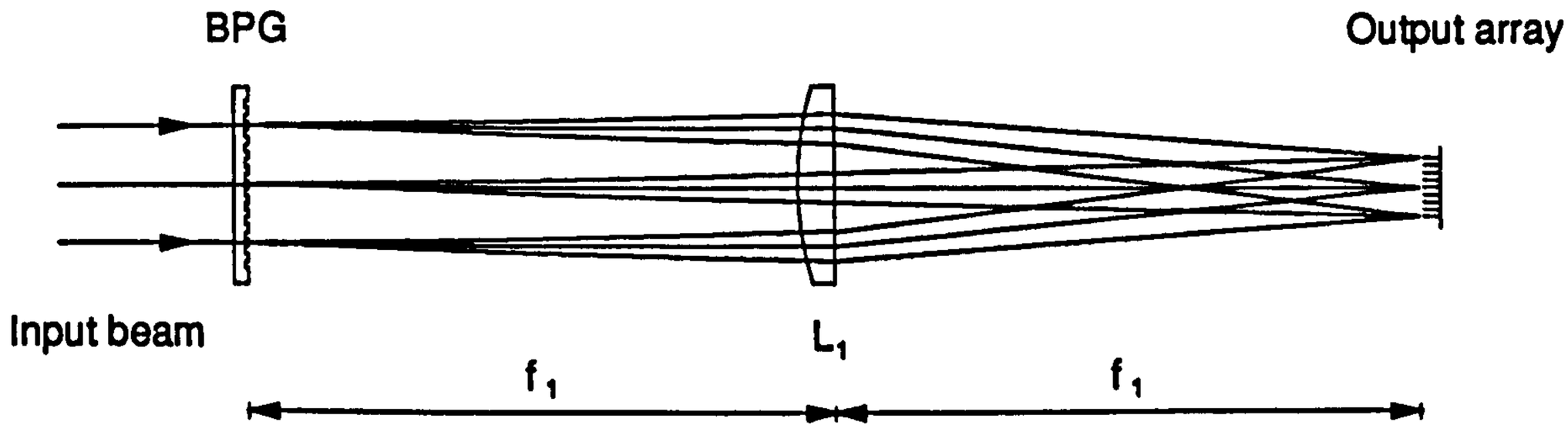

Figure 1.2 - Optical arrangement for array generation using a Dammann grating. BPG : Binary-phase grating; L_1 : Fourier-transform lens.

however, determine the profile of the individual focussed diffraction orders. By correct optimization of the transition points of the grating, it is possible to distribute equal power into a central $N \times M$ block of beams. For most practical cases, the power spectrum of the grating may be calculated using Fourier optics. In the regime where the grating period approaches the replay wavelength, more rigourous diffraction theories are required (a discussion of the various diffraction regimes is given in reference [25]). The actual efficiency of these gratings, defined as the amount of transmitted light which ends up in the central $N \times M$ block of diffraction orders, depends on the size of the array to be generated, and on the actual grating design. In the case of a two-dimensional non-separable grating, for example, efficiencies of up to ≈ 75% for a fan-out of 16×16 are possible [25,26]. A number of multi-level surface-relief gratings have also been developed. Although harder to fabricate, these components are capable of efficiencies of over 90% [27]. For a full review of the design and optimization procedures, it is suggested that the reader refer to references [25-27].

1.7 Optical data transfer

The most basic interconnection scheme is one in which direct one-to-one imaging between two device planes is required (e.g, for data transfer or parallel data acquisition from an optical memory). This can be implemented using either bulk refractive lenses or arrays

of microlenses [28,29]. The optical set-up required for this operation must meet very tight specifications; it must be capable of generating a spot smaller than the active device area over a field large enough to cover the device plane with low distortion and a high field flatness [30]. In general, this requires the use of custom made lenses, designed to meet the specific needs of a particular circuit.

1.8 Optical fan-out and fan-in

If the interconnect provides a path from processing element (i, j) in the input plane to N processing elements in the output plane, that particular input channel is said to have N-fold fan-out. Conversely, if N processing elements in the input plane are connected to one in the output plane, that output channel is said to have N-fold fan-in. Attempting to fan-in N identical optical signals to the same point will not necessarily result in an N times increase in intensity [31]. This is a result of what is commonly referred to as the constant radiance theorem [32], which states that no passive linear optical system can increase the radiance of an optical beam. Expressed mathematically, this theorem asserts that the product of the cross-sectional area of a beam, A, and the solid angle it occupies, Ω, remain constant throughout such a system.

Let us first take the case of N identical, but mutually incoherent beams (i.e., derived from different optical sources), each of which occupy an area A_1 and subtend a solid angle of Ω_1. If we attempt to fan-in these beams into a single channel having an area A_2, and subtending a solid angle of Ω_2, then the maximum amount of light which may be captured will be given by $\Omega_2 A_2 / N \Omega_1 A_1$. One of the repercussions of this relationship is that if we try to fan-in N mutually incoherent but identical beams into a single beam with the same divergence and cross-sectional area, the total power reaching the output plane will only be, at most, 1/Nth the optical power in all the beams. In practice, however, it is possible to couple a number of beams onto the same device with no power loss as long as the detector is N times greater than the individual spot sizes, or the f/number of the collecting system is $\sqrt{N}$ times larger.

Even more serious problems can occur when attempting to fan-in N identical mutually coherent beams into the same spatial mode (i.e., derived from the same source) as the total power reaching the output plane will depend on the relative phases of the incident beams.

Thus, it can be possible to get all, or none of the incident light into the output device. Lossless fan-in can, however, be achieved using a variety of techniques [33]. If the spot size of the signal beams are much smaller than the device area, they may be directed to different parts of the device. Alternatively, if the beams are incident on the output plane at slightly different angles, the interference pattern may average itself out over the detector area [34]. Finally, where only a fan-in of two is required, beams of orthogonal polarisations may be used.

The problem of coherent fan-in has been investigated by several authors. Leger [35] showed that, by accurate control of the relative phase, it is possible to coherently add a number of laser beams using a binary diffraction grating. Wakelin [30] has also discussed the problem of coherent fan-out and fan-in in relation to a nearest neighbour edge extractor circuit implemented using ZnSe logic etalon [3] and a space-invariant fan-out hologram.

1.9 Space-variant and space-invariant optical interconnects

Free-space optical interconnects may be classified according to their space-variance, a term which refers to the regularity of the interconnection pattern. If the fan-out pattern is constant across the entire array the interconnect may be described as space-invariant [10]. These components have a number of applications within the field of optical computing, including array generation [26,27] and multiple image generation [19,20]. In addition, a variety of interconnection schemes, such as nearest neighbour [7] and next to nearest neighbour fan-out, may also be implemented using space-invariant components.

If the fan-out pattern changes across the array the interconnect may be described as being space-variant [10]. Note that these definitions merely refer to the regularity of the connection pattern and do not necessarily require the interconnect to be a space-variant or invariant optical imaging system. A space-invariant optical imaging system may be described as any optical set-up in which a lateral shift in a given input distribution results only in a proportional shift in the position of the output distribution (as in the case of most image and signal processing systems). If the change in output position is not proportional to the change in input position, the system is termed to be space-variant). A number of space-variant interconnection schemes have been proposed, including several based on regular multi-stage interconnection networks such as the perfect shuffle [36-38], Butterfly

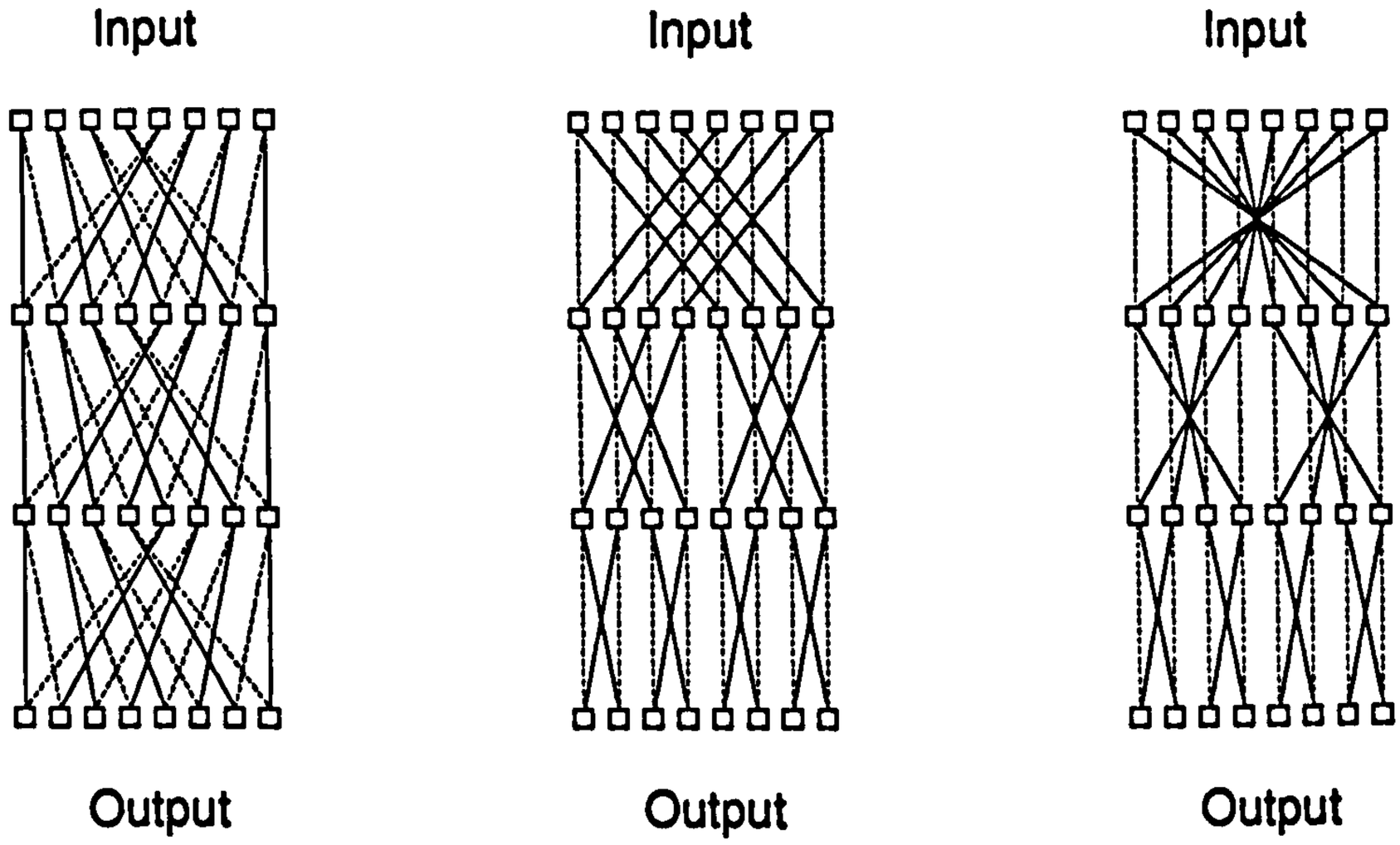

Figure 1.3 - Examples of space-variant interconnection networks. (a) The perfect shuffle. (b) The Banyan network. (c) The half-crossover network.

network [39], Banyan network [40,41] and crossover network [42,43]. Typically, these systems consist of alternating layers of optical processing elements and interconnection stages, each of which has a fan-out and fan-in of two. Examples of three interconnection networks, the perfect shuffle, Banyan network and half-crossover network, are illustrated in figure 1.3. Non-local multi-stage networks have a wide range of applications, extending from data sorting to photonic switching [4,5], in addition, the high degree of regularity exhibited by these interconnects makes them ideally suited to an optical implementation.

Other space-variant interconnection schemes which have been demonstrated include the split and shift [44,45], cyclic shift [46], and several computer generated hologram based interconnects [47,48]. Space-variant interconnects may also be realised using space-invariant optical elements. McCormick et al [22], for example, implemented a Banyan network using a diffractive, one-to three fan-out element and a mask which blocked out the unrequired signal beams.

Finally, optical interconnects may be classified with respect to their reconfigurability. A number of dynamic interconnection systems have been produced based on photorefractive elements [1] and spatial light modulators [49,50]. Although complex and difficult to set up, these have been successfully used in the implementation of a number of neural network

architectures. In practice, however, most of the digital optical processing systems currently under development, use only static interconnects in conjunction with planes of optical logic elements. These either utilise some form of space-invariant fan-out (e.g., for nearest neighbour or next nearest neighbour communication) or are based on a highly regular connection pattern such as the perfect shuffle.

1.10 Design criteria

It would be useful at this point to briefly discuss some of the requirements which must be met by any free-space optical interconnect. The first factor which must be considered is the operating wavelength of the optical circuit. This will be dictated by the type of active component employed, and typically be in the infra-red due to the availability of low power optical logic elements at these wavelengths (e.g. S-SEEDs). These devices will most probably be driven by semiconductor diode lasers which, due to their low cost, high efficiency and compact construction, are ideally suited to optical computing and communications applications. Thus, for any particular optical interconnection technology to be of any practical use it must be capable of efficient operation at these wavelengths.

It is important to minimise the switching energy required by the optical logic elements as this reduces the overall optical power requirements of the circuit, and avoids any possible heat dissipation problems. Typically, the switching energy scales with the active device area, thus devices tend to be very small, less than $100\mu m^2$ in the case of S-SEED logic elements. This demands the use of tightly focussed beams. As a result, any optical interconnection scheme must be capable of providing point source to point source operation as close to the diffraction limit as possible.

For a fixed bit error rate (BER), the speed that an optical logic element or detector may operate at will be governed by the intensity of the signal beam reaching it. The performance of the circuit will therefore be directly dependent on the efficiency of the interconnections and on the degree of fan-out required. This is probably one of the main limiting factors when scaling up an optical computing or communication system to any practical size.

In terms of system design, the interconnect must be compact and compatible with the mechanical layout of the circuit, have a high signal to noise ratio, a low reconstruction error and, in the case of a space-invariant fan-out component, the angular response must be sufficient to cover the required range of interconnection angles. A further consideration relates to the effect of fabrication errors on the performance of the interconnect. These may, for example, lead to higher levels of cross-talk and registration problems in the output plane, P_3. Exact control over the recording parameters must therefore be exercised if the interconnect is to be fabricated with the necessary degree of accuracy. Similar cross-talk and registration problems will also arise due to alignment errors. This is an important issue in terms of both the interconnect and circuit design as, in practice, fabricational and alignment tolerances will determine the applicability of any optical interconnection scheme [30,51]. The interconnect must be capable of being simply and precisely positioned, preferably with the minimum use of expensive translation mounts. Moreover, its alignment must be unaffected by external factors such as vibrations and temperature fluctuations. As has been discussed by Brubaker et al [52], this puts great emphasis on the opto-mechanical design of the interconnect and on the packaging technology used.

1.11 Thesis outline

The thesis outline is as follows. In chapter two a brief summary of the theory of volume phase holograms is given based on a coupled wave analysis. Chapter three then reviews the processing theory of dichromated gelatin and describes the techniques used throughout this thesis for pre-processing, development and post-processing Kodak 649F plates. Chapters four, five and six describe a number of methods for fabricating efficient and uniform space-invariant fan-out elements in DCG using CGH copying techniques. Initial work concentrates on employing a binary-phase Dammann grating to generate the object wavefront in an interferometric recording set-up. The results of this research is given in chapter four. In the following two chapters, the idea of using a CGH to generate the object wavefront is extended further. Rather than using a binary-phase grating, spatial filtering techniques are used to convert the wavefront produced by a binary-amplitude CGH into a wavefront which contains only phase information. The advantage of this approach lies in the higher accuracy that an amplitude CGH can be fabricated with. A binary-amplitude

CGH is used in chapter five to generate a binary-phase wavefront identical to that a Dammann grating would produce. In chapter six, a binary-amplitude CGH is used to produce a continuous phase wavefront, allowing a hybrid kinoform fan-out element to be recorded. This interconnect was found to have both an efficiency and uniformity good enough for practical interconnect applications.

Chapter seven of this thesis deals with the optical damage threshold of dichromated gelatin. This concentrates on the effects of a high power Gaussian beam on the efficiency of a sealed DCG hologram, a subject of great practical importance when dealing with interconnects which have to cope continuously with tens of Watts of optical power.

In chapter eight, a method for fabricating one-to-one space-variant interconnects based on a pair of matched, multi-faceted HOEs is reported. By using a combination of one-to-one multi-facet HOEs and lossless polarisation fan-out/in this approach can be extended to provide space-variant interconnects with a fan-out of two. Finally, a conclusion is given which outlines possible future interconnect work in DCG and compares the performance of the devices fabricated during this thesis with other, alternative interconnection technologies.

1.12 References

1) Optical Computing, Edited by B. S. Wherrett and F. A. P. Tooley, *Proceedings of the Thirty-Fourth Scottish Universities Summer School in Physics*, SUSSP Publications, University of Edinburgh (1988).

2) M. E. Prise, R. E. La Marche, N. C. Craft, M. M. Downs, S. J. Walker, L. A. D'Asaro, and L. M. F. Chirovsky, "A module for optical logic circuits using symmetric self-electrooptic effect devices", Appl. Opt. **29**, 2164 (1990).

3) B. S. Wherret, R. G. A. Craig, J. F. Snowdon, G. S. Buller, F. A. P. Tooley, S. Bowden, G. S. Pawley, I. R. Redmond, D. McKnight, M. R. Taghizadeh, A. C. Walker, and S. D. Smith, "Construction and tolerancing of an optical CLIP", Proc. Soc. Phot. Opt. Inst. Eng. **1215**, *Digital Optical Computing II* (1990).

4) A. D. McAulay, Optical Computing Architectures, John Wiley and Sons, Inc., New York (1991).

5) M. E. Prise, N. C. Craft, M. M. Downs, R. E. LaMarche, L. A. D'Asaro, L. M. F. Chirovsky, and M. J. Murdocca, "Optical digital processor using arrays of symmetric self-electrooptic effect devices", Ph.D. Thesis, Rutgers University, New Jersey (1987).

6) D. Meyerhofer, "Dichromated gelatin", in Holographic recording materials, Editor H. M. Smith, Topics in Applied Physics **20**, Springer Verlag (1984).

7) I. R. Redmond, Holographic optical elements in dichromated gelatin, Ph.D Thesis, Physics Department, Heriot-Watt University, Edinburgh (1989).

8) J. W. Goodman, "Optics as an interconnect technology", in Optical Processing and Computing, Edited by H. H. Arsenault and T. S. Szoplik, Academic Press (1989).

9) J. W. Goodman, F. I. Leonberger, S. Y. Kung, and R. A. Athale, "Optical interconnections for VLSI systems", Proc. IEE **72**, 850 (1984).

10) B. K. Jenkins, P. Chavel, R. Forcheimer, A. A. Sawchuk and T. C. Strand, "Architectural implications of a digital optical processor", Appl. Opt. **23**, 3465 (1984).

11) M. R. Feldman, S. C. Esener, C. C. Guest, and S. H. Lee, "Comparison between optical and electrical interconnects based on power and speed considerations", Appl. Opt. **27**, 1742 (1988).

12) P. R. Haughen, S. Rychnovsky, A. Husain, and L. D. Hutcheson, "Optical interconnects for high speed computing", Opt. Eng. **25**, 1076 (1986).

13) D. H. Hartman, "Digital high speed interconnects: a study of the optical alternative", Opt. Eng. **25**, 1086 (1986).

14) F. Lin, E. M. Strzelecki, and T. Jannson, "Optical multiplanar VLSI interconnects based on multiplexed waveguide holograms", Appl. Opt. **29**, 116 (1990).

15) H. S. Hinton, "Photonic Switching Fabrics", IEE Commun. **28**, 71 (1990).

16) A. Dickinson and M. E. Prise, "Free-Space Optical Interconnection scheme", *OSA Topical Meeting on Photonic Switching*, Salt Lake City (1989).

17) B. D. Clymer and J. W. Goodman, "Optical clock distribution to silicon chips", Opt. Eng. **25**, 1103 (1986).

18) A. L. Lentine, L. M. F. Chirovsky, M. W. Focht, J. M. Freund, G. D. Guth, R. E. Leibenguth, G. J. Przybylek, L. E. Smith, L. A. D' Asaro, and D. A. B. Miller, "Integrated arrays of self electro-optic effect device photonic switching nodes", *OSA Topical Meeting on Photonic Switching*, Salt Lake City (1989).

19) A. G. Kirk, W. A. Crossland, and T. J. Hall, "A compact and scalable crossbar", *Third International Conference on Holographic Systems and Applications*, IEE Conference Publication **342** (1991).

20) A. C. Walker, M. R. Taghizadeh, F. A. P. Tooley, G. Smith, I. R. Redmond, D. J. McKnight, B. Robertson, and C. P. Barrett "Optical and optomechanical design of a matrix-matrix crossbar interconnect", *in the 8th Workshop of Optics in Computing*, Topical Meeting of the European Optical Society, Paris (1992).

21) F. B. McCormick, F. A. P. Tooley, T. J. Cloonan, J. L. Brubaker, A. L. Lentine, R. L. Morrison, S. J. Hinterlong, M. J. Herron, S. L. Walker, and J. M. Sasian, "S-SEED-based photonic switching network demonstration", OSA Proceedings on photonic switching, Volume **8**, 48 (1991).

22) F. B. McCormick, T. J. Cloonan, F. A. P. Tooley, A. L. Lentine, J. M. Sasian, J. L. Brubaker, R. L. Morrison, S. L. Walker, R. J. Crisci, R. A. Novotony, S. J. Hinterlong, H. S. Hinton, and E. Kerbis, "A six stage digital free-space optical switching network using S-SEEDs", submitted to Appl. Opt. (1992).

23) N. Streibl, "Beam shaping with optical array generators", J. Mod. Opt. **36**, 1559 (1989).

24) H. Dammann and K. Görtler, "High-efficiency in-line multiple imaging by means of multiple phase holograms", Opt. Commun. **3**, 312 (1971).

25) A. Vasara, M. R. Taghizadeh, J. Turunen, J. Westerholm, E. Noponen, H. Ichikawa, J. M. Miller, T. Jaakola, and S. Kuisma, "Binary surface-relief gratings for array illumination in digital optics", Appl. Opt. **31**, 3320 (1992).

26) F. B. McCormick, "Generation of large spot arrays from a single laser beam by means of multiple imaging", Opt. Eng. **28**, 299 (1989).

27) M. P. Dames, R. J. Dowling, and D. Wood, "Efficient optical elements to generate intensity weighted spot arrays: design and fabrication", Appl. Opt. **30**, 2685 (1991).

28) N. C. Craft and A. Y. Feldblum, "Optical interconnects based on arrays of surface-emitting lasers and lenslets", Appl. Opt. **31**, 1735 (1992).

29) F. B. McCormick, F. A. P. Tooley, T. J. Cloonan, J. M. Sasian, and H. S. Hinton, "Microbeam optical interconnections using microlens arrays", *OSA Topical Meeting on Photonic Switching*, Salt Lake City (1989).

30) S. Wakelin, Design and construction of a free-space digital optical information processor, Ph.D Thesis, Physics Department, Heriot-Watt University, Edinburgh (1992).

31) J. W. Goodman, "Fan-in and fan-out with optical interconnections", Optica Acta **32**, 1489 (1985).

32) W. T. Welford and R. Winston, High Collection Nonimaging Optics, Academic Press (1989).

33) M. E. Prise, N. Streibl, and M. M. Downs, "Optical considerations in the design of digital optical computers", Opt. and Quant. Elect. **20**, 49 (1988).

34) J. Shamir, H. J. Caufield, and R. B. Johnson, "Massive holographic interconnection networks and their limitations", Appl. Opt. **28**, 311 (1989).

35) J. R. Leger, G. J. Swanson, and W. B. Veldkamp, "Coherent laser addition using binary phase gratings", Appl. Opt. **26**, 4391 (1987).

36) C. W. Stirk, R. A. Athale, M. W. Haney, "Folded perfect shuffle optical processor", Appl. Opt. 27, (1991).

37) G. Eichmann and Y. Li, "Compact optical generalized perfect shuffle", Appl. Opt. **26**, 1111 (1987).

38) N. Davidson, A. A. Friesem, and E. Hasman, "Realization of perfect shuffle and inverse perfect shuffle transforms with holographic elements", Appl. Opt. **31**, 1810 (1992).

39) H. Kobolla, N. Lindlein, O. Falkenstorfer, S. Rosner, J. Schmidt, J. Schwider, N. Streibl, and R. Volkel, "Optoelectronic interconnects with holographic optical elements", *Third International Conference on Holographic Systems and Applications*, IEE Conference Publication **342** (1991).

40) F. B. McCormick and M. E. Prise, "Optical circuitry for free-space interconnections", Appl. Opt. **29**, 2013 (1990).

41) J. Jahns, "Optical implementation of the Banyan network", Opt. Commun. **76**, (1990).

42) J. Jahns and M. J. Murdocca, "Crossover networks and their optical implementation", Appl. Opt. **27**, 3155 (1988).

43) F. A. P. Tooley, T. J. Cloonan, and F. B. McCormick, "On the use of retro-reflector arrays to implement crossover interconnections between arrays of S-SEED logic gates", Opt. Eng. **30**, 1969 (1990).

44) M. Murdocca, "Connection routing for microoptic systems", Appl. Opt. **29**, 1106 (1990).

45) J. Jahns and B. A. Brumback, "Integrated optical split-and-shift module based on planar optics", Opt. Commun. **76**, 318 (1990).

46) K. H. Brenner and A. W. Lohmann, "Cyclic shifting for optical data processing", Appl. Opt. **27**, 434 (1988).

47) B. K. Jenkins, A. A. Sawchuk, T. C. Strand, R. Forcheimer, and B. H. Soffer, "Sequential optical logic implementation", Appl. Opt. **23**, 3455 (1984).

48) H. J. White, "Experimental results from an optical implementation of a simple neural network", *Optics in Computing*, IEE Tech. Digest 122 (1988).

49) D. C. O'Brien, W. A. Crossland, and R. J. Mears, "A holographically routed optical crossbar: theory and simulation", Opt. Comp. and Proc. **1**, 233 (1991).

50) T. H. Barnes, T. Eiju, K. Matsuda, H. Ichikawa, M. R. Taghizadeh, and J. Turunen, "Reconfigurable holographic optical interconnections using a phase only nematic liquid crystal spatial light modulator", *Third International Conference on Holographic Systems and Applications*, IEE Conference Publication **342** (1991).

51) A. K. Ghosh, "Alignability of optical interconnects", Appl. Opt. **29**, 5253 4(1990).

52) J. L. Brubaker, F. B. McCormick, F. A. P. Tooley, J. M. Sasian, T. J. Cloonan, A. L. Lentine, S. J. Hinterlong, and M. J. Herron, "Optomechanics of a free-space photonic switch: the components", Proc. Soc. Phot. Opt. Inst. Eng. **1533**, 91 (1991).

Chapter 2

Theoretical Analysis of Volume Phase Holograms

2.1 Introduction

The following chapter will outline some of the basic theoretical aspects of optically recorded volume phase holograms using an analysis based on coupled wave theory. A volume hologram may be defined as any holographic component which has a grating structure extending continuously throughout a region of space. This typically results in the component exhibiting Bragg regime diffraction; efficient wavefront reconstruction only being obtained when the Bragg condition of the grating is satisfied. As a consequence, volume holograms tend to display a strong angular and spectral selectivity.

The diffractive properties of holographic volume gratings were first successfully modelled by Kogelnik in 1969 [1]. In order to simplify his analysis Kogelnik made a number of approximations. Firstly, only two wavefronts were assumed to be present; the incident wavefront and the first order diffracted wavefront. In addition, the analysis was restricted to the case where the interchange of energy between these two waves occurred over a distance much greater than the grating period. By solving the Helmholtz equation for light propagating through a medium having a periodic sinusoidal variation in its complex permittivity, Kogelnik derived a pair of coupled first-order differential equations from which the rate of interchange of energy (with respect to distance) could be calculated. A series of analytical solutions were then developed describing the behaviour of transmission and reflection gratings at on and off-Bragg incidence. The analysis was also extended to examine the effect of reconstructing the hologram with both TE and TM polarised light.

Due to its intuitive simplicity, and the ease with which it may be computationally implemented, Kogelnik's two-wave first-order coupled-wave theory has since become the basis for a number of more accurate models which have included such effects as second-order terms [2], higher diffraction orders [3,4], absorption during recording leading

to a variation in modulation with depth [5,6], nonuniformities [7-9], vector effects [10,11] and multiple gratings [8,12-16]. A review of these various subjects is contained in references [17,18]. More exact models based on either a rigourous modal expansion [19] or a rigourous coupled-wave analysis [2,18] have also been derived, along with a variety of models based on thin grating decomposition [14,20]. In general, however, these more rigourous models are difficult to implement as they require both elaborate and time consuming calculations. Coupled-wave theory, on the other hand, although making several approximations not wholly valid for practical holographic components, is straightforward to use and gives accurate results for reconstruction at, or close to, the Bragg angle. The theory is, however, only applicable in the case of thick holographic gratings, i.e., the thickness of the hologram must be much larger than the grating period. In the case of the interconnects recorded during the course of this thesis, this condition was always met.

A brief outline of coupled wave theory will be presented in the following chapter. The analysis will concentrate on volume phase transmission holograms, covering such points as their diffraction efficiency, polarisation dependence and angular sensitivity. For a more comprehensive review of the theoretical aspects of volume holography, the reader should refer to references [17] and [18].

2.2 Coupled wave analysis

Conventional optically recorded holograms are produced by exposing a photosensitive medium to the interference pattern produced by two coherent wavefronts; an object beam derived from light scattered from the subject being recorded and a reference beam. Subsequent processing of the recording medium converts this interference pattern into a spatial variation in complex permittivity which contains information of both the amplitude and phase of the object wavefront. Replaying the hologram with the same reference beam can therefore result in the complete reconstruction of the object wavefront.

In principle, optically recorded holograms can be fabricated using completely arbitrary wavefronts. As a result of this flexibility, holographic components may be fabricated which are capable of implementing highly complex interconnection patterns. For simplicity, however, the following analysis will restrict itself to the case of a volume hologram of thickness, d, recorded using two infinite plane waves. Both the object and

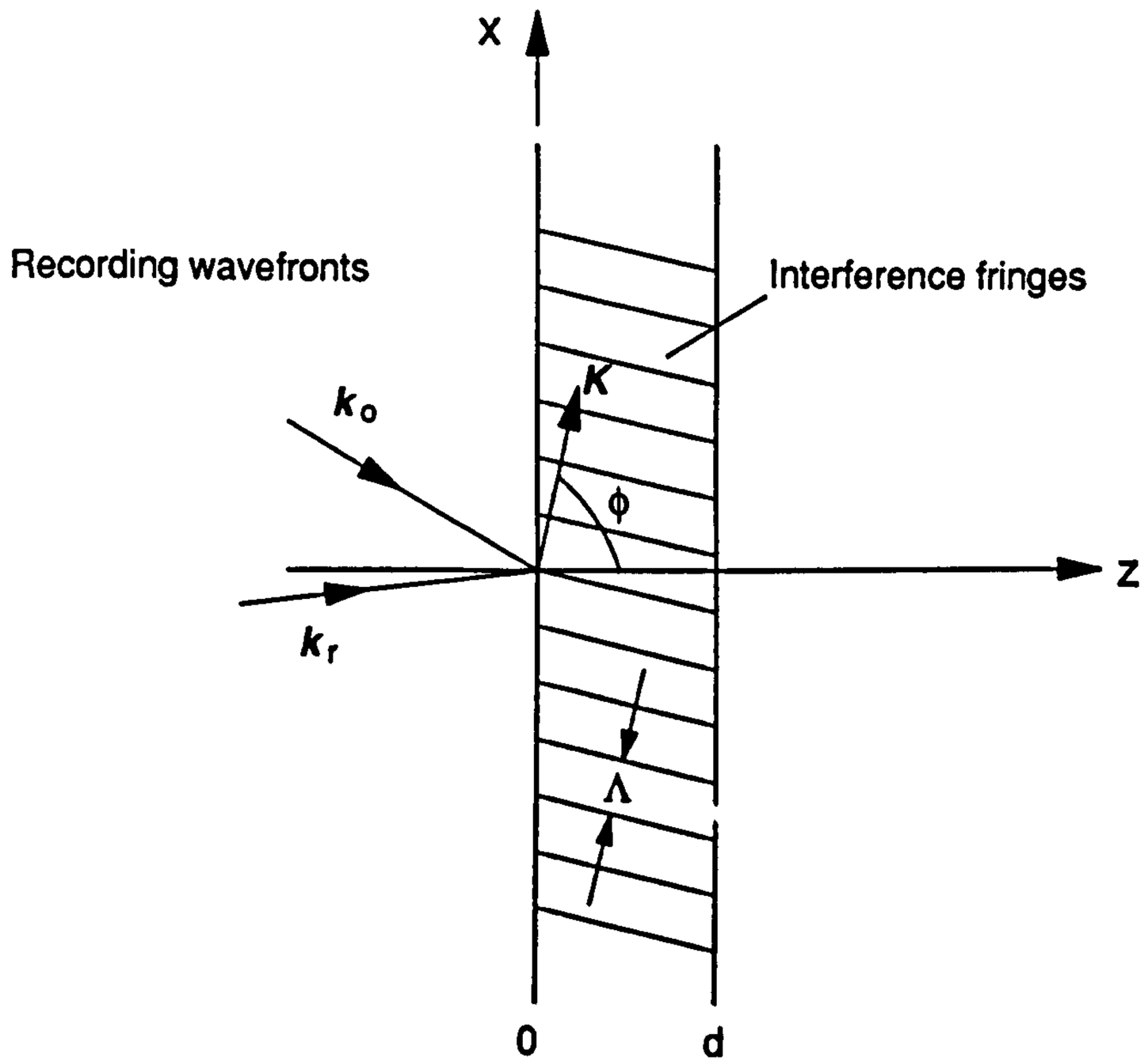

Figure 2.1 - Volume hologram recording geometry. $\mathbf{k}_o$ *: Object wave vector;* $\mathbf{k}_r$ *: Reference wave vector;* $\mathbf{K}$ *: Grating vector;* Λ *: Grating period.*

reference waves are taken to be incident in the xz plane and the same average relative permittivity is assumed to exist both inside and outside the grating boundaries (figure 2.1). The resulting interference fringes will therefore be orientated perpendicular to the plane of incidence and slanted with respect to the z-axis at an angle of ϕ. If $\mathbf{k}_o$ and $\mathbf{k}_r$ represent the propagation vectors of the recording wavefronts, then the intensity pattern caused by the interference between these two waves will be given by

$$I(x,z) = I_o + I_r + \sqrt{I_o I_r}\cos[(\mathbf{k}_r - \mathbf{k}_o)\cdot\mathbf{r}] \tag{2.1}$$

where I_o is the intensity of the object beam, I_r is the intensity of the object beam, and $\mathbf{r}$ is a position vector. Subsequent development of the hologram will convert the above intensity distribution into a periodic variation in the complex permittivity. This can be best described through the use of the grating vector, $\mathbf{K}$, which is aligned perpendicularly to the fringe planes and has a magnitude of $|\mathbf{K}| = 2\pi/\Lambda$, where Λ is the period of the grating. Ideally,

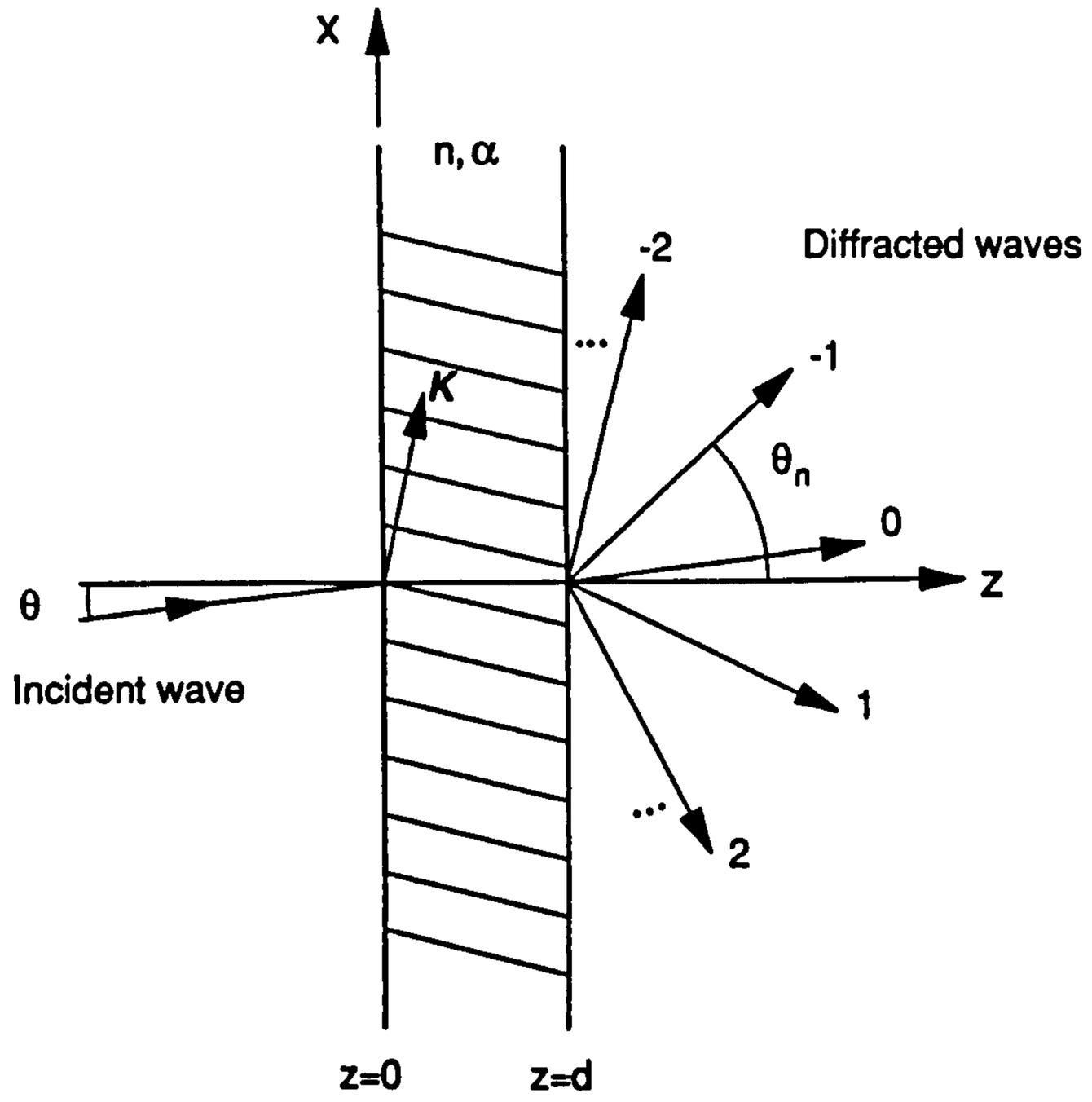

Figure 2.2 - Volume hologram replay geometry.

when such a grating is reconstructed with a plane wavefront, light will be diffracted from the incident beam into the object beam, although inevitably some fraction of the incident light ends up being diffracted into higher diffraction orders. The efficiency with which this process occurs can be found by solving the wave equation for light propagating through a periodic variation in the complex permittivity. The wave equation may be written as

$$\nabla^2\mathbf{E} - \nabla(\nabla \cdot \mathbf{E}) + \gamma(\mathbf{r})^2\mathbf{E} = 0 \tag{2.2}$$

where $\gamma(\mathbf{r})$ is the propagation constant of the hologram. Note that as we are dealing with an inhomogeneous medium, the term $\nabla(\nabla \cdot \mathbf{E})$ does not automatically reduce to zero. The propagation constant of the hologram is related to the relative permittivity, $\varepsilon(\mathbf{r})$, and the conductivity, $\sigma(\mathbf{r})$, of the grating by

$$\gamma(\mathbf{r})^2 = \omega^2\mu\varepsilon_o\varepsilon(\mathbf{r}) - j\omega\mu\sigma(\mathbf{r}) \tag{2.3}$$

where ε_o is the relative permittivity of free space and ω is the angular frequency of the replay wavefront. For simplicity the recording medium will be taken to be non-magnetic, thus the permeability of the grating, μ, is equal to that of free space, μ_o. In the following discussion it will be assumed that an infinite plane wave is incident on the hologram in the xz plane at an angle of θ with respect to the z-axis, as illustrated in figure 2.2. In addition, the reconstruction wavefront will be initially considered to be polarised normally to the plane of incidence (TE polarisation). Under these conditions $\nabla(\nabla \cdot \mathbf{E}) = 0$, and the resulting propagation of the replay wavefront through the hologram can be described using the scalar wave equation

$$\nabla^2 E(x,z) + \gamma(x,z)^2 E(x,z) = 0 \tag{2.4}$$

in which $E(x,z)$ is the complex amplitude of the y component of the electric field. In practice, it is more common to work with the refractive index, $n(x,z)$, and absorption constant, $\alpha(x,z)$, of holographic and optical materials. These are given by

$$\gamma(x,z) = (\omega/c)\, n(x,z) + \alpha(x,z) \tag{2.5}$$

where c is the speed of light within a vacuum. If the recording material has a linear response, then the change in refractive index and absorption will be directly proportional to the local exposure energy, $I(x,z)t$, where t is the exposure time. In the case of a hologram recorded using two infinite plane waves, as illustrated in figure 2.1, it follows that

$$n(x,z) = n_o + n_1 \cos(\mathbf{K} \cdot \mathbf{r}) \tag{2.6}$$

and

$$\alpha(x,z) = \alpha_o + \alpha_1 \cos(\mathbf{K} \cdot \mathbf{r}) \tag{2.7}$$

where n_o is the average refractive index, α_o is the average absorption, and n_1 and α_1 are the modulation amplitudes of these two terms. For simplicity, $n(x,z)$ and $\alpha(x,z)$ have

been considered to be modulated in phase. If the restrictions $2\pi n_o/\lambda \gg \alpha_1$, $\pi n_o/\lambda \gg \alpha_o$ and $n_o \gg n_1$ are met (i.e., the bulk absorption, and the modulation in absorption and refractive index are small), we can combine equations (2.5), (2.6) and (2.7) to obtain an expression for $\gamma(x,z)^2$ of the form

$$\gamma(x,z)^2 = \beta^2 - 2j\alpha_o\beta + 2\kappa\beta(\exp(j\mathbf{K}\cdot\mathbf{r}) + \exp(-j\mathbf{K}\cdot\mathbf{r})) \tag{2.8}$$

where we have used the substitions $\beta = 2\pi n_o/\lambda$, which denotes the average propagation constant of the hologram, and

$$\kappa = (\pi n_1/\lambda - j\alpha_1/2) \tag{2.9}$$

κ is generally referred to as the coupling constant of the grating and is of central importance to coupled wave theory as it defines the strength of the interaction between the various waves as they propagate through the hologram.

The next important question which must be considered is how do we express the total field, $E(x,z)$, within the grating. As was shown by Gaylord and Moharam [18], a number of alternative field expansions exist which, although completely equivalent, give rise to different sets of coupled-wave equations. In the following analysis we shall assume that the grating is bounded on both sides by a medium of the same average refractive index, n_o. On reconstruction, a plane wave $E_o \exp(-j\mathbf{k}_o \cdot \mathbf{r})$ is incident on the grating at an angle of θ with respect to the z-axis. Since the permittivity is periodic along the x-axis, i.e., $\varepsilon(x) = \varepsilon(x + \Lambda')$ for all x where $\Lambda' = \Lambda/\sin\phi$, it follows that the total field may be expanded as a Fourier series in the x-direction [21]

$$E(x,z) = E_o \sum_{i=-\infty}^{\infty} C_i(z) \exp[-j(v - iK\sin\phi)x] \tag{2.10}$$

where C_i is the normalized amplitude of the *ith* space-harmonic component and v is a phase factor. As the undiffracted ($i = 0$) beam must be phase matched to the incident beam at

the z = 0 boundary in the limit of zero grating modulation (i.e., the x components of the incident and diffracted propagation vectors must be equal), the condition $\nu = k_o \sin\theta$ must be met. Thus, we may write

$$E(x,z) = E_o \sum_{i=-\infty}^{\infty} C_i(z) \exp[-j(k_o \sin\theta - iK \sin\phi)x] \tag{2.11}$$

This is the fundamental coupled wave expansion of the total field within the grating and depicts the field as a series of inhomogeneous plane waves propagating in the x-direction. By defining a new function

$$A_i(z) = C_i \exp[-j(iK\cos\phi - k_{oz})z] \tag{2.12}$$

and rewriting equation (2.11) we obtain a new representation for the total field within the grating which may be written in vector form as

$$E(x,z) = \sum_{i=-\infty}^{\infty} A_i(z) \exp(-j\mathbf{k}_i \cdot \mathbf{r}) \tag{2.13}$$

where

$$\mathbf{k}_i = \mathbf{k}_o - i\mathbf{K} \tag{2.14}$$

This field expansion, which was used by Kogelnik in his original analysis, is commonly referred to as K-vector closure. The incident wavefront can be considered to be split into a series of inhomogeneous plane waves with propagation vectors defined by equation (2.13). This expansion has the advantage of producing constant coefficient differential equations which are relatively straightforward to solve. In addition, considering the field within the grating to be comprised of a series of plane waves is also intuitively appealing. A detailed discussion of the various alternative field representations is given in reference [18].

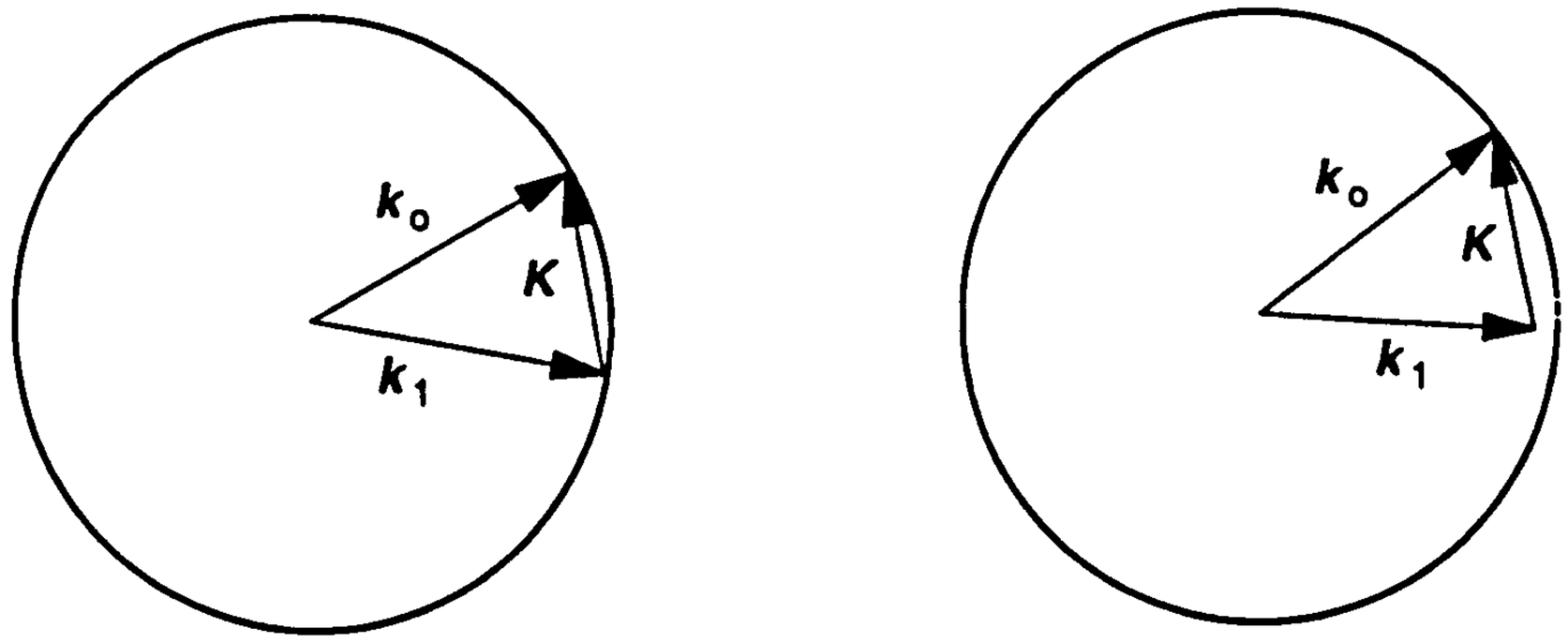

(a) (b)

Figure 2.3 - K vector closure diagram for (a) on-Bragg reconstruction and (b) off-Bragg reconstruction.

In order to calculate the direction of the diffracted beams as they exit the grating we must first phase match the *ith* space harmonic field within the hologram with the *ith* diffraction order outside the hologram. This requires that the x-components of the wave vectors in both regions be equal. Defining the angle of propagation of the *ith* diffraction order outside the grating region to be θ_i, we obtain the classic grating equation

$$\sin\theta_i = \sin\theta - i(\lambda/\Lambda)\sin\phi \tag{2.15}$$

Maximum diffraction efficiency occurs when the Bragg diffraction condition is met. This may be expressed as

$$\cos(\phi - \theta) = K/2\beta \tag{2.16}$$

The vector relationship described by equation (2.14) is shown in figure 2.3 for on-Bragg reconstruction (figure (2.3(a)) and for off-Bragg reconstruction (figure 2.3(b)). By substituting equations (2.8) and (2.14) into equation (2.4) we obtain

$$\sum_{i=-\infty}^{\infty} \exp(-j\mathbf{k}_i \cdot \mathbf{r})\left[\frac{d^2A_i}{dz^2} + 2jk_{iz}\frac{dA_i}{dz} - A_i k_i^2 + A_i\beta^2 - j\alpha_o\beta A_i\right]$$

$$+ \sum_{i=-\infty}^{\infty} 2\kappa\beta \exp(-j\mathbf{k}\cdot\mathbf{r})\left[\exp(j\mathbf{K}\cdot\mathbf{r}) + \exp(-j\mathbf{K}\cdot\mathbf{r})\right] = 0 \qquad (2.17)$$

If the energy interchange between the waves as they propagate through the hologram is slow, the second derivative may be neglected. Thus equation (2.17) reduces to the following infinite set of differential equations

$$k_{iz}/\beta\frac{dA_i}{dz} + \alpha_o A_i + j\kappa[A_{i+1} + A_{i-1}] + A_i[\beta^2 - k_i^2] = 0 \qquad (2.18)$$

It can be seen from equation (2.18) that the periodic modulation in refractive index results in the *ith* diffraction order to be coupled to both the *i+1* and *i-1* orders. This leads to energy interchange between the orders as they propagate through the hologram, the strength of this interaction being determined by the coupling constant, κ. The effects of absorption and off-Bragg reconstruction are also accounted for in the second and fourth terms of equation (2.18) respectively.

2.3 Two-wave first order coupled-wave theory

In the case of a thick holographic grating the effect of the higher diffracted orders may be ignored as, generally, they do not satisfy the Bragg conditions which lead to efficient diffraction. Under these conditions, only the first and zeroth orders need be considered. This reduces the coupled wave equations to

$$c_R\frac{dA_o}{dz} - \alpha_o A_o - j\kappa A_1 = 0 \qquad (2.19)$$

$$c_S\frac{dA_1}{dz} - (\alpha_o + j\Theta)A_1 + j\kappa A_o = 0 \qquad (2.20)$$

where c_R and c_S are commonly referred to as the obliquity factors of the grating [1]

$$c_R = K_z/\beta = \cos\theta \tag{2.21}$$

$$c_S = K_x/\beta = \cos\theta - (K/\beta)\cos\phi \tag{2.22}$$

and

$$\Theta = (\beta^2 - k_1^2)/2\beta \tag{2.23}$$

The expression, Θ, is referred to as the dephasing term. This describes the effect that either an angular, or wavelength change has on the diffraction efficiency of the hologram. For a deviation away from the Bragg condition, the reconstructed beam $A_1(z)$ is driven out of synchronisation with $A_o(z)$, thereby leading to a decrease in the interaction between the two wavefronts.

For simplicity we shall restrict the rest of this analysis to the case of a pure phase transmission grating, i.e., $\alpha_o = 0$ and $\alpha_1 = 0$ when it is replayed with a unit amplitude reference wavefront. This results in boundary conditions for the hologram of $A_o(0) = 1$, and $A_1(0) = 0$. Solving the coupled differential equations (2.19) and (2.20) gives a solution for the amplitude of the object wave of

$$A_1(z) = -j(c_R/c_S)^{1/2}\exp(-j\mu)\sin(\nu^2+\mu^2)^{1/2}(1+\mu^2/\nu^2)^{-1/2} \tag{2.24}$$

where

$$\nu = \pi n_1 d/\lambda(c_R c_S)^{1/2} \tag{2.25}$$

$$\mu = \Theta d/2c_S \tag{2.26}$$

A first order Taylor expansion of equation (2.23) in terms of $\Delta\theta$, and $\Delta\lambda$, gives an expression for Θ which is accurate for small deviations in replay angle and reconstruction wavelength

$$\Theta = \Delta\theta K \sin(\phi - \theta) - \Delta\lambda K^2/4\pi n_o \tag{2.27}$$

Thus equation (2.26) may be written as

$$\mu = (d/2c_s)\,(\Delta\theta K \sin(\phi - \theta) - \Delta\lambda K^2/4\pi n_o) \tag{2.28}$$

Defining the diffraction efficiency of the grating, η, as the amount of transmitted power which ends up in the object beam, then

$$\eta = |c_s|/c_R\, A_{-1}(z) A^*_{-1}(z) \tag{2.29}$$

from which it follows that

$$\eta = \sin^2(\nu^2 + \mu^2)^{1/2}/(1 + \mu^2/\nu^2) \tag{2.30}$$

This describes the efficiency close to or at the Bragg reconstruction angle. It takes into account the effect of a deviation in both wavelength and replay angle from the optimum reconstruction conditions. Note, however, that this analysis is only valid for a change in θ in the xz plane. In practice an interconnect may be required to handle an arbitrary incidence angle. This requires a three-dimensional vector coupled wave analysis of the replay geometry (see, for example, the work of Solymar and Cooke [17], Moharam and Gaylord [10] and Syms [11]) which is outside the scope of this thesis. Nonetheless, the angular performance of a holographic interconnect may be calculated to a first approximation using the above equations.

Finally, during this previous analysis it was assumed that the index modulation, n_1, varied linearly with exposure, i.e., $n_1 = \tau\xi$, where τ is the constant of linearity. The diffraction efficiency of a simple plane grating being replayed exactly on Bragg should therefore vary with exposure, ξ, according to the relationship

$$\eta = \sin^2[\pi d\tau\xi/\lambda(c_R c_S)^{1/2}] \tag{2.31}$$

From equation (2.31) it can be seen that the diffraction efficiency varies sinusoidally with exposure, and that for the correct index modulation, 100% conversion of the incident light into the first diffraction order is possible. In practice, however, the variation of diffraction efficiency with exposure will follow a more complex relationship due to saturation of the refractive index modulation [22] and the presence of higher diffraction orders [2]. This problem will be dealt with in chapter 3 in relation to the theoretical and experimental exposure response of DCG.

2.4 Validity of coupled wave theory

As mentioned in the introduction to this chapter, in order for a coupled wave analysis to be valid, the grating must be holographically thick. Only under this condition may the effects of the higher diffraction orders be ignored. A number of criteria for defining whether a grating falls into this regime or not have been developed. Kogelnik used the thickness or Q factor [1],

$$Q = 2\pi\lambda d/n_o\Lambda^2 \tag{2.32}$$

where λ is the replay wavelength and d is the physical thickness of the hologram. If $Q >> 1$ (i.e., the spacing of the fringes is small with respect to the thickness) the hologram may be considered as holographically thick. In the case of weakly, or strongly modulated gratings, however, this criteria fails to predict whether a hologram will exhibit Bragg diffraction or not. Moharam and Young [23] introduced a further parameter

$$p = \lambda^2 / n_0 n_1 \Lambda^2 \tag{2.33}$$

which takes into account the strength of the index modulation. If p ≥ 10, then the grating may be analysed using coupled wave theory. Magnusson and Gaylord [24] have investigated the various diffraction regimes which a transmission grating may fall into; (i) the Bragg regime, (ii) the thin grating regime, which may be described using amplitude transmittance theory, and (iii) an intermediate regime in which more complex theories, such as multi-wave coupled-wave theory are required. Their analysis showed that two-wave coupled wave theory may be used to model the behaviour of a volume grating if both the thickness parameter and the p parameter conditions are satisfied.

Typical experimental parameters for the DCG interconnects fabricated during the course of this thesis were λ = 500nm to 1 μm, n_1 = 0.02 to 0.04, d = 15μm, n_o = 1.5, and Λ = 1μm. This results in a Q parameter of between 5 and 20, and a p parameter of between 15 and 30, thus the interconnects fall within the regime covered by two-wave coupled wave theory. In practice it was found that some power did end up in the higher diffraction orders, however, this was typically only one or two percent of the total transmitted light.

2.5 Polarisation dependence of a volume hologram

The previous analysis was restricted to the case where the incident light was polarised perpendicular to the plane of incidence (TE polarisation). In some applications, however, an interconnect may be required to operate with both TE and TM polarised light. It is therefore important that it diffracts both polarisations with the same efficiency. To analyse this problem, let us consider the situation of a pure phase grating where the incident light is polarized in the plane of incidence. Firstly, the wave equation must be written in its full vector form

$$\nabla^2 \mathbf{E} - \nabla(\nabla \cdot \mathbf{E}) + \gamma^2 \mathbf{E} = 0 \tag{2.34}$$

where **E** is now a vector quantity. Again assuming that only the reference and object waves are present, the field within the hologram becomes

$$\mathbf{E} = A_0(z)\mathbf{a}_0 \exp(-j\mathbf{k}_0 \cdot \mathbf{r}) + A_1(z)\mathbf{a}_1 \exp(-j\mathbf{k}_1 \cdot \mathbf{r}) \tag{2.35}$$

where $A_0(z)$ and $A_1(z)$ are the amplitudes of the two waves and $\mathbf{a}_0$ and $\mathbf{a}_1$ are their polarization vectors. These are normalised such that

$$(\mathbf{a}_0 \cdot \mathbf{a}_0) = 1 \quad , \quad (\mathbf{a}_1 \cdot \mathbf{a}_1) = 1 \tag{2.36}$$

Kogelnik showed that the resulting coupled wave equations were identical to equations (2.19) and (2.20), with the exception of a modified coupling constant [1]. Thus, in the case of exact Bragg reconstruction, (2.31) may be rewritten as

$$\eta = \sin^2 [\pi n_1 d (\mathbf{a}_0 \cdot \mathbf{a}_1)/\lambda (c_R c_S)^{1/2}] \tag{2.37}$$

It therefore follows that a volume phase grating will, in general, exhibit different diffraction efficiencies for TE and TM polarised waves. Typically this difference will be small compared to the effect of the different Fresnel transmission coefficients.

Most of the interconnects investigated during the course of this thesis were recorded using a normally incident object beam and a reference beam incident at an angle θ. Under these conditions, equation (2.37) reduces to

$$\eta = \sin^2 [\pi n_1 d \cos(\sin^{-1}(\sin(\theta)/n_o))/\lambda (c_R c_S)^{1/2}] \tag{2.38}$$

where n_o is the bulk refractive index of the grating. The polarisation dependence of such a grating was evaluated for a number of reference beam angles. The results of these calculations, shown plotted in figure 2.4, illustrate that even at relatively high reference beam angles the difference in diffraction efficiency for a TE polarised wave, η_{TE}, and a TM polarised wave, η_{TM}, is small. Take, for example, the polarisation dependence of a grating recorded with a reference beam angle of 45°, as illustrated in figure 2.4(c). From this curve it can be seen that when $n_1 = 0.00775$, $\eta_{TE} = 100\%$ and $\eta_{TM} = 96.4\%$, thus the difference in efficiency is only 3.6%. At higher angles, however, this difference becomes more noticeable. If the incident and diffracted beams are at 90° to eachother,

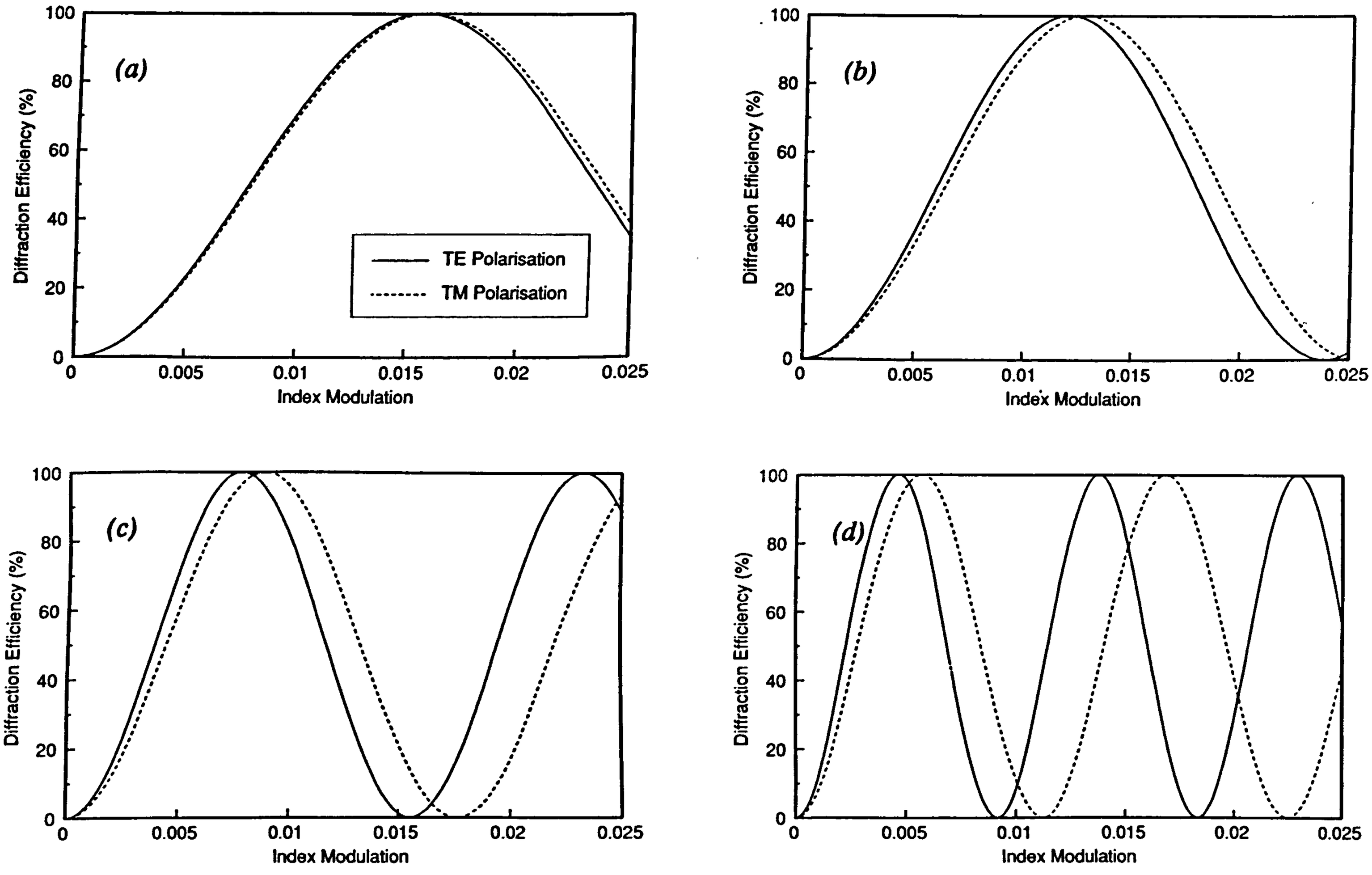

Figure 2.4 - Dependence of diffraction efficiency on index modulation for TE and TM polarised light. These curves were calculated using typical DCG grating parameters of $n = 1.5$, $d = 15\mu m$, $\lambda = 514.5nm$. *(a)* $\theta_r = 15°$, *(b)* $\theta_r = 30°$, *(c)* $\theta_r = 45°$, and *(d)* $\theta_r = 60°$.

(i.e.,$(\mathbf{a}_0 \cdot \mathbf{a}_1)=0$), the efficiency for a TM polarised wave falls to zero. A number of prototype polarising beam splitters utilising this property have been developed [8,11]. In addition, a compact polarisation dependent space-variant interconnection network based on this effect was discussed by Kato et al [25].

As discussed on page 31, the performance of a holographic interconnect when replayed at an arbitrary replay angle can only be fully analysed using rigourous vector analysis. This approach must also be used to calculate the effect that an arbitrary polarisation has when the exact Bragg replay conditions are not met [10,17].

2.6 Simultaneous replay with reference and object beams

Work has been done which on the behaviour of volume gratings when they are replayed with several coherent beams. In particular, Case [26] used coupled wave theory to analyse Bragg diffraction of light by a volume phase hologram consisting of two incoherently recorded gratings which had a common Bragg angle. Kondilenko et al. [27] also used coupled wave theory to investigate diffraction from an unslanted grating (fringes normal to the hologram surface) when it was simultaneously replayed by an object and a reference beam.

In the following analysis we shall again consider the case of a slanted phase grating recorded with a plane reference wave, $\mathbf{k}_r$, and a plane object wave, $\mathbf{k}_o$ as shown in figure 2.1. When both replay object and reference beams are on Bragg, Kogelnik's coupled differential equations reduce to

$$c_R \frac{dA_0(z)}{dz} = -j\kappa A_1(z) \tag{2.39}$$

$$c_S \frac{dA_1(z)}{dz} = -j\kappa A_0(z) \tag{2.40}$$

where $\kappa = \pi n_1/2\lambda$, and n_1 is the index modulation. Introducing the boundary conditions, $A_0(0) = B\exp[j\phi_1]$ and $A_1(0) = C\exp[j\phi_2]$, results in a solution for $A_0(z)$ and $A_1(z)$ of the

form

$$A_0(z) = B\exp(j\phi_1)\cos(\chi z) - j(c_S/c_R)^{1/2} C\exp(j\phi_2)\sin(\chi z) \tag{2.41}$$

and

$$A_1(z) = C\exp(j\phi_2)\cos(\chi z) - j(c_R/c_S)^{1/2} B\exp(j\phi_1)\sin(\chi z) \tag{2.42}$$

This gives the complex amplitude of the reference and object beams as they diffract through the hologram. The irradiances of these beams at the output plane (z = d) will therefore be given by

$$I_s = |A_1(d)|^2 = C^2\cos^2(\chi d) + (c_R/c_S)B^2\sin^2(\chi d)$$

$$+ 2BC(c_R/c_S)^{1/2}\cos(\chi d)\sin(\chi d)\sin(\psi) \tag{2.43}$$

and

$$I_r = |A_o(d)|^2 = B^2\cos^2(\chi d) + (c_S/c_R)A^2\sin^2(\chi d)$$

$$- 2BC(c_S/c_R)^{1/2}\cos(\chi d)\sin(\chi d)\sin(\psi) \tag{2.44}$$

where $\chi = \kappa/(c_R c_S)^{1/2}$ and $\psi = \phi_1 - \phi_2$. The phase difference, ψ, can be interpreted in two ways. In the above analysis it represents the relative phase difference between the object and reference beams at (x,z) = (0,0). Kondilenko [27], however, carried out a similar derivation in which ψ represented the phase shift between the holographic grating and the object/reference wave interference pattern. Both approaches give identical results.

At z = 0, the object and reference beam irradiances are given by $I_{oo} = |A_o(0)|^2 = B^2$ and $I_{ro} = |A_1(0)|^2 = C^2$. Thus equations (2.43) and (2.44) reduce to

$$I_s = (1-\eta)I_{oo} + \eta(c_R/c_S)I_{ro} + 2(I_{ro}I_{oo})^{1/2}(c_R/c_S)^{1/2}(\eta(1-\eta))^{1/2}\sin(\psi) \qquad (2.45)$$

and

$$I_r = (1-\eta)I_{ro} + \eta(c_S/c_R)I_{oo} + 2(I_{ro}I_{oo})^{1/2}(c_R/c_S)^{1/2}(\eta(1-\eta))^{1/2}\sin(\psi) \qquad (2.45)$$

where the diffraction efficiency of the grating is defined as $\eta = \sin^2(\chi d)$. These two equations relate the intensities of the object and reference beams at z = d to the relative phase difference between the beams at the grating origin.

A compact optical modulator which utilises this effect is proposed in Appendix 1 of this thesis. The modulator consists of two identical, 50% efficient volume phase holograms stacked together. By varying the optical path length between the two holograms it is possible to control the amount of light ending up in the zeroth and first diffraction orders.

2.7 References

1) H. Kogelnik, "Coupled wave theory for thick hologram gratings", Bell System Technical Journal **48**, 2909 (1969).

2) M. G. Moharam and T. K. Gaylord, "Coupled-wave analysis of planar grating diffraction", J. Opt. Soc. Am. **71**, 811 (1981).

3) R. Magnusson and T. K. Gaylord, "Analysis of multiwave diffraction of thick holograms", J. Opt. Soc. Am. **67**, 1165 (1977).

4) R. Alferness and S. K. Case, "Coupling in doubly exposed thick holographic gratings", J. Opt. Soc. Am. **65**, 730 (1977).

5) T. Kubota, "Characteristics of thick hologram grating recorded in absorptive medium", Optica Acta **25**, 1035 (1978).

6) R. Kowarschik, "Diffraction efficiency of attenuated sinusoidally modulated gratings in volume holograms", Optica Acta **23**, 1039 (1976).

7) T. Kubota, "The bending of interference fringes inside a hologram", Optica Acta **26**, 731 (1979).

8) I. R. Redmond, Holographic optical elements in dichromated gelatin, Ph.D. Thesis, Physics Department, Heriot-Watt University (1989).

9) J. C. W. Newell, Optical holography in dichromated gelatin, Ph.D. Thesis, Physics department, University of Oxford, U.K. (1987).

10) M. G. Moharam and T. K. Gaylord, "Three-dimensional vector coupled-wave analysis of planar-grating diffraction", J. Opt. Soc. Am. **73**, 1105 (1983).

11) R. R. A. Syms, "Vector effects in holographic optical elements", Optica Acta **32**, 1413 (1985).

12) H. P. Herzig, P. Ehbets, D. Prongue and R. Dandliker, "Fan-out elements by multiple beam recording in volume holograms", *Holographic Optics III: Principles and Applications*, Proc. SPIE **1507**, (1991).

13) R. Kostuk, "Comparison of models for multiplexed holograms", Appl. Opt. **28**, 771 (1989).

14) H. Ichikawa, Optical beam array generation with phase gratings, Ph.D. Thesis, Physics Department, Heriot-Watt University (1991).

15) S. Case, "Coupled-wave theory for multiply exposed holographic gratings", J. Opt. Soc. Am. **65**, 724-729 (1975).

16 L. Solymar, "Two dimensional N coupled wave theory for volume holograms", Opt. Commun. **23**, **199** (1977).

17) L. Solymar and D. J. Cooke, Volume holography and volume gratings, Academic Press (1981).

18) T. K. Gaylord and M. G. Moharam, "Analysis and applications of optical diffraction by gratings", Proc. IEEE **73**, 894 (1985).

19) F. G. Kaspar, "Diffraction by thick periodically stratified gratings with complex dielectric constant", J. Opt. Soc. Am. **63**, 37 (1973).

20) R. Alferness, "Analysis of optical propagation in thick holographic gratings", Appl. Phys. **7**, 29 (1975).

21) D. Maystre, "Rigourous vector theories of diffraction gratings", in Progress in Optics, Volume XXI, Editor E. Wolf, North-Holland Physics Publishing (1984).

22) L. T. Blair and L. Solymar, "Grating profiles in dichromated gelatin", Opt. Commun. **77**, 365 (1990).

23) M. G. Moharam and L. Young, "Criteria for Bragg and Raman-Nath regime", Appl. Opt. **17**, 1757 (1978).

24) R. G. Magnusson and T. K. Gaylord, "Diffraction regimes of transmission gratings", J. Opt. Soc. Am. **68**, 809 (1978).

25) M. Kato, H. Ito, T. Yamamoto, F. Yamagishi, and T. Nakagami, "Multichannel optical switch that uses holograms", Opt. Lett. **17**, 769 (1992).

26) S. Case, "Coupled-wave theory for multiply exposed holographic gratings", J. Opt. Soc. Am. **65**, 724-729 (1975).

27) V. Kondilenko, V. Markov, S. Odulov and M. Soskin, "Diffraction of coupled waves and determination of phase mismatch between holographic grating and fringe pattern", Opt. Acta. **26**, 239-251 (1979).

Chapter 3

Holographic Properties of Dichromated Gelatin

3.1 Introduction

In the following chapter, the basic holographic characteristics of dichromated gelatin (DCG) will be outlined. This will cover such points as the mechanism of hologram formation, exposure response, spectral sensitivity and enviromental stability. In addition, the processing techniques used during the course of this thesis will be described. These were based primarily on the work of Redmond [1]. For a more comprehensive discussion of DCG holography, the reader should refer to Meyerhofer [2] and Chang [3].

3.2 Hologram formation in DCG

Gelatin consists of irregularly shaped polypeptide chains of amino acids which are derived from the natural protein collagen [4,5]. In the presence of water-soluble dichromate compounds, for example ammonium dichromate, gelatin becomes photosensitive. On exposure to light a photochemical reaction occurs, resulting in the formation of permanent bonds between neighbouring gelatin molecules. Although the actual mechanism by which this occurs is still uncertain, it is generally accepted that the hexavalent dichromate ion is reduced to a Cr^{3+} ion by the absorption of a photon. These trivalent ions then react with two separate carboxyl sites to form a coordinated complex between neighbouring molecules. A stable crosslink is thereby formed, causing local hardening of the gelatin layer and, as a result, the exposed areas become less soluble in water than the unexposed areas. If the gelatin layer has not been hardened initially, the unexposed regions of gelatin will be washed away when immersed in water, leading to the creation of a surface relief grating [2,3]. If, on the otherhand, the gelatin has been sufficiently pre-hardened, the

gelatin film will absorb water and swell. Due to the presence of the photochemical bonds formed during exposure, however, a differential swelling occurs within the volume of the film; heavily exposed areas swelling less than areas which are not exposed. After the gelatin layer has been dried, therefore, a spatial variation in density, and thus refractive index, exists throughout the film.

Although it is possible to record volume phase holograms by this method [2], the level of modulation is typically not large enough to be of any practical use. In 1968, however, Shankoff [6] found that the index modulation of the holographic grating could be greatly enhanced by adding an extra step to the development procedure. In his revised process the washed gelatin layer was rapidly dehydrated by immersing it in a bath of isopropanol. This resulted in a greatly amplified index modulation, allowing holograms with diffraction efficiencies approaching 100% to be recorded. Several possible explanations for this effect have been put forward. Curran and Shankoff [7] proposed that the alcohol caused rapid dehydration and shrinkage of the gelatin, setting up large strains within the material which eventually lead to cracking along the fringe planes. Bragg diffraction would then take place as a result of scattering from the resulting air/gelatin interfaces. Although this model explains the high diffraction efficiencies which can be obtained, it fails to account for the high optical quality and low scattering loss of DCG. Case [8] attributed the index modulation to the appearance of tiny voids which formed a more gradual variation in the refractive index, whilst Meyerhoffer [2] suggested that the Cr^{3+}-gelatin-isopropanol complexes themselves were the cause. It is now generally accepted, however, that the increase in modulation is due to molecular distortion and rearrangement, an idea first proposed by Chang and Leonard [9]. The dehydration of the gelatin is thought to be so rapid that the molecules do not have time to rearrange their positions, possibly because gelatin loses some of its flexibility in the absence of water. As a result, the latent hardness image produced during exposure is converted into a spatial variation in density.

3.3 Holographic characteristics of DCG

In the following section the holographic characteristics of DCG will be outlined. These include its exposure response, spectral sensitivity, spatial resolution, scattering and

absorption losses and environmental stability. A comprehensive review of the properties of DCG and other commonly used holographic materials (e.g., silver halide and photopolymer) is given in reference [2].

3.3.1 Exposure response

The analysis presented in chapter 2 assumed that the change in refractive index was directly proportional to the exposure energy. In practice, however, holographic recording materials only exhibit a linear response over a small exposure range.

The holographic characteristics of dichromated gelatin were first investigated by Chang and Leonard [9]. This work led to the development of a simple bulk exposure model in which the change in index modulation, Δn, and the exposure, ξ, were related by

$$\Delta n = \Delta n_m[1 - \exp(-a\xi/\Delta n_m)] \tag{3.1}$$

where Δn_m is the maximum available index modulation and a represents the sensitivity of the gelatin. These two parameters, which determine the exposure response of a DCG hologram, depend on a wide variety of factors, for example the source of the gelatin, its bias hardness and the processing techniques used. In order to obtain reproducible results, therefore, it is vital that accurate control over all the recording parameters is maintained.

From equation (3.1) it can be seen that, at low exposures, an approximately linear relationship between index modulation and exposure exists. At higher exposures, however, the index modulation starts saturating. This results in the appearance of higher harmonic gratings which effectively reduces the maximum index modulation which can be achieved [10,11]. In order to investigate this effect further, let us return to the recording geometry described in section 2.2 (figure 2.1). In the case of a volume hologram recorded using two plane waves, the exposure will be

$$\xi(\mathbf{r}) = [I_o + I_r + 2\sqrt{I_o I_r}\cos(\mathbf{K}\cdot\mathbf{r})]\,t \tag{3.2}$$

where $\mathbf{r}$ is a position vector, I_o is the intensity of the object beam, I_r is the intensity of the

reference beam and t is the exposure time. Combining equations (3.1) and (3.2) allows the resulting spatial variation in refractive index modulation to be calculated

$$\Delta n(\mathbf{r}) = \Delta n_m[1 - \exp(-a\xi(\mathbf{r})/\Delta n_m)] \tag{3.3}$$

As $\Delta n(\mathbf{r})$ is periodic in Λ it may be expanded as a Fourier series in the direction of the grating vector,

$$\Delta n = \sum_{p=0}^{\infty} n_q \cos(q\mathbf{K} \cdot \mathbf{r}) \tag{3.4}$$

Saturation of the refractive index modulation therefore leads to the formation of an infinite series of harmonic gratings. The *qth* harmonic grating has a period of $q\Lambda$, and an amplitude coefficient given by

$$n_q = 2/\Lambda \int_{-\Lambda/2} \Delta n_m[1 - \exp(-a\xi(s)/\Delta n_m)] \cos(2\pi q s/\Lambda) ds \tag{3.5}$$

where s is a dummy variable and

$$\xi(s) = [I_o + I_r + 2\sqrt{I_o I_r}\cos(Ks)]t \tag{3.6}$$

Using equation (3.5), the amplitude of the fundamental grating (q = 1) may be calculated as a function of exposure for a given set of recording parameters are known. Note that, even at high levels of saturation, Kogelnik's two-wave coupled-wave theory will still be valid. This is because the harmonic gratings will, in general, not meet the Bragg condition necessary for efficient diffraction. Saturation of the index modulation will, however, result in a reduction of n_1 at very high exposure levels, thereby reducing the maximum diffraction efficiency which can be achieved.

The typical exposure response of a Kodak 649F plate is shown in figure 3.1 alongside the best fit calculated using equation (3.5). This curve describes the variation in diffraction efficiency with average exposure energy, ξ_A, which is defined as the average intensity at the hologram plane multiplied by the exposure time

$$\xi_A = (I_o + I_r)t \tag{3.7}$$

which may be re-written as

$$\xi_A = I_o (1 + B)t \tag{3.8}$$

where B is the beam ratio, given by $B = I_r / I_o$. The results shown in figure 3.1 were obtained using recording and replay parameters of $d = 15\mu m$, $\lambda = 514.5nm$, $B = 1$, $\theta_o = 0°$, $\theta_r = 30°$ (where θ_o and θ_r are the angles that the object and reference beam make with respect to the z-axis). The corresponding best fit occurs for a maximum index modulation of 0.03475 and a sensitivity of $0.84 \times 10^{-5} J/m^2$ (giving an exposure energy for peak efficiency of around 2.75 - 3 kJm^2). These exposure parameters were typical for the plates used during the course of this work.

Further practical complications arise due to the high absorption of ammonium dichromate sensitized gelatin, which can lead to the formation of a non-uniform index modulation throughout the volume of the hologram [12]. In addition, distortion of the fringes and variations in the bulk refractive index may also occur during processing (due to swelling or shrinking of the gelatin layer) [13]. The effect of these non-uniformities on grating performance has been discussed elsewhere (e.g., references [1,11-13]).

3.3.2 Spectral sensitivity

One of the problems associated with recording dichromated gelatin holograms is its limited spectral sensitivity. This is roughly a factor of a hundred less than fine grain silver halide emulsions such as 8E56HD. Stringent control over the stability of the recording set-up must therefore be exercised if optimum results are to be obtained. The sensitivity of

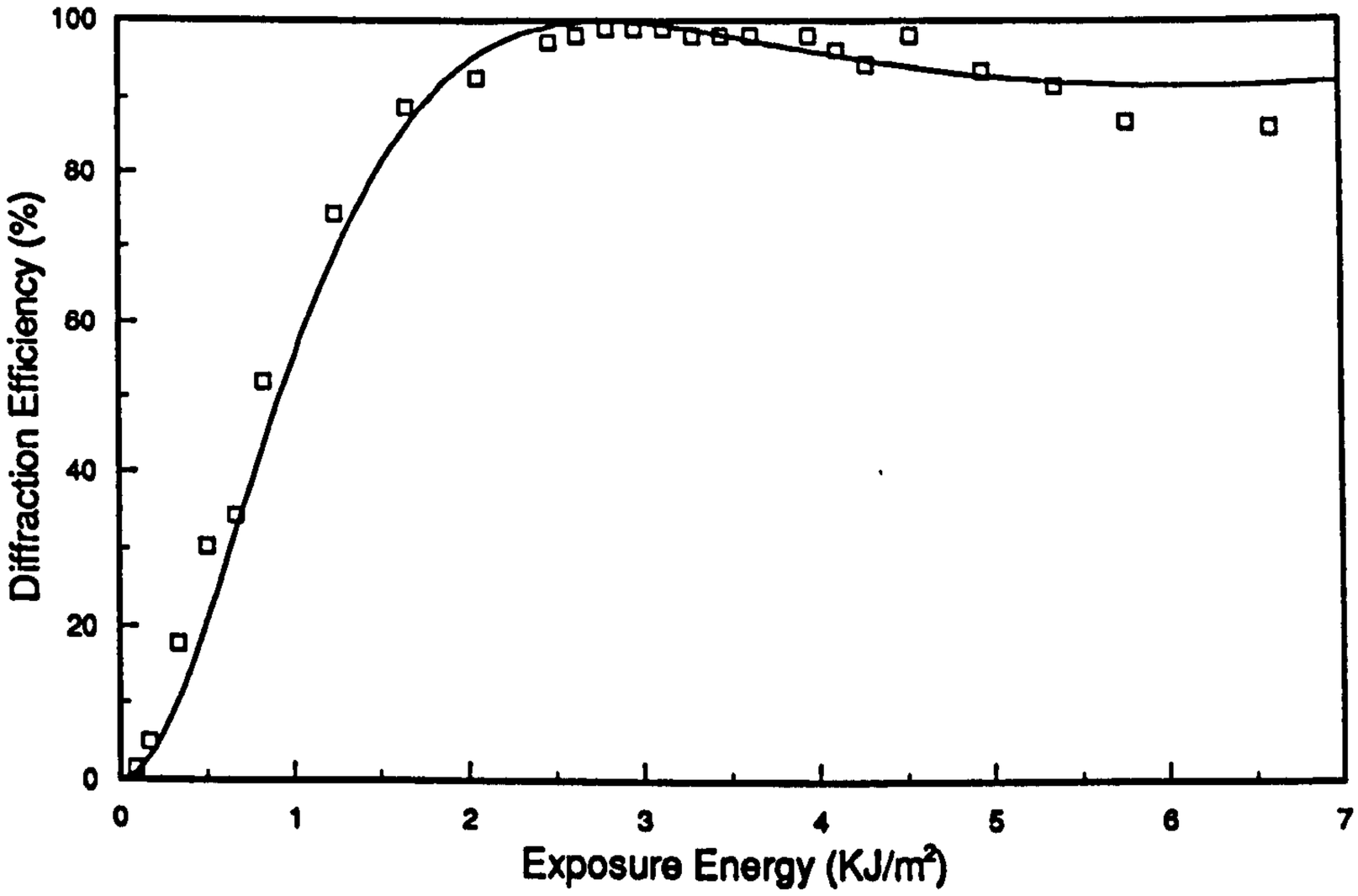

Figure 3.1 - Exposure characteristics of a Kodak 649F plate (Processed according to the techniques described in sections 3.4). Experimental parameters were $d = 15\mu m$, $\lambda = 514.5nm$, $\theta_o = 0°$, and $\theta_r = 30°$.

ammonium dichromate sensitized gelatin peaks in the UV and blue-green region of the spectrum, but drops off essentially to zero at 580nm [2]. Most DCG holograms are therefore recorded using either the 488nm or 514.5nm lines of an Argon-Ion laser, due to the high powers available at these wavelengths. In general, the 514.5nm line is preferred to the 488nm line because scattering is lower and, as the absorption at this wavelength is less, the holograms are recorded more uniformly throughout the depth of the film. At extremely low exposure levels, however, it may be preferable to record at 488nm due to the greater sensitivity of the gelatin at this wavelength (approximately four times higher than 514.5nm [2]).

At present it appears that optical computing and communications circuits will operate with near infra-red light sources (e.g., Semiconductor lasers or diode pumped YAG lasers). Several methods for fabricating DCG holograms at longer wavelengths have been developed. These have included both direct exposure [14] and dye sensitization techniques [15,16]. Using methylene blue as the sensitizing dye, for example, transmission gratings with more than 80% efficiency have been recorded at 633nm [16]. Typically, however, these techniques require high concentrations of dyes, which leads to nonuniform modulation. Moreover, careful control over the pH must be maintained during processing. In practice, therefore, any holographic component must be recorded in the blue/green. Replaying a hologram at a wavelength which is different from the recording wavelength will, in general, lead to the reconstruction of an aberrated wavefront. This problem may be minimised through proper optimization of the recording set-up, i.e., by finding an exposure geometry that gives the best combination of Bragg mismatch and spot size. Using these techniques, a number of groups have managed to produce HOEs capable of close to diffraction limited performance in the near infra-red [1,17].

A different approach involves a two step fabrication process, requiring the fabrication of an intermediate hologram in a material sensitive to the replay wavelength. This hologram is then copied onto DCG using an Argon-ion laser to produce an efficient, unaberrated HOE. This technique was used by Lin [18] to produce DCG elements for operation at 632.8nm. Alternatively, the intermediate hologram may be replaced by a specially optimized CGH. An examples of this technique is given in reference [19].

3.3.3 Spatial frequency response

In order to successfully fabricate an off-axis HOE, the recording material must be capable of accurately following the object/reference beam interference pattern. If the material does not have a sufficiently high resolution, there will be a loss in image resolution and a corresponding deterioration in the reconstructed wavefront [20]. This makes dichromated gelatin appear particularly attractive for fabricating HOEs. Measurements performed by Chang and Leonard [9] showed that DCG has a resolution of greater than 5000 lines/mm. In addition, they found that the spatial frequency response remained unchanged over a broad range of frequencies (from 100 lines/mm to 5000 lines/mm), an effect which can be explained by the fact that the index modulation occurs on a molecular scale.

3.3.4 Absorption and scattering losses

Noise can be defined as the unwanted light diffracted or scattered from a hologram in the same direction as the reconstructed wavefront. In terms of interconnect design this is an important parameter as it affects the signal to noise ratio (SNR) of the system. This light has several sources [20], including random scattering due to the granularity of the recording medium (during recording and replay) and inhomogenities and surface deformations of the hologram. In order to record a practical interconnect, therefore, it is important that the scattering be as low as possible. As gelatin is essentially grainless, the resulting scattering losses can be very small. This results in the formation of holograms of good optical quality and with very high SNRs. The scattering loss of a properly processed gelatin layer is typically less than one percent. If, however, the gelatin is too soft the amount of scatter can become significantly larger, characterised by the gelatin taking on a milky white appearance. This was not a problem in relation to the interconnects described in this thesis.

Another important feature of dichromated gelatin is its low absorption loss in both the visible and the near infra-red region of the spectrum. This results in the hologram having a high optical throughput and increases its ability to handle high optical powers. Figure 3.2 shows the transmission spectrum of a standard processed 15µm thick Kodak 649F plate (section 1.4). This illustrates that from 400nm to 2µm, the loss is only 2-4%.

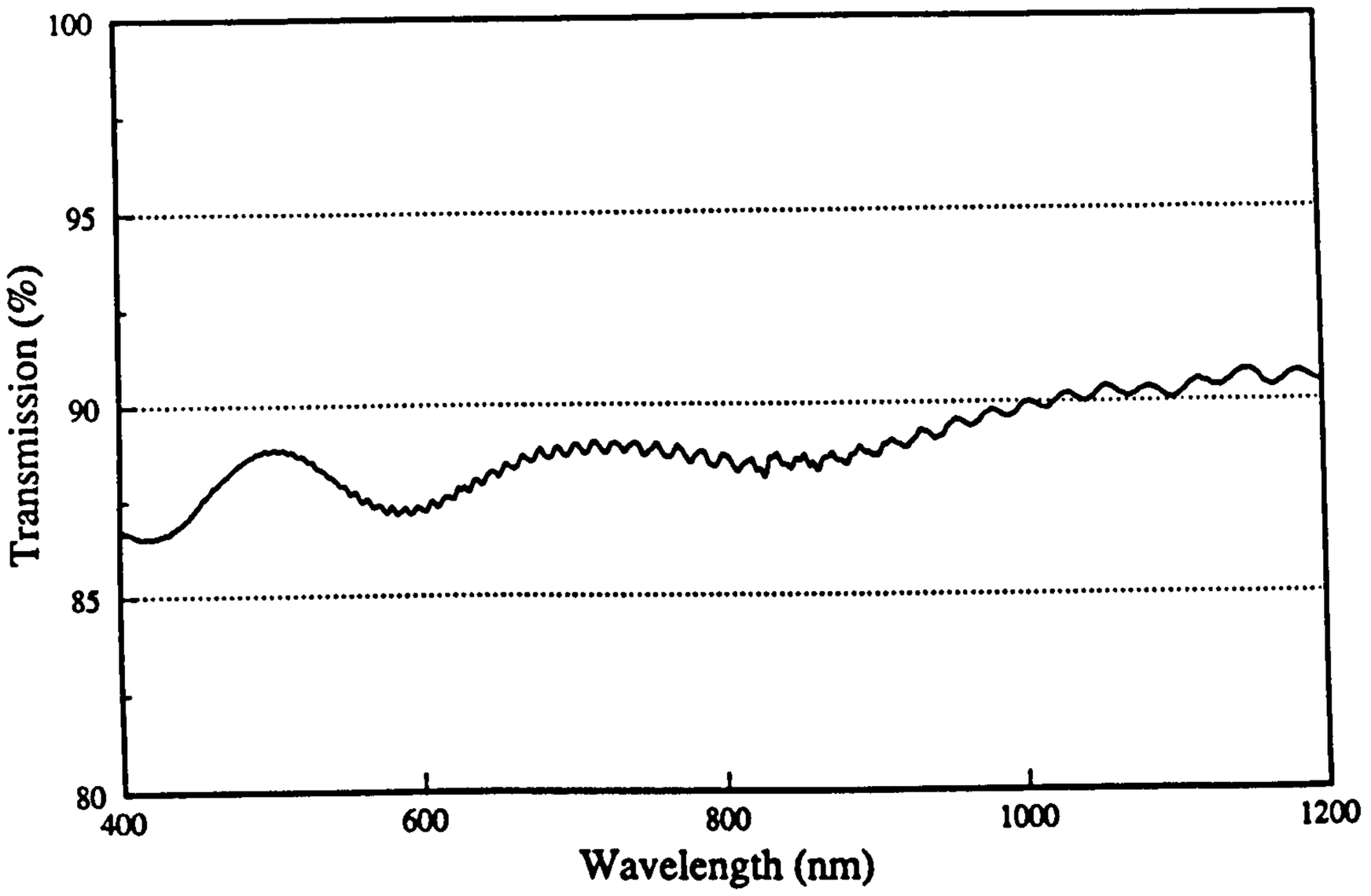

Figure 3.2 - Transmission spectrum of a Kodak 649F plate which was processed according to the techniques outlined in section 3.4.

3.3.5 Environmental stability

In many applications, the suitability of a particular holographic recording material will be determined by its ability to cope with a wide range of adverse environmental conditions (e.g. temperature and humidity). This will be a particular problem in the case of military or aerospace systems where severe operating conditions may be encountered. Investigations into the environmental stability of DCG have shown that it is particularly susceptible to high humidity levels. At an R.H. of only 50%, for example, the diffraction efficiency of a processed DCG hologram starts to gradually deteriorate [21]. This problem may be avoided, however, by securing a glass coverplate to the gelatin with a non-porous optical cement. Experiments have shown that when a developed hologram is properly sealed it is no longer affected by high external humidity levels [3]. Using a coverplate in this fashion can lead to problems if any water remains trapped inside the gelatin. The hologram can become susceptible to thermal damage, for example, through an increase in

the ambient temperature or via laser induced heating. By thoroughly drying the gelatin before sealing, however, DCG holograms capable of withstanding over 100°C may be obtained [3]. Moreover, as will be discussed in detail in chapter 7, the optical power handling capabilities of the hologram will be greatly enhanced.

3.4 Fabrication of DCG holograms

3.4.1 Production of gelatin layers

Several methods for producing gelatin layers have been developed, including dip-coating, doctor blading, gravity settling, spin-coating and casting [2]. Although good optical layers can be obtained, these techniques are generally time consuming and complex processes. A more convenient approach involves modifying commercially available photographic emulsions, such as Kodak 649F [23], Agfa 8E75 and Agfa 8E56 spectroscopic plates [22]. This is a simpler procedure, requiring the removal of the unwanted silver halide and dyes from the emulsion and adjustment of the bias hardness. Unfortunately this technique is not suitable for mass producing plates and does not allow for a substantial variation in the holographic characteristics of the gelatin. Plates produced by coating techniques, on the otherhand, can have both their thickness and bias hardness specified. This allows a large degree of control to be exercised over, for example, the holograms sensitivity and replay bandwidth. In addition, greater flexibility exists in choosing the type of substrate. As will be shown in chapter 7, this is an important consideration when dealing with the optical damage threshold of the HOE.

One of the prime factors affecting the recording and replay properties of a dichromated gelatin hologram is its hardness. If the gelatin is too soft it will tend to scatter whilst, if the gelatin is too hard, the film will be insensitive and limited in the maximum index modulation which it can achieve. Moreover, the bias hardness affects both the sensitivity of the gelatin and the degree of swelling which occurs during processing. Thus, unless accurate control over the bias hardness is maintained, it will become impossible to predict the exposure characteristics of the gelatin, making it difficult to obtain reproducible results. A variety of methods have been developed for controlling the bias hardness. If the gelatin

is too soft it can be hardened through heating, exposure to U.V. radiation or via the use of organic and inorganic hardening agents (e.g. formaldehyde or ammonium dichromate) [5]. Alternatively, if a gelatin layer is too hard, it may be softened by soaking in water at a high temperature [23]. In practice, the degree of hardening required can be determined by measuring the ability of the gelatin to absorb water, quantified by its swelling ratio, S

$$S = \frac{w_w - w_o}{w_o} \tag{2.2}$$

where w_o is the weight of a dried gelatin film, and w_w the weight of the film after it has been soaked in water gelatin [4,24]. For holographic purposes a DCG layer should have a swelling ratio somewhere between 2 and 3.

3.4.2 Recording on Kodak 649F plates

Kodak 649F spectroscopic plates were used to record most of the interconnects developed during the course of this thesis. These plates have been found to be particularly well suited to fabricating DCG HOEs. Efficient holograms of good optical quality can be readily recorded and, because their bias hardness is quite close to the optimum level, the preparation required, although time consuming, is relatively straightforward. Recording a DCG hologram on Kodak 649F plates consists of four stages; preprocessing, sensitization, exposure and development. In addition, some form of post-processing may be necessary to "tune" the HOE so that it meets the desired performance specifications. The standard procedures used to pre-process, sensitize and develop a 649F plate (unless otherwise specified) are given in Tables 3.1 - 3.3. These were based on the work of Redmond, a detailed description of which is contained in reference [1].

Several factors must be considered when trying to record a holographic optical element in DCG. These include, for example, the temperature and humidity, both of which must be accurately controlled if reproducible results are to be obtained. All the holograms described in this thesis were, therefore, recorded in a temperature and humidity stabilised lab (typically within 10% of 22°C and 40% R.H.). Other factors must also be taken into

Step	Procedure	Time (minutes)	Temperature
1	20% Agfa g334 fixer (part A) (Complete darkness)	10	20°C
2	Water wash increase temperature from 20°C to 32°C at 1.5°C/min	8	
3	Water wash	15	32°C
4	leave to stand	5	20°C
5	20% Agfa g334 fixer plus 3.5% hardener	10	20°C
6	Wash	15	20°C
7	Leave to dry	overnight	20°C

Table 3.1 - Procedure for pre-processing Kodak 649F plates.

account include the pH of the processing chemicals, sensitizer concentration, dark reaction time, processing times and drying rates. Detailed discussions concerning the effect of these parameters are given elsewhere [1-7].

3.4.3 Sensitization

After drying, the 8cm × 10cm pre-processed Kodak 649F plate was cut up into either six ≈ 3cm x 4cm plates or four 4cm × 5cm plates, depending on the application. The gelatin was then sensitized in 5% ammonium dichromate solution [$(NH_4)_2Cr_2O_7$] for three minutes under red-light conditions. Any excess ammonium dichromate solution was removed from the surface of the substrate using filter paper. The sensitized plates were then left to dry in the lab overnight in complete darkness and used the next day.

Ammonium dichromate is the most commonly used sensitizer in DCG holography, primarily because of its ease of use and high sensitivity. In addition, it is highly soluble in water, allowing the gelatin to take up large amounts of dichromate before crystallisation occurs. Measurements have shown sensitizer concentrations of up to 10% can be used. Although this will improve the sensitivity, due to the higher light absorption of the gelatin,

Step	Procedure	Time (minutes)	Temperature
1	5% $(NH_4)_2Cr_2O_7$ solution (+ 3 drops photoflow)	3	20°C
2	Dry in air	overnight	20°C

Table 3.2 - Procedure for sensitizing a Kodak 649F plate.

the hologram will be recorded less uniformly through the depth of the film. The effect of this is to increase the angular bandwidth of the hologram. Sensitizer concentration has also been shown to effect both the thickness and refractive index of the film, both of which will influence the replay angles of the HOE [11].

3.4.4 Development

The standard development procedure used throughout this thesis is given in Table 3.3. This was again based on the work of Redmond [1], with all steps being carried out at room temperature. By processing the plates at a higher temperature, however, the sensitivity of the plates can be greatly increased although with correspondingly greater scatter. Higher sensitivities can also be achieved by using a water wash [1]. By omitting the sodium metabisulphate bath and extending the water bath to approximately one hour, both a greater modulation and a lower absorption can be obtained. Although scattering is again higher, the lower absorption of the hologram greatly enhances its ability to handle high optical powers (section 7.10).

3.4.5 Post-processing

One of the main difficulties encountered during the course of this was work was that of accurately controlling the replay parameters of a DCG interconnect. This was found to be a particular problem in relation to changes in the reconstruction angles, which could alter during processing by up to a few degrees. As was discussed by Newell [11] and

Step	Procedure	Time (minutes)	Temperature
1	0.5% $(NH_4)_2Cr_2O_7$	3	20°C
2	0.5% $Na_2S_2O_7$	4	20°C
3	Water wash	12	20°C
4	50% Isopropanol soln	3	20°C
5	75% Isopropanol soln	3	20°C
6	Pure Isopropanol	3	20°C
7	Dry in air	overnight	20°C

Table 3.3 - Development procedure

Redmond [1], the shift in replay angle is caused by changes in both the thickness and bulk refractive index of the gelatin. Optical interconnects must, in general, meet very tight reconstruction tolerances. Thus, if DCG interconnects are to be of any practical use, this effect must be controlled.

This problem may, in principle, be overcome by optimising the recording geometry to compensate for changes in the gelatin thickness and refractive index. Alternatively, post-processing techniques may be used. By baking [1], or reprocessing [25], for example, it is possible to alter the Bragg replay angle, bandwidth and peak diffraction efficiency of a DCG hologram. The performance of an HOE may therefore be adjusted, or "tuned" to the required values.

3.5 Conclusions

Due to its holographic characteristics, dichromated gelatin appears an attractive choice for fabricating optical interconnects. Both transmission and reflection HOEs may be recorded and, in the case of simple grating structures, efficiencies approaching 100% are obtainable. In addition, when properly processed, DCG has low absorption and scattering losses, a high spatial resolution and a good environmental stability when sealed. Unfortunately, as a result of its poor spectral sensitivity, care must be taken when recording HOEs for the

infra-red. Furthermore, variations in the processing and exposure conditions (e.g., the bias hardness, temperature, humidity, dark reaction times and the pH) must be restricted if reproducible results are to be obtained. By exercising accurate control over these parameters, however, a variety of practical optical interconnects can be fabricated in DCG for replay at either a visible or near infra-red wavelength.

3.6 References

1) I. R. Redmond, Holographic optical elements in dichromated gelatin, Ph.D. Thesis, Physics Department, Heriot-Watt University, U.K. (1989) and references therein.

2) D. Meyerhofer, "Dichromated gelatin", in Holographic Recording Materials, Editor H. M. Smith, Topics in Applied Physics **20**, Springer Verlag (1984).

3) B. J. Chang, "Dichromated gelatin holograms and their applications", Opt. Eng. **19**, 642-648 (1980).

4) A. Graube, "Holographic optical element materials research", Technical Report, Hughes Research Laboratories, *AFOSR - TR - 78 - 1626* (1982).

5) C. E. Kenneth Mees, The theory of the Photographic process, MacMillan Co., New York (1944).

6) T. A. Shankoff, Phase holograms in dichromated gelatin", Appl. Opt. **7**, 2101-2105 (1968).

7) R. K. Curran and T. A. Shankoff "The mechanism of hologram formation in dichromated gelatin", Appl. Opt. **9**, 1651-1657 (1970).

8) K. Case and R. Alferness, "Index modulation and spatial harmonic generation in DCG films", J. Opt. Soc. Am. **65**,724 (1975).

9) B. J. Chang and C.D Leonard, "Dichromated gelatin for the fabrication of holographic optical elements", Appl. Opt. **18**, 2407-2417 (1979).

10) L. T. Blair and L. Solymar, "Grating profiles in dichromated gelatin", Opt. Commun. **77**, 365 (1990).

11) J. C. Newell, Optical holography in dichromated gelatin, Ph.D. Thesis, Physics Department, Oxford University, U.K. (1987) and references therein.

12) T. Kubota, "Characteristics of thick hologram grating recorded in absorptive medium", Opt. Acta **25**, 1035 (1978).

13) L. B. Au, J. C. Newell, and L. Solymar, "Non-uniformities in thick dichromated gelatin transmission gratings", J. Mod. Opt., **34**, 1211 (1987).

14) C. Solano, R. A. Lessard and P. C. Roberge, "Red sensitivity of dichromated gelatin films", Appl. Opt. **24**, 1189-1192 (1985).

15) A. Graube, "Holograms recorded with red-light in dye sensitized dichromated gelatin", Opt. Commun. **8**, 251 (1973).

16) T. Kubota and T. Ose, "Methods of increasing the sensitivity of methylene blue sensitized dichromated gelatin", Appl. Opt. **18**, 2538 (1979).

17) D. Prongue, Diffractive optical elements for interconnections, Ph.D. Thesis, Universite de Neuchatel, Institute de Microtechnique, Switzerland (1992).

18) L. H. Lin, "Hologram formation in hardened dichromated films", Appl. Opt. **10**, 2550-2551 (1971).

19) H. P. Herzig, "Holographic optical elements (HOE) for semiconducter lasers", Opt. Commun. **58**, 144 (1986).

20) R. J. Collier, C. B. Burckhardt, L. H. Lin, Optical Holography, Academic Press Inc., Student Edition (1971).

21) G. M. Naik, A. Mathur, S. V. Pappu, "Dichromated gelatin holograms: an investigation into their enviromental stability", Appl. Opt. **29**, 5292 (1990).

22) M. Chang, "Dichromated gelatin of improved optical quality", Appl. Opt. **10**, 2550-2551.

23) J. Oliva, P. G. Boj and M. Pardo, "Dichromated gelatin holograms derived from Agfa 8E75HD plates", Appl. Opt. **23**, 196-200 (1980).

24) T. G. Georgekutty and H. K. Liu, "Simplified dichromated gelatin hologram recording process", Appl. Opt. **26**, 372-376 (1987).

25) B. J. Chang, "Post-processing of developed dichromated gelatin holograms", Opt. Commun. **17**, 270-272 (1976).

Chapter 4

Fabrication of Fan-out Holograms Using Binary-Phase CGH Copying Techniques

4.1 Introduction

Many of the free-space optical data processing systems currently under investigation require some form of optical fan-out element for their operation. The applications of these components are varied, ranging from optical power supply and multiple-image generation to space-invariant array-to-array communication. As a result, the development of efficient fan-out components has become one of the most active areas of interconnect research. A variety of fan-out technologies have been investigated over the past two decades. These include, for example, Talbot self-imaging, periodic diffraction gratings and Fresnel zone plates [1]. An alternative approach involves the use of multiple grating volume phase holographic fan-out elements. Although at first sight it would appear that recording a fan-out HOE should be a relatively straightforward task, in practice, the reconstruction errors associated with these components have been found to be too high for most practical systems applications. In addition, the maximum achievable diffraction efficiency generally falls well below that attainable by a simple plane grating.

A number of methods of fabricating volume phase fan-out holograms have been demonstrated. These include sequential recording procedures [2], grating copying systems [3,4] and recording set-ups in which the object wavefront is generated from an array of point sources [5-8]. In the following chapter a recording technique which allows efficient volume phase fan-out holograms to be fabricated in dichromated gelatin will be described. The technique is similar in form to the specific contact-sheet recording system detailed by Liu et. al. [3], however, a binary-phase Dammann grating (section 1.5) is used instead of the contact-sheet to generate the object wavefront [9-11]. As the Dammann grating has a far higher uniformity, better quality fan-out holograms are obtainable using this approach.

The recording set-up was designed so that the grating and its focussing lens were combined to form a single HOE, thereby allowing us to construct a series of compact space-invariant array generators. A number of experiments were carried out to investigate the trade off between diffraction efficiency and uniformity exhibited by these components. The effect of spatially filtering out the higher diffraction orders generated by the Dammann grating during recording was also investigated along with the role that the beam ratio plays in determining the reconstruction error of the hologram. The results of this work have allowed us to determine experimentally some of the conditions required for the fabrication of a high efficiency volume phase fan-out hologram.

4.2 Theory of volume phase fan-out holograms

4.2.1 Simultaneous and sequential exposure

In the following section the basic theory associated with volume phase fan-out holograms will be outlined. We shall deal primarily with one to N fan-out holograms which divide a single input wavefront into a regular one or two dimensional array of N angularly separated object waves. A schematic outline of the recording geometry used to fabricate a holographic fan-out element is illustrated in figure 4.1. This set-up assumes that N collimated object beams, $E_i(\mathbf{r}) = E_i \exp[-j(\mathbf{k}_i \cdot \mathbf{r} + \phi_i)]$, and a reference beam, $E_0(\mathbf{r}) = E_0 \exp[-j(\mathbf{k}_0 \cdot \mathbf{r} + \phi_0)]$ are incident at the holographic plane H. Each of the object beams have an amplitude of E_i, a propagation vector of $\mathbf{k}_i$, and a phase of ϕ_i, whilst the reference wavefront has an amplitude of E_0, a propagation vector of $\mathbf{k}_0$, and a phase of ϕ_0. For simplicity we have considered the grating to be surrounded on both sides by a medium of the same average refractive index, n_o. Thus, $\mathbf{k}_0$ and $\mathbf{k}_i$ refer to the propagation vectors of the wavefronts within the hologram. In the case of the holographic fan-out elements described in this thesis, the angle between adjacent object beams, δ, was typically of the order of 0.05°.

Multiple grating fan-out holograms may be fabricated using either a sequential or simultaneous recording technique. In the case of a sequentially exposed hologram, each of the N object beams are recorded one at a time with the reference beam, leading to the formation

of N primary gratings. Simultaneous recording occurs if all the object beams are present at the same time. The resulting interference between the object beams leads to the formation of an additional set of N(N - 1)/2 secondary, or intermodulation gratings. On replay these gratings diffract power between the N reconstructed signal beams, resulting in a higher reconstruction error and a reduced diffraction efficiency. Although a sequential exposure technique avoids the problem of intermodulation gratings it does demand a higher dynamic exposure range than a simultaneously recorded hologram [12]. In addition, the intrinsic nonlinearity of the recording material will lead to each grating requiring a different exposure energy.

4.2.2 Recording of a multiple grating hologram

A number of groups have used coupled wave theory to investigate the operation of volume phase fan-out holograms. Solymar [13] and Kostuk [14] employed this approach when analysing the performance of an N-grating fan-out transmission hologram recorded with a common Bragg angle. These models were later extended to cover the effects of higher grating orders, multiple grating interaction [6,15-17] and material nonlinearity [18]. In addition, coupled wave theory was adapted by Kowarschik [19] and Kostuk [20] to study the problem of multiple grating reflection holograms. Thin grating decomposition has also been used to evaluate the power spectrum of fan-out holograms [21,22]. This technique was used, for example, by Ichikawa [22] to analyse the hybrid kinoform fan-out elements which are described in chapter 6.

For simplicity, let us consider the case of a one-dimensional (one to N) fan-out hologram fabricated using the recording set-up shown in figure 4.1. As in chapter 2 it will be assumed that all the recording beams are polarized perpendicular to the plane of incidence, and the holographic recording medium is aligned normal to the z-axis. In addition, the analysis will be restricted to the case where all the object beams are centred symmetrically about the z axis, and the maximum fan-out angle corresponding to the *Nth* object beam, θ_N, is only of the order of a few degrees. This is useful replay geometry for optical interconnection and array generation applications. If all the beams are incident simultaneously, the field generated at the holographic plane, $E(x,z)$, will be given by

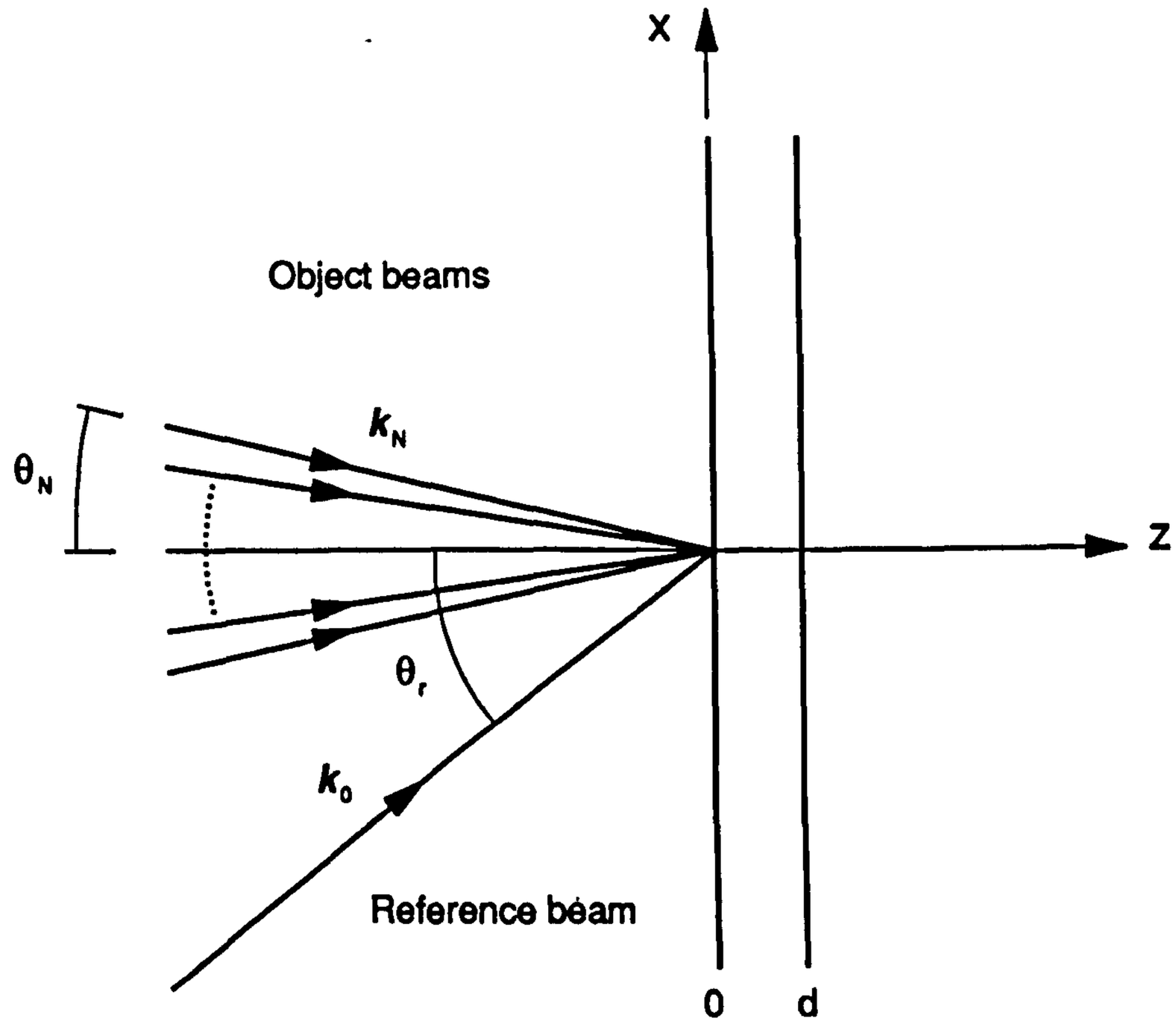

Figure 4.1 - Recording geometry.

$$E(x,z)=E_0(x,z)+\sum_{i=1}^{N}E_i(x,z) \tag{4.1}$$

In the case of a linear recording material, the change in the refractive index modulation, $\Delta n(x,z)$, will be proportional to the exposure energy, $I(x,z)t$, thus

$$n(x,z)=n_0+\tau t\,\{E_0^2+E_i^2+\sum_{i=1}^{N}E_0E_i\,[\exp(-j(\mathbf{K}_{0i}\cdot\mathbf{r}+\phi_{oi}))+\exp(j(\mathbf{K}_{0i}\cdot\mathbf{r}+\phi_{oi}))]$$

$$+2\sum_{i=1}^{N}\sum_{p>i}^{N}E_iE_p\,[\exp(-j(\mathbf{K}_{ip}\cdot\mathbf{r}+\phi_{ip}))+\exp(j(\mathbf{K}_{ip}\cdot\mathbf{r}+\phi_{ip}))]\,\} \tag{4.2}$$

where τ is a linearity constant, t is the exposure time, $\phi_{0i}=\phi_0-\phi_i$, and $\phi_{ip}=\phi_i-\phi_p$. From equation (4.2) it can be seen that beside the N primary gratings, $\mathbf{K}_{0i}=\mathbf{k}_0-\mathbf{k}_i$, an additional N(N - 1)/2 secondary intermodulation gratings, $\mathbf{K}_{ip}=\mathbf{k}_i-\mathbf{k}_p$, are generated by the interference between the object beams. During replay, these gratings can couple with the signal beams, leading to the formation of a series of spurious diffraction orders, as shown in figure 4.2. This affects both the efficiency and reconstruction error of the hologram. The appearance of these spurious diffraction orders has been discussed by a variety of authors including Slinger and Lewis [23], Slinger and Solymar [15] and Cawte [16]. These studies showed that spurious diffraction orders can be caused by a variety of factors, including intermodulation gratings, multiple-diffraction and higher grating orders and saturation effects.

As the first and second parts of equation (4.2) simply represent the change in average refractive index caused by reference and object beams respectively, these terms can be incorporated within the bulk refractive index of the processed hologram, n_0. The spatially varying refractive index of the hologram can thus be expressed as

$$n(x,z)=n_0+\sum_{i=1}^{N}\Delta n_{0i}\cos(\mathbf{K}_{0i}\cdot\mathbf{r}+\phi_{0i})+\sum_{i=1}^{N}\sum_{p>i}^{N}\Delta n_{ip}\cos(\mathbf{K}_{ip}\cdot\mathbf{r}+\phi_{ip}) \tag{4.3}$$

where $\Delta n_{0i}=2\tau E_0E_it$, and $\Delta n_{ip}=2\tau E_iE_pt$. The resulting coupled wave equations for this

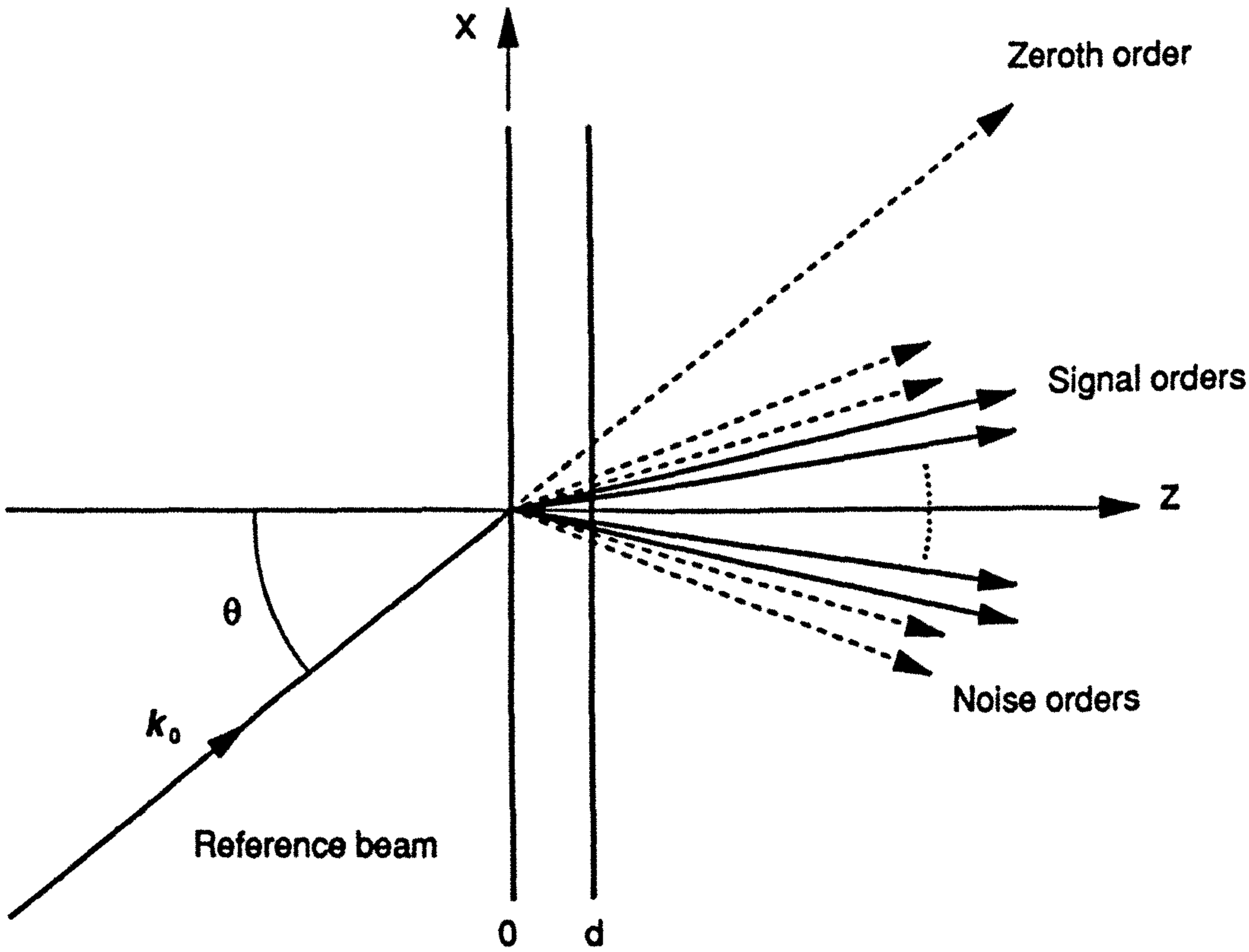

Figure 4.2 - Reconstruction of a volume phase fan-out hologram.

multiple grating can be found by solving the Helmholtz equation for the hologram using a procedure similar to the one described in chapter 2. Again the Helmholtz equation may be written in the form

$$\nabla^2 E(x,z)+\gamma^2(x,z)E(x,z)=0 \tag{4.4}$$

in which the propagation constant of the hologram is given by

$$\gamma^2(x,z)=(\omega/c)^2 n^2(x,z)-2j(\omega/c)n(x,z)\alpha(x,z) \tag{4.5}$$

and the terms $n(x,z)$, and $\alpha(x,z)$ correspond to the spatially varying refractive index and absorption. As in chapter 2, it will be assumed that we are dealing with a pure phase hologram, thus $\alpha(x,z)$, the absorption constant equals zero. Combining equations (4.3), and (4.5) we obtain

$$\gamma^2(x,z)=\beta^2+2\beta\sum_{i=1}^{N}\kappa_{0i}\cos(\mathbf{K}_{0i}\cdot\mathbf{r}+\phi_{0i})+2\beta\sum_{i=1}^{N}\sum_{i>p}^{N}\kappa_{ip}\cos(\mathbf{K}_{ip}\cdot\mathbf{r}+\phi_{ip}) \tag{4.6}$$

where $\beta=2\pi n_0/\lambda$, and the parameters $\kappa_{0i}=2\pi\Delta n_{0i}/\lambda$ and $\kappa_{ip}=2\pi\Delta n_{ip}/\lambda$ represent the coupling constants of gratings $\mathbf{K}_{0i}$ and $\mathbf{K}_{ip}$ respectively. When replayed with a plane wave, $A_0(\mathbf{r})=A_0\exp(-j\mathbf{k}_0\cdot\mathbf{r})$, at an angle θ, the fan-out hologram should generate an array of diffraction orders corresponding to the original signal beams. Again it will be assumed that the reconstruction wavefront is incident in the xz plane and polarized in the y direction. Using the approach described by Kostuk [14], the electric field within the hologram may be written as

$$E(x,z)=A_0(z)\exp(-j\mathbf{k}_0\cdot\mathbf{r})+\sum_{i=1}^{N}A_i(z)\exp(-j\mathbf{k}_i\cdot\mathbf{r})+\sum_{i=N+1}^{M}A_i(z)\exp(-j\mathbf{k}_i\cdot\mathbf{r}) \tag{4.7}$$

where $A_0(z)$ is the amplitude of the replay wavefront and $A_i(z)$ are the amplitudes of the reconstructed diffraction orders. The first N terms of the summation represent the principle or signal diffraction orders, whilst the second set of N + 1 to M terms (where

$M = N + N(N-1)/2$ are due to the intermodulation gratings. By substituting equation (4.7) back into equation (4.4), and assuming that the propagation vectors of the diffracted waves within the grating, $\mathbf{k}_i$, are given by

$$\mathbf{k}_i = \mathbf{k}_0 - \mathbf{K}_{0i} \tag{4.8}$$

we end up with a series of second order coupled wave equations. Applying the slowly varying amplitude approximation described in chapter 2 leads to the formation of a set of first-order differential equations from which the distribution of power in the various diffraction orders may be determined.

The above model assumes that only one diffraction order is produced by each grating. As described in chapter 2, whether this is valid or not will be determined by the Q factor; only if $Q > 10$ (i.e., the grating is holographically thick) will one significant order be present. The fan-out holograms fabricated during the course of this thesis were typically recorded in 15μm thick gelatin layers with $\lambda = 488nm$, $\theta = 30^o$, and $\delta = 0.05^o$. This results in a Q factor for the primary gratings of approximately 15 and a Q factor for the intermodulation gratings as low as $\approx 1\times10^{-4}$. The intermodulation gratings are therefore holographically thin, and will diffract some power into their higher (i.e., $\pm 1, \pm 2$, etc) diffraction orders over a large range of angles. As a result, a series of spurious diffraction orders will be generated about the zeroth order beam.

4.2.3 Replay parameters

The performance of a fan-out interconnect may be quantified with respect to its efficiency and reconstruction error. In the following thesis we shall define the diffraction efficiency of a hologram, η_d, to be the ratio of the power in the signal orders to the power in all the orders

$$\eta_d = \frac{\sum_{i=1}^{N} P_i}{P_0 + \sum_{i=1}^{M} P_i} \tag{4.9}$$

where P_i is the power measured of the *ith* diffraction order. The real efficiency of the hologram, η_r, is defined as the ratio of the power in the signal orders to the total incident power. This is an important measure of the performance of the fan-out grating as it includes the effects of absorption in the gelatin, Fresnel reflection losses and scattering losses.

If the recording has been successful, all the incident light will be diffracted into the N signal beams, however, in practice this is difficult to achieve and some light will always be diffracted into spurious diffraction orders. Moreover, there will exist a reconstruction error, ΔR, associated with the power diffracted into the signal beams. The maximum reconstruction error is given by

$$\Delta R = {}_{\max}[P_i/P_i^t - 1] \tag{4.10}$$

where P_i is the measured power and P_i^t is the theoretical power of the *ith* signal beam. Most practical optical interconnection applications require fan-out holograms which are capable of generating arrays of uniform intensity beams. Under these conditions, the reconstruction error may be defined to be equal to the uniformity of the array, i.e.,

$$\Delta R = \frac{P_{\max} - P_{\min}}{P_{\max} + P_{\min}} \tag{4.11}$$

where P_{max} is the maximum signal beam power and P_{min} is the minimum signal beam power. Unless otherwise stated, the uniformity, or reconstruction error of the DCG fan-out holograms described in this thesis will have been determined using equation (4.11).

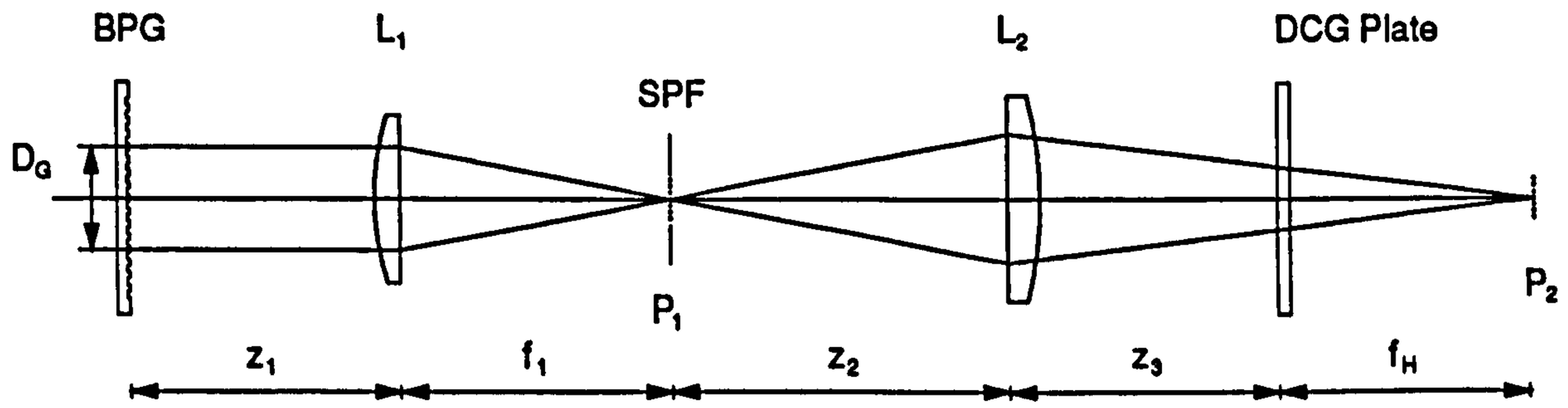

Figure 4.3 - Expanded view of the object arm of recording set-up. BPG : Binary-phase Dammann grating; H : Holographic plate; SPF : Spatial filter.

4.2.4 Basic BPG copying set-up

Figure 4.3 illustrates the basic experimental arrangement used to record an interferometric copy of a binary-phase Dammann grating. For simplicity we shall initially consider a 1-D fan-out grating which has been designed to produce a central 2M + 1 block of equally intense beams. Using this set-up it is possible to combine both the grating and focussing lens to form a single, compact holographic optical element. To generate the object wavefront the binary-phase grating (BPG) is placed in front of lens L_1 and illuminated with an expanded and spatially filtered collimated Gaussian beam. In order to maximise performance of the hologram only the central, approximately uniform portion of the beam is used. The BPG generates an array of diffraction orders which are focussed at plane P_1, the back focal plane of lens L_1. The directions of propagation of the beams produced by this grating, θ_m, are given by the diffraction formula

$$\sin\theta_m = m\lambda/2T \tag{4.12}$$

where T is the period of the diffraction grating, λ is the recording wavelength, and m is the order of the diffracted beam ($m = \pm 0,1,2,..$). The diffraction orders focussed in plane

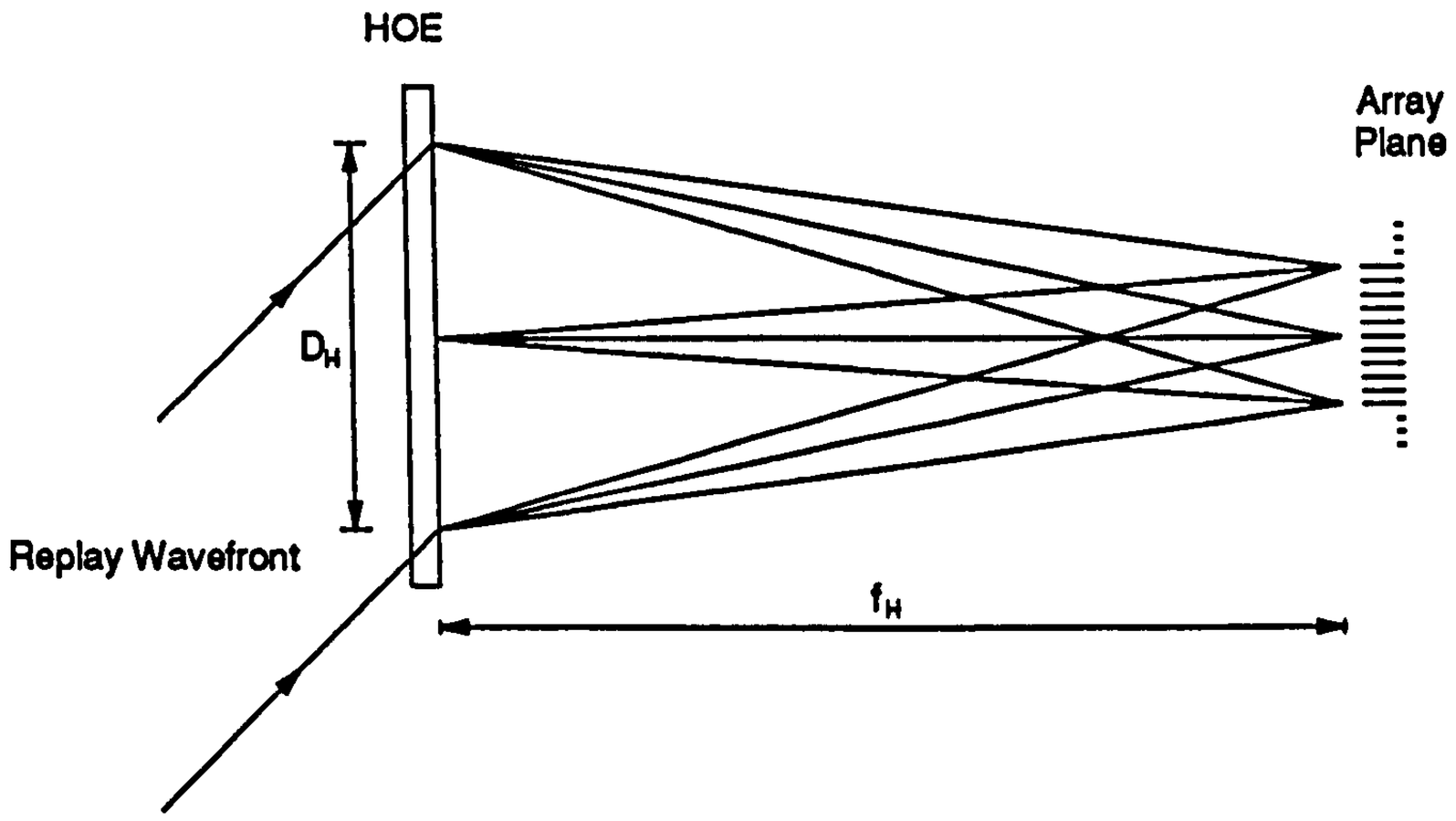

Figure 4.4 - Replay set-up

P_1 may be treated as optical point sources with complex amplitudes

$$G(m)=C(m)\exp[j\phi(m)] \tag{4.13}$$

with relative amplitudes of C(m) and phases of $\phi(m)$. The amplitudes and phases of these sources may be calculated from the grating transition points of the BPG. A spatial filter *(SPF)* positioned at plane P_1 can be used to control the number of orders used to produce the object beam. The diffraction orders that are passed by this filter are imaged by lens L_2 at plane P_2. Finally, the recording system is arranged such that the wavefront leaving the BPG plane is imaged at the holographic plate *H*. Thus, it follows that if no spatial filtering of the diffraction orders occurs, the wavefront at the holographic plane will be identical to the wavefront generated by the BPG, having a uniform amplitude and containing only phase information.

By introducing a collimated reference beam, a conventional, off-axis interferometric copy of the Dammann grating may be recorded. When this component is replayed with a plane wave at its Bragg angle, an array of diffraction orders will be generated a distance f_H in front of the hologram (figure 4.4). This distance is defined as the focal length of the array generator. Finally, in order to ensure that the optimum array uniformity can be realized,

a sufficient number of grating periods must be copied (generally at least 5) [24]. This also applies when replaying the hologram; if too few periods are illuminated a significant deterioration in the array uniformity will result.

4.2.5 Effect of spatial filtering

For simplicity, let us assume that a 1:1 imaging system is used to record the hologram. If the efficiency of the Dammann grating is given by η_g, then the amplitude of these signal beams will be equal to $C(m) = \eta_g/(2M + 1)$, where $m = -M,...,M$. In addition, as the Dammann grating exhibits inversion symmetry, $G(-m) = G^*(m)$ and $\phi(-m) = -\phi(m)$. Thus, if all the higher orders are filtered out, the object field at the holographic plane, $E_0(x)$, will be given by

$$E_0(x) = C(0) + \sum_{m=-M}^{M} C(m) \exp[j\phi(m)] \exp[2\pi j m x/T] \tag{4.14}$$

where T is the period of the Dammann grating, and we have set $\phi(m) = 0$. Equation (4.14) may be written as

$$E_o(x) = \frac{\eta_g}{2M+1}\left[1 + 2\sum_{m=1}^{M} \cos(\phi(m) + 2\pi m x/T)\right] \tag{4.15}$$

from which it can be seen that the amplitude of the field at the holographic plane varies periodically with a period also of T [25]. If the object field does not change noticeably through the depth of the recording material (corresponding to a small angular spread between the signal beams) we may, to a first approximation, treat the object wavefront as a plane wave which has a locally varying amplitude given by equation (4.15) and an average propagation vector $\mathbf{k}_0$. For simplicity the signal beams will be considered to be spread symmetrically about the z-axis. The resulting irradiance at the holographic plane will therefore be

$$I_T(x) = I_r + I_o(x) + 2\sqrt{I_r I_o(x)} \cos(2\pi \sin\theta_r/\lambda) \tag{4.16}$$

where $I_o(x)$ is the local irradiance of the object beam, I_r is the irradiance of the reference beam, and θ_r is the angle between the reference beam and the z-axis. As a result, the index modulation, and hence the diffraction efficiency, will vary periodically across the hologram (with period T). Moreover, the average diffraction efficiency of the fan-out hologram

$$\eta_d = \frac{1}{T}\int_0^T \eta(x)dx \tag{4.17}$$

will always be less than the maximum efficiency which can be achieved for a single grating recorded using two plane waves. Redmond [6] analysed this effect for the case of a fan-out to two hologram fabricated in a linear recording medium. His results showed that when $\delta \ll \theta$, the maximum obtainable diffraction efficiency which could be obtained was $\approx 65\%$. In practice, however, saturation of the index modulation will tend to raise this value. For higher levels of fan-out the object wavefront will begin to resemble that generated by a diffuse source. The performance of a hologram recorded using a diffuse object was investigated by Upatnieks and Leonard [26]. Their analysis, which again assumed a linear recording medium, showed that the maximum diffraction efficiency which could be achieved was 64%. From these results it can be concluded that, in order to maximise the diffraction efficiency of a fan-out hologram, it is necessary to minimise the amplitude fluctuations of the object beam. This can be achieved by proper alignment of the recording set-up illustrated in figure 4.3. If all the diffraction orders generated by the BPG (including the noise orders) are passed by the spatial filter, the field at the hologram plane will have a uniform amplitude. In principle, therefore, it should be possible to obtain close to maximum diffraction efficiency using this approach.

4.3 Experimental results

4.3.1 Complete wavefront copy

Initial experiments were carried out using a binary-phase Dammann grating fabricated in photoresist and optimized to generate a 15x15 array of equally intense diffraction orders.

The grating, designed and manufactured at the Helsinki University of Technology, had a period of 1.25mm and its surface relief depth was correct for about $\lambda = 500$ nm. Its theoretical efficiency, defined as the percentage of transmitted power in the central uniform block of diffraction orders [27], was 65%. The central axes of the central 15×15 array had a measured uniformity of ±30% (at 488nm). This was believed to be mainly due to the photoresist having suffered from some humidity damage. The deterioration, however, had been confined to the axes, the rest of the array being relatively unaffected with a uniformity of ±6%. It was, therefore, decided to use this uniformity measurement to judge the fidelity of the DCG copies as it gave a far more sensitive indication of copying accuracy.

The experimental arrangement used to record the Dammann grating copies is shown in figure. 4.5. For simplicity, a 1:1 imaging system was used with recording parameters of $\lambda = 514.5$nm and $f_H = 23.5$cm. A series of test plates were first fabricated to allow the optimum exposure energy to be determined. Once this was found, a set of high efficiency DCG holograms were recorded with $D_H = 14$mm. All the components described in this chapter were developed using the same standard processing technique outlined in chapter 3.

To ensure that the diffraction efficiency over the entire surface of the copy was constant, only the central, approximately uniform portions of the spatially filtered beams were used. Thus, by accurate alignment of the recording system, an almost uniform intensity wavefront was generated at the holographic plate, however, observable periodic amplitude variations still existed within the object wavefront. This was attributed to the finite numerical aperture of lenses L_1 and L_2 cutting off some of the higher-order spatial frequencies generated by the BPG. Additional random amplitude variations also occurred as a result of the inevitable dust contamination of the optics. Finally, a neutral density filter was index matched using di-n-butylphalate to the back of the substrate to reduce the strength of the reflected object and reference beams. This is an important point as light reflected back through the hologram can form noise gratings which will degrade the performance of the hologram.

4.3.2 Performance

The set-up used to reconstruct the Dammann grating copies is shown in figure 4.4. When replayed with a plane wave at 514.5nm, these components generated a good quality output array with a spot separation of 100μm (figure 4.6). The replay angle was, however, found

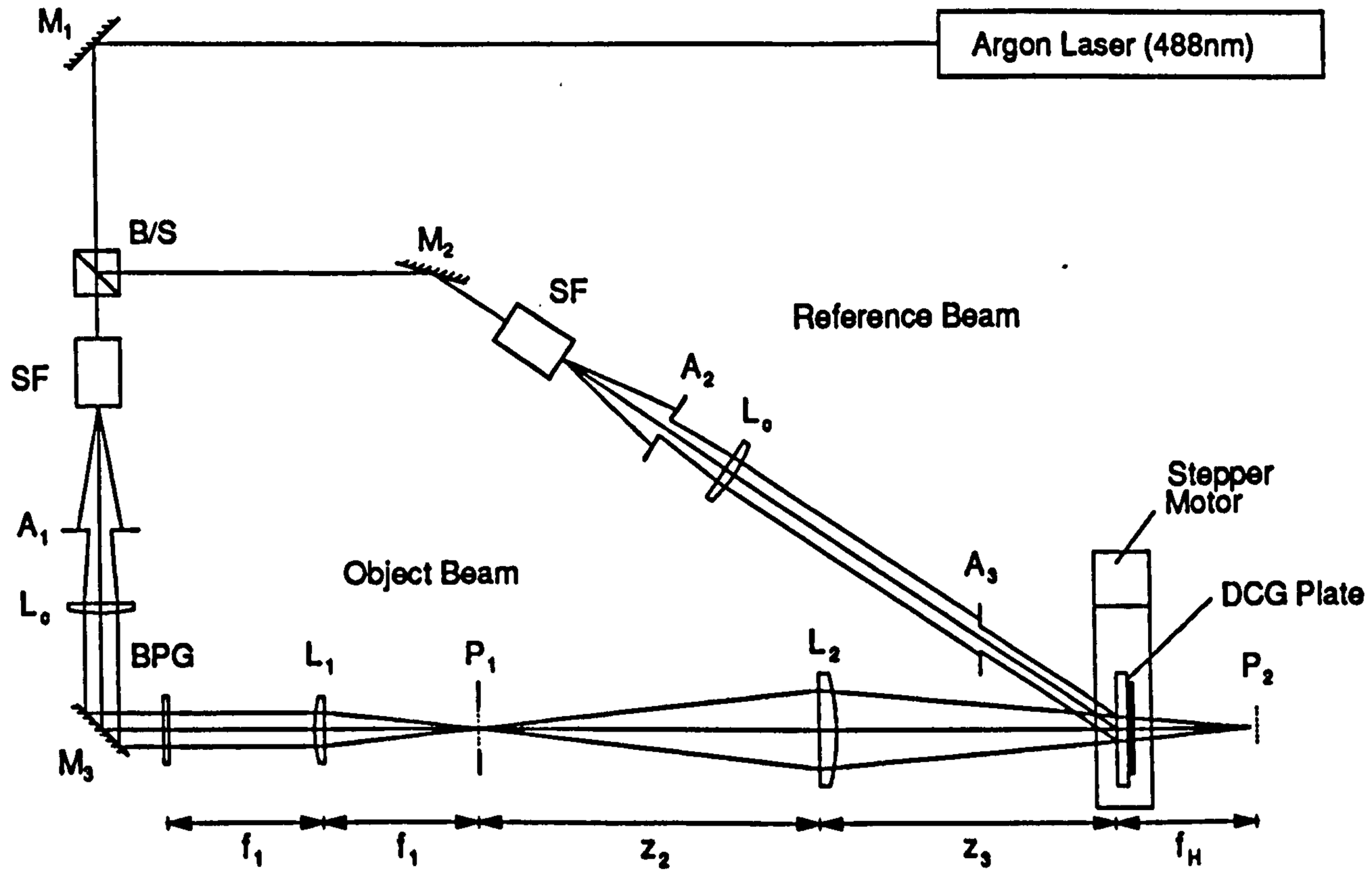

Figure 4.5 - Recording set-up used to fabricate Dammann grating copy. BS : Beamsplitter; SF : Pinhole spatial filter; M_1 - M_3 : Mirrors; L_c : Collimating lens; L_1, L_2 : Imaging system; A_1 - A_3 : Apertures; BPG : Binary-phase grating.

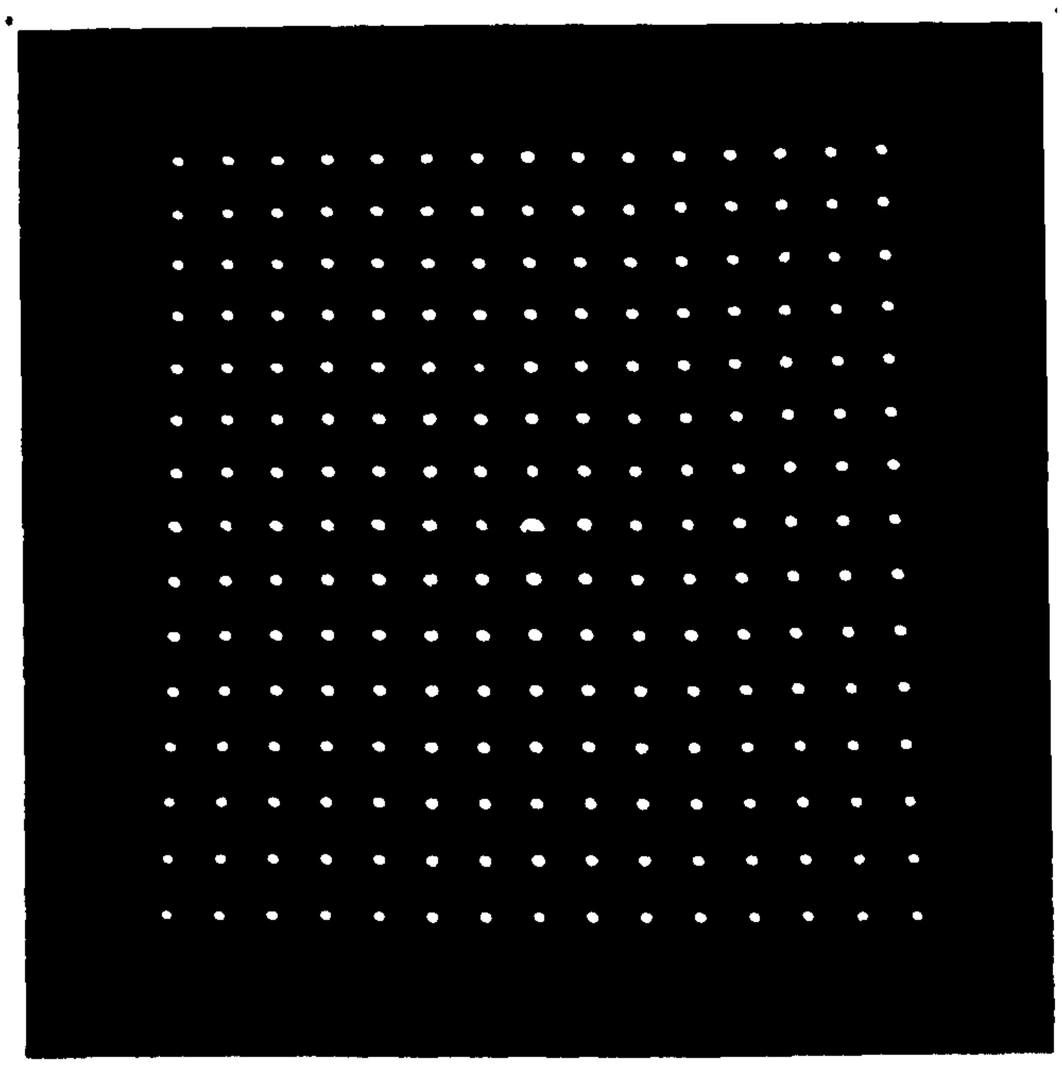

Figure 4.6 - Array generated by Dammann grating copy (all diffraction orders passed by spatial filter, B = 1).

to have shifted by ≈ 1° from the recording angle due to changes in the gelatin thickness and refractive index. In addition, it was observed that the quality of the focal spots were extremely sensitive to any changes in hologram alignment and, in particular, to rotation about the plane containing the incident and reconstructed wavefronts. This may be explained by considering the diffractive nature of the holograms. Any deviation in the replay conditions away from the recording conditions will lead to aberrations. As a result, problems such as alignment errors, changes in the refractive index and thickness of the gelatin, wavelength shifts and curvature in the replay beam will all contribute to a deterioration in the spot quality. It was estimated that the tolerance on the alignment accuracy was only about 2°, however, by accurate positioning of the hologram, it was possible to obtain a good quality array. When properly aligned the DCG copy generated an ≈ 18μm spot, the same as in the original recording set-up. This compares well with the diffraction limit of 10.4μm (Rayleigh criterion).

The maximum diffraction efficiency obtained was 70%, corresponding to 46% of the incident power ending up in the central 15×15 block of diffraction orders. As mentioned in section 4.2.5, this high efficiency could only be obtained because of the near uniform intensity of the object wavefront; close to peak diffraction efficiency could therefore be realized across the entire hologram surface without saturating the index modulation as in the case of a normal optically recorded array generator. The reconstruction error of the array had, however, increased during the copying process, rising from 6% to 12%. The performance of the Dammann grating copy was therefore inadequate for most interconnect applications.

4.3.3 Effect of beam ratio on reconstruction error

The effect that the beam ratio, B, has on the performance of an optically recorded volume phase fan-out element has been discussed by several authors including Benlarbi and Solymar [27] and Kostuk [16]. Previous investigations have shown that by using a high beam ratio it is possible to record low efficiency fan-out elements which have a reconstruction error and signal to noise ratio good enough for interconnection applications. Similar experimental research into the effect that beam ratio has on the fidelity of a volume

hologram recorded using an arbitrary object wavefront was carried out by Bartelt and Case [28]. The results of this work also showed that the reconstruction error associated with the reconstructed image improved with increasing beam ratio.

The beam ratio was defined in chapter 3 to be the ratio of the power in the reference beam to the power in the object wavefront. Thus, in the case of the fan-out hologram shown in figure 4.1, the beam ratio is given by

$$B = |E_0|^2 / \sum_{i=1}^{N} |E_i|^2 \tag{4.18}$$

As all the object beams have the same amplitude during recording we may write $E_i = E_1$, and $B = |E_0|^2 / N|E_1|^2$. The grating coupling constants therefore simplify to $\kappa_{0i} = \kappa_1$ for the primary gratings, and $\kappa_{ip} = \kappa_2$ for the intermodulation gratings, where $\kappa_1 = \Gamma E_0 E_1$, $\kappa_2 = \Gamma E_1 E_1$, and $\Gamma = 4\pi\tau/\lambda$. The ratio of the two coupling constants is given by

$$\kappa_1/\kappa_2 = E_0/E_1 = (NB)^{1/2} \tag{4.19}$$

i.e., κ_1/κ_2 is proportional to the square root of the beam ratio. Increasing the beam ratio therefore has the effect of suppressing the intermodulation gratings and, as a consequence, both the reconstruction error and the amount of light lost into the spurious diffraction orders will be reduced. Due to the higher background DC level, however, the maximum achievable diffraction efficiency will decrease as the refractive index modulation saturates. This saturation also leads to the formation of harmonic gratings which, at high exposure levels, can diffract a significant amount of light. In the case of a multiple grating fan-out hologram, these harmonic gratings will eventually increase the coupling between the various signal beams leading to higher levels of reconstruction error.

4.3.4 Copying of the spatially filtered wavefront

As was mentioned in the introduction, one of the drawbacks associated with binary-phase Dammann gratings is the amount of light which appears in the higher diffraction orders. This is both wasteful of optical power and prevents the gratings from being used as general

fan-out interconnects (section 1.4). In an attempt to improve the performance of the holographic array generator it was therefore decided to remove these higher unwanted diffraction orders during copying. The recording system used in this experiment was based on the system described in section 4.6. A variable aperture, *A*, was placed at plane P_1 and adjusted to spatially filter out everything except for the central 15×15 uniform block of diffraction orders. As predicted in section 4.2.5, modifying the object wavefront in this manner was observed to introduce quite strong periodic intensity variations at the hologram plane.

Initial copies were made with a beam ratio of one. Under these conditions the DCG copies were found to generate a very nonuniform array in which the higher orders were still present, the uniformity growing worse with higher diffraction efficiencies. This trade-off between efficiency and uniformity has been observed in relation to other, optically recorded fan-out holograms (see for example reference [6]). As the beam ratio was increased, array uniformity improved and the higher orders vanished. This is consistent with the discussion given in the previous section; raising the beam ratio suppresses the intermodulation-gratings and reduces the amount of power diffracted into the noise orders. Eventually, using a beam ratio of 50, a good quality space-invariant array generator was fabricated which generated negligible higher orders. The diffraction efficiency of this HOE was measured to be 24% and its uniformity ±13%. This is only a slight increase over the reconstruction error of the complete wavefront copy. Diffraction efficiency was, however, reduced considerably, implying that the spatial filtering operation is not a practical option unless a specific application requires complete removal of the higher orders (e.g., for a space-invariant fan-out interconnect).

4.4 Design considerations

4.4.1 Replay parameters

Recording holographic array generators using this technique offers a great deal of flexibility when choosing the holograms replay properties. For example, it is possible to alter the object beam by spatially filtering it at plane P_1. Furthermore, the focal length, f_H, the

diameter, D_H, and the spot spacing, d_H can all be adjusted by altering the recording set-up. Thus, by using only one high quality master Dammann grating (i.e., recorded on silicon nitride [30]) with the required number of output beams, we can fabricate a wide range of HOEs tailor made for any specific application. It is important, however, to ensure that the dimensions of the array exactly match up with the device it is to be used with. Any error in d_H, for example, will result in a imperfect registration between the optical logic gates, biasing beams and signal beams. This requires a careful alignment of the optics when setting up the recording system.

The parameters f_H, D_H and d_H can all be derived from elementary imaging laws and are given by the following algebraic relations

$$f_H = \frac{(f_1 f_2)^2}{(z_2 - f_2)[(z_2 - f_2)(f_1 - z_1) + (f_1)^2]} \tag{4.20}$$

$$D_H = D_G \frac{f_1 f_2}{(f_1)^2 + (z_2 - f_2)(f_1 - z_1)} \tag{4.21}$$

$$d_H = \frac{f_2}{(z_2 - f_2)} d_G \tag{4.22}$$

Here D_G and d_G are the diameter and spot spacing of the Dammann grating, respectively, and the notation of figure 4.4 has been used. Obviously, f_H must be positive and the DCG plate should located behind L_2. These conditions are fulfilled if $z_1 \leq f_1$ and $z_2 \leq f_2$. Note that if 1:1 imaging ($d_H = d_G$) is desired, we have $z_2 = z_3 = 2f_2$, $f_H = f_2$, and $z_1 = f_1$.

4.4.2 Angular variation of beams

An important factor which must be considered when using such a fan-out element is the angular spread across the output array (figure 4.4). Let us consider the case of a Dammann grating copy designed to generate an M×M array of equally intense spots. The angular spread in the diffracted beams, $\pm \theta_{max}$, will be given by

$$\tan\theta_{max} = (M-1)\, d_H / \sqrt{2} f_H \tag{4.23}$$

Thus, in the case of holographic fan-out elements described in section 4.3, the angular deviation across the output array equals 0.24°, which amounts to only an 0.27% change in the angle of incidence (with respect to normal incidence). This may become a drawback if the holographic copy is to be used with an array of etalon-based optical logic gates. Any change in beam parameters (i.e., spot size, angle of incidence) may cause a variation in switching characteristics and threshold level across the array. This problem may, of course be avoided by using a 4-F imaging system in the object arm and employing a separate focussing lens in an exact Fourier transform set-up in reconstruction - a technique which will be discussed in more detail in chapters 5 and 6. In some situations, however, the angular spread will not be a problem and the compactness and potentially lower cost of an integrated beam splitter and lens will be an advantage.

4.5 Conclusion

Although both a high efficiency and good uniformity can be achieved using this technique, the performance of the Dammann grating copy was not sufficient for all practical inter-connect applications. In spite of this, it does offer a promising approach of fabricating compact space-invariant array generators. By starting from a master grating, a wide range of DCG HOEs, tailor made for a specific application, can be made. In addition the copied wavefront may be enhanced by spatial filtering techniques, although at the cost of a lower diffraction efficiency. Two main limitations are associated with this approach; the sensitivity of the Dammann grating copy to misalignment effects, a problem which may be avoided by recording a plane grating fan-out hologram and using an external refractive focussing lens, and the requirement of accurately fabricating the original binary phase grating. In the following Chapter we shall describe a technique which allows us to improve the quality of the uniformity of the input array. A binary amplitude CGH is used, with appropriate spatial filtering, to generate the binary phase wavefront. This allows a far better quality object wavefront to be generated.

4.6 References

1) N. Streibl, "Beam shaping with optical array generators", J. Mod Opt. **36**, 1559 (1989).

2) G. Mendes, S. Hart, K. Bazargan, and S. Xu, "Holographic optical element (HOE) for free-space optical interconnection using junction lasers", Opt. Lett.

3) H. K. Liu and J. G. Duthie, "Real-time screen-aided multiple-image optical holographic matched-filter correlator", Appl. Opt. **21**, 3278 (1982).

4) Y. Z. Liang, D. Zhao and H. K. Liu, "Multifocus dichromated gelatin hololens", Appl. Opt. **22**, 3451 (1983).

5) G. Groh, "Multiple imaging by means of point holograms", Appl. Opt. **7**, 1643 (1968).

6) I. R. Redmond, Holographic Optical Elements in Dichromated Gelatin, Ph.D Thesis, Physics Department, Heriot-Watt University, Edinburgh, U.K. (1989) and references therein.

7) C. W. Slinger, R. R. A. Syms, and L. Solymar, "Multiple holographic transmission gratings in silver halide emulsion", Appl. Phys. B, **42**, 121 (1987).

8) J. C. Kirsch, D. A. Gregory, T. D. Hudson, and D. J. Lanteigne, "Design of photopolymer holograms for optical interconnect application", Opt. Eng. **27**, 301 (1988).

9) B. Robertson, M. R. Taghizadeh, J. Turunen and A. Vasara, "Fabrication of space-invariant fannout components in dichromated gelatin", Appl. Opt. **29**, 1134 (1990).

10) L. Wang, W. Z. Geng, and R. K. Kostuk, "Efficient multiple-image holographic optical element", Opt. Eng. **29**, 257 (1990).

11) M. Oren, "Interferometric recording of volume computer generated hologram on Polymer material", IEE conference (1990).

12) LaMacchia and C. J. Vincelette, "Comparison of the diffraction efficiency of multiple exposure and single exposure holograms", Appl. Opt. **7**, 1857 (1968).

13) L. Solymar, "Two-dimensional N-coupled wave theory for volume holograms", Opt. Commun. **23**, 199 (1977).

14) R. Kostuk, "Comparison of models for multiplexed holograms", Appl. Opt. **28**, 771 (1989).

15) C. W. Slinger and L. Solymar, "Grating interactions in holograms recorded with two object waves", Appl. Opt. **25**, 3283 (1986).

16) P. S. Cawte, "The diffraction efficiency of double-grating holographic fan-out elements", J. Mod. Opt. **38**, 1365 (1991).

17) H. P. Herzig, P. Ehbets, D. Prongue, R. Dandliker, "Fan-out elements by multiple beam recording in volume holograms", Proc. Soc. Photo-Opt. Instrum. Eng. **1507**, (1991).

18) L. T. Blair and L. Solymar, "Double exposure planar transmission holograms recorded in nonlinear dichromated gelatin", Appl. Opt. **30**, 775 (1991).

19) R. K. Kostuk, J. W. Goodman, and L. Hesselink, "Volume reflection holograms with multiple gratings: an experimental and theoretical evaluation", Appl. Opt. **25**, 4362 (1986).

20) R. Kowarschik, "Diffraction efficiency of sequentially stored gratings in reflection volume holograms", Opt. Quantum Electron. **10**, 171 (1978).

21) R. Alferness and, S. K. Case, "Coupling in doubly exposed thick holographic gratings", J. Opt. Soc. Am. **65**, 730 (1975).

22) H. Ichikawa, Optical beam array generation with phase gratings, Ph.D Thesis, Physics Department, Heriot-Watt University, Edinburgh, U.K. (1992) and references therein.

23) J. W. Lewis and L. Solymar, "Spurious waves in thick phase gratings", Optics commun. **47**, 23 (1983).

24) J. Turunen, Personal communication

25) J. Upatnieks, C. Leonard, "Efficiency and image contrast of dielectric holograms", J. Opt. Soc Am. **60**, 297 (1970).

26) B. Benlarbi and L. Solymar, "The effect of the relative intensity of the reference beam upon the reconstructing properties of volume phase holograms", Optica Acta **26**, 271 (1978).

27) H. Bartelt and S. K. Case, "High-efficiency hybrid computer-generated holograms", Appl. Opt. **21**, 2886 (1982).

28) M. R. Taghizadeh, J. I. B. Wilson, J. Turunen, A. Vasara and J. Westerholm, "Optimization and fabrication of grating beam-splitters in silicon nitride", Appl. Phys. Lett. **54**, 1492 (1989).

Chapter 5

Fabrication of Fan-Out Holograms Using Binary-Amplitude CGH Copying Techniques

5.1 Introduction

In the following chapter an alternative method for fabricating DCG fan-out holograms will be described. A binary-amplitude Dammann grating is used to generate the object wavefront in an interferometric recording system similar to that employed in chapter 4. Spatial filtering is then used to convert the wavefront generated by the CGH into one corresponding to that which would be produced by an equivalent binary-phase Dammann grating [1]. This recording technique, which was developed by J. Turunen [2], avoids the problems of having to produce a binary-phase grating with the necessary phase-delay and uniformity accuracy required for optical interconnect applications. The exposure system was also designed such that all the recording beams were plane waves. Thus, in order to replay the DCG fan-out hologram, a separate Fourier-transform lens was required. As will be shown, this has two advantages; it allows the DCG copy to be wavelength shifted (operated at a wavelength different from that it was recorded at) without any aberrations appearing in the spot profiles, and simplifies the alignment procedure.

5.2 Theory

A schematic diagram of the optical recording system is shown in figure 5.1. The binary-amplitude CGH is placed in the front focal plane, P_1, of lens L_1 and illuminated with a uniform amplitude plane wave. As the CGH is periodic, the resulting frequency spectrum generated in plane P_2, the back focal plane of L_1, is discrete, consisting of an array of diffraction orders separated by $\delta = f_1\lambda/T$, where T is the grating period and λ is the recording wavelength. Lens L_2 then Fourier transforms this spectrum to form an image of the CGH in plane P_3, where the holographic plate is situated. In order to convert this object wavefront

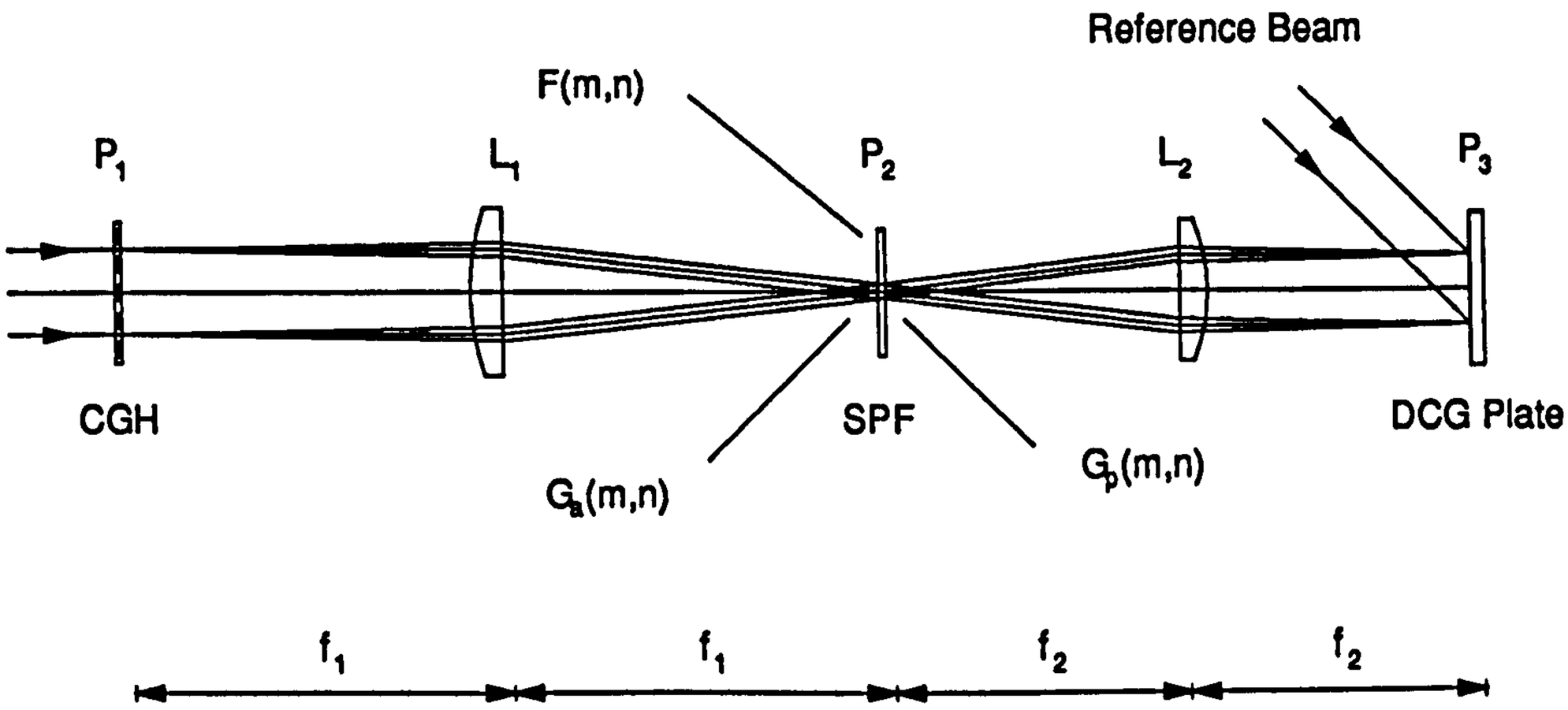

Figure 5.1 - Schematic of amplitude grating copying set-up. CGH : Binary amplitude Dammann grating; SPF : Spatial filter.

into one which an equivalent binary-phase grating would produce, a spatial filter is placed in plane P_2. The transmission function of the filter, F(m,n), is designed such that it modifies the angular power spectrum of the amplitude grating, $G_a(m,n)$ into one proportional to the spectrum of the equivalent phase grating, $G_p(m,n)$, i.e.,

$$G_p(m,n)=\frac{1}{\zeta}F(m,n)\,G_a(m,n) \tag{5.1}$$

where F(m,n) is the transmission function of the filter and ζ is a constant related to the difference in light transmission between the amplitude and phase gratings. If this condition is met, a phase-only wavefront will be generated at the holographic plane, P_3. Thus, by introducing an off-axis reference wave, an interferometric volume phase hologram can be recorded.

Although this recording technique eliminates the problem of accurately fabricating a binary-phase grating, it does demand that the spatial filtering be performed with a high degree of precision. The spatial filter must therefore be accurately positioned with respect to plane P_3 and fabricated so that it exactly modifies the power spectrum of the CGH in

the required fashion. This brings us to the first point which must be considered; how can a periodic amplitude-only wavefront be converted into a phase-only wavefront with a filter straightforward enough to be practical. For simplicity, consider only the one dimensional case and let us assume that an infinite number of grating periods are involved. The angular spectrum of a periodic amplitude-only wavefront, $T(x)$, is discrete with the components given by [3,4]

$$G_a(m)=\int_0^1 T(x)\exp[-i2\pi mx]\,dx \tag{5.2}$$

where m is an integer denoting the diffraction order of the grating and the grating period is normalized to unity. Assume that the desired wavefront has a uniform amplitude and a periodic phase profile $\Psi(x)$. The corresponding discrete angular spectrum can be calculated from

$$G_p(m)=\int_0^1 \exp[i\Psi(x)-i2\pi mx]\,dx \tag{5.3}$$

In order to convert the amplitude profile into a phase profile, the angular spectrum of the amplitude grating, $G_a(x)$, must be modified by the filter such that

$$G_p(m)=\frac{1}{\zeta}F(m)\,G_a(m) \tag{5.4}$$

In general, the structure of the spatial filter will be too complicated to be realised practically and the conversion technique is therefore impractical. In the case of a binary CGH, such as a Dammann grating, however, the situation becomes far simpler. It can be shown that the angular spectrum components of a binary-amplitude and binary-phase (2Ψ phase delay) wavefront which have the same modulation structure are related by

$$G_p(m)=2G_a(m)\sin\Psi \tag{5.5}$$

for the m ≠ 0 diffraction orders, and

$$G_p(0) = (2G_a(0) - 1)\sin\Psi + i\cos\Psi \tag{5.6}$$

for the zeroth-order m = 0 beam. The transmission function of the filter can be found by combining equations (5.4)-(5.6), to give

$$F(m) = 2\zeta\sin\Psi \tag{5.7}$$

and

$$F(0) = \frac{\zeta}{G_a(0)}\{(2G_a(0) - 1)\sin\Psi + i\cos\Psi\} \tag{5.8}$$

By choosing $\Psi = \pi/2$ it can be seen that the filter needs only to modify the phase and amplitude of the undiffracted beam. In addition, the filtering operation can be further simplified by allowing $\zeta = 1/2$, which is often the case, reducing equation (5.8) to

$$F(0) = 1 - \frac{1}{2G_a(0)} \tag{5.9}$$

Thus, in order to convert the binary-amplitude wavefront into a binary-phase wavefront, the spatial filter must be real and is only required to attenuate the zeroth order. This novel spatial filtering operation therefore has much in common with the well known central dark ground method for observing phase objects. If the hologram has been designed such that $G_a(0) = 1/2$, all the power in the zeroth order beam must be blocked. The filter can therefore be considered as binary ($S(0) = 0$ and $S(m) = 1$ for all $m \neq 0$). From equation (5.5) this requires that $G_p(0) = 0$, i.e., the phase grating is optimised to reconstruct no zeroth order beam. If a two-dimensional grating is formed using the one-dimensional optimisation results, no power will be diffracted into any of the axial orders, i.e., $G_p(m,0) = G_p(0,n) = 0$ for all m,n. The amplitude mask satisfies $G_a(m,0) = G_a(0,n) = 0$ for $m \neq 0$, $n \neq 0$ and $G_a(0,0) = 1/2$. Therefore, it is still possible to construct a filter which blocks the zeroth-

order without interfering with any of the other diffraction orders. The fact that the central axial orders vanish as well is, in some respects, an advantage. Any grating irregularities and impurities show up as a cross artefact and lead to a reduction in the uniformity of the axial orders [5-7]. This was observed in the case of the photoresist grating used in chapter 4. As these orders are, however, no longer present, a higher array uniformity can be obtained.

Such an array generator could be used in an optical computing circuit to generate four adjacent arrays, each dealing with a separate task. If an array with regular spacing is required, however, the CGH can be designed so that it diffracts no light into any even diffraction order [6,7]. This can be achieved with virtually no increase in the computational complexity. For the sake of simplicity, however, the holograms used in the following work were designed with only the central diffraction orders missing.

5.3 Experimental results (1-D copy)

5.3.1 Recording system

In order to investigate the feasibility of this recording technique, a set of 1×14 linear fan-out holograms were fabricated using the optical system shown in figure 5.2. A Dammann grating which satisfied the criteria $G_p(0) = 0$ was designed by A. Vasara at the Helsinki University of Technology. Standard photolithographic procedures were then used to generate a binary-amplitude mask from the optimised transition points. For the purposes of this experiment the period of the grating was set at 2.5mm and lenses L_1 and L_2 were chosen to have focal lengths of 250mm and 100mm respectively. The period of the DCG copy was therefore reduced to 1mm, allowing for a more compact replay set-up to be used. In addition, the uniformity of the array generated by the binary-amplitude grating (excluding the central zeroth order) was found to be ±4%, approaching the values required by optical computing systems.

Conversion of the binary-amplitude wavefront generated by the CGH into a binary-phase wavefront at the holographic plate, was achieved by spatially filtering out the central zeroth diffraction order at plane P_2 using a filter consisting of a thin (50μm diameter) strand of copper wire. To ensure that the spatial filter was precisely positioned, a rotation mount

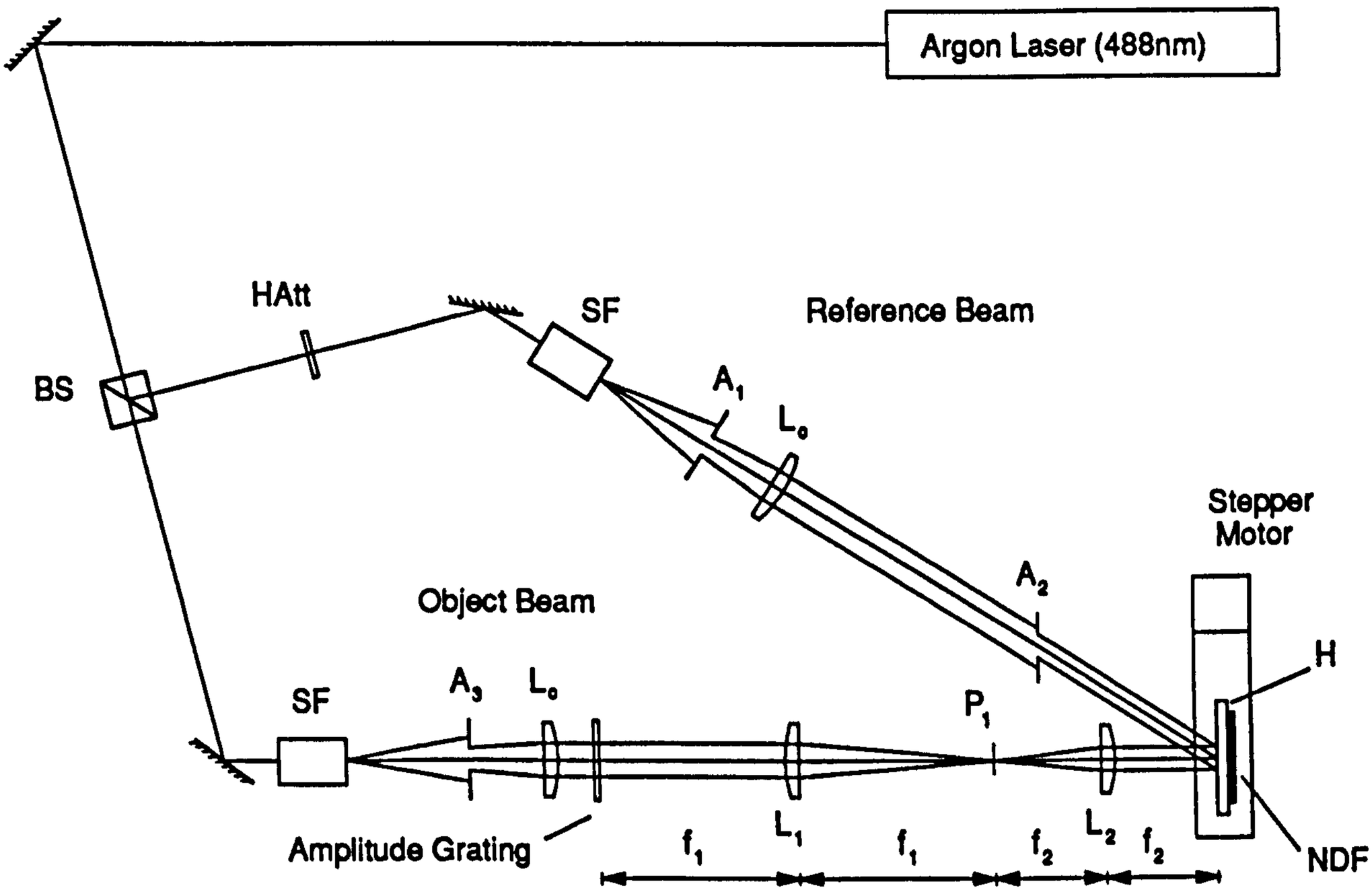

Figure 5.2 - Experimental recording set-up. SF = Pinhole spatial filter; BS : Beam splitter; L_c : Collimating lens; L_1 : 250mm; L_2 : 100mm; A_1-A_3 : Aperture; Hatt : Holographic attenuator; NDF : Neutral density filter.

and three-axis translation stage were used to provide accurate alignment. This set-up was found to be very stable, with no observable drift in alignment occurring even after several hours. The filter was also found to be unaffected by the effects of heating during exposure, (e.g., expansion of the wire causing a change in the object wavefront), and vibrational problems.

Although in theory removing the central zeroth order should have resulted in the formation of an almost uniform intensity wavefront at P_3, slight periodic fluctuations in intensity were still apparent, particularly in the region of the grating transition points. These variations were attributed to the finite numerical apertures of lenses L_1 and L_2 causing some of the higher-order spatial frequencies to be lost during imaging (section 4.4). In addition, due to the low diffraction efficiency of the amplitude grating, the exposure intensity at the holographic plate was found to very low; I_H was measured to be only $40W/m^2$. It was therefore decided to record the holographic copies at 488nm, due to the higher sensitivity that DCG has at this wavelength. The exposure response of the gelatin was also maximised by ensuring that the beam-ratio during recording was set at one. The beam ratio was adjusted using a holographic attenuator positioned in the object arm [9]. Kodak 649F plates were used along with the standard pre-processing and development procedures outlined in chapter 2.

In order to ensure that the diffraction efficiency over the entire surface of the copy was constant, only the central, approximately uniform portions of the spatially filtered beams were used. As a result, each of the diffraction orders generated at P_2 had an Airy function intensity profile (figure 5.3(a)). This was found to introduce several practical difficulties. In particular, if the compression ratio (ratio of the spot separation to spot size) of the diffraction orders at P_2 was too low (i.e., the diameter of the object beam was not large enough), a noticeable degree of overlap between the higher order diffraction rings of the first diffraction order and the other orders occurred. It was therefore impossible to fully filter out all of the central zeroth order without affecting the neighbouring signal orders. Although weak in intensity, the remaining portions of the higher order diffraction rings will still generate a background noise level at the holographic plate. Thus, in order to minimise this problem, it is necessary to have a high compression ratio at P_2. This will allow most of the central zeroth order to be filtered out.

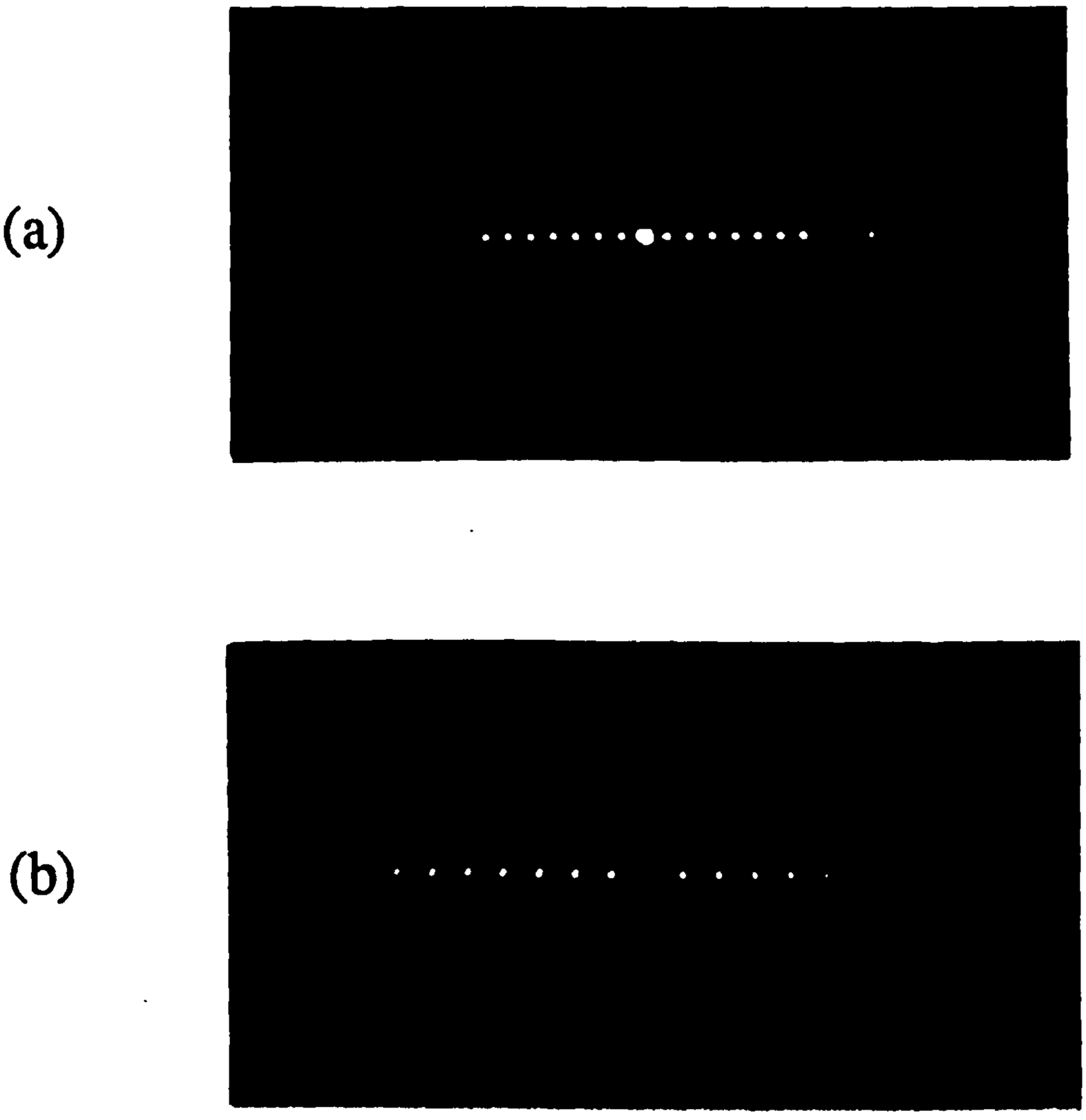

Figure 5.3 - (a) Array generated by the 1×14 binary-amplitude Dammann grating; (b) array generated by the DCG copy.

The array of diffraction orders produced by the binary-amplitude Dammann grating at plane P_2 is shown in figure 5.3. The separation between these orders was measured to be 48μm and the spot size was just over 10μm (Rayleigh criteria), giving a compression ratio of approximately five. In this particular experimental set-up, therefore, the interference effects were minimal.

An additional complication arose as a result of scattering of the higher order diffraction rings from the edges of the spatial filter. Some of the stray light ended up at the holographic plate and led to the recording of spurious noise gratings. In practice, however, the proportion of scattered light which reached the recording plane was very small, and any light that did tended to appear at the edges of the filtered wavefront. The amount of noise in the output array, therefore, only became noticeable when the diameter of the replay wavefront approached that of the HOE, D_H. As long as the replay wavefront did not overfill the HOE, therefore, this effect was not a problem.

An improvement could also be made by using Gaussian recording beams within the recording system. This would reduce the overlap effect, allowing a more uniform array to be generated at P_3, and decrease the amount of light scattered from the filter. An aperture could then be placed at the holographic plate to pick out the central uniform part of the recording beams. Unfortunately this technique requires the lenses to have a much larger numerical aperture, a demand which may be impossible to meet. In addition, scattering may be reduced by using a less reflective material for the spatial filter, e.g. by painting the copper black.

5.3.2 Performance of copy

Figure 5.3(b) shows the output array generated by a high efficiency DCG copy of the 1×14 Dammann grating wavefront. The replay set-up is shown in figure 5.4. The first point to note is the very high reconstruction fidelity; no central zeroth order was produced when the DCG copy was replayed and the array uniformity had risen only slightly to ±6%. The properties of the reconstructed wavefront were therefore almost identical to those of the original object wavefront. The diffraction efficiency of the HOE used to generate the array shown in figure 5.3(b) was measured to be 75% (including reflection and absorption

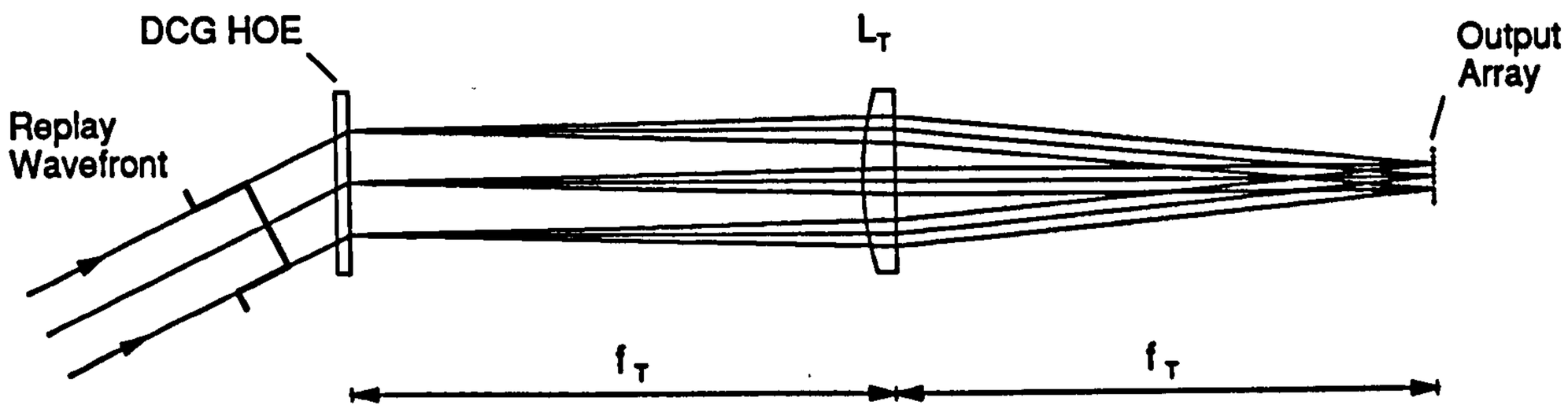

Figure 5.4 - Replay set-up.

losses). Thus 60% of the power incident upon the holographic copy ended up in the central 1x14 block of diffraction orders (theoretically, the efficiency of a one dimensional binary phase Dammann grating is 80% [3,4]).

5.4 Experimental results (2-D copy)

5.4.1 Recording system

The next set of results describes the performance of a two-dimensional fan-out interconnect fabricated using this technique. Once again the recording system shown in figure 5.2 was employed. This time, however, the amplitude mask was designed to generate a 15×15 array of diffraction orders with the condition $G_p(m,0) = G_p(0,n) = 0$ being met for all m,n. The amplitude-mask was therefore optimised to diffract no power into any of its axial orders as shown in figure 5.5(a). The advantage of this design is that it simplifies the spatial filtering problem, i.e., the zeroth order can be filtered out at plane P_1 using simply a cross-hair filter without any of the other diffraction orders being affected. As in the previous experiment, the period of the binary-amplitude mask was set at 2.5mm and a 2.5:1 image reduction step was used.

(a)

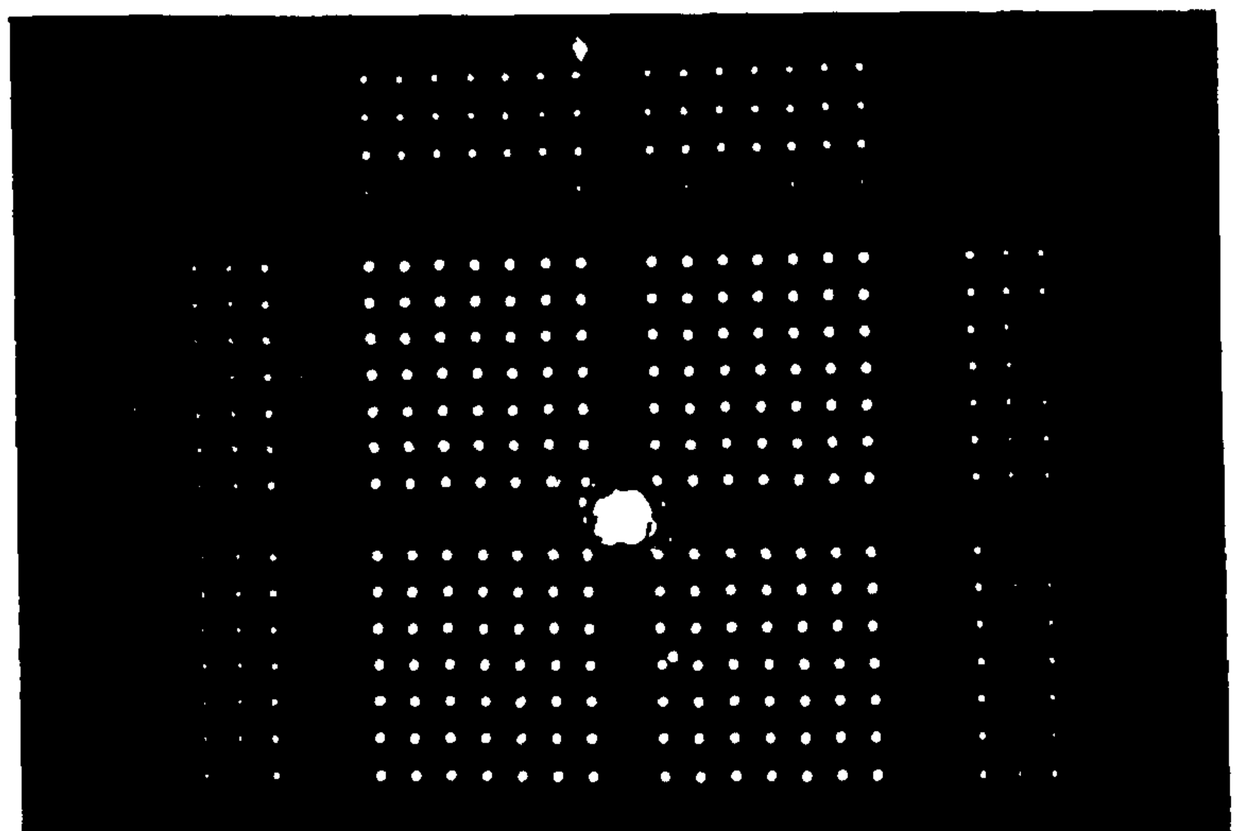

(b)

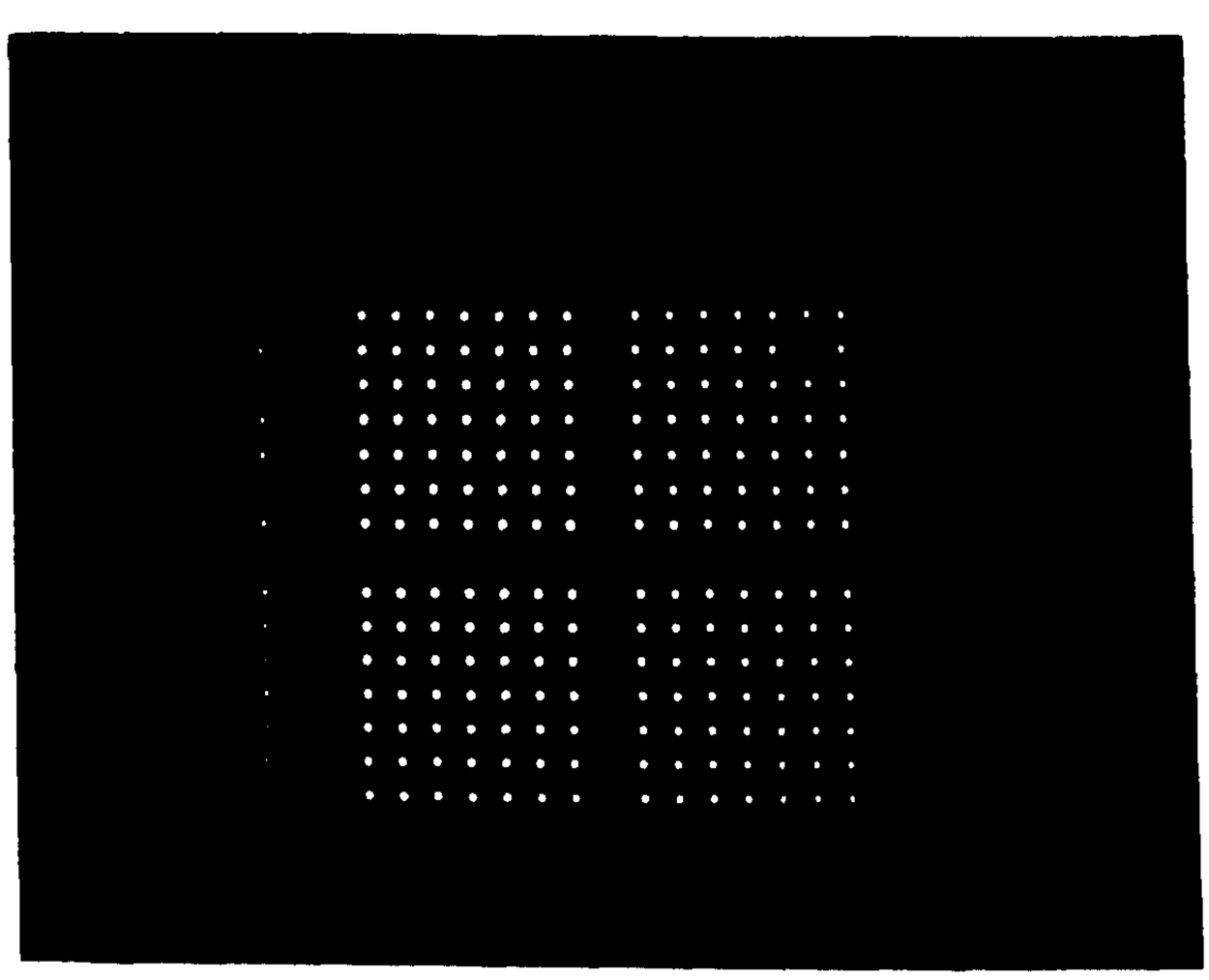

Figure 5.5 - (a) Array generated by the 14×14 binary-amplitude Dammann grating; (b) array generated by the DCG copy.

Using a spatial filter constructed from two perpendicular strands of 50μm diameter copper wire, the zeroth order was filtered out. This had the effect of converting the binary-amplitude object wavefront at P_3 into an almost uniform intensity, binary-phase wavefront. The limited numerical apertures of lenses L_1 and L_2, however, again introduced small periodic variations in intensity, particularly in the region of the grating transition points. Intensity variations, caused by the presence of dust on the optics, were also present.

5.4.2 Performance of copy

The array generated by the DCG copy at a replay wavelength of 488nm is shown in figure 5.5(b). As can be seen, negligible power appeared in the central axial orders and the reconstruction fidelity is very good. Grating diffraction efficiency was measured to be 76%, and 46% of the incident power ended up in the 14x14 array (theoretical efficiency of a two dimensional Dammann phase grating is 65%). In addition the array uniformity was found to be ±12%, a value which tallies well with the 1-D result. Typically, if a 1-D array has a reconstruction error of ΔR, a similarly fabricated 2-D array will have an error of $\approx 2\Delta R$, if ΔR is small [5,6].

An experimental set-up similar to the one shown in figure 5.4 was used to reconstruct the DCG copy. Again a uniform amplitude replay wavefront (D_H = 2.5cm) and a 100mm focal length achromat lens were used. It was found that, by accurate alignment of the replay lens, a very good quality spot with minimal aberrations could be obtained across the entire array. This was found to be a far easier task than aligning the combined Dammann grating/focussing lens HOE described in chapter 4. The array separation was measured to be 100μm and the spot size was found to be 12μm (to first Airy ring), which compares well with the calculated values of 100μm and 10μm respectively. It can be concluded, therefore, that the DCG copy is capable of operating close to the theoretical diffraction limit.

5.5 Variation of performance with wavelength

In the case of a conventional binary-phase Dammann grating, any deviation of the reconstruction wavelength away from its design value will be equivalent to a phase-delay error. As a result, the array uniformity will deterioate, and a far greater amount of power

will be diverted into the zeroth order. This does not, however, occur in the case of an interferometric, off-axis copy. As the holographic copy consists of a series of overlapping plane gratings, it is possible to replay at any wavelength as long as each grating is close enough to its Bragg condition. Since the maximum fan-out angle for these components is typically only a fraction of a degree, the above condition is easily satisfied. To investigate this, the 1×14 array generator was replayed at 632.8nm using a set-up similar to that described in figure 5.4. The interconnect replayed at a lower diffraction efficiency and only a slight reduction in spot quality. This was thought to be due to non perfect alignment in the recording set-up, the object and reference wavefronts having a slight curvature to them. Replaying the combined focussing lens/Dammann grating described in section 4.3 at a wavelength different from that with which it was recorded would, however, result in severe aberrations. This problem can, in principle, be reduced by optimising the recording set-up to minimise any wavelength shift aberrations [8,9]. The effect of wavelength shifting a DCG fan-out interconnect will be discussed in greater detail in the next chapter.

5.6 Off-axis nature of array generator

Unlike a conventional on-axis Dammann grating, the DCG copy operates off-axis, thus the input wavefront will be compressed in one direction. From this it follows that any circular input beam will be focussed down into an array of elliptical spots. This problem can be avoided by using two, close cascaded HOEs as illustrated in figure 5.6. HOE2 is the off-axis array generator whilst HOE1 is simply a plane volume grating which diffracts the input wavefront through an angle, θ, equal to the Bragg replay angle of HOE2. This results in the input wavefront being fanned-out along the optical axis as shown. Such a replay geometry also has two additional advantages; it allows for easier alignment of the optical system and exhibits a far greater wavelength stability [10].

Alternatively, if the reconstruction wavefront is elliptical, as in the case of a diode laser, the DCG copy can be designed to generate an array of circular spots [11]. This gives an off-axis array generator a distinct advantage as it is envisioned that many of the future optical circuits will operate with diode lasers.

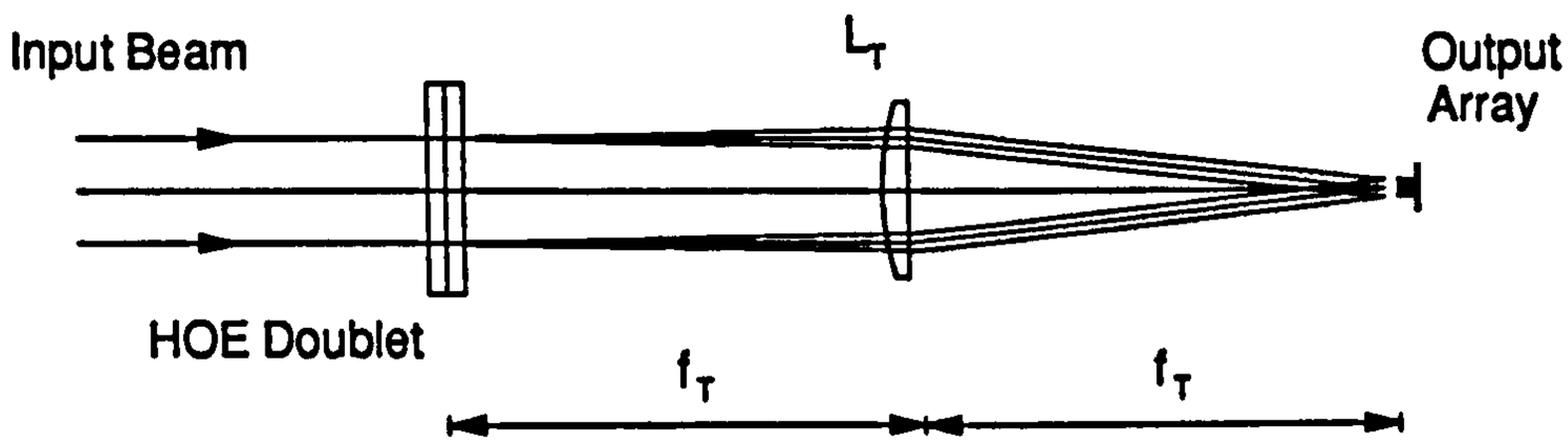

Figure 5.6 - Close cascaded HOE fan-out element.

5.7 Conclusions

In conclusion, preliminary results show that it is possible to record successfully an off-axis interferometric copy of a binary-phase Dammann Grating directly from an amplitude mask. By proper optimisation of the original mask and appropriate spatial filtering within the recording set-up, efficient and uniform array generators can be produced. Moreover, operation of a single DCG array generator at a wavelength different from that it was recorded at resulted in no deterioation in array uniformity. This gives the copy a greater tolerance to wavelength shifts.

So far this technique has only been used with nonregular array structures most suited to the spatial filtering requirements. It is, however, possible to design an even-order missing amplitude mask which will result in a regular array generating being recorded. More interestingly, it also opens up the possibility of recording continuous phase components, more commonly referred to as Kinoforms. This is the subject of the next chapter.

5.8 References

1) B. Robertson, M. R. Taghizadeh, J. Turunen and A. Vasara, "High-Efficiency, wide-bandwidth optical fannout elements in dichromated gelatin", Opt. Lett. **15**, 694 (1990).

2) J. Turunen, Personal communication.

3) J. Turunen, A. Vasara, J. Westerholm, A. Salin, "Stripe-geometry two-dimensional Dammann gratings ", Opt. Commun. 3, 245 (1989).

4) J. Turunen, A. Vasara, J. Westerholm, A. Salin, and G. Jin, "Two-dimensional Dammann gratings ", J. Phys. D 21, S102 (1988).

5) A. Vasara, Array generation with periodic Fourier-transform holograms, Licentiate Thesis, Physics Department, Helsinki university of Technology, Finland (1989).

6) R. L. Morrison and S. L. Walker, "Binary phase gratings generating even numbered spot arrays", *Annual Meeting of the Optical Society of America*, (Optical Society of America, Washington, D.C., 1989), Technical Digest Series 1989, TuFF6 (1989).

7) A. Vasara, M. R. Taghizadeh, J. Turunen, J. Westerholm, E. Noponen, H. Ichikawa, J. M. Miller, T. Jaakkola, S. Kuisma, "Binary surface-relief gratings for array illumination in digital optics", Appl. Opt. 31, 3320 (1992).

8) Y. Amitai and J. W. Goodamn, "Design of substrate-mode holographic interconnects with different recording and readout wavelengths", Appl. Opt. 30, 2376 (1991).

9) I. R. Redmond, Holographic optical elements in dichromated gelatin, Ph.D. Thesis, Physics Department, Heriot-Watt University (1989).

10) T. W. Stone, Holographic optical elements, Ph. D. Thesis, University of Rochester, U.S.A. (1986).

11) J. Upatnieks, J. O. Abshier, C. R. Christensen, and J. Stensby, "Multiple Fourier transform generation for coherent optical correlators", Appl. Opt. 29, 1589 (1990).

Chapter 6

Fabrication of Hybrid Kinoform Fan-Out Elements in Dichromated Gelatin

6.1 Introduction

Over the past few year, a great deal of work has been directed into the design and fabrication of diffraction gratings which have continuous, phase profiles. These components, generally referred to as kinoforms [1], can theoretically generate arrays of equal intensity beams with a diffraction efficiency approaching 100%. Fabricating optical elements which have a continuous surface-relief or refractive-index profile has, however, proven to be a difficult task. Although several kinoforms have been recorded as surface-relief structures in photoresist, an extremely high phase-relief accuracy is required if the levels of uniformity needed for optical interconnections are to be met [2,3]. An alternative approach involves fabricating a kinoform which has a only a few, discrete, equally spaced phase levels since, in principal, these structures may be fabricated in a relatively straightforward manner using standard microlithographic techniques [4-7]. Several groups have recently demonstrated multiple-phase kinoforms, for example, Dames et al., demonstrated a four level kinoform which had a diffraction efficiency of over 74% and a ±1% uniformity [8].

In the following chapter, a procedure for fabricating periodic Fourier-transform kinoforms in DCG is described. This technique, which was first proposed by J. Turunen [9], involves recording an off-axis volume phase hologram using a plane reference wave and an object wavefront generated from a binary-amplitude CGH. The CGH is designed such that, by spatially filtering out all but its first diffraction order, an almost uniform amplitude, continuous phase wavefront can be generated at the holographic plane [10,11]. Using this wavefront, an off-axis volume phase hologram can be recorded which, when replayed with

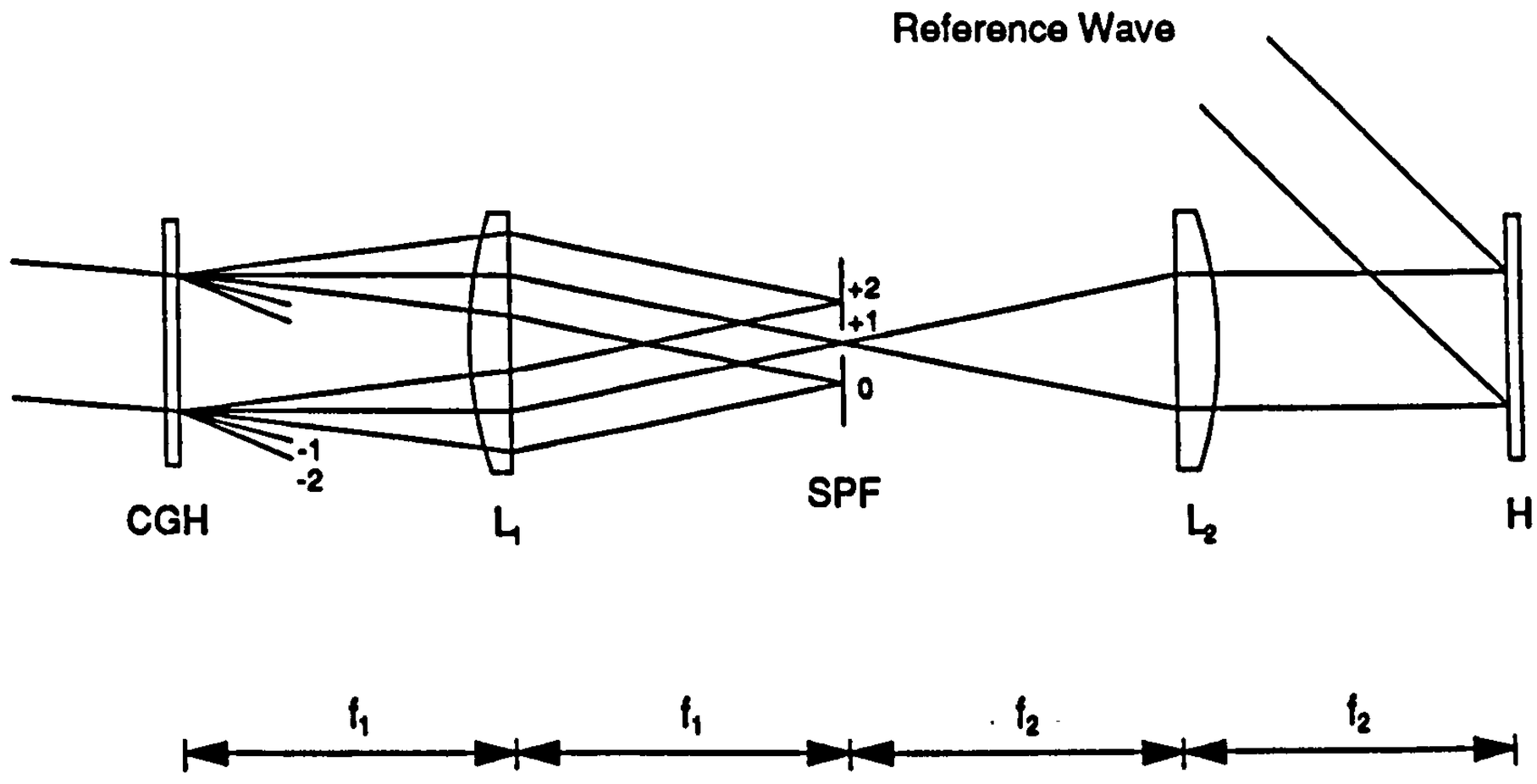

Figure 6.1 - Experimental arrangement for recording a hybrid kinoform. CGH : Computer generated hologram which generates the hybrid kinoform wavefront; -2,....,2 denote the diffraction orders of the carrier grating; SPF : Spatial filter which passes only the first order of the carrier grating; H : Sensitized DCG plate.

a plane wave, generates the kinoform wavefront. As this fabrication technique has much in common with the concept of the hybrid hologram, first proposed by Bartelt and Case [12], the resulting fan-out elements will be referred to as hybrid kinoforms. It should also be noted that, in many respects, it is similar to the recording techniques used in the previous two chapters. As a continuous, as opposed to binary wavefront is recorded, however, the performance of the fan-out elements will be, in theory, much better.

A schematic diagram of the recording set-up is shown in figure 6.1. The binary-amplitude CGH is imaged by lenses L_1 and L_2 onto plane H where a sensitized holographic plate is positioned. In its first diffraction order the CGH produces a wavefront corresponding to that which would be produced by an equivalent phase-only kinoform with a trapezoidal profile (figure 6.2). Thus, by filtering out all the other orders except the first order, the required continuous phase wavefront can be generated at H. Such a spatial filtering operation can be performed quite precisely with a variable aperture slit placed exactly at the back focal plane of lens L_1, allowing control to be exercised over the number of

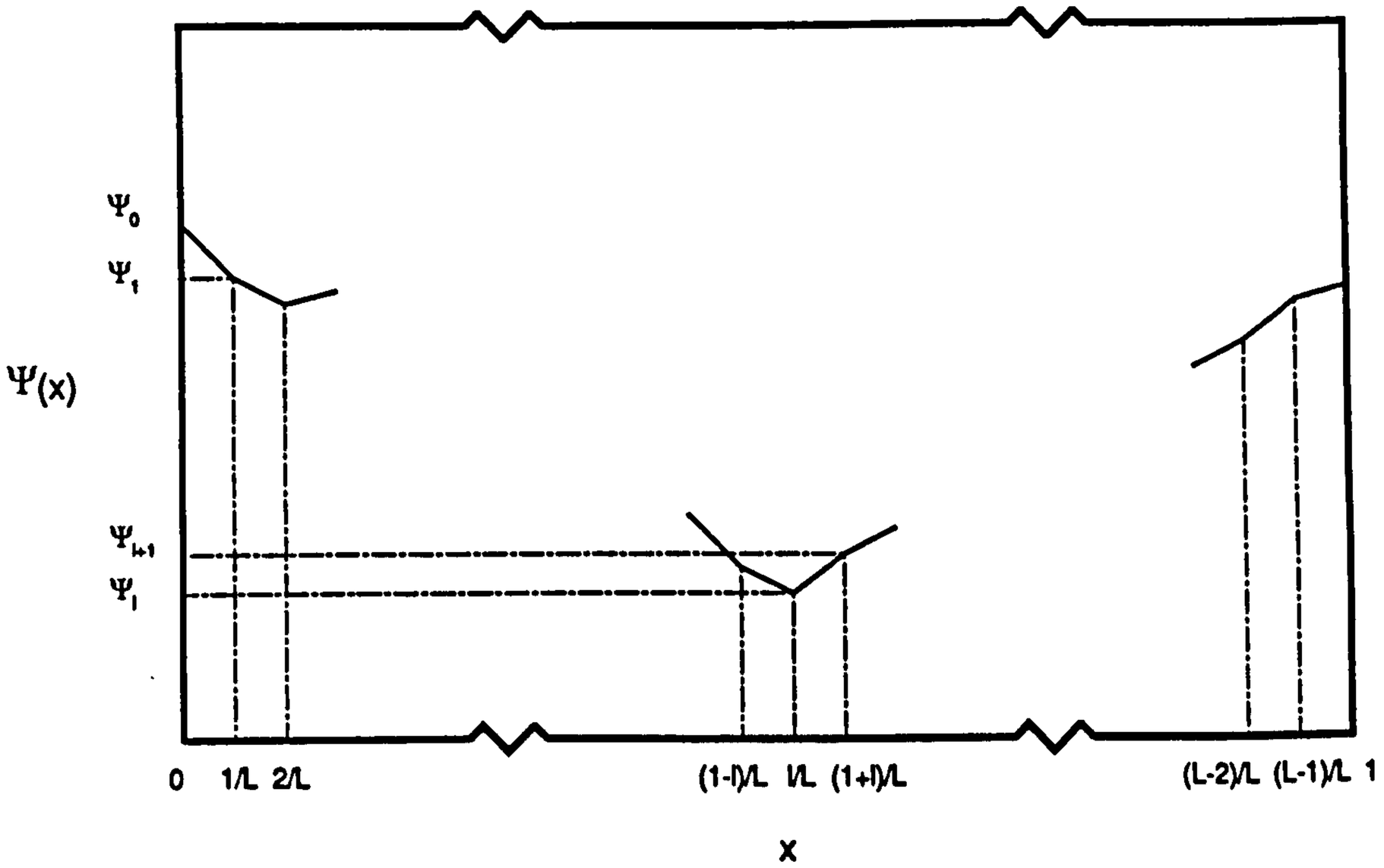

Figure 6.2 - Trapezoidal phase profile of the kinoform.

diffraction orders passed. The reference wavefront consists simply of a plane wave incident at an angle to the sensitized DCG plate as shown in figure 6.1. Standard exposure and processing techniques can then be applied to record an off-axis, volume phase HOE.

Using this fabrication technique, a set of hybrid kinoforms were recorded in DCG which produced a linear, one to eight fan-out. Overall diffraction efficiencies of up to 88% along with array uniformities of be better than ±4% were obtained in these initial experiments. Moreover, only 4% of the light diffracted into the first Bragg angle appeared in the unwanted, higher diffraction orders; the component could therefore be used in a general fan-out configuration without any cross-talk problems arising. These results constitute, by far, the best performance of a fan-out element obtained during the course of this thesis.

6.2 Theory of technique

6.2.1 Kinoforms with trapezoidal phase profiles

Before describing how the amplitude CGH was designed and optimized, let us first consider the properties of an on-axis kinoform which has a cellular trapezoidal phase profile, as

shown in figure 6.2. Such a phase function can be expressed, mathematically, in the form

$$\Psi(x)=\Psi_l+L(\Psi_{l+1}+\Psi_l)\,(x-l/L)\,,\quad x\in(l/L\,,(l+1)/L) \tag{6.1}$$

where $l=0,\ldots,L-1$, $\Psi_l=\Psi(l/L)$, and the grating period has been normalised to unity. This allows us to generate a continuous phase profile using only a finite number of transition points. The relative amplitudes of the grating's diffraction orders, U_m, can be calculated from the Fourier coefficients of the grating profile, i.e.

$$U_m=\int_0^1 \exp[-i(\Psi(x)-2\pi mx)]\,dx \tag{6.2}$$

and thus it can be shown that

$$U_m=(\pi L)^{-1}\sum_{l=0}^{L-1} sinc[(B_l-2\pi m)/2\pi L]$$
$$\times\exp[i((\Psi_l+B_l/2L-\pi m(2l+1))/L)] \tag{6.3}$$

where the substitutions $B_l=L(\Psi_{l+1}-\Psi_l)$ and $sinc(x)=\sin(\pi x)/(\pi x)$ are used. The power spectrum of the kinoform, $P_m=|U_m|^2$, can therefore be calculated directly from the gratings amplitude coefficients.

By optimizing the values of Ψ_l, the power in $N=M_2-M_1$ adjacent orders, where $m=M_1,\ldots,M_2$, may be equalised. This requires that the grating period contain at least $L\approx N$ independent line segments. In addition, for practical interconnection applications, the diffraction efficiency, defined as the amount of incident power diffracted into the desired orders, must be maximised, and the array non-uniformity minimised. This results, typically, in goal efficiencies of around 97% and in array uniformities of better than ±1%, depending on the actual fan-out (considering only a binary power spectrum). As only a small amount of power appears in the higher unwanted diffraction orders, cross-talk problems, which can occur when operating in a space-invariant fan-out mode, are reduced.

In addition, unlike a binary grating, a kinoform does not have to have inversion symmetry. Thus, more flexibility exists with this approach as it is possible to fabricate components with arbitrary fan-out patterns and weightings. Full details of the optimization procedures used to design these components is given in reference [11] along with an analysis of their diffractive properties based on beam propagation theory.

6.2.2 Design of amplitude CGH

As mentioned in the introduction, fabricating such a phase profile would be an extremely difficult task using, for example, conventional photolithographic techniques. It is, however, possible to generate a wavefront having a trapezoidal phase profile from a binary-amplitude CGH. The technique used follows on from the concept of the detour phase kinoform, described by Turunen et al [13]. A linear phase term, $2\pi Qx$ where Q is an integer, is added to the trapezoidal phase profile, resulting in a new phase term

$$\Psi_c(x)=\Psi(x)+2\pi Qx \tag{6.5}$$

- This has the effect of shifting the output array by Q orders from its original position, thereby separating it from the zeroth order of the kinoform. It does not, however, alter the power spectrum of the grating. An increased zeroth order intensity, caused by an error in the phase depth for example, would therefore not affect the signal beams. The next step involves quantising the new phase profile, $\Psi_c(x)$, to give a periodic binary-amplitude transmission function, t(x), with transition points determined from

$$t(x)=\begin{cases}1, \Psi_c(x)\in(k\pi,(k+1)\pi)\\ 0, \Psi_c(x)\in((k+1)\pi,(k+2)\pi)\end{cases} \tag{6.6}$$

where k is an integer. This transmission function is then used to fabricate a binary-amplitude mask. As t(x) is a periodic function in $\exp(i\Psi_c(x))$, it may be expressed in the form of a generalised Fourier series [14]. That is

$$t(x) = \sum_{n=-\infty}^{\infty} c_n \exp(in\Psi_c(x)) \tag{6.7}$$

where $c_o = 1/2$ and $c_n = [1 + (-1)^n]/2\pi n$. If the grating is illuminated by a unit amplitude plane wave, the diffracted field consists of a superposition of component wavefields proportional to $\exp(i\Psi_c(x))$ which propagate in different directions and the $q = 1$ order corresponds to the required kinoform wavefront. Thus, in the back focal plane of lens L_1, the $q = 1$ wavefront will consist of an array of diffraction orders, which have the kinoform power spectrum. Problems can arise when considering the effect of noise contributions from the other $q \neq 1$ wavefronts. As these cannot be separated from the desired wavefront, no matter how large Q is, some distortion in the object beam wavefront may occur [10,11]. In practice, however, this was not found to significantly affect the performance of the CGH used in these preliminary experiments.

When designing a kinoform which generates an even fan-out, two approaches may be employed. The first involves optimizing the power spectrum such that $N = 2M$ orders have equal power in the range $m = -M + 1, \ldots, M$. Alternatively, an even order missing design can be used (i.e., the $N = M$ odd orders between $m = -2M + 1, \ldots, 2M - 1$ are equalised, the even orders being kept at zero). This has the added advantage of removing the central zeroth and, in the 2D case, axial orders, which are more sensitive to noise caused by non uniformities.

6.3 Fabrication of hybrid kinoform fan-out elements

6.3.1 Recording set-up

In order to investigate the performance of an interconnect fabricated using this approach, a set of linear one to eight fan-out components were recorded in DCG. The amplitude mask was optimised by J. Turunen (see reference 9) and plotted on an electron beam writer at the Rutherford Appleton laboratories by J. M. Miller. A period of 2.5mm and a value for Q = 250 (producing a 2.8° angle between the zeroth and first orders of the amplitude CGH) were chosen (detailed descriptions of the design and optimization procedures used are given in reference [11]). The theoretical uniformity of the central eight signal beams

was calculated to be 2.6%, however, due to the finite accuracy of the electron beam writer, the measured uniformity of the array generated by the amplitude mask was found to be slightly higher with a value of 2.8% (at 488nm). The average feature size of the amplitude mask was 5μm and the smallest feature was determined to be 1.3μm. These mask dimensions are within the capabilities of any electron beam writer capable of recording sub-micron features.

The recording set-up used to fabricate the hybrid kinoforms is shown in figure 6.3. Lenses L_1 and L_2 were chosen to have focal lengths of 250mm and 100mm respectively and were positioned so as to provide a telecentric imaging system (as in chapter 5). The grating period was therefore imaged down from 2.5mm to a measured value of 988±2μm. This permitted a more compact optical system to be used on replay. Imaging down also presents a method of overcoming the e-beam writers limited spatial bandwidth, i.e., the e-beam system will not record a 1mm grating to the same accuracy.

In order to obtain a high quality object wavefront, a great deal of care was taken whilst setting up the recording system. This required exact normal alignment of both the imaging lenses and the holographic plate to the object beam, i.e. the first diffraction order of the CGH. In addition, the CGH itself was tilted at ≈2.8° to the object axis to ensure that the kinoform wavefront was imaged precisely at the holographic plane, *H* (figure 6.1). Finally, as in the previous experiments, the reference beam was adjusted so as to be incident at 30° to the object beam axis.

The spatial filter could be adjusted to control the number of diffraction orders passed, i.e., to transmit only the set of orders $Q-M_1,\ldots,Q+M_2$. The resulting field distribution produced in the holographic plane by these diffraction orders can be calculated from

$$E(x)=\sum_{m=Q-M_1}^{Q+M_2} A_m \exp[i2\pi(Q-m)x] \qquad (6.7)$$

Here the tilt between the propagation direction of the wave incident on the CGH, and the orientation of the DCG plate has been compensated for by introducing the term $\exp(-i2\pi Qx)$. As a consequence of spatially filtering the wavefront produced by the CGH, the field distribution, E(x), at the holographic plane can no longer be strictly phase only.

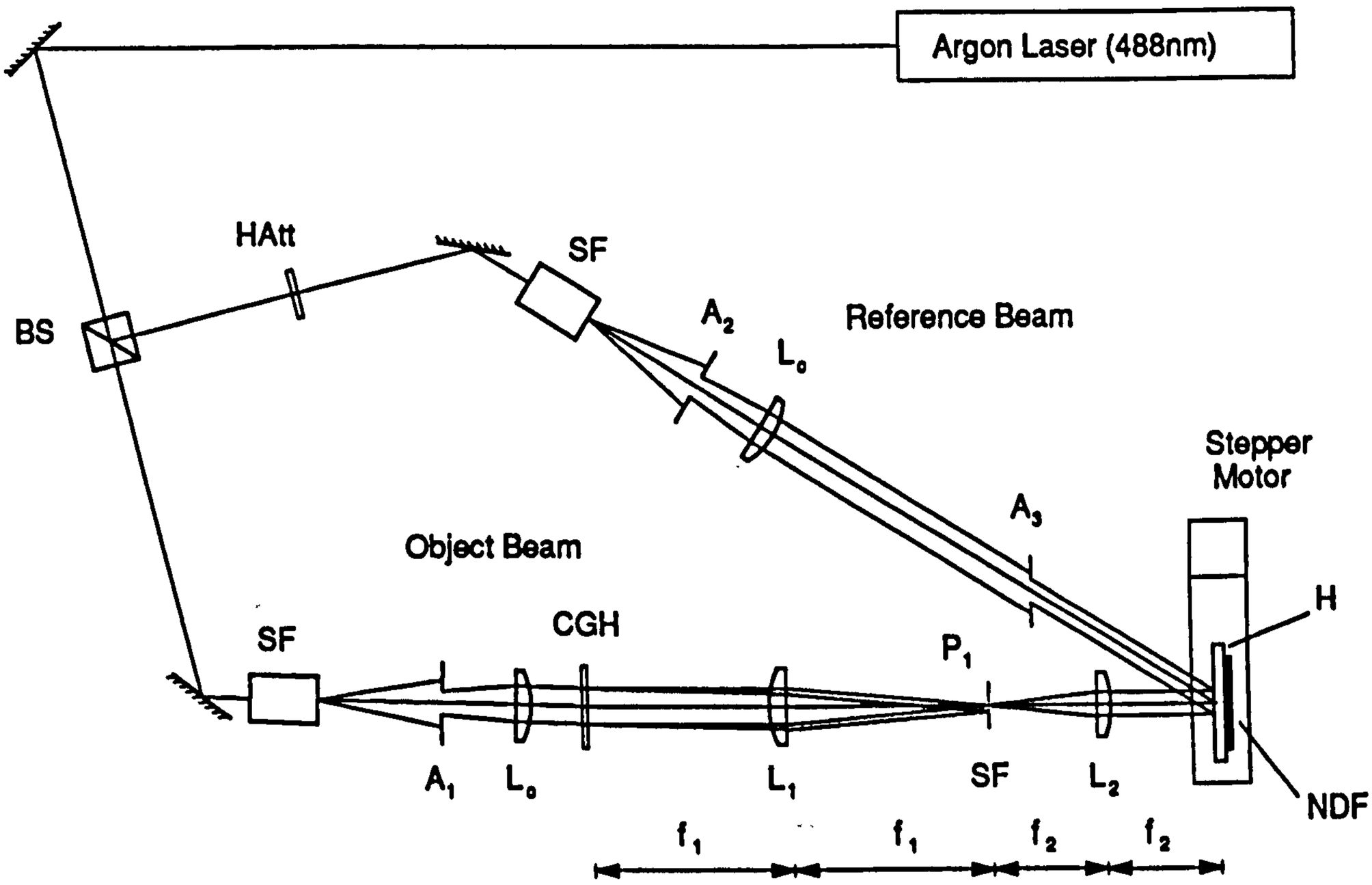

Figure 6.3 - Experimental set-up used to record the hybrid kinoform.

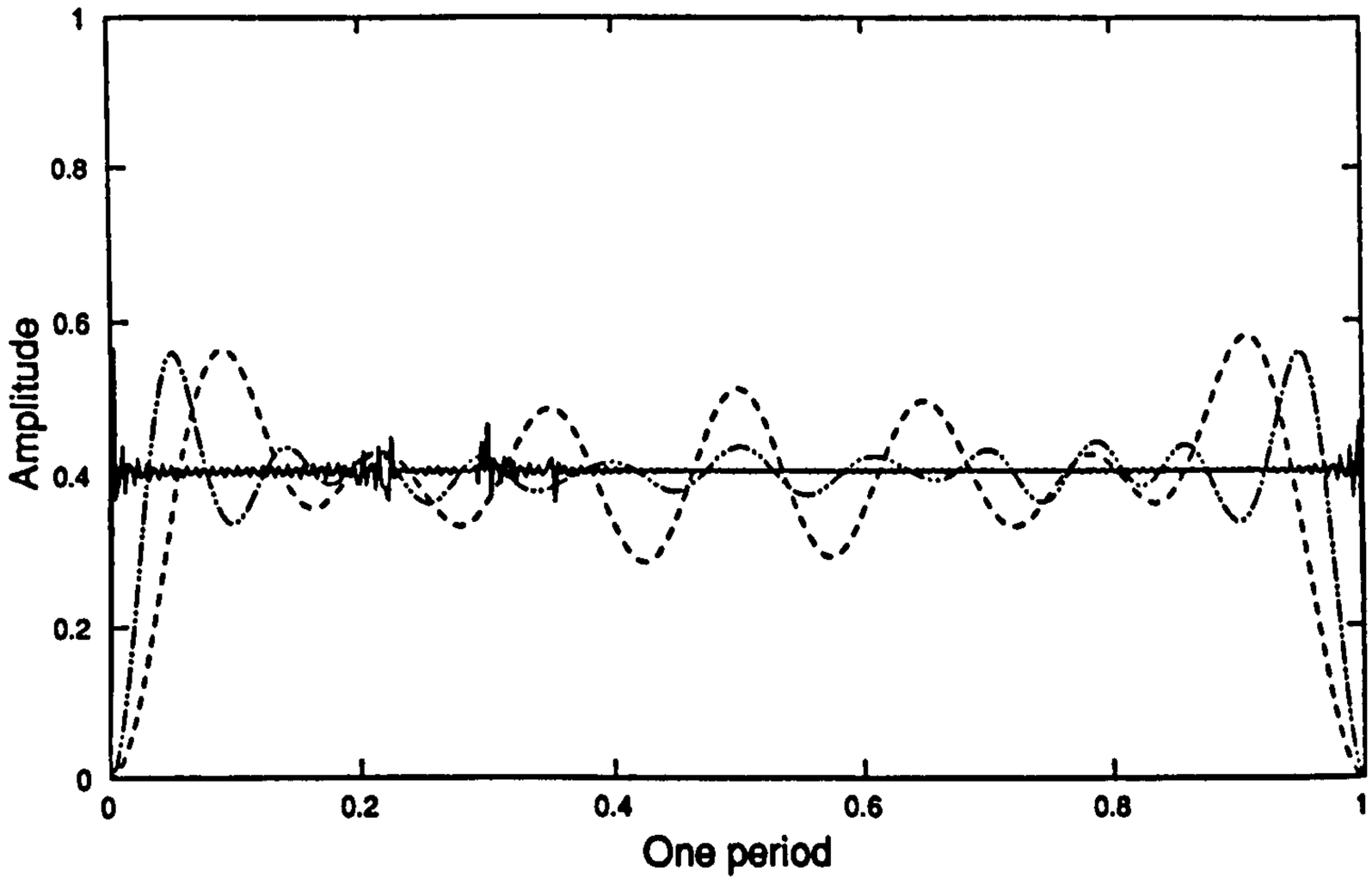

Figure 6.4 - Calculated amplitude variations in the DCG plane of figure 6.1 caused by the spatial filter removing the higher diffraction orders. Dashed line, 8 orders; dashed-dotted line, 20 orders; solid line, 500 orders. (After Ichikawa [10]).

If enough orders are transmitted, however, the variations in amplitude across the object wavefront will be minimal. This is illustrated in figure 6.4, where the theoretical amplitude profile due to the central 8, 20 and 500 diffraction orders are shown ($M_1 = M_2 = 4$, 10 and 250). It is apparent from these theoretical profiles that as more orders are passed the amplitude distribution becomes more uniform; even with only 20 orders passed a reasonably flat amplitude profile is obtained, and when 500 orders are passed, the variations are minimal.

It is important to note that the object wavefront produced by this technique differs noticeably from those generated by the binary gratings used in the previous two chapters. The wavefront derived from a binary-grating contains greater amplitude fluctuations due to the loss of higher order spatial frequencies through the imaging optics. In the case of an equivalent kinoform wavefront, however, much more of the power is concentrated in the central diffraction orders. The loss of the higher orders will therefore have a far smaller effect on the field produced at the holographic plane.

6.3.2 Complete wavefront copy

Initially, a series of complete wavefront copies were recorded at 488nm. The spatial filter was set to transmit approximately 200 diffraction orders (i.e., $Q-M,....,Q+M$ orders where $M=100$). A scanning slit and phototdiode system was set-up and used to measure the intensity profile of the wavefront generated at the holographic plane. The result of this scan is shown in figure 6.5(a). As can be seen, the hybrid kinoform object wavefront has an almost uniform intensity profile. For comparison, a similar scan was made of the wavefront diffracted in the first Bragg angle by the hybrid kinoform (figure 6.5(b)). To avoid interference from the other Bragg orders, the measurement was actually performed in the image plane of the DCG grating.

Figure 6.6, shows a photograph of the output array generated by one of the hybrid kinoforms. The hologram was replayed at 488nm using the optical arrangement described in figure 6.7. The uniformity across the central eight signal beams was measured to be 3.2% whilst the holograms (Bragg) diffraction efficiency was found to be 96.3%, i.e. 96.3% of the transmitted power ended up in the reconstructed kinoform wavefront. Higher diffraction efficiencies of almost 98.5% (real efficiency 89.1%) were obtained during the course of this work, however, due to saturation of the refractive index modulation the uniformity of the output grew slightly worse, increasing to ≈5%.

In the previous CGH copying experiments, described in chapters 5 and 6, the array uniformity tended to double during the recording process. The results obtained using this technique, however, showed only a slight decrease in uniformity. For example, in the interconnect shown in figure 6.6, the uniformity was measured to rise from an initial 2.8% to just 3.2%. This can be put down to the far better quality of the object beam wavefront. A slight dependence of the uniformity on replay angle could also be observed: a 1° tilt caused it to increase from 3.2% to 4%. In most practical situations such a small variation will not cause any problem. This shall be discussed in more detail in section 6.3.3.

It is important to ensure that as much light as possible ends up in the signal beams. Not only does this maximise efficiency, it also prevents cross-talk becoming a problem when the hybrid kinoform is used to fan-out a number of input beams. Measurements of the power spectrum of the reconstructed kinoform wavefront depicted in figure 6.6 showed

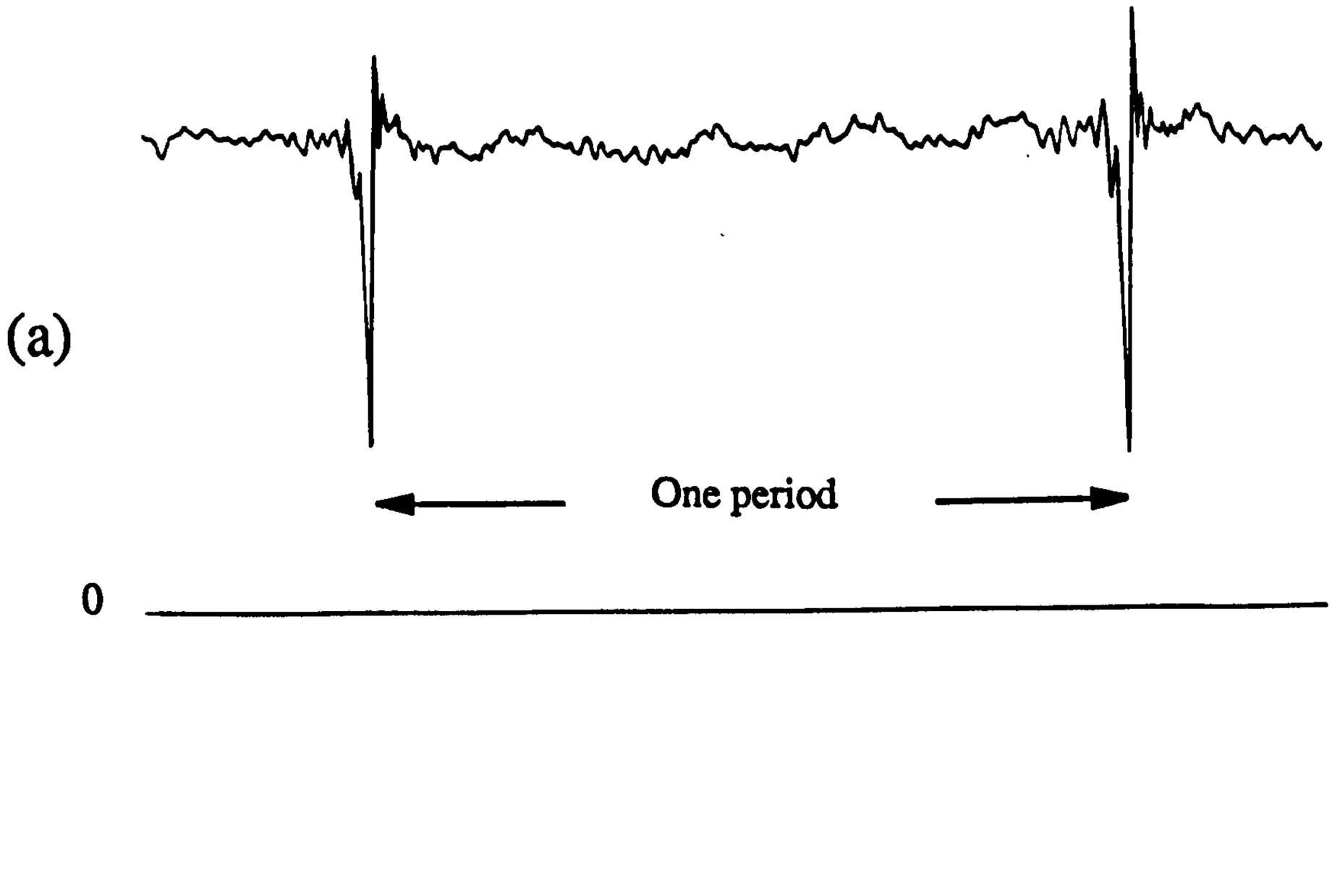

Figure 6.5 - Experimentally measured intensity profiles (a) Generated at the holographic plane by the CGH. (b) Generated at the holographic plane when the hybrid kinoform was replayed.

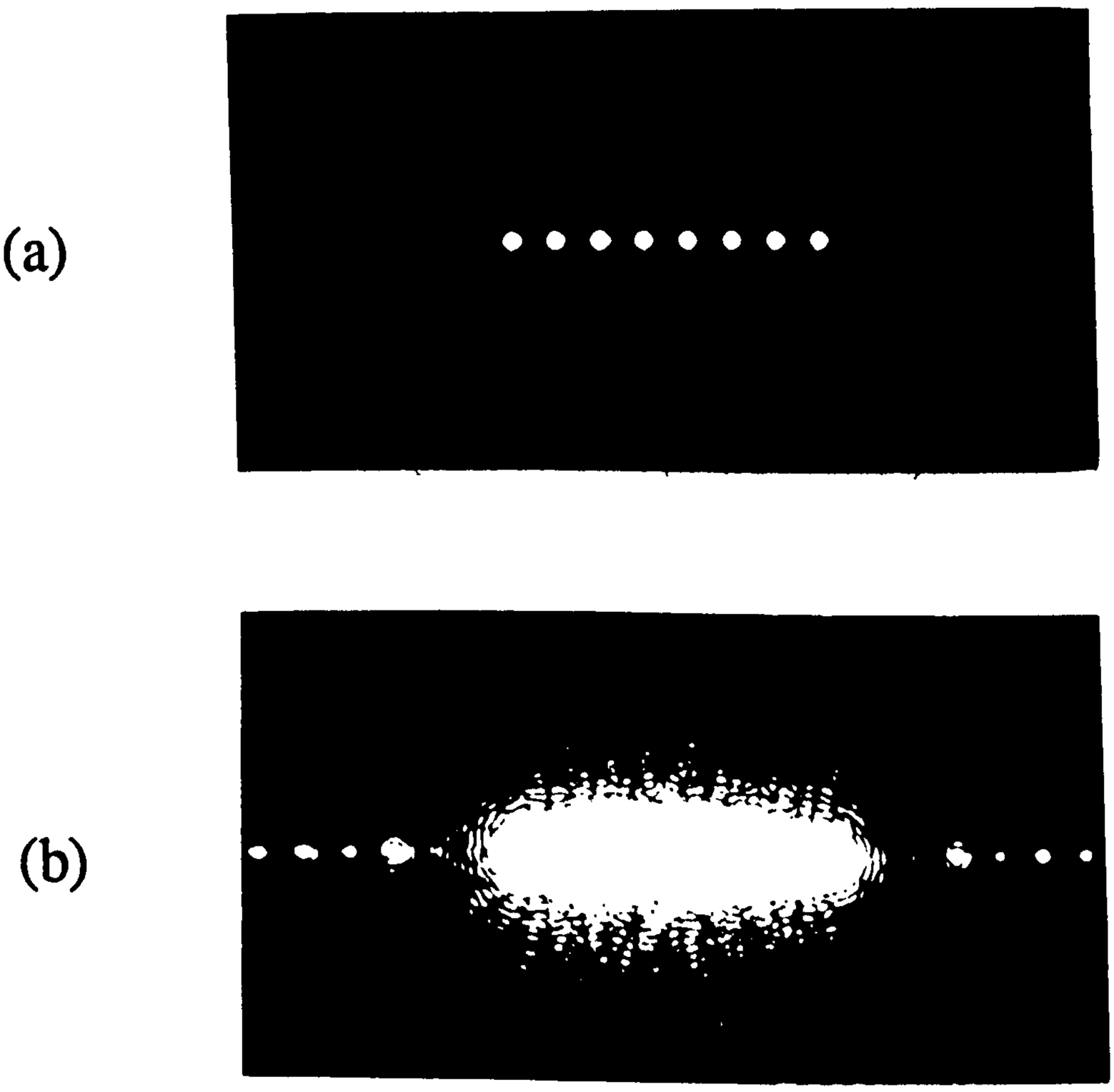

Figure 6.6 - (a) Array produced by the hybrid kinoform with approximately 200 orders included. (b) Same array overexposed to show up the higher diffraction orders.

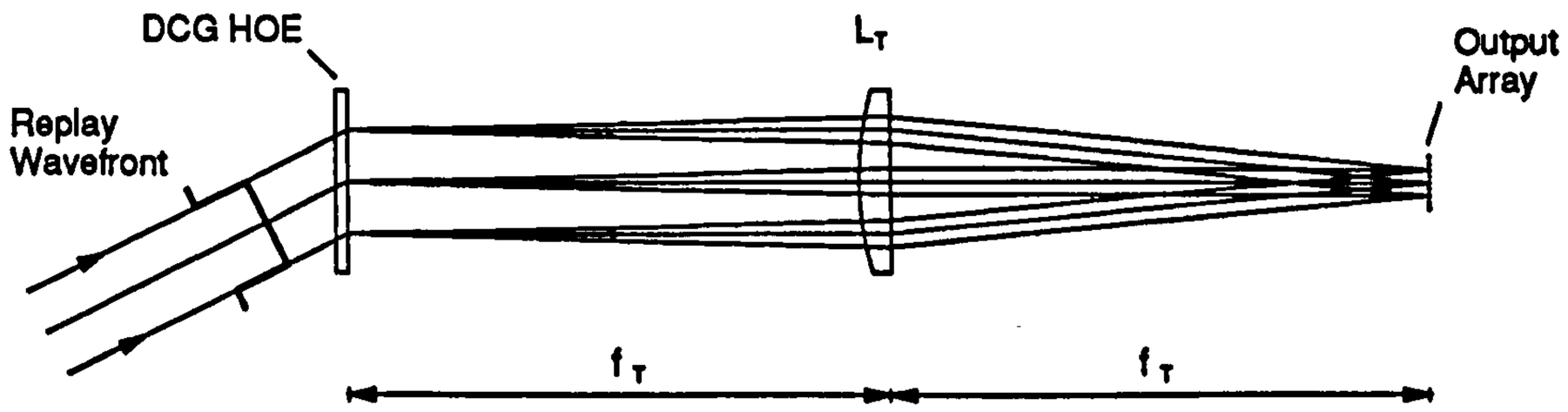

Figure 6.7 - Optical arrangement used to reconstruct the hybrid kinoform.

that 96% of the light diffracted into the first Bragg angle appeared in the central eight kinoform orders (compared to the design value of 95.95%). The power in the higher, unwanted diffraction orders is therefore low enough to ensure that cross-talk will not cause difficulties. In the case of a fan-out to eight interconnect, a minimum of 88% of the diffracted power must end up in the signal beams for correct operation to occur (ignoring any interference effects). The DCG hologram recorded in this experiment safely met this criteria, diffracting 96% of the light into these orders.

The real efficiency of the hybrid kinoform, defined as the amount of power in the reconstructed object wavefront with respect to the incident power, was determined to be 87.7%. This was due to a Fresnel reflection loss at the input face of the DCG copy of 5.8% (the exit face being sealed with an antireflection coated coverplate to minimize reflection losses) and absorption and scattering losses in the DCG, optical cement and coverplate of about 3%. The efficiency of the hybrid kinoform could, in theory, be increased to over 90% by using an appropriately A.R. coated substrate. It can therefore be concluded that this recording technique may be used to produce fan-out holograms which have both a high diffraction efficiency and a good uniformity.

6.3.3 Angular acceptance

One of the most important factors affecting the performance of a hybrid kinoform is its angular acceptance. In particular, if such an element is to be used as a space-invariant

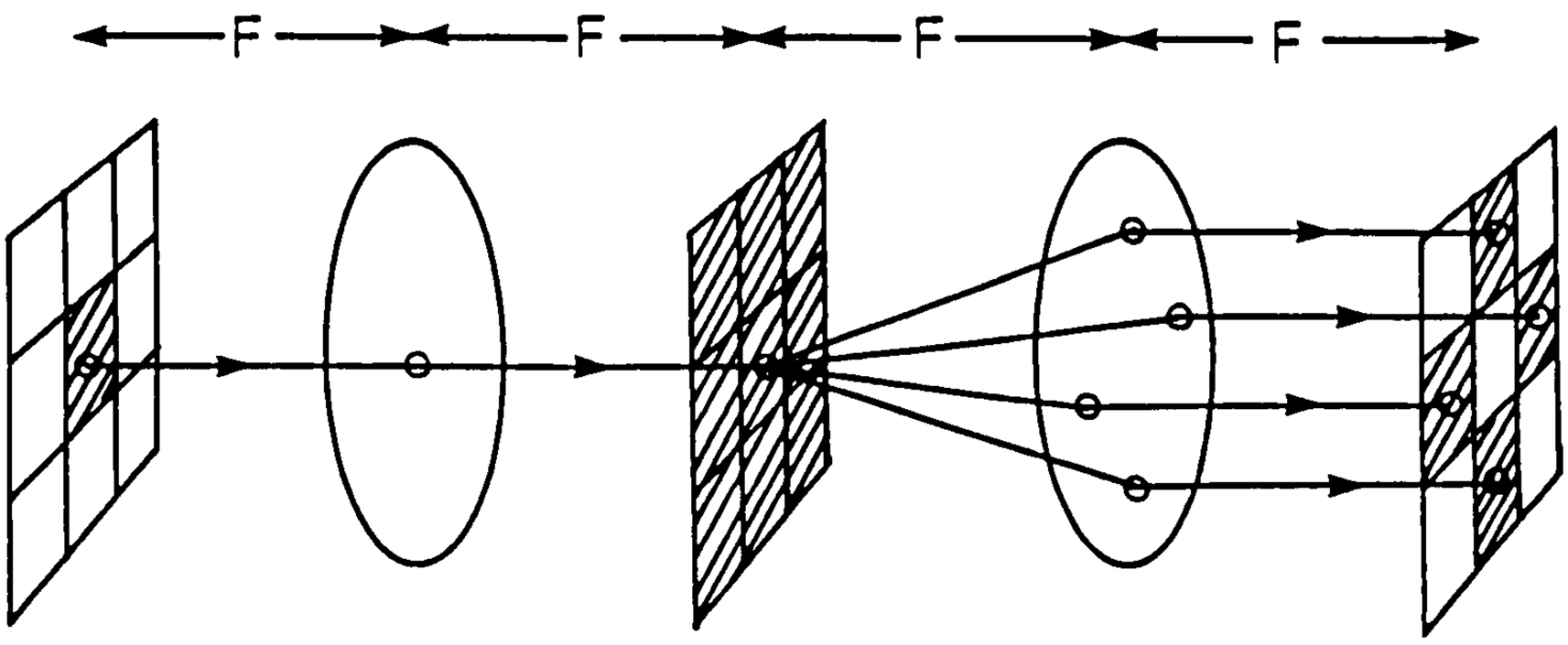

Figure 6.8 - Fan-out hologram operating as a nearest neighbour space-invariant interconnect. (After Redmond [15]).

interconnect its response must remain constant across the required range of input angles. To illustrate this problem, let us first consider the optical system outlined in figure 6.8. This shows a space-invariant fan-out element interconnecting two N×N arrays of optical logic elements together. Each of the input beams, generated at plane P_1, are collimated by lens L_1. The collimated light passes through the fan-out element where it is split into a number of angularly separated beams. These beams are then finally focussed down by lens L_2 onto the output plane, P_3. It should be noted at this point that the set-up in figure 6.8 shows an on-axis interconnect, whilst the hybrid kinoforms described in this chapter are off-axis components. In practice, however, the hybrid kinoform would be used with a compensator plate, thereby allowing the on-axis system to be employed.

Let us assume the spacing between the processing elements at both planes P_1 and P_3 is d. The maximum interconnection angle, θ_{max}, will therefore be given by $\tan\theta_{max} = Nd/\sqrt{2}f_1$, where f_1 is the focal length of lens L_1. This defines the minimum angular acceptance that a hybrid kinoform must have if it is to be a viable interconnection element. To consider this problem further, let us first consider the variation of diffraction efficiency with reconstruction angle. If the condition $\delta \ll \theta$ (i.e., the fan-out angles are small) holds true, we may, to a first approximation, treat the hybrid kinoform as a simple plane grating. The

angular response of the hologram can therefore be calculated using the coupled wave theory described in chapter 2. In order to analyse this problem more rigourously, a three-dimensional vector coupled wave theory (e.g., as described by Syms [16]) must be used. The simpler 1-D approach described in chapter 2 does, however, allow us to estimate the potential usefulness of the hybrid kinoform.

In order to evaluate the bandwidth of the hybrid-kinoform the variation in zeroth order power was measured. The results of this experiment are shown in figure 6.9. As can be seen, the efficiency drops off very rapidly as we move away from Bragg reconstruction angle, reaching a minimum at $\Delta\theta \approx \pm 6°$. The theoretical curve also shown in figure 6.9 was calculated using equation (2.30) with the parameters $n = 1.5$, $n_1 = 0.015$, $\lambda = 488nm$ and $d = 14\mu m$. The close correspondence between the experimental and theoretical results indicates that, in terms of its angular response, the hybrid kinoform behaves very much like a plane grating. Taking the useful angular bandwidth to be the region where the power varies by less than 5%, the hybrid-kinoform has an angular acceptance of about $\pm 0.8°$. As the angle between the fanned-out beams, $\delta = 0.028°$, the maximum array size which can be handled by the hologram will be of the order of 20×20. Combining the hybrid kinoform with a compensator plate to provide on-axis operation will, however, reduce the angular acceptance (i.e., the total throughput will be given by the product of the efficiencies of both elements. It is important, therefore to improve the angular response of the hybrid kinoform and compensator plate. This may be achieved by using either thinner gelatin, or by using a larger grating period (i.e., using a smaller reference beam angle). The performance of hybrid kinoforms recorded in thin gelatin layers has been investigated by Ichikawa [11]. The results of his work show that by using 5μm thick gelatin layers, the angular acceptance of a hybrid kinoform can be approximately doubled.

In order for the hybrid kinoform to operate successfully as a space-variant fan-out component, no variation in the weighting of the beams must occur across the interconnection field. A slight dependence of the uniformity on replay angle was, in fact, observed; it was found that a 1° change in the replay angle caused it to increase from 3.2% to 4%. In most practical situations, however, such a small deviation will not introduce any problems. A discussion of this effect is also given in reference [11]

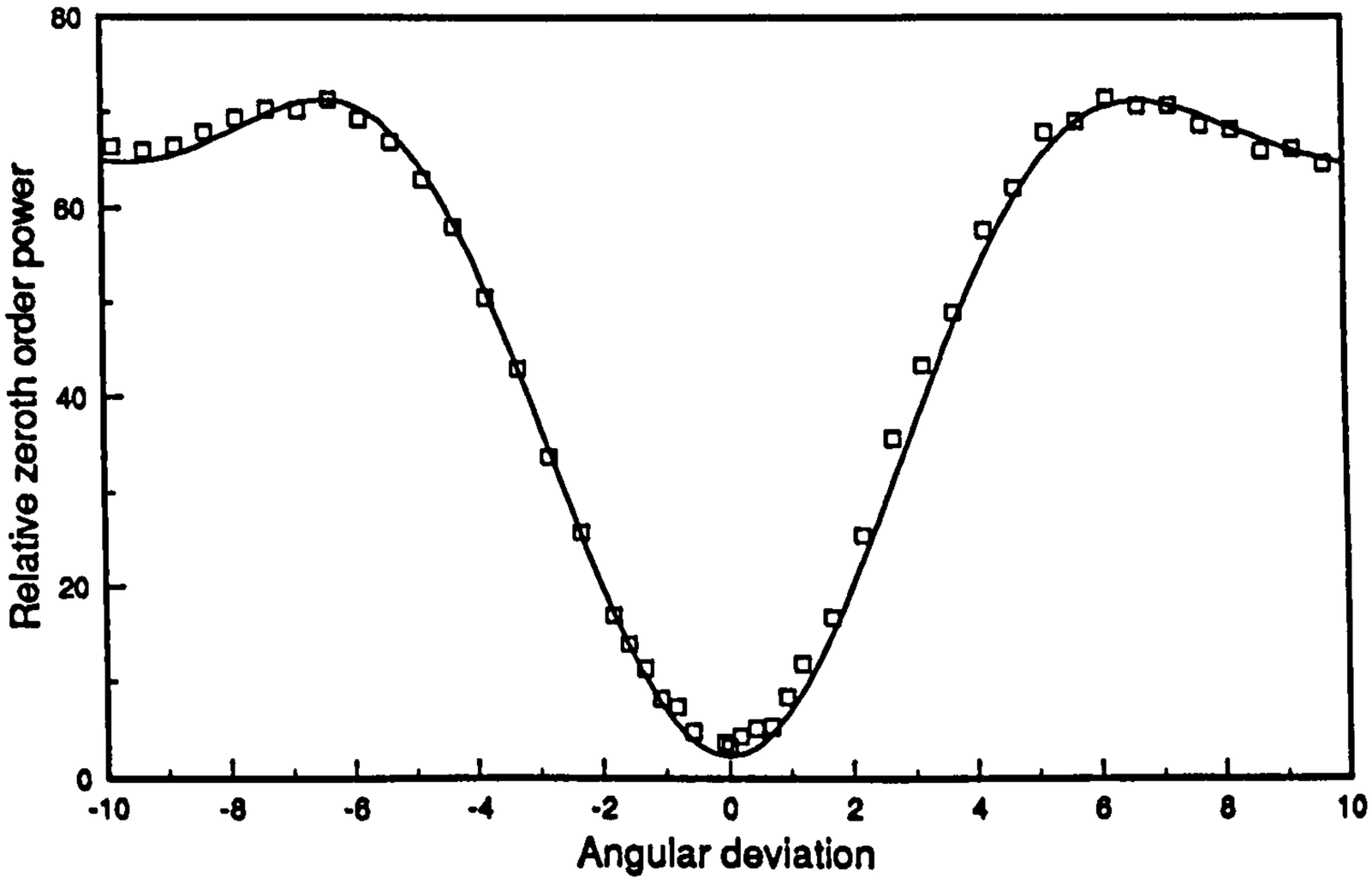

Figure 6.9 - Variation of zeroth order power with reconstruction angle.

6.4 Wavelength Dependence

Many of the optical circuits currently under development are designed to run in the near-infra red. If the hybrid kinoform is to be a useful alternative to binary and multilevel phase elements, therefore, it must be capable of operating at these wavelengths with the same sort of performance as at 488nm. Two experiments were performed to investigate the wavelength shifted performance of the hybrid kinoform. In the first it was replayed with a plane wavefront at 633nm, and in the second it was replayed with a Gaussian beam at 1.06μm.

6.4.1 Operation at 633nm

Figure 6.10 shows an intensity scan of the output array produced by the hybrid kinoform when it was replayed with a uniform amplitude plane wave at 632.8nm. The experimental set-up used a 250 mm focal length lens to focus the beams down and a CCD camera to measure the resulting intensity distribution. The full width of the spot was measured to

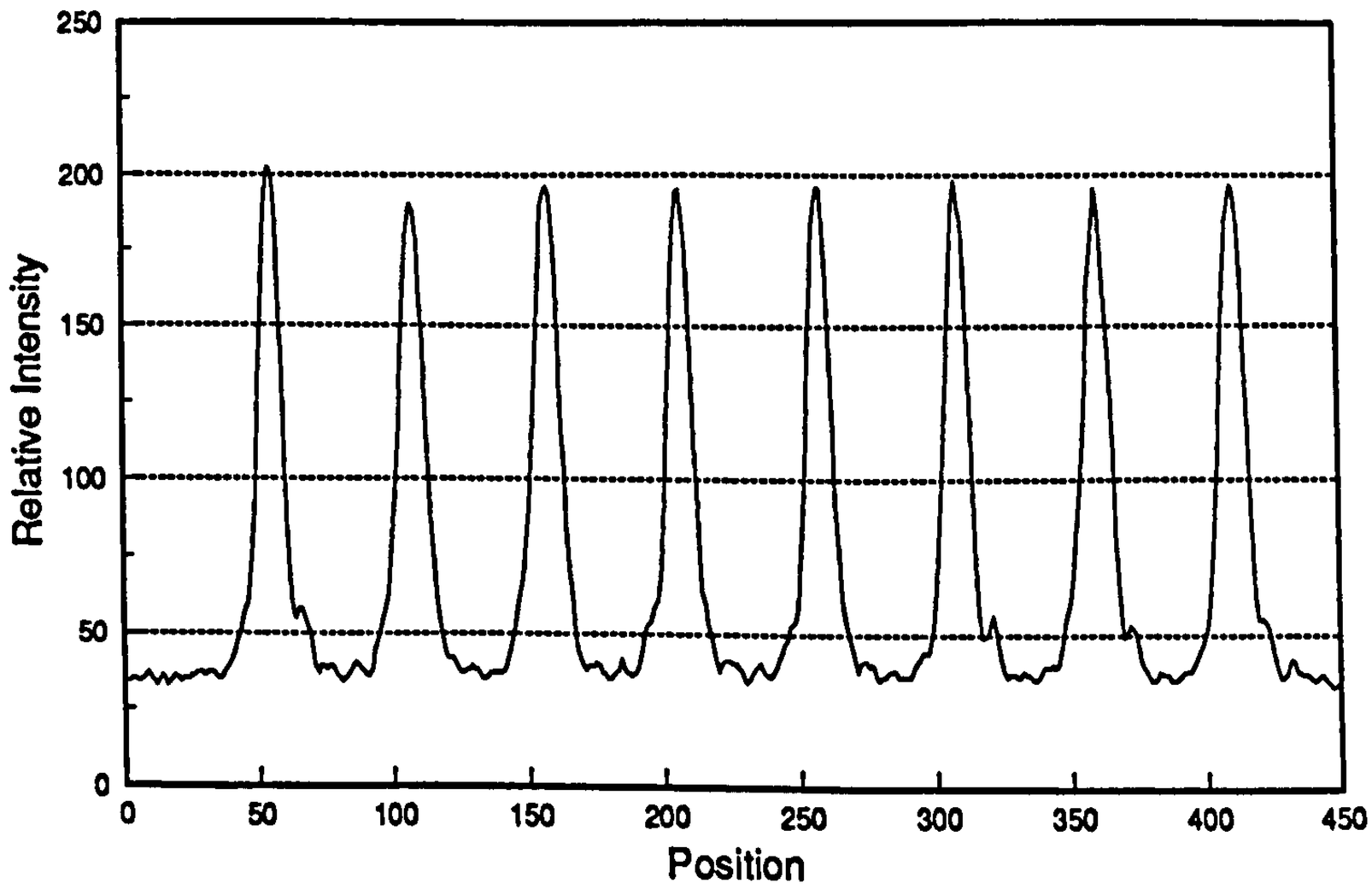

Figure 6.10 - Scan of intensity profile generated at 633nm by the hybrid kinoform.

be 66μm ±3%, which agrees very well with the theoretical value of 62μm. This indicates that the hybrid kinoform is capable of close to diffraction limited performance. The diffraction efficiency of the hybrid kinoform was found to have fallen from 96% to 60%. In principle, however, it should be possible to optimize the exposure levels during recording to produce elements with higher efficiencies.

Due to the finite number of pixels and their somewhat different sensitivities, the array uniformity cannot be measured directly using a CCD camera, although the scans do give a good indication of the intensity profiles. The uniformity of the array was therefore measured directly, using a power meter, and found to be ±4%. This is shows that the hybrid kinoform can be replayed at a different wavelength with negligible deterioration in uniformity and close to diffraction limited spots.

6.4.2 Operation at 1.06μm

In all the previous experiments, a uniform intensity plane wavefront was used to reconstruct the hybrid kinoform. Any practical optical circuit will, however, operate with Gaussian beams. It was therefore decided to investigate the performance of the hybrid kinoform when it was replayed with a Gaussian beam at 1.06μm. The experimental arrangement used in this study is shown in figure 6.11.

Once again a CCD camera was used to evaluate the output array generated at plane P_1. Figure 6.12 shows a photograph of the array taken from the CCD monitor. From this photograph it can be seen that, although slightly aberrated, the quality of the spots are still good. The uniformity of the array was measured, using a power meter, to be ±4.5%. It can therefore be concluded that the hybrid kinoform can operate in the near infra-red with a Gaussian beam and with only a slight deterioation in the array uniformity. In order to improve the usefulness of this device, however, it must be shown that the hybrid kinoform can be recorded such that the axis of the object beams lies normal to the hologram plane. This will make it easier to produce a useful, on-axis doublet arrangement.

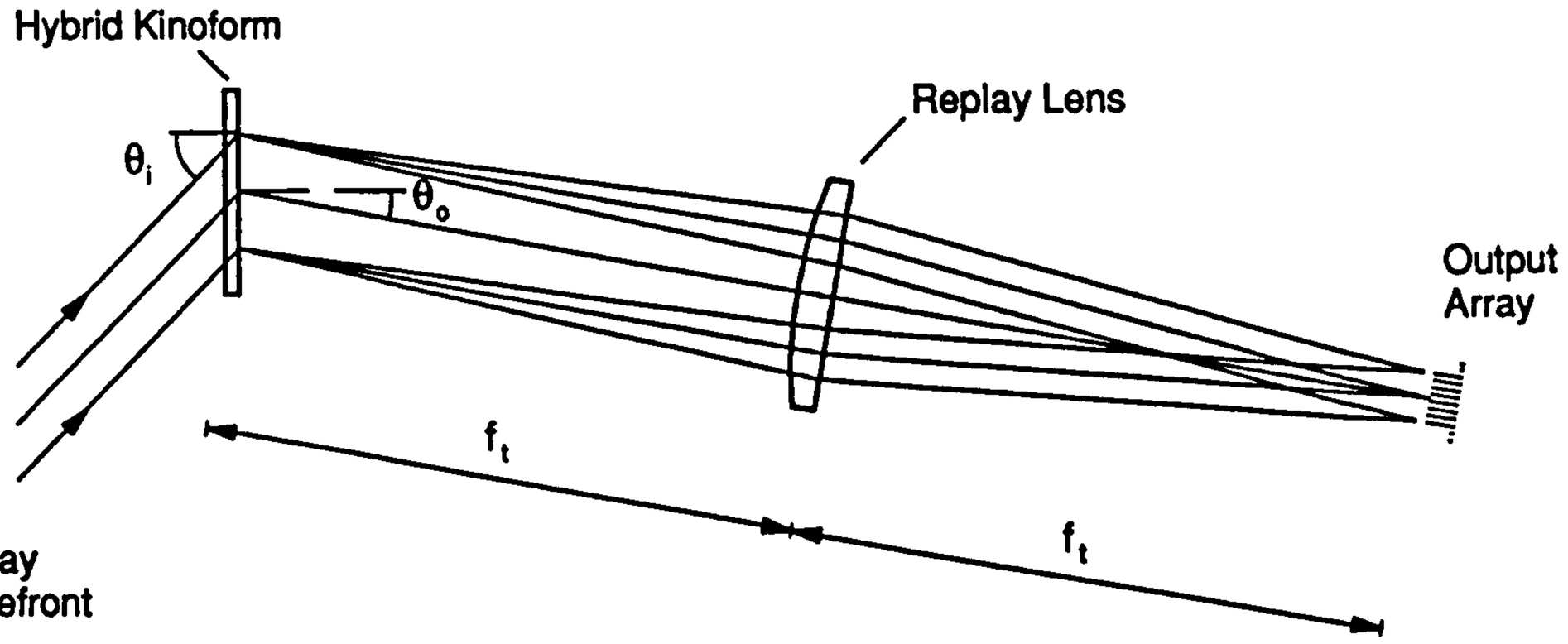

Figure 6.11 - Replay set-up used to reconstruct the hybrid kinoform at 1.06μm with a Gaussian beam.

6.4.3 Wavelength Stability

In order to get the best performance out of any holographic fan-out element, the replay light source must have a narrow bandwidth and a good stability. Problems may therefore arise when operating a hybrid kinoform with a diode laser as the output characteristics of these devices are sensitive to variations in temperature and to optical feedback. Several commercially available diode lasers, for example, exhibit wavelength changes of several nanometers unless some form of active temperature stabilisation is employed. This will affect the performance of the hybrid kinoform by changing both the fan-out angles and the orientation of the optical axis. By using a doublet configuration [17] (as described in chapter 5), however, the dependence of replay angle on wavelength may, to a first approximation, be avoided.

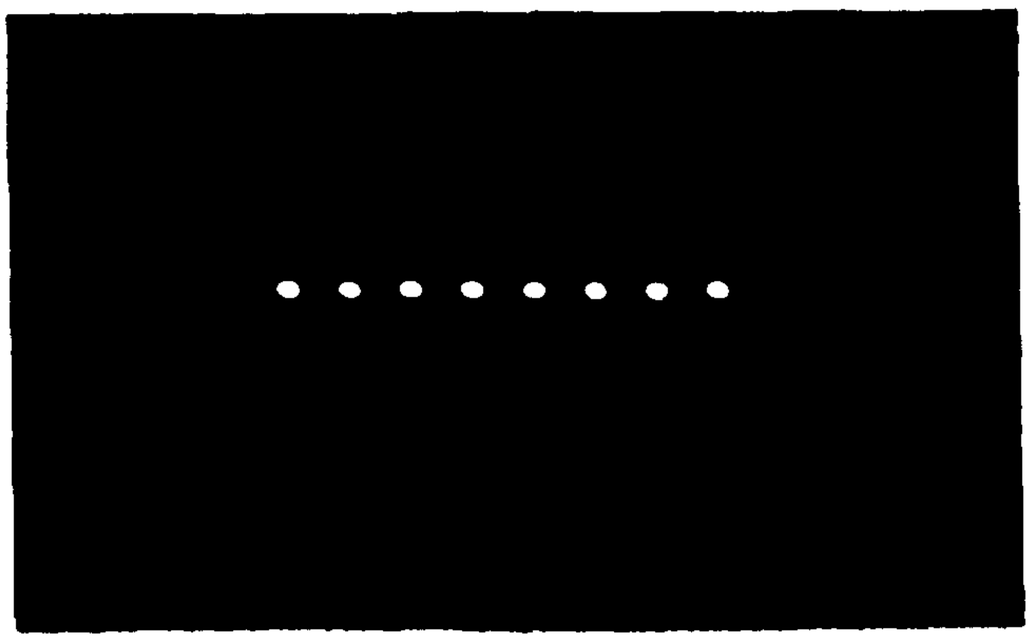

Figure 6.12 - Array generated by the hybrid kinoform when reconstructed at 1.06μm.

6.5 Conclusions

A new technique for recording volume phase fan-out holograms is described in this chapter. A continuous phase object wavefront was generated by spatially filtering the output of a specially designed CGH. The resulting hybrid kinoform fan-out components were measured to have a uniformity and an efficiency suitable for optical interconnection applications. In addition, it was found that operation in the near infra-red was possible without any appreciable increase in the reconstruction error.

Provisional measurements show that the hybrid-kinoforms had a useful angular bandwidth of just under 1°. Further work is needed, however, to fully characterise the angular response of these components. This requires both a theoretical and experimental evaluation of the diffraction efficiency and polarisation dependence for arbitrary reconstruction angles.

6.6 References

1) L. P. Lesem, P. M. Hirsch and J. A. Jordan, "The kinoform: a new wavefront reconstruction device", IBM J. Res. Dev. **13**, 150 (1969).

2) P. Ehbets, H. P. Herzig, D. Pronue, M. T. Gale, "High-efficiency continuous surface-relief gratings for two-dimensional array generation", Opt. Lett. **17**, 908 (1992).

3) H. P. Herzig, "Design and fabrication of highly efficient fan-out elements", Jpn. J. Appl. Phys. **29**, L1307 (1990).

4) J. Turunen, A. Vasara and J. Westerholm, "Kinoform phase relief synthesis: a stochastic method", Opt. Eng. **28**, 1162 (1989).

5) A. Vasara, J. Turunen, J. Westerholm and M. R. Taghizadeh, "Stepped-phase kinoforms" in *Optics in Complex Systems*, Proc. Soc. Photo-Opt. Instrum. Eng. **1319**, 298 (1990).

6) S. J. Walker and J. Jahns, "Array generation with multilevel phase gratings", J. Opt. Soc. Am. A **7**, 1509 (1990).

7) M. Ekberg, M. Larsson, S. Hard and B. Nilsson, "Multilevel phase holograms manufactured by electron-beam lithography", Opt. Lett. **15**, 568 (1990).

8) M. P. Dames, R. J. Dowling, P. McKee and D. Wood, "Efficient optical elements to generate intensity weighted spot arrays: design and fabrication", Appl. Opt. **30**, 2685 (1991).

9) J. Turunen, personal communication.

10) B. Robertson, J. Turunen, H. Ichikawa, J. M. Miller, M. R. Taghizadeh and A. Vasara, "Hybrid kinoform fanout holograms in dichromated gelatin", Appl. Opt. **30**, 3711 (1991).

11) H. Ichikawa, Optical Beam Array Generation with Phase Gratings, Ph.D. Thesis, Heriot-Watt University, Edinburgh, UK, 1992.

12) H. Bartelt and S. K. Case, "High-efficiency hybrid computer-generated holograms", Appl. Opt. **21**, 2886 (1982).

13) J. Turunen, J. Fagerholm, A. Vasara and M. R. Taghizadeh, "Detour-phase kinoform interconnects: the concept and fabrication considerations", J. Opt. Soc. Am. A **7**, 1202 (1990).

14) W. H. Lee, "Computer-generated holograms: techniques and applications", in Progress in Modern Optics, Editor E. Wolf, North-Holland Physics Publishing, Volume XVI, (1978).

15) I. R. Redmond, Holographic Optical Elements in Dichromated Gelatin, Ph.D. Thesis, Heriot-Watt University, Edinburgh, UK, (1989).

16) R. R. A. Syms, "Vector effects in holographic optical elements", Optica Acta **32**, 1413 (1985).

17) T. W. Stone, Holographic Optical Elements, Ph.D. Thesis, University of Rochester, U.S.A. (1986).

Chapter 7

DCG Holography : An Investigation into Laser Induced Damage

7.1 Introduction

In many practical situations, DCG HOEs will be required to cope with high optical irradiances. This applies particularly to holographic components such as attenuator gratings [1,2], Gaussian to flat-top converters [3], array generators [4] and laser optics [5,6], all of which operate with the direct output of a laser. It has been observed, however, that above a certain, critical power level, the diffraction efficiency of a sealed DCG hologram will deteriorate over a relatively short period of time [4,7]. This point, which we shall refer to as DCGs optical damage threshold, is of great importance in the design of any holographic component as it determines the maximum power which can be safely handled. As there exists no reciprocal relation between the amount of damage induced at high power levels over a short time, and low power levels over a long time, it can be concluded that the damage mechanism is primarily temperature related, as opposed to any photochemical effect. Thus, even though the absorption of processed DCG is very low, typically a couple of percent, at high power levels the amount of energy absorbed will be large enough to cause significant heating.

In the following chapter, an investigation into the effect that laser induced heating has on the diffraction efficiency of a sealed DCG hologram will be presented. In particular, our work concentrates on the damage caused by a high power Gaussian laser beam as HOEs dealing with such beams, e.g. the array generators described in the previous chapters, tend to handle the largest optical powers. Both the actual mechanisms involved, and the relationship between the amount of damage produced and the temperature to which the gelatin is heated are considered. In addition, a model describing the temperature profile generated by a laser beam which has a Gaussian intensity profile is presented. This model

was developed to allow us to optimize the power handling capacity of a DCG HOE, and to calculate its optical damage threshold. Finally, throughout this chapter, practical methods of substantially increasing the damage threshold of DCG HOEs will be described. This has led to the development of holographic components capable of taking several Watts of power directly from a laser without any measurable deterioration in diffraction efficiency.

7.2 The effect of direct heating on diffraction efficiency

One of the main disadvantages associated with DCG is its extreme sensitivity to high humidity levels [8]. At room temperature and at a relative humidity (R.H.) of greater than 60%, for example, the diffraction efficiency of a DCG hologram will deteriorate rapidly over a period of only a few hours. This problem can, however, be avoided by cementing a glass coverplate to the gelatin using non-porous optical cement. The edges of the HOE must also be sealed to prevent water moisture diffusing through to the gelatin via these surfaces.

One of the problems with using a coverplate is that if any water remains trapped within the gelatin layer the hologram can be damaged by heating at high temperatures [9]. The amount of damage incurred increases significantly as the temperature of the gelatin rises above a certain threshold value T_{th}. Below this minimal deterioration occurs. Furthermore the threshold temperature, T_{th}, and hence the amount of damage produced at a certain incident power level, is closely related to the level of moisture present in the gelatin.

In order to explain these effects, the role that water concentration has on the grating stability must be fully understood. An experiment was therefore set-up to study the behaviour of a dried and undried DCG hologram when subjected to direct heating. First, two identically processed and exposed gratings, H1 and H2, were recorded at 514.5nm on gelatin derived from Kodak 649F plates. This was done using the standard pre-processing and development procedures described in chapter 2. H1 was sealed under normal lab conditions (40% RH and 22°C) while H2 was placed in an oven at 40°C, the temperature being gradually raised to 70°C so as to drive off most of the moisture contained in the gelatin film. H2 was then sealed in the oven, still at 70°C, to prevent any reabsorption of moisture. Drying

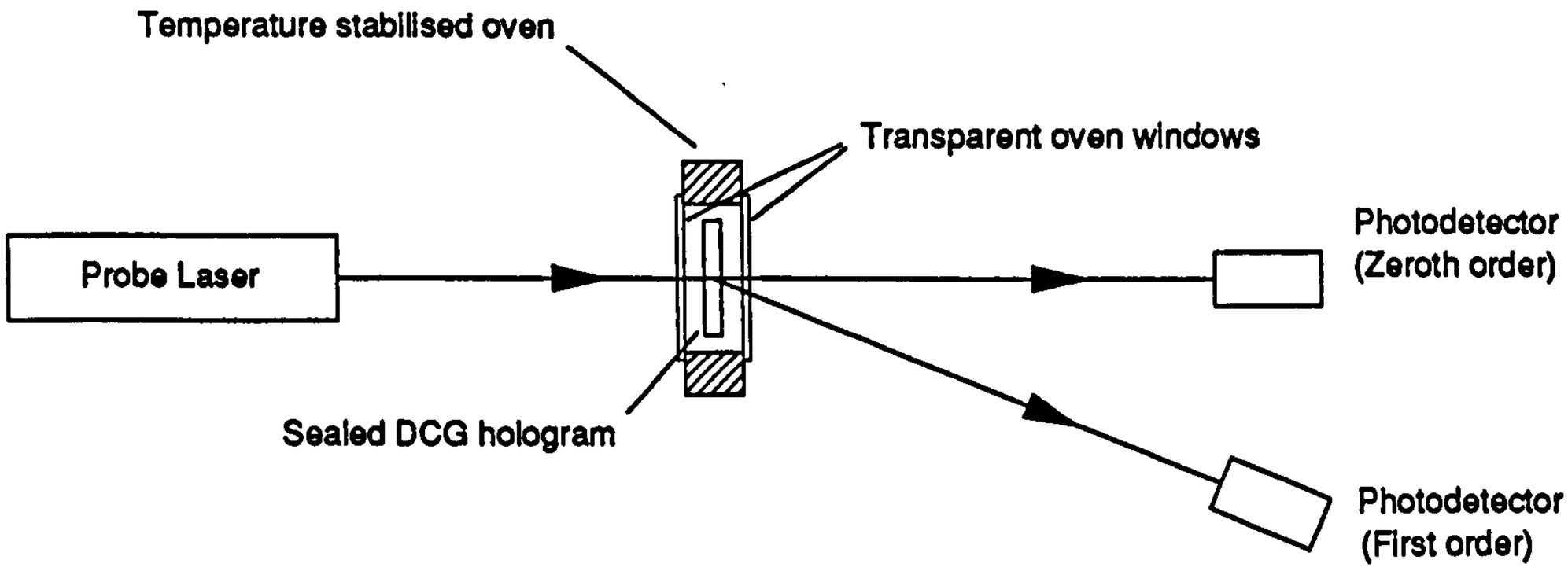

Figure 7.1 - Experimental set-up used for measuring the change in diffraction efficiency with heating.

out the gelatin in this fashion has been shown previously to improve the environmental stability of DCG [4,9,10]. Moreover, several authors have used post-process baking techniques to control the index modulation and film thickness of a developed DCG hologram [1,11]. Thus, if careful control over the baking time and temperature is exercised, it is possible to fine tune the replay wavelength and diffraction efficiency to the required value.

The experimental system described in figure 7.1 was set-up in order to compare the holograms resistance to damage from continuous heating. It was constructed around a temperature stabilised oven in which the holograms were kept at a preset temperature. Transparent oven windows allowed a low power probe HeNe beam through to measure the diffraction efficiency of the holograms. Thus, by monitoring the variation in zeroth and first order (Bragg) powers, it was possible to observe any variation in grating performance. The results of heating at 60°C are given in figure 7.2. It can be seen that, over the first few hours, the efficiency of the hologram sealed under normal lab conditions (H1) decreases. The deterioration is initially rapid but begins levelling off at a constant diffraction efficiency after four to five hours. Further longer term experiments have shown that no more noticeable change occurs after another 30 hours of continuous heating,

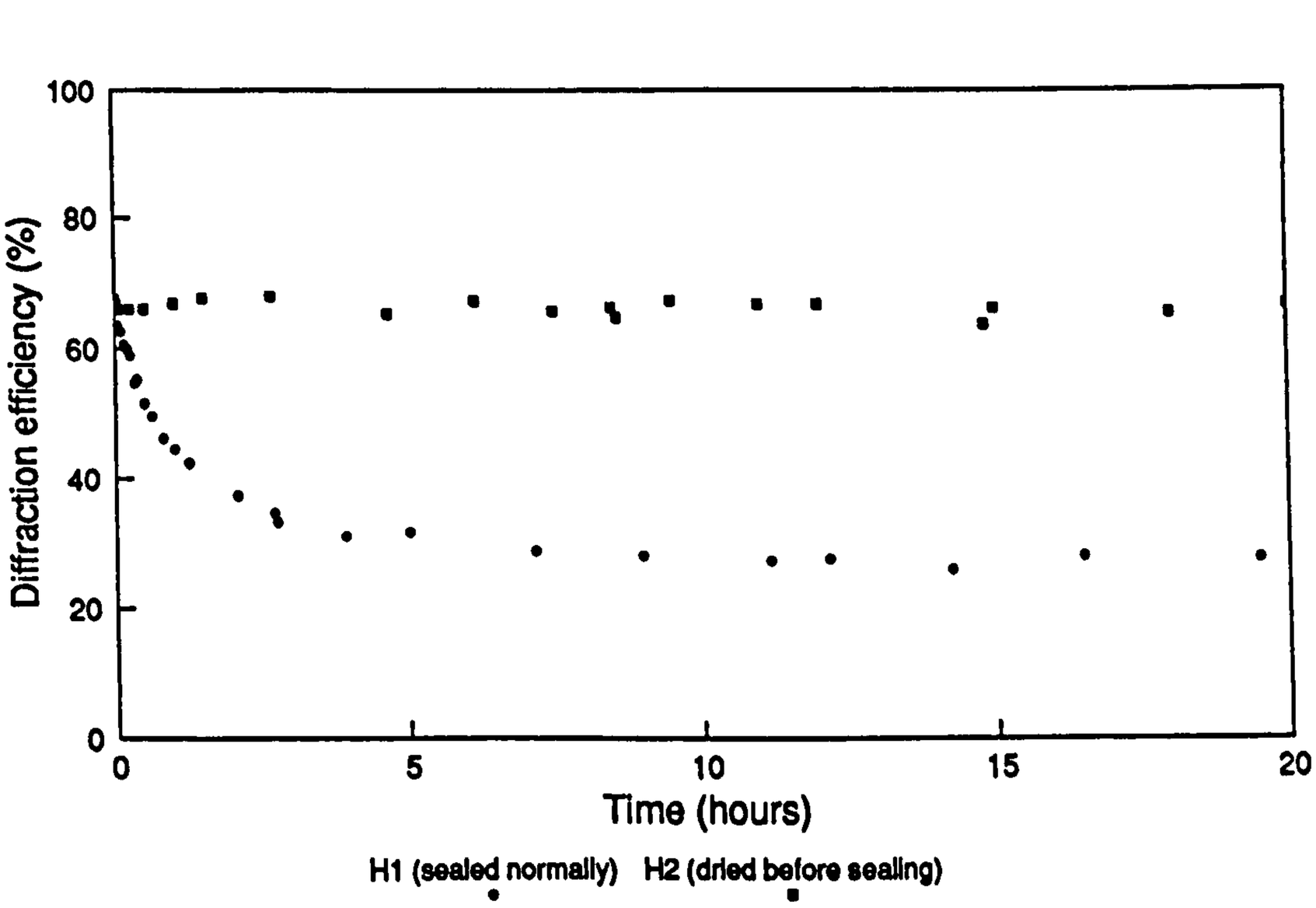

Figure 7.2 - Variation of diffraction efficiency with continuous heating at 60°C (measurement made at 632.8nm). H1 sealed under normal lab conditions, H2 dried before sealing.

implying that only a certain amount of the index modulation can be damaged by heating at this temperature. The dried, or treated hologram (H2) on the other hand suffers negligible deterioration, even after 48 hours of continued testing.

The above experiment was repeated over a range of temperatures. In each case the undried DCG gratings exhibited an initial rapid fall in efficiency which again began levelling out at a constant value after only a few hours. The final diffraction efficiency, η_f, which was reached was also found to vary strongly with temperature. In order to investigate this further the dependence of final efficiency on temperature after four hours continuous heating was measured using a probe beam generated by an Argon laser operating at 514.5nm (figure 7.3). Although after this time the efficiency will not have quite reached η_f, the result still gives a good indication of the degree of damage incurred when operating a DCG hologram at any particular temperature. The experimental results were obtained using a single, sealed, undried DCG grating of 85% initial diffraction efficiency.

From figure 7.3 it can be seen that the breakdown point occurs between 40°C and 45°C. The damage threshold, T_{th}, of untreated DCG therefore lies somewhere in this temperature range. As the temperature is increased above 45°C the amount of damage incurred rapidly rises until, at 80°C, the diffraction efficiency has fallen to only a few percent and the hologram is almost completely destroyed. Alternatively, if the DCG grating is dried before cementing on the coverplate the damage threshold will lie at a much higher temperature. Measurements by Chang and Leonard have shown that a thoroughly dried and sealed DCG hologram will remain stable even when continuously heated at temperatures of up to 110°C [9]. As a consequence, a dried DCG HOE will also be able to operate with higher optical powers without any damage occurring.

The above experimental dependence of diffraction efficiency on temperature (figure 7.3) can be closely modelled using the empirically derived formula

$$\eta(T)=\frac{\eta_o}{1+\exp(-B[\Theta-T])} \tag{7.1}$$

where η_o is the initial diffraction efficiency, $\eta(T)$ is the diffraction efficiency after the hologram has been heated over four hours at a temperature of T(°C) and B and Θ are constants which were adjusted to provide the best fit to the experimental data (the best fit to the experimental results was obtained with values for B and Θ of 0.215°C^{-1} and 62°C respectively). The theoretical dependence calculated using these values is shown alongside the experimentally determined points in figure 7.3, illustrating the close agreement between model and experiment. This empirical relationship will be made use later when the effect that laser induced heating has on diffraction efficiency is considered.

7.3 Measurement of moisture content

The water content of gelatin under normal lab conditions was found by measuring its weight before and after it had been thoroughly dried. Any weight difference would therefore be due to the loss of water. It was found that the amount of moisture originally present in gelatin under normal lab conditions (40% RH and 22°C) is 16±2% by weight. This compares favourably with the value quoted in Mees [12] of 18% at 42% RH on the deabsorption curve (initial drying).

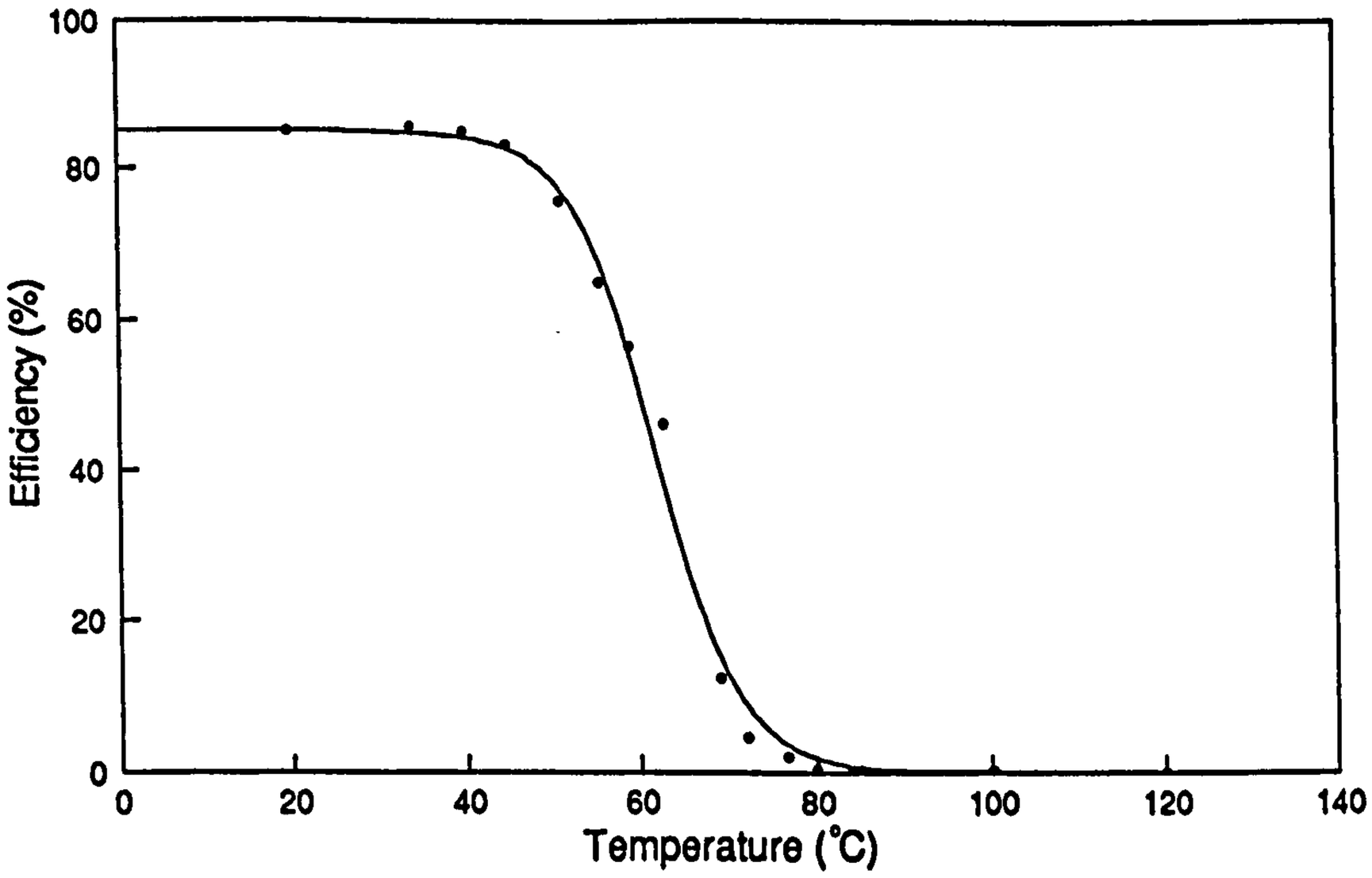

Figure 7.3 - Dependence of final diffraction efficiency on temperature after four hours heating (HOE sealed under normal lab conditions).

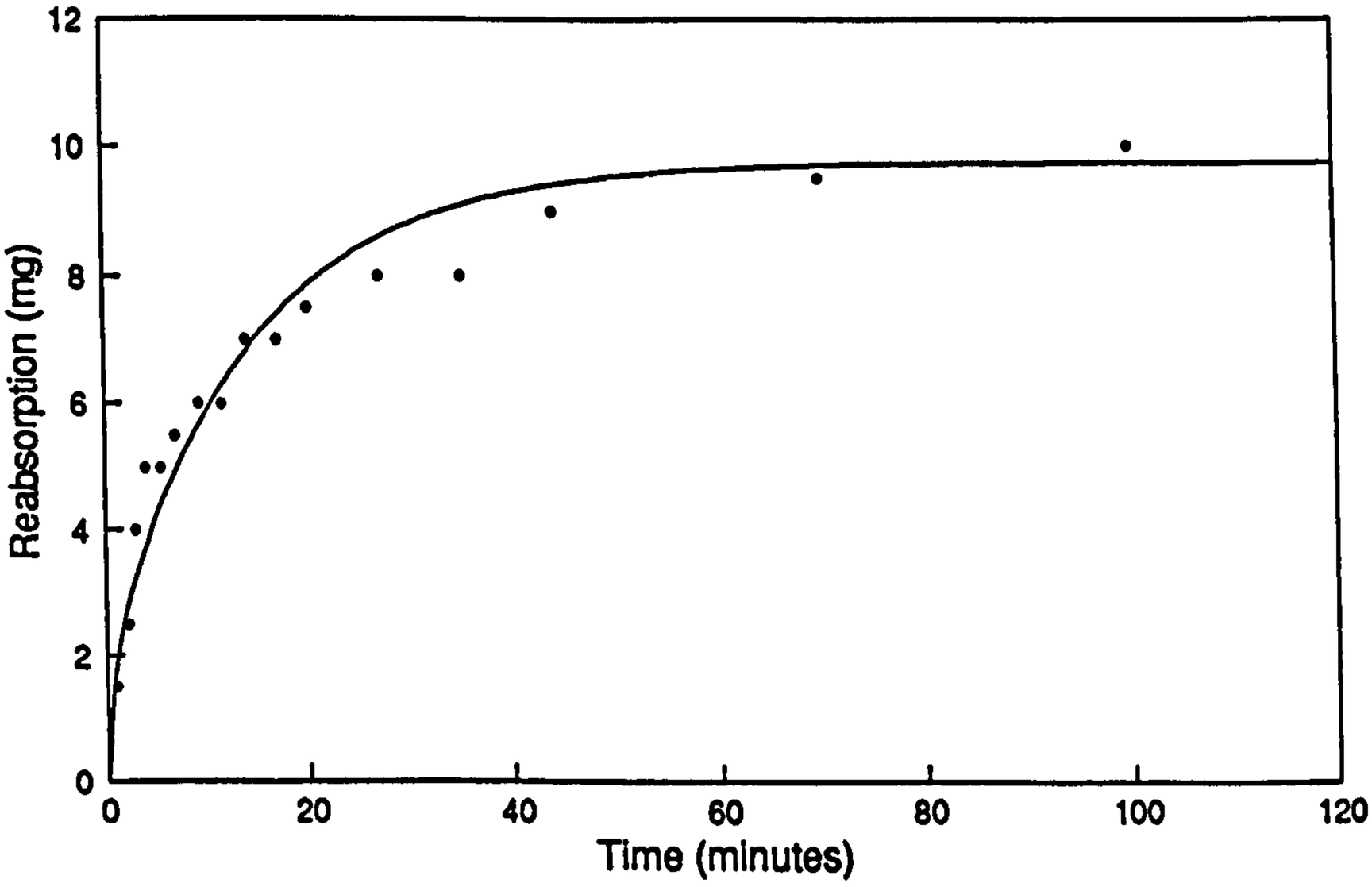

Figure 7.4 - Reabsorption of water moisture by a dried DCG plate with time.

When the plate was removed from the oven it was observed to rapidly reabsorb water from the atmosphere. Figure 7.4 shows the experimental results of amount of moisture taken up against time. Note that less water was taken up during reabsorption than was lost initially (only 14±2% by weight) due to a hysterisis effect [12]. The mechanism of reabsorption will be returned to in section 10 as it is of practical importance when trying to properly protect DCG holograms.

7.4 Model for damage mechanism

From the above experimental results it can be concluded that drying DCG plates in an oven does indeed drive off a substantial amount of water moisture from the gelatin (16% by weight of the original gelatin is water). Furthermore the dried plates are less susceptible to thermally induced damage than the untreated ones. This can be explained using a model for gelatins microscopic structure similar to that proposed by Rebordao et al [13].

Gelatin molecules are irregularly shaped polypeptide chains of amino acids. In the gel phase these chains are surrounded by water molecules, some of which are bonded to the gelatin. Electrostatic crosslinkages and hydrogen bonds also appear between neighbouring gelatin molecules, causing them to become partially aligned and loosely held together. During the preprocessing and processing of DCG plates further bonds are formed. These bring the gelatin to the correct bias hardness. Finally, exposure of the hologram results in photochemical induced crosslinking. Thus, after processing, and under laboratory conditions (22°C and 40% RH), the relative positions of these gelatin chains remain fixed in such a way as to form a periodic variation in density [14]. Generally the period is of the order of 1μm.

Heating causes the individual gelatin molecules to become less securely held and more mobile. Eventually they may become free enough to move, thereby reducing the index modulation. This 'relaxing of the fringe structure' is similar to the process which occurs when the external humidity rises above 40%. A higher humidity leads to a higher concentration of water in the gelatin. The gelatin molecules therefore become less tightly bound and so more mobile, moving from regions of high concentration to low

concentration. How tightly bound a gelatin molecule is depends on several factors - the temperature, the moisture concentration and the number and type of crosslinkages - and, if a molecule becomes mobile enough, it will be able to alter its position.

Holograms suffering from humidity damage can be reprocessed to a high diffraction efficiency, again indicating that the photochemical bonds are not completely disrupted [1]. This is also the case for low levels of temperature induced damage where deterioration is reversible. At higher temperatures, however, it is impossible to recover the index modulation due to the breaking of photochemical bonds. Eventually, at high enough temperatures, the melting point of the gelatin will be reached [12], resulting in the breaking of all the inter-molecular bonds.

After processing the density of the gelatin varies across the hologram. This implies that both the concentration of water moisture and the number of gelatin-gelatin bonds will depend on position, thus, it follows that a variation in gelatin mobility will be observed. Slight heating will disrupt only the mobile, loosely held strands, and destroy only a fraction of the index modulation. Increasing the temperature, however, causes the mobility of a larger amount of gelatin to rise significantly and, as a result, the diffraction efficiency falls further. This behaviour was observed experimentally (figure 7.3).

Drying the gelatin, i.e. by heating it unsealed in an oven [1,9,10], vacuum drying [9,10] or by microwave drying [13], will reduce the concentration of water moisture. The mobility of the gelatin molecules will therefore fall and so the grating stability will improve, as verified in section 7.2 (figure 7.2). Note that this process does not noticeably affect the diffraction efficiency of the grating because the water is driven out quickly enough to prevent deterioration. It is only when a hologram is sealed and the water trapped that damage occurs.

7.5 Laser induced heating effects

Being able to calculate the temperature distribution produced by laser induced heating is of great practical importance to the design of high power DCG holographic components. To prevent any damage occurring it must be ensured that the peak temperature rise does not exceed the damage threshold of the gelatin, T_{th}. Thus, by relating the increase in gelatin temperature to the optical input power we can calculate the maximum power which can

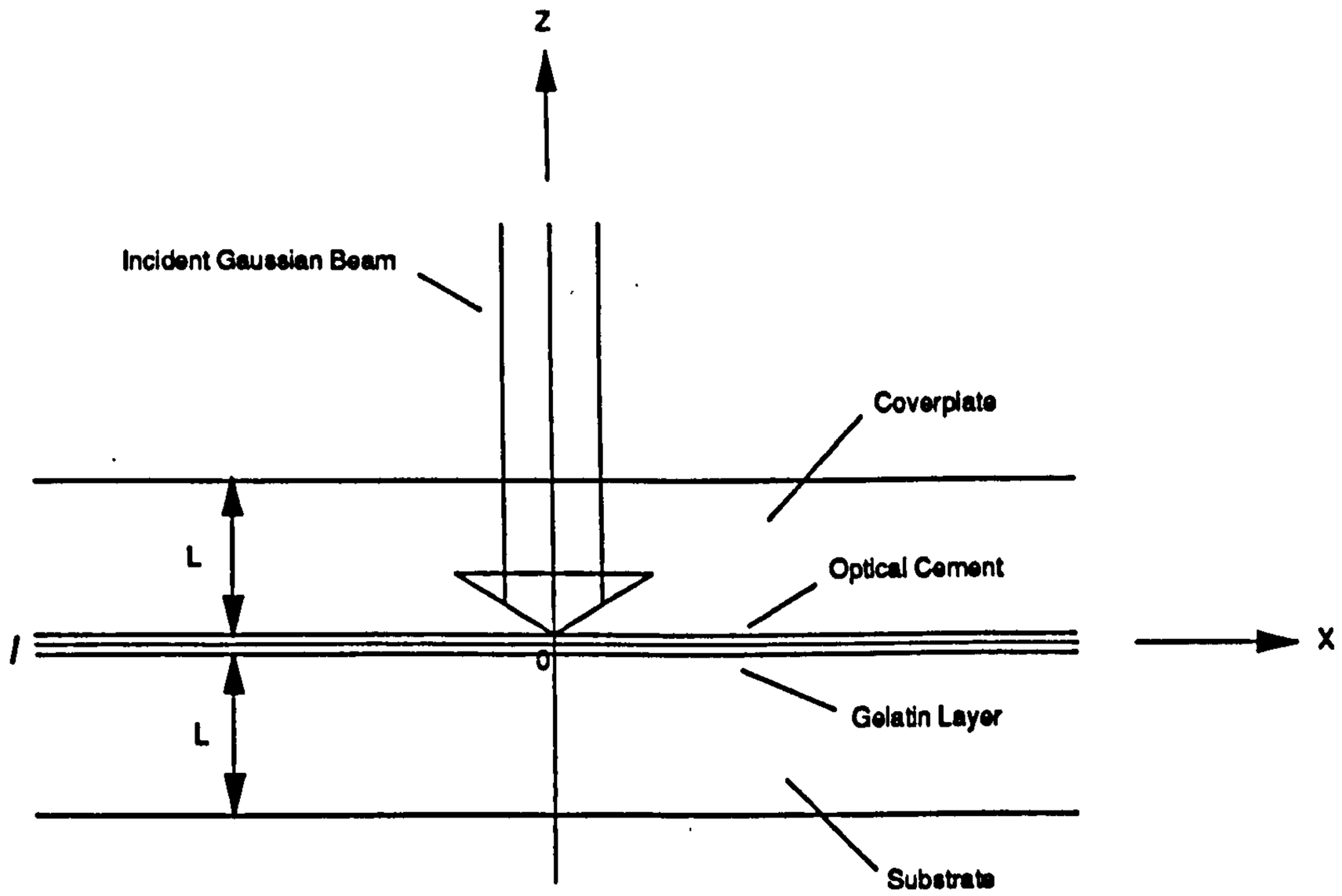

Figure 7.5 - Structure of a sealed DCG hologram.

be handled by the hologram. Of particular interest is the temperature profile induced by a laser beam which has a Gaussian intensity profile. This is because so many high power applications deal with such beams, for example array generators and attenuator gratings. In the following section, therefore, we shall develop a model which predicts the temperature rise generated by a Gaussian beam.

The structure of a typical sealed DCG HOE is illustrated in figure 7.5. The hologram consists of a substrate , the gelatin layer, a thin layer of optical cement and a coverplate. In general, each of these will have a different thickness and thermal conductivity, thus, the thermal analysis of this system constitutes a rather complicated problem. Several simplifications are, however, possible. Firstly it can be assumed that the film, the substrate and the coverplate are infinite in the x and y directions but have a finite depth. This will hold if, as is generally true, the lateral dimensions of the HOE are much greater than the incident spot radius. For the purposes of this work, the spot radius, s, is defined as the distance at which the intensity of the incident beam has fallen to 1/e of the value at its centre. The second simplification which can be made is that the optical cement and gelatin

are of the same order of thickness and have about the same thermal characteristics. This allows them to be treated as a single, composite thin film with a linear absorption coefficient, α and thickness l. A further reduction in the models complexity may also be made if the substrate and coverplate are assumed to have a negligible absorption. Heat will therefore only be generated in the composite film. In the case of a 649F plate this is a valid assumption as the absorption of the substrate is less than 1%.

Finally, in the following analysis the substrate and coverplate will be considered as identical, i.e. having the same dimensions and thermal conductivities. Thus, from the symmetric nature of the structure, it follows that any heat generated in the composite gelatin/optical cement layer will flow equally into both of the glass slabs. Moreover, only heat loss by radiation will be assumed to occur at the outer surfaces of the HOE (i.e., at $z = \pm L$), the effects of convection being ignored. The model used in this work, therefore, consists essentially of a thin, absorbing layer sandwiched between two, identical, transparent substrates which exhibit radiative losses. Previous theoretical studies have shown that, generally, the thermal characteristics of such a system will be dominated by the substrate/coverplate [15,16].

Although diffraction occurs as soon as the beam starts propagating through the hologram it was decided that, because the gelatin thickness is so small (15μm), negligible separation between the zeroth and first Bragg orders will have occurred before they exit the film. As a result, a uniform Gaussian intensity profile will exist throughout the film thickness. A laser beam of power P_o, normally incident on either a transmission or reflection hologram, will therefore generate a heat source which has a cylindrically symmetric Gaussian profile. Note that interference effects which occur in the gelatin/optical cement film due to surface reflections will be ignored in this analysis.

The method used to model to the temperature distribution in a sealed DCG hologram consisted of finding the proper Greens function of the model described in figure 7.5 using the Bessel Transform method [17,18]. The Greens function can be thought of as describing the temperature rise, $\Delta T(\mathbf{r})$, due to a point source. Any heat source can be represented by a continuous distribution of point sources. The steady state temperature distribution throughout the HOE can therefore be calculated by 'summing up' these point sources, each source being weighted by the amount of heat liberated at that point. That is

$$\Delta T(r)=\int_V \frac{Q(\underline{r}')}{K_s} G(\underline{r}-\underline{r}')d\underline{r}'^3 \tag{7.2}$$

where $\Delta T(\mathbf{r})$ is the temperature rise, Q the heat energy generated per second as a function of position, G the steady state proper Greens function of the system and K_s the thermal conductivity of the substrate and coverplate. This problem was solved by Godsalve [17], who showed that the temperature rise was given by

$$\Delta T=\frac{P_o \alpha l}{4\pi K_s}\int_0^\infty W(\zeta,L,K_s)\exp(-\zeta^2 s^2/4)\,J_o(\zeta r)d\zeta \tag{7.3}$$

in which J_o is a first order Bessel function and ζ is a dummy variable

$$W(\zeta,L,H)=\frac{2\exp(-\zeta L)}{(\zeta+H)}(\zeta-H)\exp(-\zeta L)\{\zeta\cosh(\zeta(L+z))+H\sinh(\zeta(L+z))\}$$

$$\times\frac{\zeta\cosh(\zeta L)+H\sinh(\zeta L)}{(\zeta^2+H^2)\sinh(2\zeta L)+2\zeta H\cosh(2\zeta L)}$$

$$+\frac{2\exp(-\zeta(L+z))}{(\zeta+H)}(\zeta\cosh(\zeta L)+H\sinh(\zeta L)) \tag{7.4}$$

A full derivation of this expression is given in Appendix 2. Equation (7.3) may be used to calculate the temperature profile existing inside the hologram if the following restrictions are met

1) The composite film thickness must be much less than the substrate thickness($l \ll L$). This ensures that there is effectively a plane heat source at $z = 0$. In the case of a Kodak 649F plate the gelatin layer is around 15μm thick and it was found that,

typically, the optical cement had a similar thickness of about 20μm. This was calculated by measuring the increase in absorption that the layer of optical cement produced and comparing this with its absorption coefficient. The composite film thickness is therefore several orders of magnitude smaller than the substrate/coverplate thickness, L, which is generally about 1mm.

2) The substrate and coverplate have the same thermal conductivity, K_s, and thickness L. All the holograms used in this work were sealed with a cleaned 649F substrate, ensuring that this condition was met.

3) If $s < l$, then $\alpha l << 1$. That is, the amount of power absorbed per unit length is very small. This implies that there is uniform heating throughout the depth of the film. Experimental values put $\alpha l \sim 0.04$, although this varies depending on the replay wavelength, type of gelatin and the processing conditions. If, on the otherhand, $\alpha l \approx 1$, then $(l/s) << 1$, i.e. the spot radius must be larger than the gelatin thickness, as is typically the case. These two restrictions, in general, present no problem.

4) The transverse dimensions of the HOE be greater than the spot radius. In most practical situations this is the case, moreover, transmission holograms may have their edges thermally contacted to a large heat-sink to ensure that all the heat generated can flow outwards away from the HOE.

It should be noted at this point that although this analysis is intended primarily for use with DCG it is also valid for many other holographic materials, such as bleached silver halide and photopolymer. Equation (7.3) may therefore be used to predict the temperature profile induced by a Gaussian beam in any thin film HOE as long as the above restrictions are met.

7.6 Discussion

The above theoretical analysis shows that the temperature rise is directly proportional to the absorption of the composite film, αl. Thus reducing the absorption coefficient increases the amount of power a DCG HOE can handle before deterioration occurs. In general the absorption of a gelatin layer processed according to the methods of Chang and Leonard is around 2%. By using a water based processing technique [1], however, it is possible to

reduce this to less than 1% while still maintaining a high efficiency and good uniformity. In order to minimise absorption due to the optical cement (typically around 2%) as little cement as possible should be used during sealing. Alternatively the damage threshold of the HOE can be raised by employing a substrate and coverplate which have a high thermal conductivity. Using sapphire ($K_s = 27.21\ Wm^{-1}K^{-1}$, $E = 0.53$) instead of float glass ($K_s = 0.85\ Wm^{-1}K^{-1}$, $E = 0.94$), for example, significantly improves the holograms power handling characteristics. This is illustrated in Fig. 7.6 where the theoretical temperature profile of both a glass and sapphire based HOE are shown. Typical experimental values were chosen for the rest of the design parameters ($s = 1$ mm, $L = 1$ mm, $P_o = 3$ Watts, $\alpha l = 4\%$). It can be seen that using sapphire instead of standard float glass decreases the temperature rise at the spot centre by a factor of just over 20, allowing the HOE to cope with far higher optical powers.

Figure 7.7 shows a family of curves, calculated from equation (7.3), which describe the radial variation in the increase of film temperature for several different substrate thicknesses, all other system parameters being held constant. Again, typical experimental data was used in the calculation, ($s = 1$ mm, $P_o = 3$ Watts, $\alpha l = 4\%$, $K_s = 1.0\ Wm^{-1}K^{-1}$, $E = 0.94$), while the substrate thickness had values (0.25, 0.5, 1, 2, 4, 8 and 16 mm). It can be seen that for large values of L the temperature distribution changes very little, however, as L decreases the film temperature gradually starts rising. When the spot size is of the same size as the substrate thickness a strong dependence of temperature on L is observed. Thus, for a given set of input conditions, the larger the substrate thickness the lower the temperature rise and the better the holograms power handling characteristics.

As a practical example, let us calculate the optical damage threshold of a DCG attenuator grating designed for use with a 2 mm radius ($s = 2$ mm) Gaussian beam. If the gelatin has been thoroughly dried before sealing then, in order to prevent any damage from occurring, it must be ensured that the peak gelatin temperature is always kept below 100°C [9]. First, let us consider the case where the HOE has been fabricated using a 1mm thick glass substrate and coverplate ($L = 1$ mm, $K_s = 1.0\ Wm^{-1}K^{-1}$). Assuming typical design parameters of $\alpha l = 4\%$, $E = 0.94$ and $T_o = 22°C$, the maximum power which can be safely handled is almost 10 Watts. If, however, the substrate and coverplate were 2.5 mm thick, the optical damage threshold rises to over 17 Watts. This shows that quite high optical powers can be safely handled by a DCG holographic optical element.

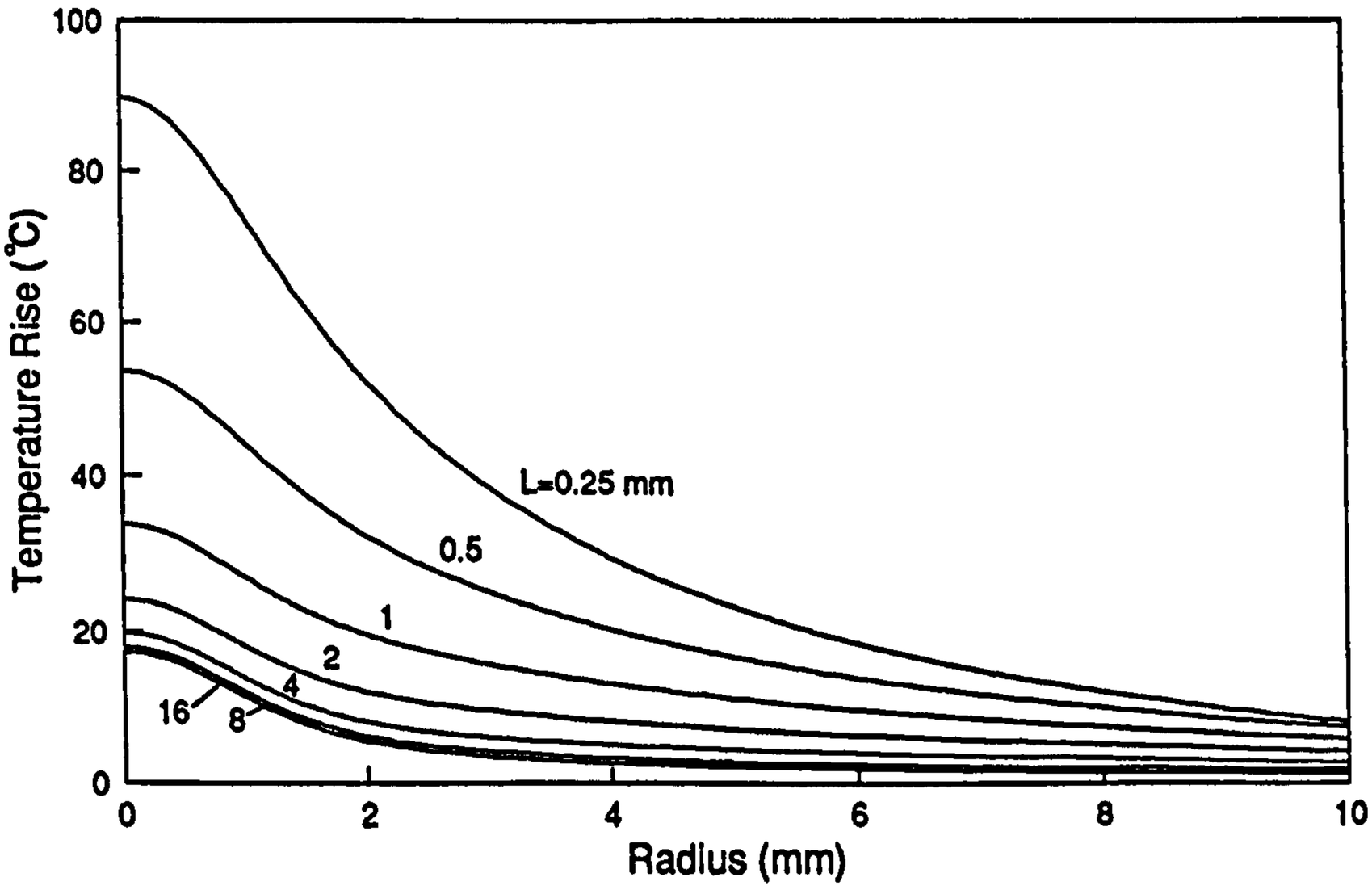

Figure 7.6 - Radial variation in rise of composite film temperature for two different substrates: glass($K_s = 0.85\ Wm^{-1}K^{-1}$) and sapphire ($K_s = 27.21\ Wm^{-1}K^{-1}$). ($s = 1mm, L = 1mm, P_o = 3$ watts, $\alpha l = 4\%$).

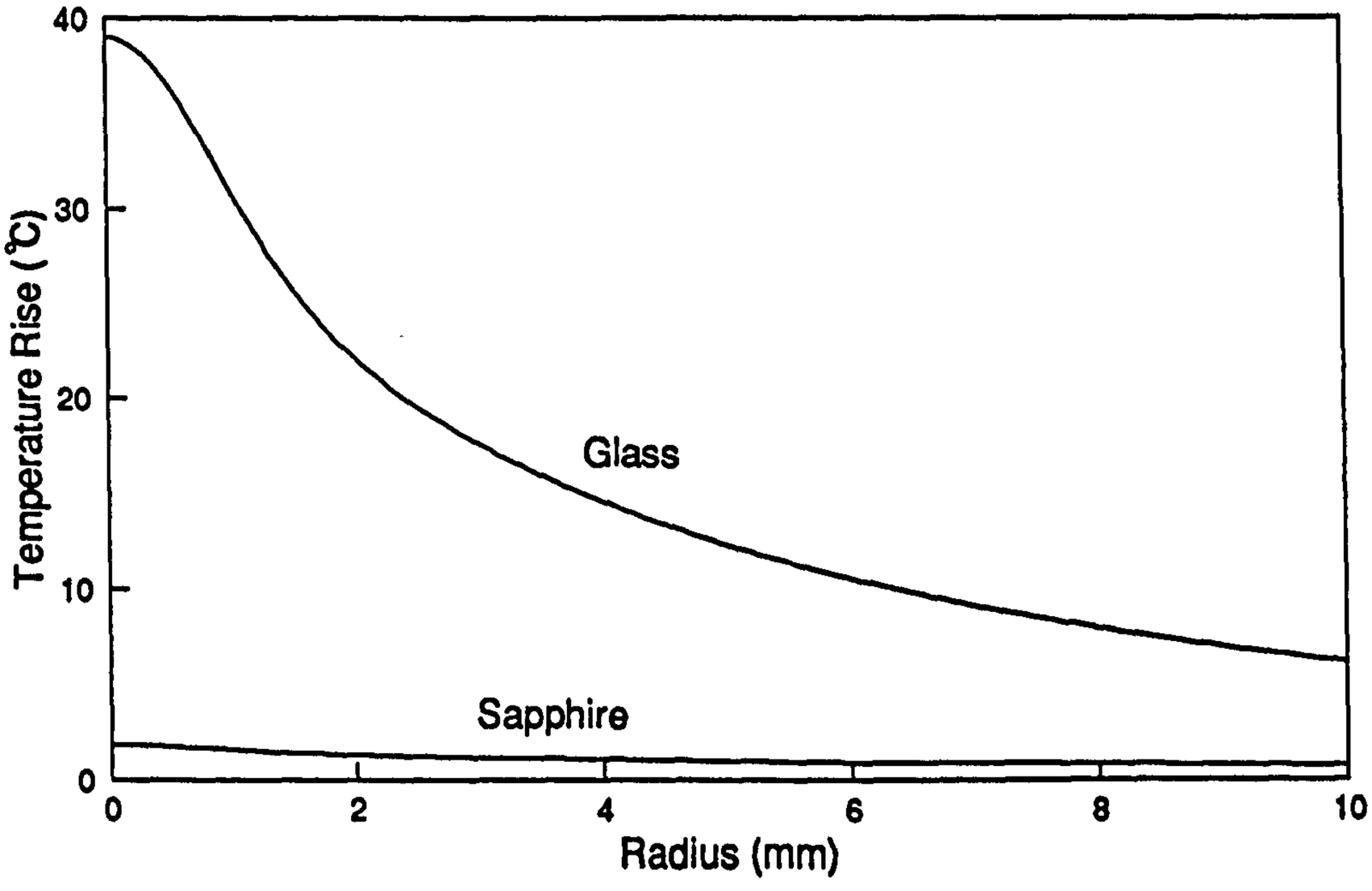

Figure 7.7 - Radial variation in rise of composite film temperature for various substrate thicknesses, ($L = 0.25, 0.5, 1, 2, 4, 8,$ and $16mm$). ($s = 1mm, K_s = 1\ Wm^{-1}K^{-1}, P_o = 3$ watts, $\alpha l = 4\%$ and $E = 0.94$).

For a transmission hologram, using too thick a substrate and coverplate may prove impractical because of the greater overall absorption losses which would result. A reflection hologram, on the other hand, could easily have its substrate fixed to a good heat-sink, for example a highly thermally conductive material such as copper. This would greatly enhance the power handling capabilities of the HOE without affecting its optical performance, making it ideal for many high power applications.

7.7 Effect of dust contamination

This analysis has so far concentrated entirely on the laser damage caused by the intrinsic absorption of the gelatin and optical cement. In practice, however, the optical damage threshold of a DCG hologram will also be affected by the presence of contaminants, such as dust, which becomes trapped on the gelatin surface during sealing. These will heavily absorb the incident beam, thereby causing extreme localised heating effects. It was observed that if enough optical power is absorbed, e.g., by focussing a high power beam onto a large piece of dust, intense heating can occur which can split the cover plate from the gelatin.

In order to calculate the temperature profile within the HOE, both the temperature rise due to the absorption of the gelatin and optical cement, $\Delta T_i(\mathbf{r})$, then the temperature rise caused by dust, $\Delta T_e(\mathbf{r})$, must be known. If, however, the power absorbed by the dust is much less than the power absorbed by the gelatin and optical cement, $\Delta T_e(\mathbf{r}) < \Delta T_i(\mathbf{r})$, and the intrinsic absorption of the hologram will determine the optical power handling capabilities of the hologram. In order to analyse this problem further, let us assume that a single dust particle is positioned at the centre of an incident Gaussian beam. If we assume that the dust absorbs all the incident light, then the radius of the incident Gaussian beam, s, must be much greater than the radius of the dust particle, s_d, for $\Delta T_e(\mathbf{r}) < \Delta T_i(\mathbf{r})$. Under these conditions, the dust particle can be considered to be uniformly illuminated by a beam of irradiance I_0, and may be treated as a circular heat source emitting heat at a rate of $\pi I_0 s_d^2$ Joules/sec. Maximum dust particle sizes on the holograms observed during the course of this work were typically only of the order of $s_d = 25\mu m$. Thus, for most practical situations, the condition $s >> s_d$ will hold. The resulting temperature rise, $\Delta T_e(\mathbf{r})$, may be calculated using the procedure described in section 7.5 for a circular heat source. A full analysis of this problem is outside

the scope of this thesis, however, to a first approximation we may treat the dust particle as a Gaussian heat source of radius s_d, and use equation (7.21) to estimate the resulting temperature rise.

For a practical example, let us return to the problem described in the previous section of a DCG attenuator grating designed for use with a 2mm radius Gaussian beam. The HOE will be assumed to have been fabricated using a 1mm thick glass substrate and coverplate ($L = 1mm$, $K_s = Wm^{-1}K^{-1}$), and typical design parameters of $\alpha l = 4\%$, $E = 0.94$ and $T_0 = 22^0C$ will be used. If the incident power is 1 Watt, the temperature rise at the beam centre due to heating of the gelatin and optical cement will be 7.9^0C. The estimated temperature rise due to the presence of a totally absorbing dust particle of radius 25μm positioned at the centre of the beam will be 0.9^0C. Thus, as long as the dust particle radius is kept below 25μm, the optical damage threshold of the HOE will be determined by the absorption of the gelatin and optical cement.

Contamination of the optical surface may occur for a number of reasons, for example, impurities in the holographic chemicals and dust landing on the plate during the exposure and processing. Thus, the holograms should be exposed, developed and sealed under clean room conditions to ensure that the recording and processing conditions remain as uncontaminated as possible. In addition, all the processing chemicals should be freshly made up using deionised water.

7.8 Experimental results - induced heating of a sealed grating

Figure 7.8 shows a schematic diagram of the experimental system which was used to investigate the effect that laser induced heating has on a sealed DCG grating. Initially, in order to compare the performance of a dried and undried hologram, two identical, slightly underexposed gratings, H1 and H2, were fabricated. As in section 2, H1 was sealed under normal lab conditions while H2 was dried out at 60°C for an hour before sealing. The holograms were then placed in front of the direct output of a Coherent Innova 20 argon laser (P_o=4 Watts at 514.5nm) and angularly tuned for maximum diffraction efficiency. The change in diffracted power with time was recorded using two photodiodes placed in front of the zeroth and first order beams.

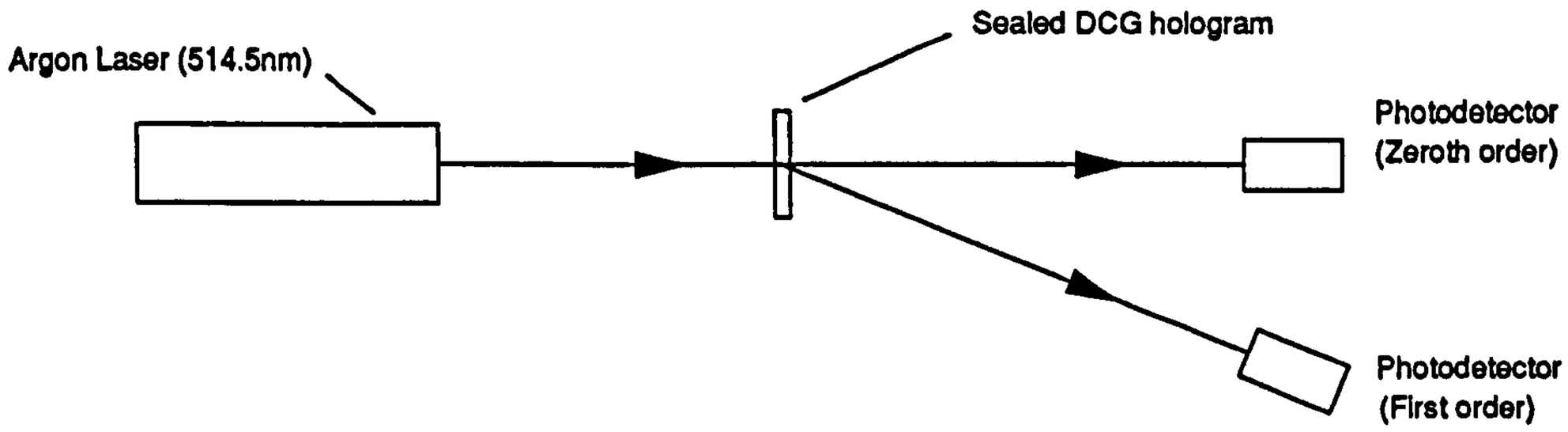

Figure 7.8 - Schematic diagram of set-up used in laser induced heating experiments.

Great care was taken to ensure that conditions were identical for both tests, thereby allowing a direct comparison between the performances of the dried and undried DCG gratings. Experimental results of the variation in zeroth order power with time are given in figure. 7.9. From the two curves it can be seen that there is a dramatic improvement in the ability of a DCG hologram to cope with laser induced heating if it is dried before sealing. Over 150 minutes, the relative zeroth order power of H1 increased by 414%, while that of H2 rose by only 6%. Thus, drying before sealing has increased the DCG holograms resistance to damage by a factor of ~70.

An interesting point to note is that the reduction in first order power of the treated hologram was less than expected from the corresponding change in zeroth order power. This discrepancy was traced to an increase in absorption of the gelatin film with heating [8]. The increase in absorption is thought to arise from a temperature induced chemical reaction which causes a slight browning of the film (as noted in the damaged regions of several gratings). It is believed that this is related to the presence of impurities in the gelatin, introduced either during processing or development (i.e. failing to remove all excess ammonium dichromate during processing).

7.9 Comparison of laser induced and direct heating results

In the following section the effect that laser induced heating has on the efficiency of a DCG hologram will be investigated in detail. As was discussed in section 7.5, a Gaussian laser beam will generate a radially dependent temperature profile which may be calculated

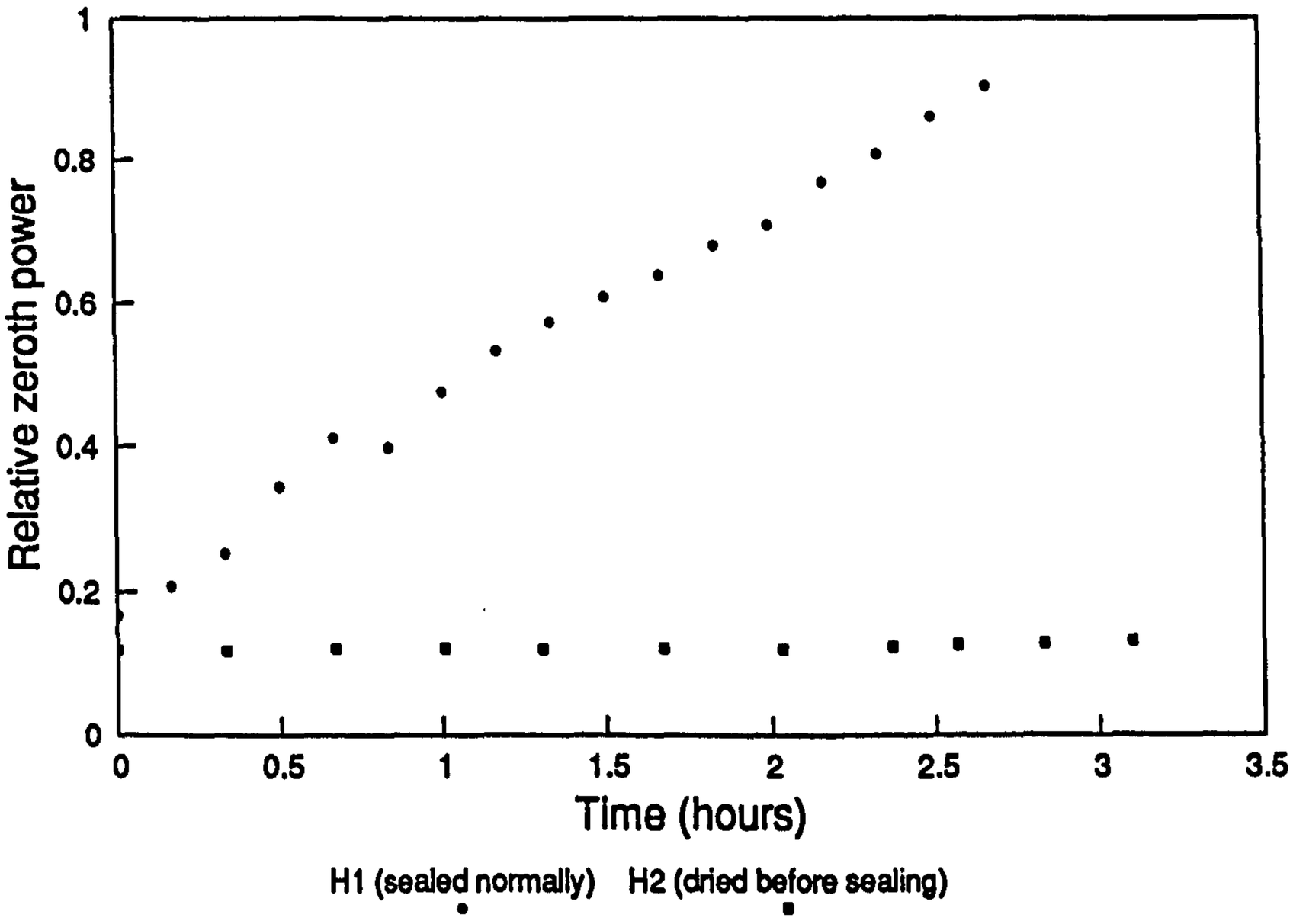

Figure 7.9 - Change in relative zeroth order power with laser-induced heating.

using equation (7.3). This, in turn, results in a radial variation in the amount of grating damage suffered; only where the film temperature, T(r), is greater than the damage threshold, T_{th}, will damage occur and, moreover, the amount of damage will increase with the temperature (figure 7.3). As a consequence, the diffraction efficiency will exhibit a positional dependence. Using the empirically derived equation. (7.1), and assuming the ambient air temperature is T_o, it follows that, after four hours heating, the radial variation in diffraction efficiency will be given by

$$\eta(r)=\frac{\eta_o}{1+\exp(-B[\Theta-(T_0+\Delta T(r))])} \tag{7.5}$$

where $\Delta T(\mathbf{r})$ may be calculated using equation (7.3). The total power diffracted by the grating into its first order, P_d, can therefore be calculated by integrating across the beam profile, i.e.

$$P_d=\int_o^{\infty}\eta(r)\,I_o\exp(-r^2/s^2)\,2\pi r\,dr \tag{7.6}$$

in which the intensity profile of the Gaussian beam is described by $I(r) = I_o\,exp(-r^2/s^2)$. If no damage has occurred, $\eta(r)=\eta_o$, and so the total power initially diffracted into the first order, P_i, will simply be $P_i=\eta_o I_o \pi s^2$. It therefore follows that the change in normalised diffracted power, P_d/P_i, will be given by

$$P_d/P_i=2/\eta_o s^2\int_o^{\infty}\eta(r)\exp(-r^2/s^2)\,r\,dr \tag{7.7}$$

In order to check the validity of the above theory, the experiment described in section 7.8 was repeated using a high power Gaussian beam and a DCG hologram sealed under normal lab conditions (22°C and 40%R.H.). To allow a direct comparison between the actual and theoretically predicted reduction in diffracted power, the DCG hologram was fabricated

with the same initial diffraction efficiency, and from the same 649F plate as the hologram used in section 7.2. It therefore follows that the empirically derived values for B and Θ given in section 7.2 can be used in the following analysis ($B = 0.215°C^{-1}$ and $\Theta = 62°C$).

As the coverplate used to seal the DCG hologram had identical thermal characteristics to the substrate ($L = 1mm$ and $K_s = 0.85\ Wm^{-1}K^{-1}$), equation (7.5) could be used to evaluate the theoretical temperature profile, T(r). The various experimental parameters were measured and found to be $T_o = 22°C$, $\eta_o = 85\%$, $P_o = 3.85$ Watts, $s = 1.2mm$ and $\alpha l = 4.15\%$ (at 514.5nm) and, in addition, an emmissivity of 0.94 was assumed for the coverplate and substrate [19]. Using these values, the spot temperature was calculated to be 69°C, far higher than the experimentally measured damage threshold of undried DCG. Equation (7.5) was also used to determine the radial variation in the temperature rise, $\Delta T(r)$. This is plotted alongside the normalized Gaussian intensity profile in figure 7.10. From these two curves it is apparent that there is a considerable variation in temperature across the laser beam. The resulting change in normalised diffracted power, P_d / P_i, with time was recorded and is shown plotted in figure 7.11. The first point to note is that, as in the direct heating case, initially there is a rapid deterioration in the diffracted power which then begins to flatten out after several hours. This signifies that a stable, steady state temperature profile has been set up in the grating. From figure 7.11 it can be seen that after four hours, the amount of light diffracted into the first diffraction order has fallen to nearly half of the initial value, i.e., $P_d / P_i = 0.58$. This compares well with the theoretical estimate for P_d / P_i which was calculated using equations (7.8) and (7.6) to be 0.53. Such a close agreement between the theoretical and experimental values supports the validity of the model which we used to calculate the temperature profile.

7.10 Practical example

As a practical example, consider the case of a DCG hybrid kinoform (chapter 6) designed to deliver biasing power to a nonlinear interference optothermal etalon (i.e., a ZnSe interference filter [20]). Typically, the threshold power of an individual switch will be somewhere between 5 and 10mW, thus if 32×32 gates (200μm spacing and 10μm spot

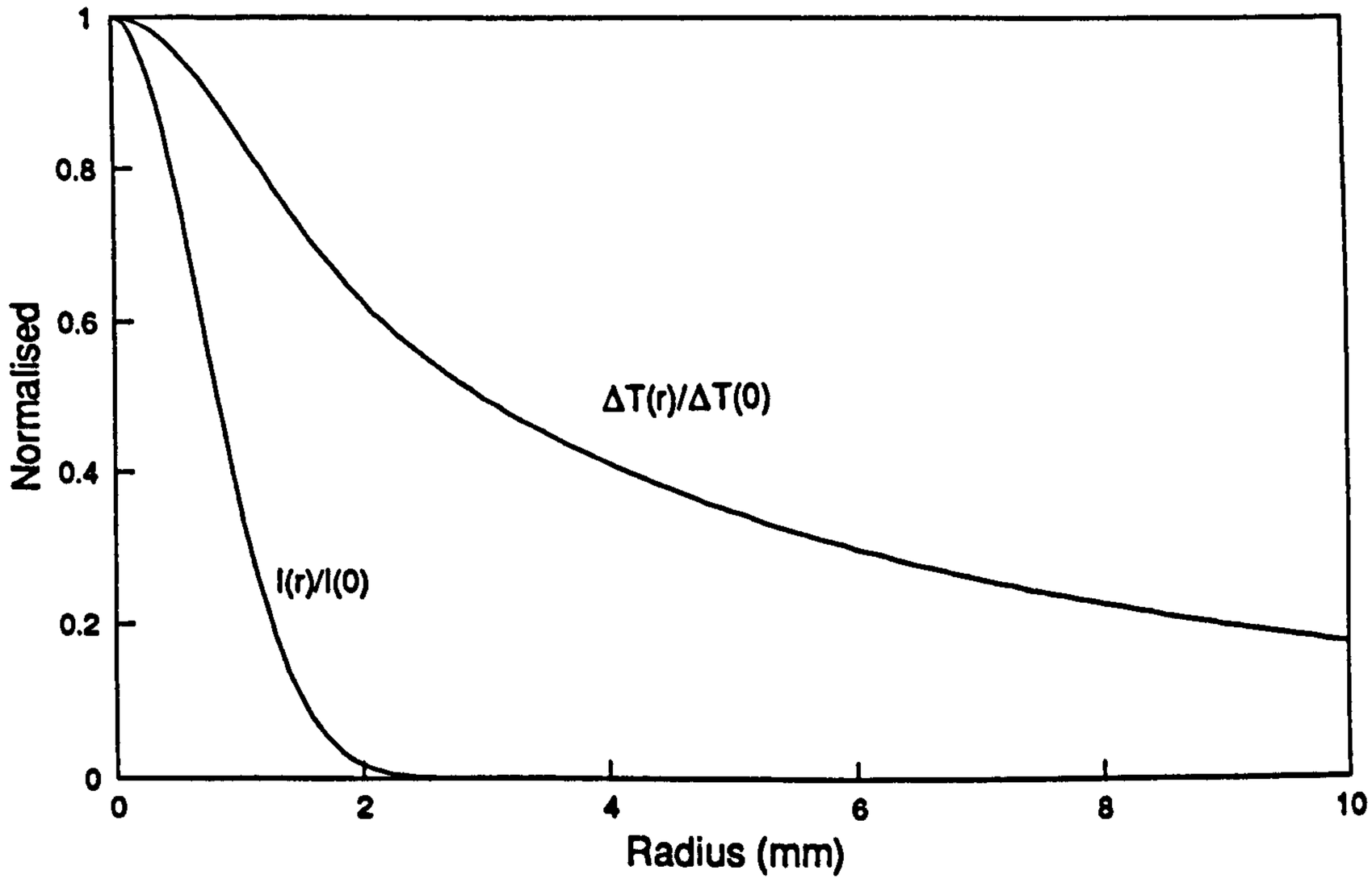

Figure 7.10 - Radial variation in gelatin temperature shown plotted alongside the normalised Gaussian intensity profile. ($T_0 = 22°C$, $s = 1.2mm$, $L = 1mm$, $K_s = 0.85\ Wm^{-1}K^{-1}$, $P_o = 3.85$ Watts, $\alpha l = 4.15\%$ and $E = 0.94$).

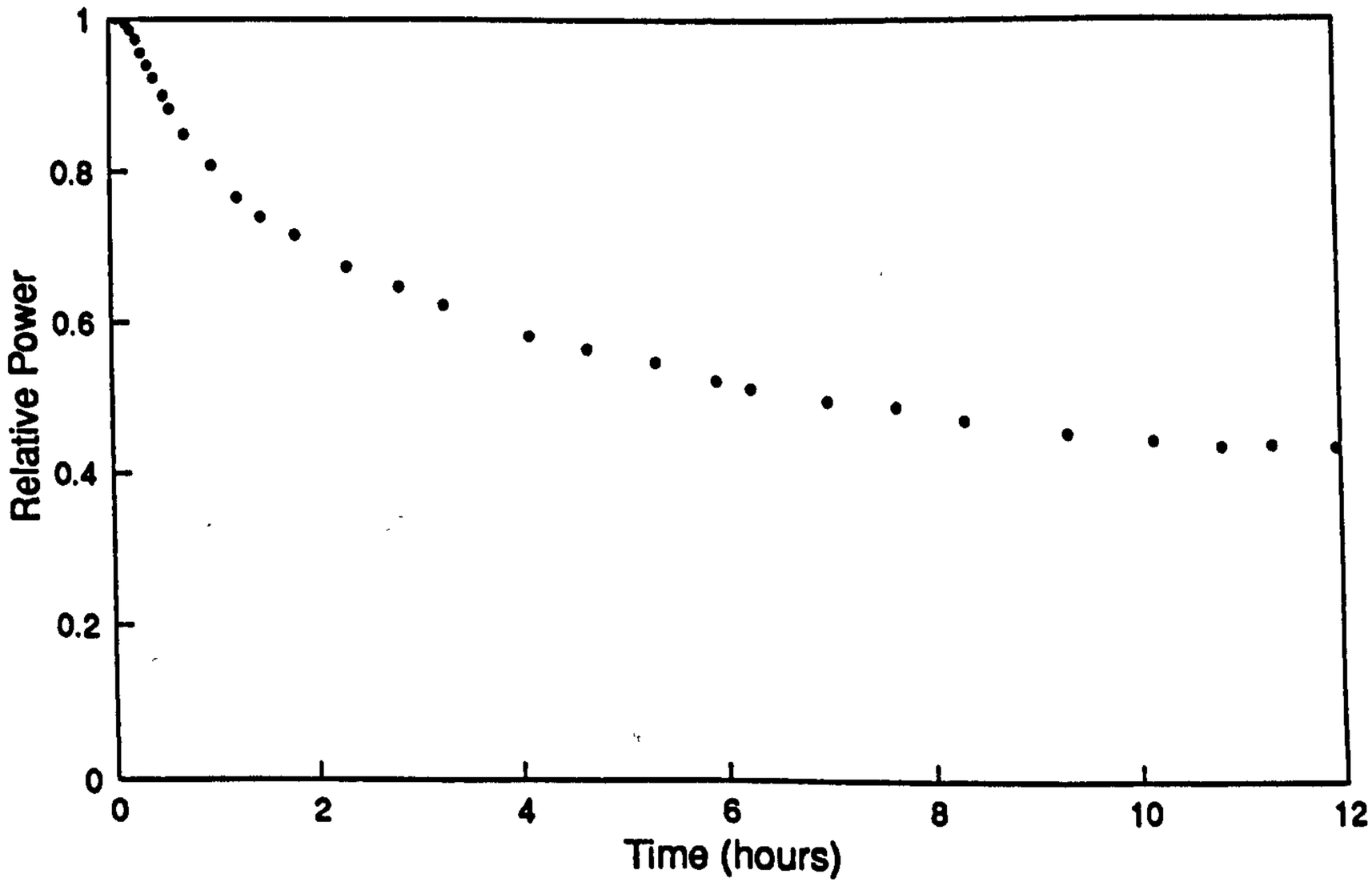

Figure 7.11 - Change in relative diffracted power with time - caused by laser induced heating.

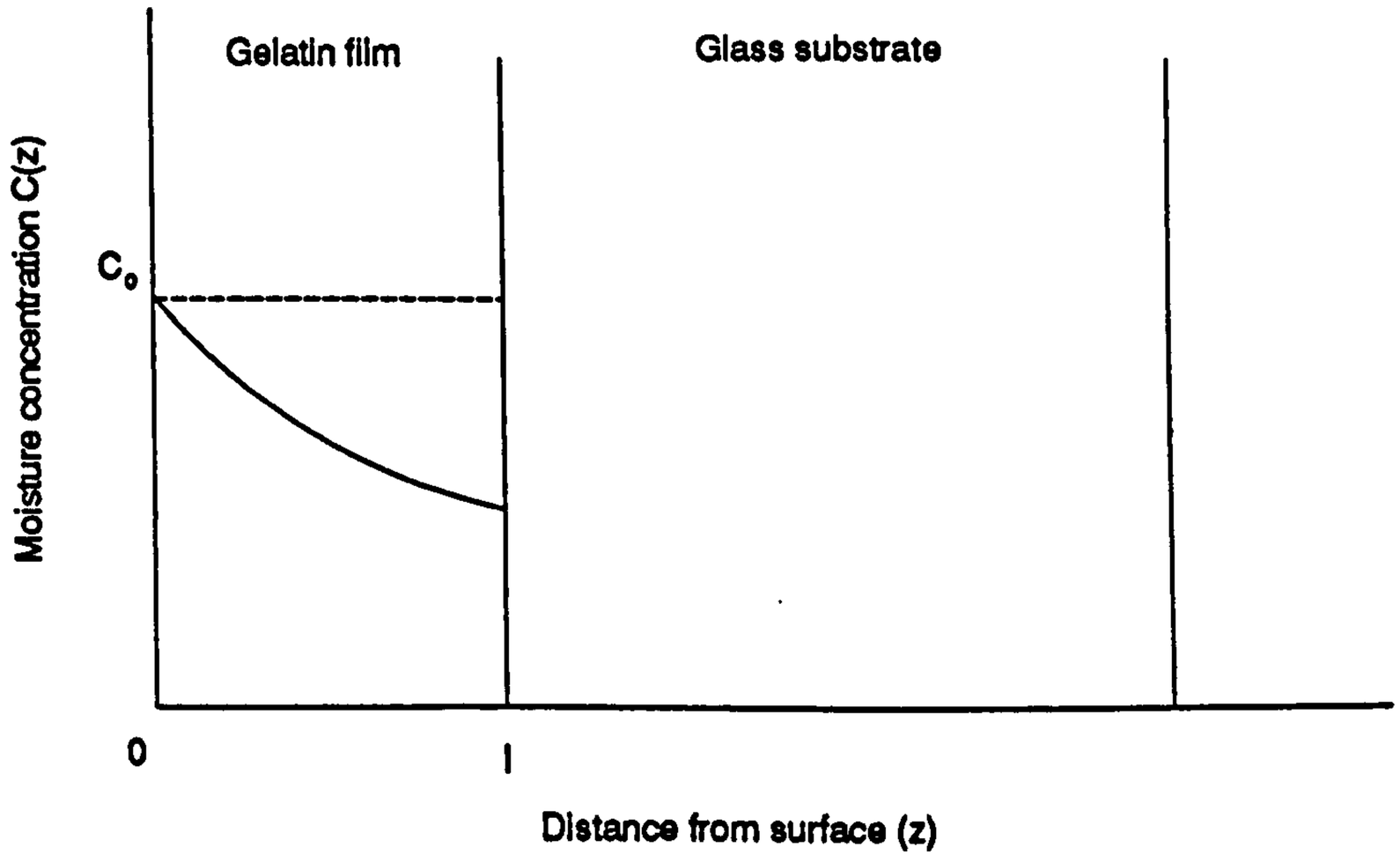

Figure 7.12 - Model used in reabsorption calculations.

size) are to be run in parallel the total power required, taking into account HOE efficiency and reflection losses, will be of the order of 10 W. Assuming an input beam diameter of 1cm, an ambient temperature of 22°C, an absorption of 3%, and a substrate thermal conductivity of $K_t = 0.85\ Wm^{-1}K^{-1}$, the temperature at the beam centre will be 50°C. This is well above the damage threshold of undried gelatin, thus post-processing will be required if the array generator is to successfully cope with this power. Alternatively, the float glass substrate can be replaced with a sapphire substrate, thereby increasing the power the hologram can safely handle (for the same temperature rise) by a factor of ≈20.

7.11 Reabsorption of water moisture

A final point of concern is the mechanism through which dried gelatin reabsorbs water moisture from the atmosphere. Consider the model shown below (figure 7.12). C(z,t) is the concentration of moisture in the gelatin as a function of position, z, and time, t. At the front surface $C(0,t) = C_o$, where C_o is the external surface moisture concentration. This

will be dependent on, among other things, external vapour pressure [21]. For $z > l$, C(z,t) = 0, i.e., the glass substrate is impermeable. The concentration gradient at $z = l$ is therefore always zero.

$$\frac{\partial C}{\partial z}\Big|_{z=l} = 0 \tag{7.8}$$

From the symmetry of the model it follows that C is independent of x and y. The diffusion equation therefore reduces to

$$\frac{\partial C}{\partial t} = D\,\frac{\partial^2 C}{\partial z^2} \tag{7.9}$$

It will be assumed that the gelatin is homogeneous and the diffusivity is independent of moisture concentration. Thus, equation (7.9) can be solved using the given boundary conditions and has a solution [18]

$$C(z,t) = C_o + \frac{4C_o}{\pi}\sum_{n=0}^{\infty}\frac{(-1)^{(n+1)}}{2n+1}A(t)\cos\left[\frac{(2n+1)\pi z}{2l}\right] \tag{7.12}$$

in which $A(t) = \exp(-D(2n+1)^2\pi^2 t/4l^2)$. To calculate the weight of water absorbed with time, equation (7.10) must be integrated as follows

$$M(t) = \int_o^l C(z,t)\,m\,dz \tag{7.11}$$

where m is the weight of water moisture per unit concentration. Thus

$$M(t) = mC_o l + \frac{8mC_o l}{\pi^2}\sum_{n=0}^{\infty}\frac{A(t)}{(2n+1)^2} \tag{7.12}$$

Letting $mC_o l = M_T$, the maximum amount of moisture which can be absorbed, it follows that

$$M(t)=M_T\left[1-C_1\exp(-C_2t)-\frac{C_1}{9}\exp(-9C_2t)-\frac{C_1}{25}\exp(-25C_2t)-\ldots\right] \quad (7.13)$$

where $C_1 = 8/\pi^2$ and $C_2 = \pi^2 D/4l^2$. The theoretical reabsorbtion of water moisture calculated using equation (7.13) is plotted in figure 7.4 alongside the experimental results. As can be seen there is a good correspondence between the two curves. The best fit to the experimental data was found when $M_T = 9.75$mg and $C_2 = 1.18\text{x}10^{-}3\text{sec}^{-1}$. Thus, the diffusion constant of the gelatin, D, is $1.08\text{x}10^{-9}\text{cm}^2\text{sec}^{-1}$. The most important point to note from this result is the rapid speed with which the water is reabsorbed, i.e. after only ten minutes almost half the moisture has returned to the gelatin. Sealing must therefore be performed immediately, whilst the gelatin is still dry. This can be done by keeping the hologram on a hot-plate whilst it is being sealed [1].

7.12 Conclusion

The thermal damage threshold of DCG depends strongly on the amount of moisture contained in the gelatin, thus, by thoroughly drying a hologram before sealing it is possible to raise the temperature at which deterioration begins. Under normal lab conditions (22°C and 40% R.H.), for instance, the thermal damage threshold is in the region of 45°C. A completely dried DCG hologram on the other hand can remain stable even at 100°C. Similar results were obtained in the case of laser induced heating, for example, drying a DCG hologram before sealing was found to increase its resistance to damage by a factor of about 70.

The theoretical analysis of laser induced heating by a beam with a Gaussian intensity distribution showed that the optical damage threshold depended strongly on (a) the absorption, (b) the thermal conductivity of the substrate and coverplate and (c) the ratio of the spot size to the thickness of the substrate and coverplate. In order to increase the damage threshold of a DCG HOE, therefore, the absorption of the gelatin and optical cement must be minimised, a high thermal conductivity substrate and coverplate should be used (i.e. Sapphire) and the thickness of the substrate and coverplate should be much

greater than the spot size. The ability to model the temperature distribution generated by Gaussian laser beam is of great practical importance because of the number of high power applications which deal with such beams.

Using this analysis the theoretical deterioration in the amount of power diffracted by a DCG hologram into its first diffraction order due to laser induced heating was modelled. Our work shows that this model is in close agreement with the experimentally determined fall in diffracted power (the theoretical value being within 10% of the experimental value). Thus, using the analysis presented in this paper, the optical damage threshold of a DCG HOE may be predicted and its power handling characteristics optimized.

7.13 References

1) I. R. Redmond, Holographic Optical Elements in Dichromated Gelatin, Ph.D. Thesis, Physics Department, Heriot-Watt University, U.K. (1989) and references therein.

2) Patent No. 86927, Luxemborg.

3) C. Y. Han, Y. Ishii and K. Murata, "Reshaping collimated laser beams with Gaussian profile to uniform profiles", Appl. Opt. **22**, 3644 (1983).

4) B. Robertson, M. R. Taghizadeh, J. Turunen and A. Vasara, "Fabrication of space-invariant fanout components in dichromated gelatin", Appl. Opt. **29**, 1134 (1990).

5) J. R. Leger, G. J. Swanson and W. B. Veldkemp, "Coherent laser addition using binary phase gratings", Appl. Opt. **28**, 4391 (1987).

6) J. H. Yi, S. H. Baik, J. B. Kim and J. Lee, "Efficient, spectrally narrow pulsed dye laser using a volume holographic transmission grating", Appl. Opt. **30**, 629 (1991).

7) L. Wang et Al, "Interference filters as nonlinear decision making elements for three spot pattern recognition and associative memories", Appl. Opt. **27**, 1715 (1988).

8) G. M. Naik, A. Mathur and S. V. Pappu, "Dichromated gelatin holograms: an investigation of their environmental stability", Appl. Opt. **29**, 5292 (1990).

9) B. J. Chang and C.D Leonard, "Dichromated gelatin for the fabrication of holographic optical elements", Appl. Opt. **18**, 2407 (1979).

10) B. J. Chang, "Dichromated gelatin holograms and their applications", Opt. Eng. **19**, 642 (1980).

11) D. Meyerhofer, "Phase holograms in dichromated gelatin", RCA Review **33**, 110 (1972).

12) C. E. Kenneth Mees, The Theory of the Photographic Process, (Macmillan, New York, 1944).

13) J. M. Rebordao and A. A. Andrade, "Microwave drying effects on dichromated gelatin holograms", Appl. Opt. **28**, 4393 (1989).

14) D. Meyerhofer, "Dichromated Gelatin", in Holographic Recording Materials, H. M. Smith ed., Vol 20 of Springer Series in Applied Physics (Springer-Verlag, Berlin, 1977).

15) E. Abraham, J. M. Halley, "Some calculations of the temperature profiles in thin films with laser heating", Appl. Phys. A **42**, 279 (1987).

16) I. Janossy, M. R. Taghizadeh, J. G. H. Matthew and S. D. Smith, "Thermally induced optical bistability in thin film devices", IEEE J. Quantum Electron. **QE-21**, 1447 (1985).

17) C. Godsalve, Passive Optical Bistability in Etalons with Diffusive Nonlinearities with Applications to Optical Computing, Ph.D. Thesis, Physics Department, Heriot-Watt University, U.K. (1991) and references therein.

18) H. S. Carslaw, J. C. Jaeger, Conduction of Heat in Solids, (Claredon Press, Oxford, 1959).

19) CRC Handbook of Chemistry and Physics, D. R. Lide, ed., 70th ed., (CRC Press, Florida, 1990), p. E-385.

20) D. J. McKnight, I. R. Redmond, A. C. Walker, M. R. Taghizadeh, G. S. Buller, J. G. H. Mathew, and S. D. Smith, "Parallel optical digital data transfer between bistable logic arrays", Opt. Comp. and Proc., **1**, 137 (1991).

21) S. Voyutsky, Colloid Chemistry, 2nd ed., (MIR, Moscow, 1978), Chap. 4.

Chapter 8

Space-Variant Interconnects

8.1 Introduction

Over the past few years, a number of optical processing and communication architectures have been developed which have at their heart some form of space-variant interconnection scheme [1-5]. As mentioned in chapter 1, these systems typically utilise interconnection topologies, such as the perfect shuffle, Banyan network, butterfly network and crossover network, that are highly regular, thereby simplifying the optical implementation of the circuit. A variety of regular space-variant interconnects have already been developed based on bulk optics, micro-optics, planar optics, holographic optical elements and diffractive optics (see, for example, the references cited in chapter 1). In general, however, the performance of these interconnects have been found to be limited by a variety of problems, including low optical throughput, scaling restrictions and nonuniform image magnification. As a result, the task of fabricating space-variant interconnects has become one of the most challenging problems in the field of free-space optical interconnection technology.

In the following chapter a method for fabricating versatile and compact one-to-one space-variant interconnects (SVIs) will be described. The interconnects consist of a matched pair of multi-facet HOEs, similar to those proposed by Haumann et al. [6], however, by including focusing power in the elements, point to point interconnections can be realised. Furthermore, the inclusion of an aperture imaging system in the recording set-up allows for the construction of short focal length elements with small facet sizes ($<200\mu m$). Only regular multi-stage interconnection fabrics, such as those based on the half-crossover network or the perfect shuffle (figure 8.1), were considered during the course of this work, although in principle, completely arbitrary one-to-one interconnects may be fabricated using this technique.

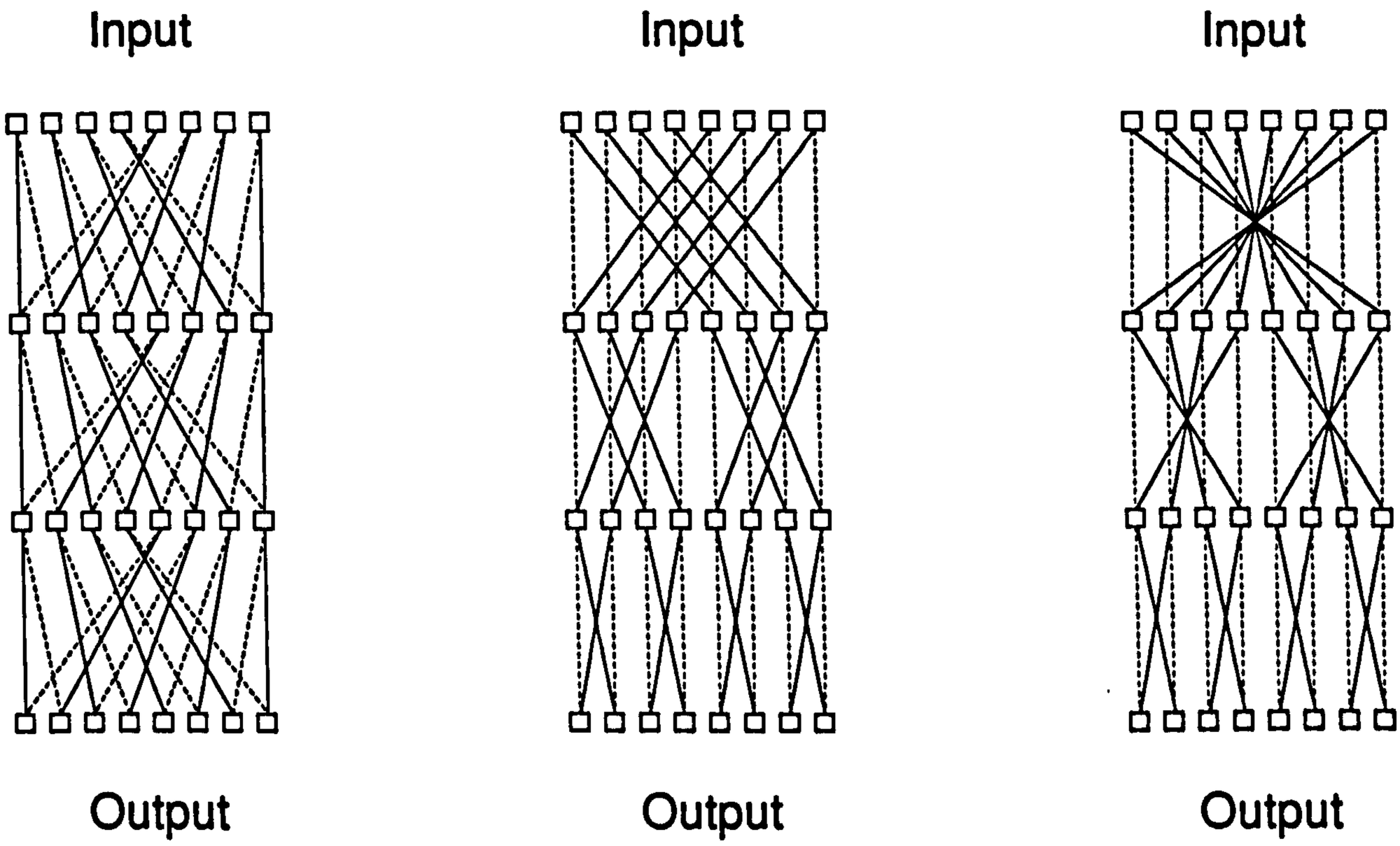

Figure 8.1 - Regular multi-stage space-variant interconnects. (a) The perfect shuffle. (b) The Banyan network. (c) the half-crossover network.

8.2 Two Element, Off-Axis SVI

Multi-facet space-variant HOEs were originally developed by Case et al. [7] for use within wavefront transformation systems [7,8]. Since then a variety of interconnection schemes based on holographic optical elements have been proposed which require either one or more multi-facet holograms for their implementation [9-14]. The arrangement investigated during the course of this work is shown in figure 8.2. The input signals (eg. from an array of optical switches) are incident on the first space-variant hologram (H_1) which consists of an array of holographic lenses. Thus, if H_1 is properly aligned one focal length from the input plane, P_1, the signal beams will all become collimated. As the lenses have slightly different reconstruction angles the beams cross-over to produce the required spatial

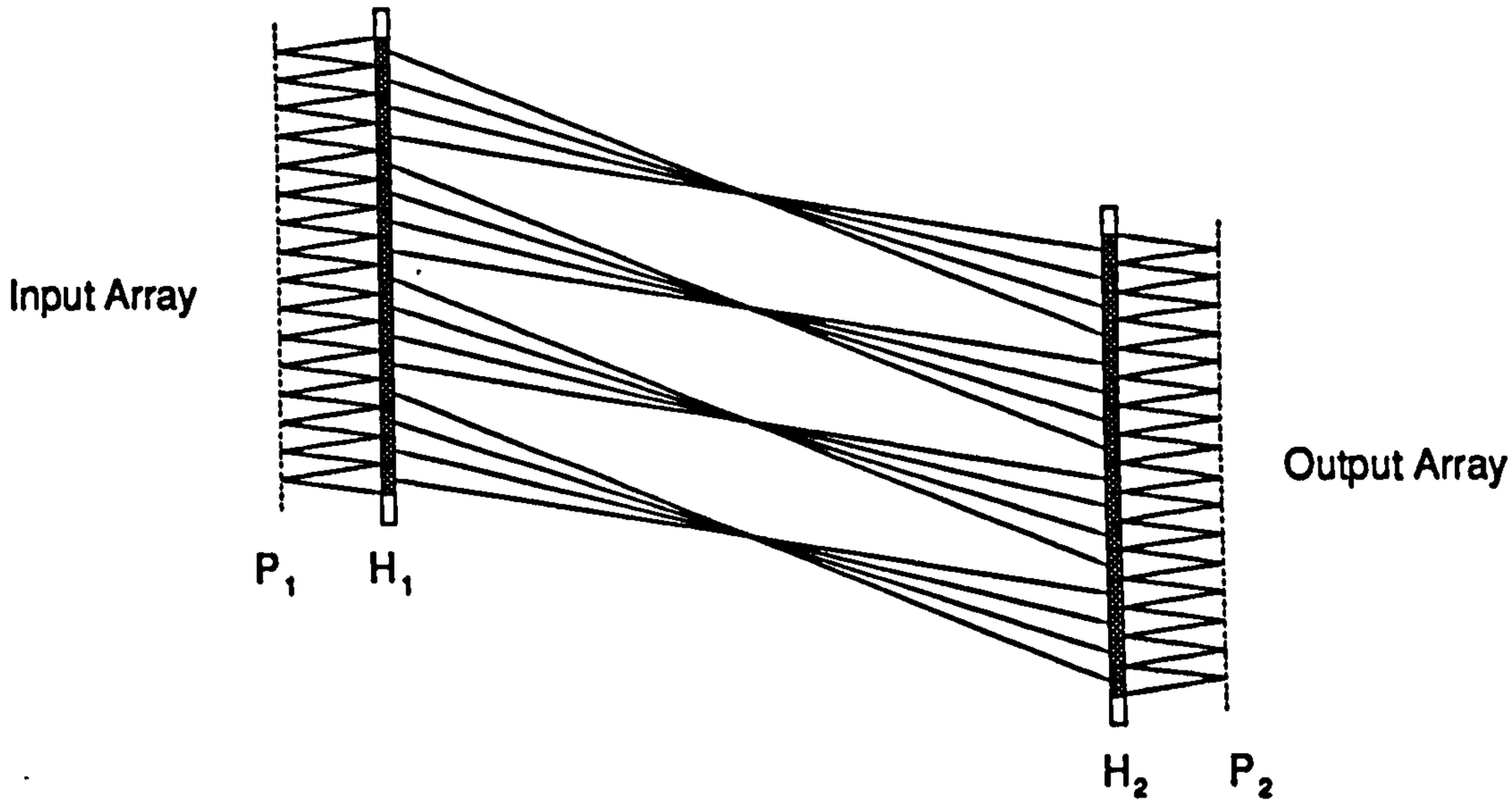

Figure 8.2 - Two element space-variant interconnect.
P_1 : input plane; P_2 : output plane.

permutation a distance L from H_1 where a second, mirror image or inverse function SVI (H_2) is placed. This has the effect of redirecting and focussing the beams such that concurrent spatial focusing of the beams occurs at the output plane P_2.

Although it is possible to fabricate a single SVI which produces the required permutation, all the beams arrive at the next logic plane with slightly different angles. The two element interconnect shown in figure 8.2 on the other hand allows for all the beams to come out along parallel axes. Although the input and output optical axes are laterally displaced, such a scheme is still capable of being used with a telecentric imaging set-up, leading to easier alignment and better performance of the overall optical system. It is also more compatible with angle sensitive switching devices, such as those based on Fabry-Perot etalons, waveguide structures and fibres, and can provide a small output spot size. For these reasons it was decided to concentrate only on cascaded, multi-facet HOEs.

In order to minimise cross-talk effects it must be first ensured that the input beams do not overfill the aperture of an individual pixel. Secondly, it is necessary to take into account the diffraction of the beams between H_1 and H_2. This will be helped if the input corresponds to an array of Gaussian beams, for example, as generated by a Dammann grating or a holographic fan-out element (chapter 4-6). Section 8.8.2 will cover more fully the limitations that this places on the design of a SVI.

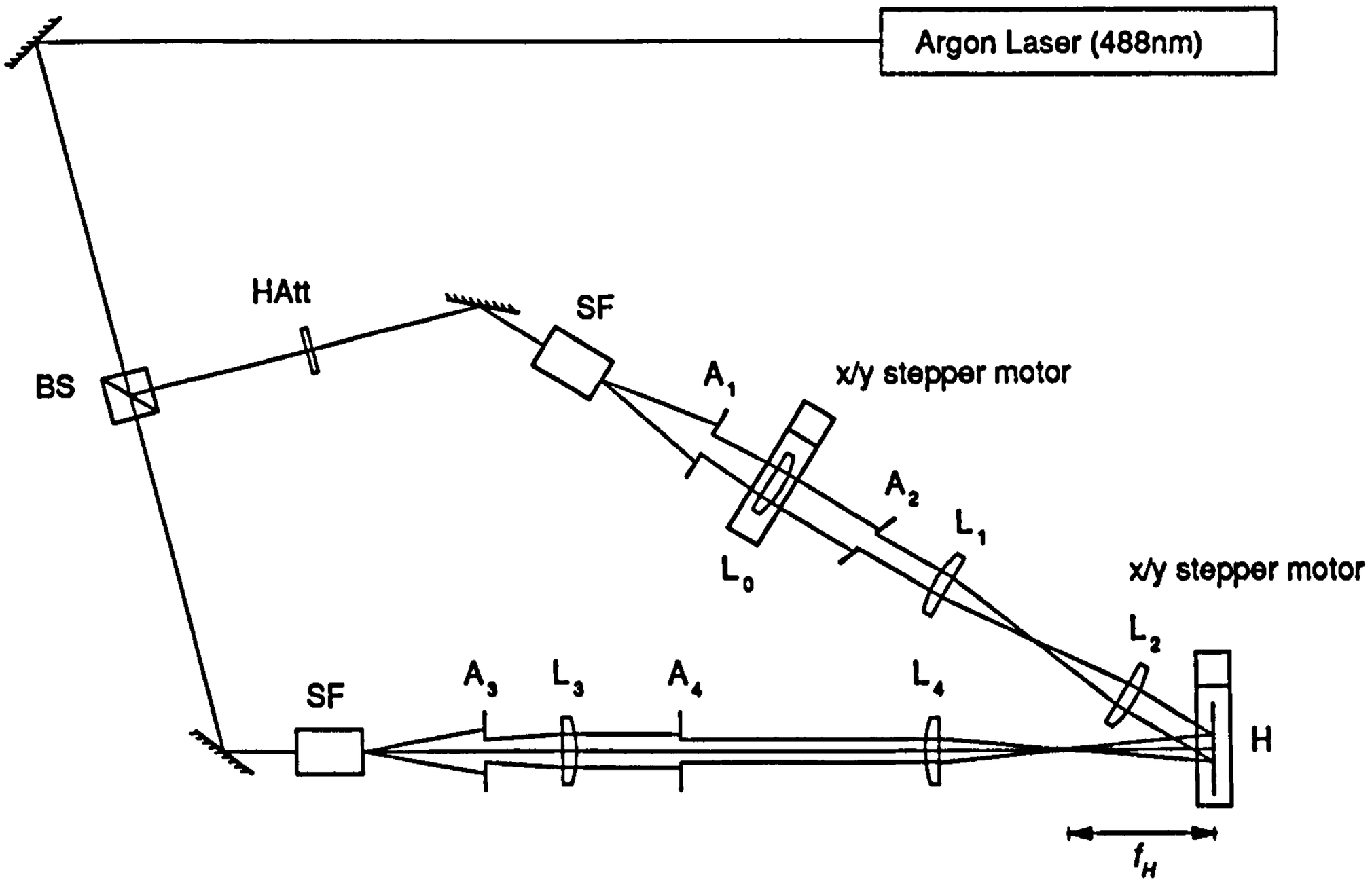

Figure 8.3 - Two element recording system. BS : Beam splitter; SF : Spatial filter; HAtt : Holographic attenuator; L_0 - L_4 : Lenses; A_1 - A_4 : Apertures.

8.3 Recording System

The recording system used to fabricate these space-variant interconnects is shown in figure 8.3. This was capable of accurately producing the type of space-variant interconnects required. It is based on the step and repeat exposure systems previously used to record high quality lenslet arrays [15], with the exception that the object arm collimating lens (L_0), is mounted on an x/y stepper motor.

The reference beam is derived from a spatially filtered and collimated plane wave. Lens L_4 produces a point source a distance f_H in front of the holographic plane (H) while aperture A_4 is positioned so as to be precisely imaged at H. Similarly the object arm consists of a spatially filtered and collimated beam which illuminates the aperture A_2. A 4-F lens system

(L_1 and L_2) then images this aperture at the holographic plane, accurately overlapping with the object beam. Each facet of the SVI therefore has well defined edges, allowing the maximum possible interconnect density to be achieved.

A variation in the replay angle $\Delta\theta$ is obtained by translating collimating lens, L_0, a distance p normal to the object beam optic axis. This causes a slight angular displacement of the collimated beam with respect to the aperture (figure 8.3) which is related to the lens movement by the following relations:

$$\tan(\Delta\theta) = p/f_0 \tag{8.1}$$

where f_0 is the focal length of L_0. If a precise 4-F imaging system is used then the wavefront present at A_2 will be reproduced at the holographic plane. Thus a translation of L_0 will cause a change in the object beam angle and hence in the replay angle of the reconstructed wavefront. If there is no translation then the HOE facet will reconstruct at the standard replay angle, θ. To relate this to an actual spatial permutation consider figure 4.4. If the two interconnecting HOEs are separated by a distance D and each facet has dimensions of $d_H \times d_H$, then to link facet n to facet n + m requires an angular displacement of $\theta + \Delta\theta_m$, which can be derived using the relation:

$$\tan(\theta + \Delta\theta_m) = (h + m d_H)/D \tag{8.2}$$

where h is the lateral translation of H_2 with respect to H_1. Substituting this into equation (8.1), we find that the distance we are required to translate the collimating lens is given by:

$$p_m = f_o \tan\left[\tan^{-1}((h + m d_H)/D) - \theta\right] \tag{8.3}$$

Thus to record a SVI with this system we simply translate F_0 to give the required object beam angle and expose a facet. By successively stepping the holographic plate vertically

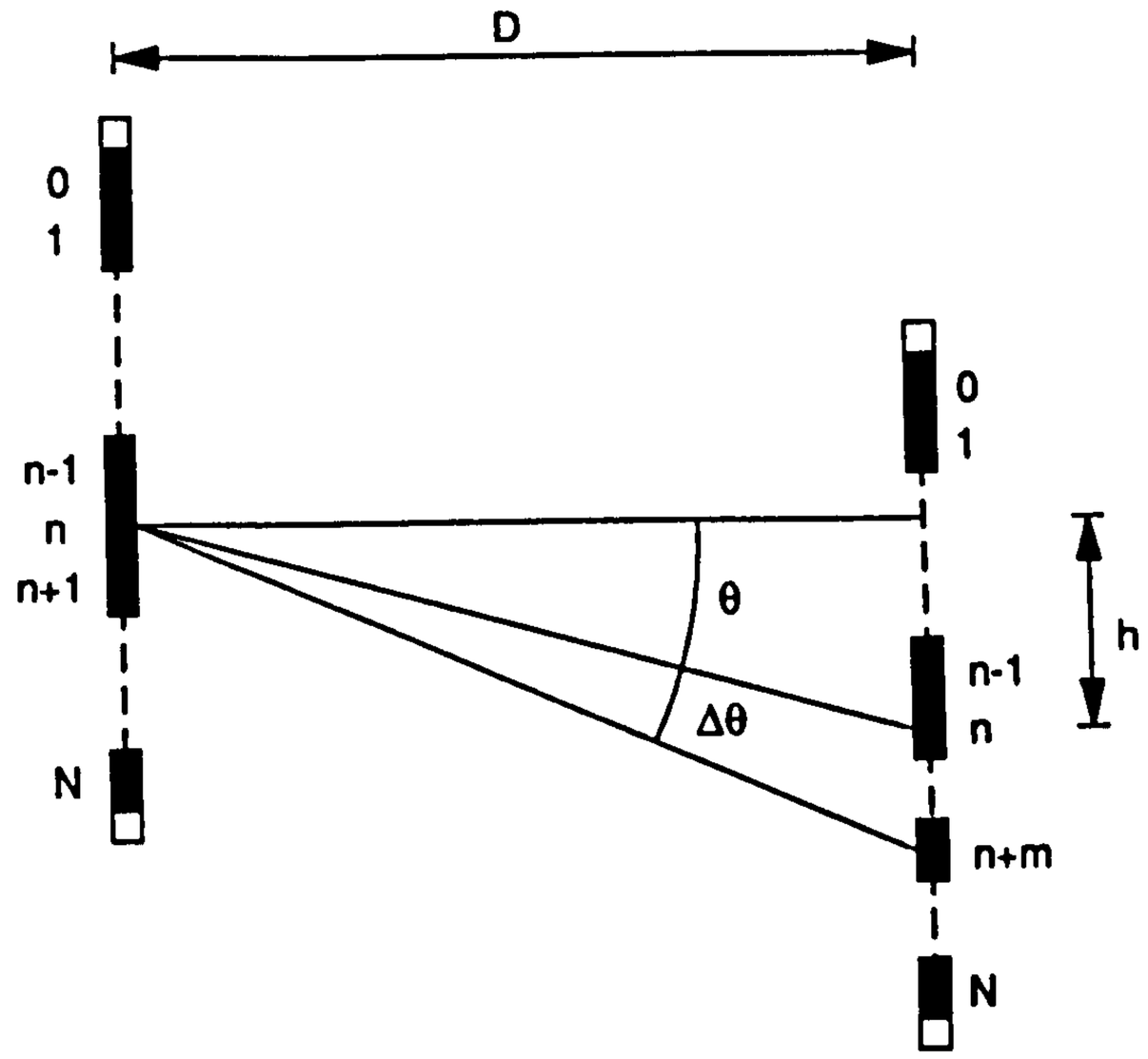

Figure 8.4 - Detailed replay set-up. D : seperation between H_1 and H_2; θ : average replay angle.

and/or horizontally and repeating the process a complex, two-dimensional, space-variant interconnect can be realised. The advantage that this technique has over the alternative recording schemes discussed in section 8.2 lies in the accuracy to which apertures A_2 and A_4 can be imaged and overlapped at H. As a result, a very high interconnect packing density can be achieved. Problems can, however, arise when trying to record large replay angle variations. Firstly, the maximum variation in recording angle, $\Delta\theta_{max}$, which can be realised during fabrication is limited by the numerical aperture of the recording optics. Secondly, as larger angles are approached, aberrations become more significant. These two factors impose an upper limit on $\Delta\theta_{max}$ of only a few degrees which, as a consequence, restricts the minimum allowable hologram separation, D, for any particular SVI scheme.

Several other difficulties can arise during the recording process which lead to fabrication errors, such as maintaining a precise overlap between the object and reference beam and setting up for exactly the required focal length in the recording set-up. In addition, positional errors can be caused by inaccuracies in the stepper motor (i.e. nonlinear translation or wobble), and any mismatch between the facet spacing and channel spacing. Further difficulties arise in the case of a DCG interconnect due to the swelling and change in

refractive index of the gelatin film between exposure and development. This generally causes a change in the reconstruction angles of the interconnect which must be compensated for by some form of post-processing [15,16].

An alternative recording technique used by Roberts [9], Haumann [6] and Kobolla [13] involves using a tilting mirror to provide the varying recording angles. In both systems, an aperture placed very close to the holographic plate ensures the facets have well defined edges. This has allowed very good results to be obtained, e.g., Kobolla et al. [13] recently reported a 16×16 perfect shuffle with facet sizes of ≈200μm. It also has the benefit of permitting larger variations in recording angles to be realised. A second approach involves producing a multi-facet CGH and copying this onto a high efficiency volume phase material, such as DCG.

8.4 Results.

Several prototype, off axis SVIs have been fabricated using the recording system shown in figure 8.3, including several stages of a half cross-over network, Banyan network and a 10×10 stacked perfect shuffle interconnect. All the holograms were recorded and replayed at 514.5nm using DCG derived from Kodak 649F plates and standard pre-processing and development procedures (chapter 3). Note that, for simplicity, $L_1 = L_2 = 100$mm.

When recording interconnects with the system described in figure 8.3 several practical problems have to be taken into account. First, it must be ensured that the beam in the object arm has been sufficiently expanded so that only the central, uniform part of the beam is used. If this is not the case then, as can be seen from figure 8.3, the amplitude profile across the aperture will vary with $\Delta\theta$ which, in turn, will cause the beam ratio to vary during the holographic recording. To overcome this problem, an exposure test can be made for each $\Delta\theta_{max}$ of the interconnect. This allows the peak exposure for each interconnect angle to be found.

Figure 8.5 shows the masked input array to a 10×10 stacked inverse perfect shuffle and the resulting output of the interconnect. In this particular case the facet size was 500μm, the standard replay angle, θ, was 30 degrees, the interconnection distance was 5cm and the SVIs replay focal length, f_H, was 2cm at 514.5nm. The efficiency of each SVI was measured to be 90%, giving the overall interconnect an 81% efficiency. As can be seen

(a)

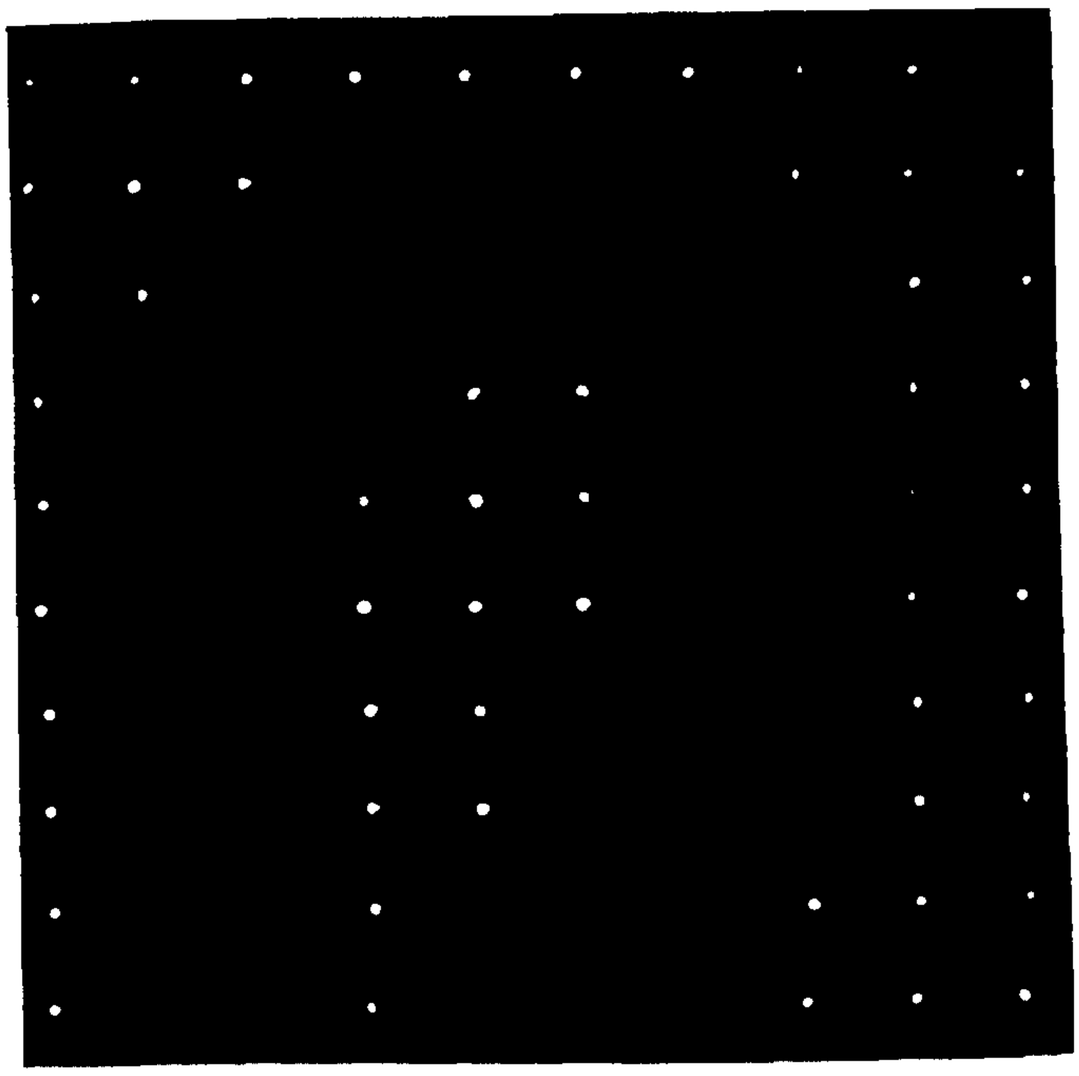

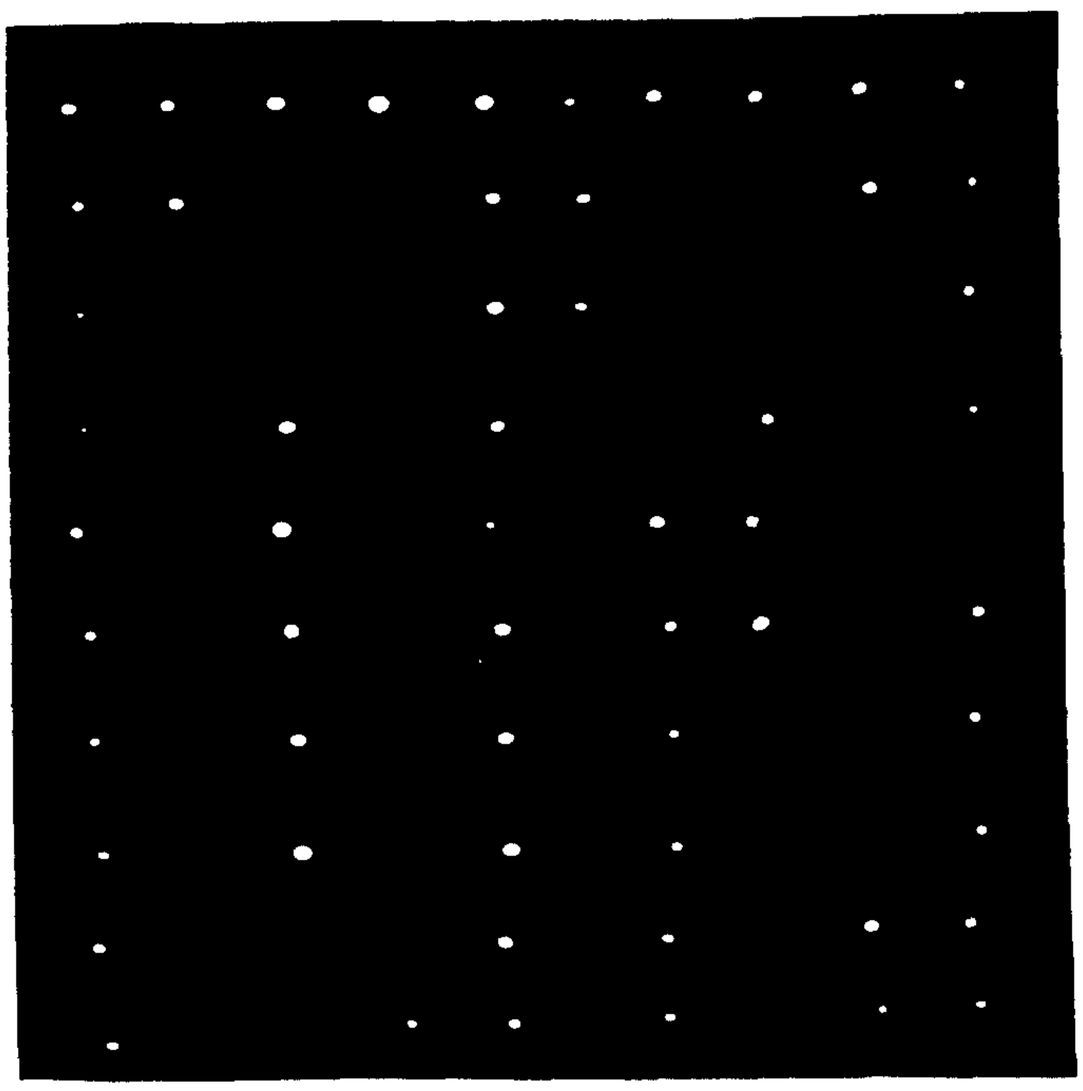

(b)

Figure 8.5 - Performance of the 10×10 stacked inverse perfect shuffle.

(a) Input pattern. (b) Output pattern

from the figure, there is a slight positioning error. This is principally due to inaccuracies in the positioning of the holographic plate by the stepper motor system; a problem which can easily be avoided by using a better translation stage. Further fabrication problems arise if the DCG plate is not aligned parallel to the image plane. The object and reference beams no longer remain perfectly overlapped across the entire array and, as a result, the useful facet area will decrease.

Misalignment effects were found to limit the performance of the space-variant interconnect, leading to higher levels of cross-talk and distorting the regularity of the output array. An analysis of alignment errors for a pair of on-axis lenslet arrays was performed by McCormick et al. [17]. This analysis showed that the focal length and the positioning of the facets must be tightly controlled if optimum performance is to be obtained, particularly when small channel separations are needed. Indeed, even with a facet size of 500μm, some difficulty in providing for adequate positioning was found. This was mainly due to the off-axis nature of the SVI which made it difficult to define the optic axis. The implementation of practical SVIs where facet sizes are less than 200μm will therefore be highly dependent on the alignment capabilities of the system. This puts great emphasis on the mechanical design of the interconnect and the packaging technology used. It also leads us to the conclusion that a four-element design, which will be described in section 8.5 is a better interconnect option due to its on-axis nature.

8.5 Four-Element, On-Axis SVI

An alternative scheme to the two element SVI discussed in the previous section is to create a four element space-variant interconnect. This involves separating the focusing and directing operations into two separate HOEs; a lenslet array and a corresponding array of plane grating elements which are sealed together to form a holographic doublet, thereby reducing reflection losses (figure 8.6). This has the benefit of making the interconnect on-axis and so ensures that alignment is a much simpler task. In addition, as all the beams travel more or less normally to the HOE surfaces, its polarisation dependence will be extremely low.

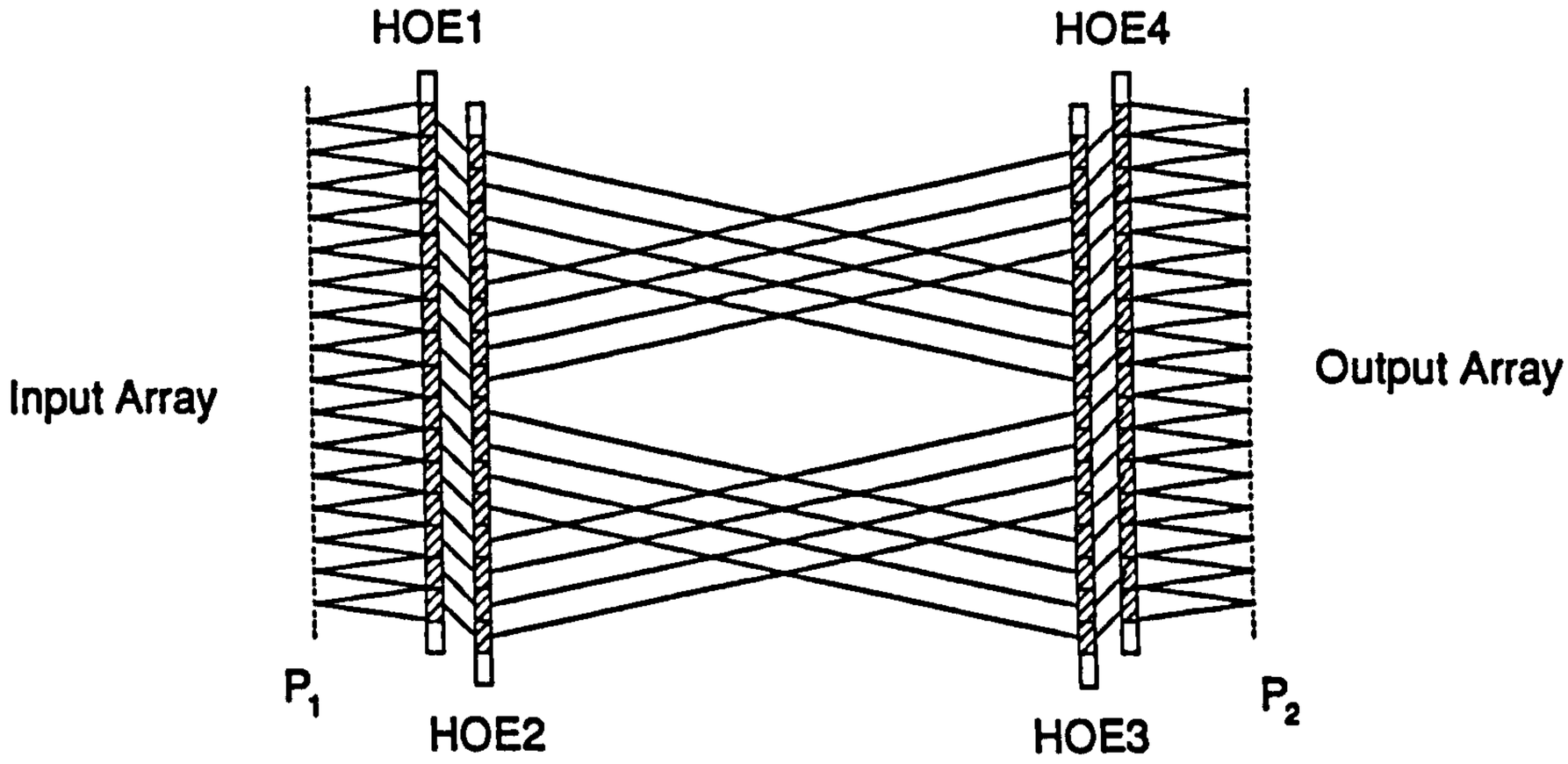

Figure 8.6 - Four element SVI.

Using a four-element interconnect also simplifies the task of designing a DCG SVI for operation at a wavelength different to that it was recorded at. If a two-element SVI were to be wavelength-shifted to a near-infrared wavelength it would become difficult to fabricate as each facet would require a different plane wave recording angle to ensure Bragg matching at the replay wavelength. In the case of a four hologram SVI, however, it is much simpler to build a wavelength shift into the separate elements; planar gratings are simple and high quality DCG lenslet arrays designed for replay at 850nm and 1064nm have been recently demonstrated [16,18]. Finally, the close cascaded nature of the holograms has the effect of reducing the interconnects sensitivity to changes in replay wavelength [19].

8.6 Design Considerations.

Several important points must be taken into account when designing a space-variant interconnect for an optical processor or communication system. These include, for example, diffractive effects, wavelength-shift-induced aberrations and alignment tolerances. In many cases, such difficulties can lead to severe restrictions being imposed upon

the interconnect beyond which either fabrication or operation is impractical. It is therefore important to understand the effect of these restrictions if a high interconnect performance is to be obtained.

8.6.1 Interconnect Packing Density

The finite thickness of the HOE will effect the performance of a SVI interconnect in two ways. Firstly, the incomplete overlap of the reference and object beams during recording will reduce the effective facet size. In the case of an interconnect recorded on 15μm thick gelatin with recording angles of 0 and 30°, for example, the facet size will be decreased by ≈5μm. Secondly, as the diameter of the replay beam approaches the holograms thickness, the diffracted beam will become distorted. This is due to the incomplete conversion of the zeroth order beam into the first order beam [20]. Taking the incident beams to have a Gaussian intensity profile with a $1/e^2$ spot radius of w_{H1} at H_1 and using the same HOE parameters as above, the distortion will only become apparent when $w_{H1} \approx 15\mu m$. In practice, however, the minimum facet size of the interconnect will be determined by the imaging optics. For the fabrication system described in figure 8.3, this will lie somewhere between 100μm and 200μm.

Although such a facet size may be adequate for some of the current demonstration circuits, many future systems will require far smaller spacings, e.g., S-SEED based circuits can have spacings as low as 10μm [3]. High quality imaging optics must therefore be used to magnify the channel separation up to the level of the SVI facet spacing. This underlines the advantage of using a two element as opposed to a single element interconnect: as all the input and output beams travel along parallel axes, such a set-up can be used with a telecentric imaging system. This gives rise to better overall optical performance and easier alignment capabilities.

8.6.2 Diffractive Effects

With facet sizes of between 100μm and 200μm, the effects of diffraction must be taken into account when designing any SVI. Unless proper account is taken of diffraction the signal beams will end up overfilling the pixels, leading to power loss and to higher levels

of cross-talk, both of which can fundamentally limit the performance of the interconnect. For simplicity it will be assumed that all the incident beams have the same Gaussian intensity profile. Due to the off-axis nature of the HOEs the wavefront diffracted by H_1 will be astigmatic [21], an effect which may be predicted using paraxial ray analysis and Gaussian beam propagation theory. This problem can be avoided, however, by using the four element system shown in figure 8.6. Obviously the optimum solution corresponds to one in which a beam waist is relayed half way between the two space-variant HOEs. The beam radius at H_2, w_{H2}, will then be equal to the beam radius at H_1, w_{H1}. This problem was analysed by McCormick et. al. in relation to refractive lenslet arrays [17]. A slight difference arises due to the different path lengths for each n to n+m interconnect mapping. This will give rise to variations in w_{H2}, and to the position and size of the output waist. Because the difference in path length is so small however, typically only a fraction of a percent, this will have a minimal effect. Take, for example, a 16x16 stacked perfect shuffle of 200μm channel separation, 2.5mm focal length and an interconnect separation of 5cm. The variation in path length for this particular geometry is approximately 25μm. McCormick et al. [17] showed that in the case of on-axis lenslet arrays, even a variation in path length of up to 10% can have very little effect on the performance of the interconnect. In comparison, stringent control over the relative positioning of the input array with respect to H_1 must be exercised.

8.6.3 Overfilling Aperture

As the intensity profile of a Gaussian beam extends to infinity, a fraction of the incident power will spill over into adjacent pixels. Consider the case of a Gaussian beam of radius w_H ($1/e^2$ intensity points) incident on a square holographic lenslet of dimensions $d_H \times d_H$. The total power incident on this facet, P_F, is given by

$$P_F = 4 \int_0^{d_H/2} \int_0^{d_H/2} I(x,y)\, dx\, dy \tag{8.6}$$

where $I(x,y) = I_o \exp[-2(x^2+y^2)/w_H^2)]$. Equation (8.6) can be shown to reduce to

$$P_F = \frac{\pi I_o w_H^2}{2} [erf(d_H/\sqrt{2}w_H)]^2 \tag{8.7}$$

where erf is a standard error function, defined as [22]

$$erf(z) = \frac{2}{\sqrt{\pi}} \left[\int_0^z \exp[-t^2] dt \right] \tag{8.8}$$

As the total power in the incident beam, P_T, is given by $P_T = I_o \pi w_H^2/2$, it follows that the fraction of incident light which ends up in the correct interconnection channel, F, is

$$F = P_F/P_T = [erf(d_H/\sqrt{2}w_H)]^2 \tag{8.9}$$

The light which overfills the aperture will not necessarily be diffracted along the neighbouring interconnect paths if the Bragg condition is not correctly satisfied. Instead it will remain in the zeroth-order and propagate away from the output plane. Whilst this reduces the possibility of any cross-talk occurring from pixel over-fill, the spot size should nonetheless be kept well within the dimensions of the pixel to optimise overall efficiency. The dependence of F on d_H/w_H is shown in figure 8.7. From this graph it can be seen that a high coupling efficiency is obtained when $3w_H < d_H$ (over 99% of the power ends up in the correct facet). The design condition, $3w_H = d_H$ is therefore a useful criteria to use when designing any SVI system.

A second consequence of clipping the beam is its effect on the relayed waists position and size. McCormick et. al. [17] showed that in the case of a Gaussian beam clipped by a circular aperture the change in these parameters can be quite significant. When $w_H = 2d_H$, for example, the spot size and waist position can change by up to 5%. In the region where $w_H < 3d_H$, however, these effects are insignificant. Thus, again taking the criteria, $w_H = 3d_H$ we should theoretically get over 99% of the input power into the correct channel with negligible effect on its Gaussian propagation characteristics. In the case of the perfect shuffle interconnect described in section 1.5, this corresponds to a optimum waist size at H_1 of ≈163μm.

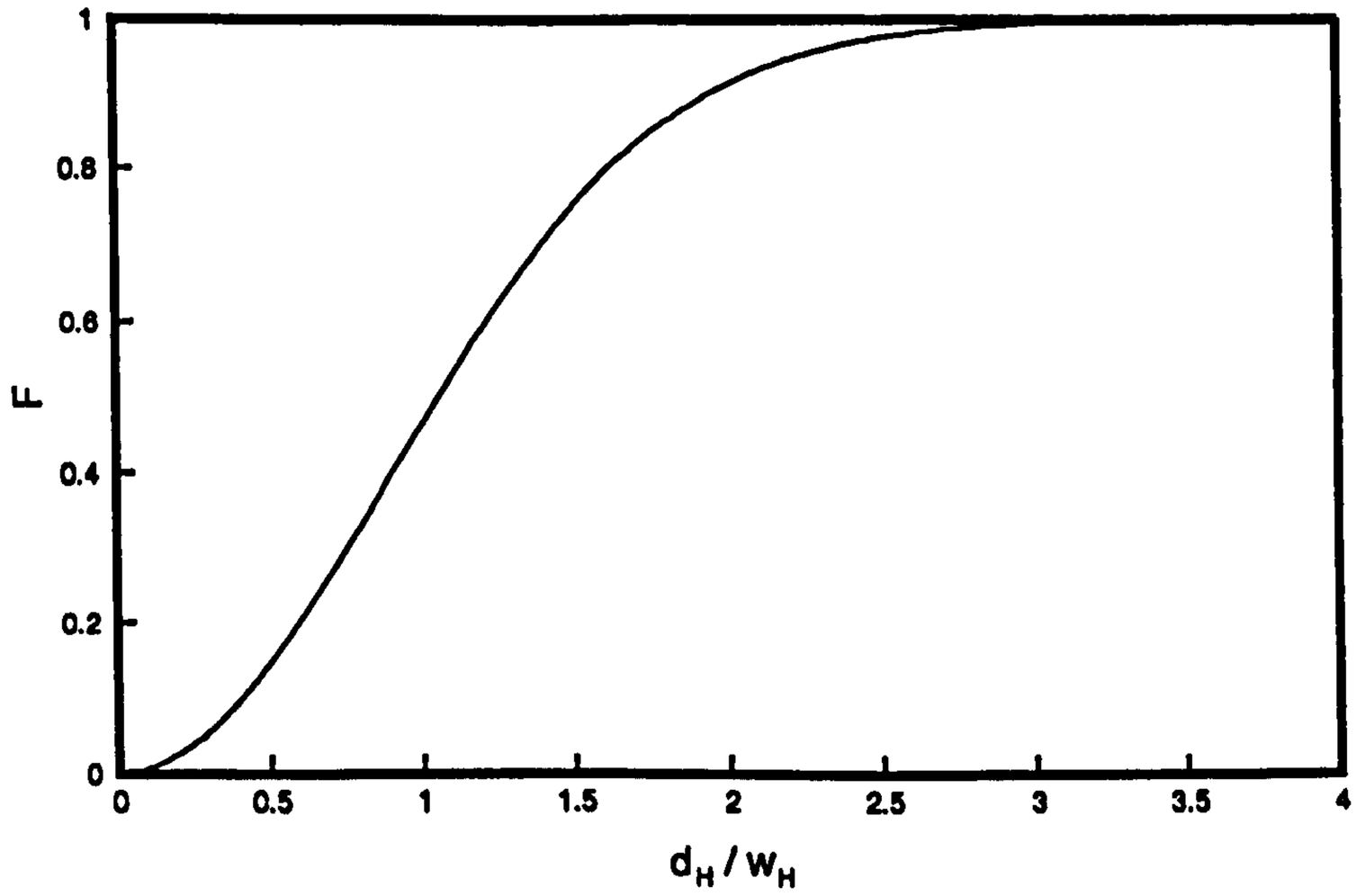

Figure 8.8 - Dependance of the fraction of incident light ending up in the correct interconnection channel, F, on the ratio of facet size, d_H, to beam radius, w_H.

8.7 Conclusions

Using the recording techniques described in this chapter, a number of prototype space-variant interconnects based on a pair of matched multi-facet DCG holograms have been demonstrated. Due to the off-axis nature of the HOEs, however, problems with alignment and diffraction effects will limit the scalability of this technique. In comparison, a four element, on-axis system should provide a more practical approach as alignment is easier and the beams are no longer astigmatic. Such a system would also be simpler to wavelength shift and more tolerant to fluctuations in replay wavelength.

Although this technique does have the potential for providing functional SVIs, much more work must be carried out in order to investigate its limitations. This applies in particular to aspects such as wavelength shifting, packaging and fabrication accuracy.

8.8 References

1) A. D. McAulay, Optical Computing Architectures, John Wiley and Sons, Inc., New York (1991).

2) M. J. Murdocca, A. Huang, J. Jahns and N. Streibl, "Optical design of programmable logic arrays", Appl. Opt. **27**, 1651 (1988).

3) M. E. Prise, N. C. Craft, R. E. LaMarche, M. M. Downs, S. J. Walker, L. A. D'Asaro and L. M. F. Chirosvsky, "Module for optical logic circuits using symmetric self-electrooptic effect devices", Appl. Opt. **29**, 1111 (1990).

4) M. J. Murdocca, A. Huang, J. Jahns and N. Streibl, "Optical design of programmable logic arrays", Appl. Opt. **27**, 1651 (1988).

5) F. B. McCormick and M. E. Prise, "Optical circuitry for free-space interconnections", Appl. Opt. **29**, 2013 (1990).

6) H. J. Haumann, J. Hausmann, H. Koballa, F. Sauer, W. Stark, N. Streibl, M. Testorf and R. Volkel, "Holographic optical interconnects in dichromated gelatin (DCG)", International Symposium on Optics in computing, 137 Toulouse, France (1989).

7) S. K. Case, P. R. Haugen and O. J. Lokberk, "Multifacet holographic optical elements for wavefront transformations", Appl. Opt. **20**, 2670 (1981).

8) H. Bartelt and S. K. Case, "Multi-facet HOEs", Opt. Eng. **22**, 497 (1983).

9) N. C. Roberts, "Free-space holographic optical interconnects", in *Optical Interconnects*, IEE Technical Digest **121**, 6 (1988).

10) B. Robertson, E. J. Restall, M. R. Taghizadeh and A. C. Walker, "Space-variant holographic optical elements in dichromated gelatin", Appl. Opt. **30**, 2368 (1991).

11) E. J. Restall, B. Robertson, M. R. Taghizadeh and A. C. Walker, "Two-dimensional spatially variant optical interconnects", OSA Conference on Optical Computing, Technical Digest Series **6**, 49 Salt Lake City, Utah, U.S.A. (1991).

12) E. J. Restall, B. Robertson, M. R. Taghizadeh and A. C. Walker, "Two dimensional non-local multi-facet holographic interconnects in dichromated gelatin", in *Holographic Systems, Components and Applications*, IEE Conference Publication **342**, 127 (1991).

13) H. Kobolla, N. Lindlein, O. Falkenstorter, S. Resner, J. Schmidt, J. Schwider, N. Streibl, R. Volkel, "Optoelectronic interconnects with holographic optical elements", in *Holographic Systems, Components and Applications*, IEE Conference Publication **342**, 123 (1991).

14) J. M. Wang, L. Cheng, A. A. Sawchuk, "Optical 2-dimensional perfect shuffles based on a one-copy algorithm", Appl. Opt. **31**, 5464 (1992).

15) B. J. Chang, "Post-processing of developed dichromated gelatin holograms", Opt. Commun. **17**, 270 (1976).

16) I. R. Redmond, "Holographic optical elements in dichromated gelatin", Ph.D Thesis, Heriot-Watt University, Scotland (1989).

17) F. B. McCormick, F. A. P. Tooley, T. J. Cloonan, J. M. Sasian and H. S. Hinton, "Microbeam optical interconnections using microlens arrays", OSA Topical Meeting on Photonic Switching, 90 Salt Lake City, Utah, U.S.A. (1991).

18) I. R. Redmond, E. J. Restall, and A. C. Walker, "High performance holographic optics for the visible and near infra-red", in *Holographic Systems, Components and Applications*, IEE Conference Publication **311**, 190 (1989).

19) T. W. Stone, Holographic Optical Elements, Ph.D. Thesis, University of Rochester, U.S.A (1986).

20) R. S. Chu, J. A. Kong, T. Tamir, "Diffraction of Gaussian beams by a periodically modulated layer", J. Opt. Soc. Am. **67**, 1555 (1977).

21) The Physics and Technology of Laser Resonators, Edited by D. R. Hall and P. E. Jackson, (IOP Publishing Ltd 1989).

22) Handbook of Mathematical Functions with Formulas, Graphs and Mathematical Tables, Edited by M. Abramowitz and I.A. Stegun, *National Bureau of Standards*, Applied Mathematics Series, **55** (1964).

Chapter 9

Conclusions

Holographic optical interconnects recorded in dichromated gelatin have several features which make them appear ideal for applications within the fields of optical computing and communications. Due to the flexibility of the recording process, complex interconnection patterns may be implemented which are difficult to realize using conventional reflective and refractive optics. In addition, dichromated gelatin is capable of high diffraction efficiencies, approaching 100% in both refection and transmission, has a low absorption and, by proper optimization of the recording geometry, it is possible to fabricate components which have near diffraction limited performance in the near infra-red.

A number of techniques for recording volume phase fan-out elements were developed during the course of this work. Initial research concentrated on using binary-phase and binary-amplitude Dammann gratings to generate the object wavefront in an interferometric recording set-up. Although this approach allowed a series of high efficiency off-axis array generators to be realised, the reconstruction error associated with these elements was found to be too high for practical interconnection applications. In addition, the maximum achievable efficiency could only equal that of the equivalent binary-phase element. Higher efficiencies can, in principle, be obtained using continuous, or multilevel phase profiles. These components, commonly referred to as kinoforms, are, however, difficult to fabricate using conventional lithographic manufacturing techniques. In an attempt to circumvent this problem, a new recording process was developed which allowed a continuous phase object wavefront to be produced from a binary-amplitude CGH. The resulting off-axis fan-out holograms, or hybrid kinoforms, were found to have a performance good enough for use in most optical computing and communication circuits. Further work is, however, needed to characterise the performance of these elements. In particular, a full theoretical and experimental analysis of their angular acceptance, covering such points as efficiency,

polarisation dependence and linearity, is required. Moreover, it would be interesting to see if the hybrid kinoform recording technique can be successfully used to produce volume phase reflection holograms.

An investigation into the optical and thermal damage threshold of a sealed DCG hologram was carried out. The results of this research indicate that the intrinsic optical damage threshold of DCG depends strongly on the amount of moisture contained in the gelatin, thus, thoroughly drying a hologram before sealing can dramatically increase the amount of optical power it can safely handle. A theoretical model designed to predict the temperature rise induced in a sealed volume phase hologram hologram by a Gaussian laser beam was developed. This analysis showed that the optical damage threshold of a hologram may also be increased by reducing the absorption of the gelatin, using a higher thermal conductivity substrate and cover plate, and ensuring that the thickness of the coverplate and substrate are much greater than the spot size.

A technique for recording compact multi-facet space-variant interconnects was also developed. Although high diffraction efficiencies were obtained, preliminary results showed that tight recording and replay parameters must be met if useful interconnects are to be produced. This problem was also found to be true of the fan-out elements recorded during the course of this thesis. It therefore follows that if DCG components are to compete effectively with alternative interconnection technologies, greater control over their replay parameters must be exercised. In principle this may be achieved using a combination of post-processing techniques and accurate optimization of the recording geometry. Furthermore, by using compensator plates, it will be possible to implement on-axis interconnection geometries, an advantage both in terms of optical circuit design and reconstruction tolerances. Alternatively, other volume phase recording materials should be investigated to see if they have more controllable characteristics. The results presented in this thesis do show, however, that DCG volume phase holographic optical interconnects have a potential role to play in the fields of optical computing and communications.

APPENDIX 1

Stacked Volume Phase Holograms

In section 2.6 the behaviour of a single plane grating when simultaneously replayed with both the reference and object beams was described. The analysis showed that the output from such a system depended strongly on the relative phase between these two wavefronts as they entered the hologram. In the following appendix the diffractive properties of a holographic doublet consisting of two identical plane transmission gratings, HOE1 and HOE2, will be described. A similar analysis for an étalon based on two volume phase reflection holograms was performed by Kuo et. al. [1]. The geometry of the system is shown in figure A.1.1. For simplicity, it will be assumed that the doublet is replayed with a single reference beam of irradiance I_i. The output from HOE1 will therefore consist of an object beam, I_{o1}, and an undiffracted reference beam, I_{r1}, given by

$$I_{r1} = (1-\eta_1)I_i \qquad (A.1.1)$$

$$I_{o1} = \eta_1(c_R/c_S)I_i \qquad (A.1.2)$$

where η_1 is the diffraction efficiency of HOE1. If these two wavefronts overlap as they propagate through HOE2, the coupling effects described in section 2.6 will occur. The output from HOE2, which will consist of an object beam, I_{o2}, and a reference beam, I_{r2}, can therefore be calculated using equations (2.44) and (2.45). It therefore follows that

$$I_{r2} = I_i[(1-\eta_1)(1-\eta_2)+\eta_1\eta_2-2(\eta_1\eta_2(1-\eta_1)(1-\eta_2))^{1/2}\sin(\psi)] \qquad (A.1.3)$$

where η_2 is the diffraction efficiency of HOE2, and ψ is the phase difference defined in

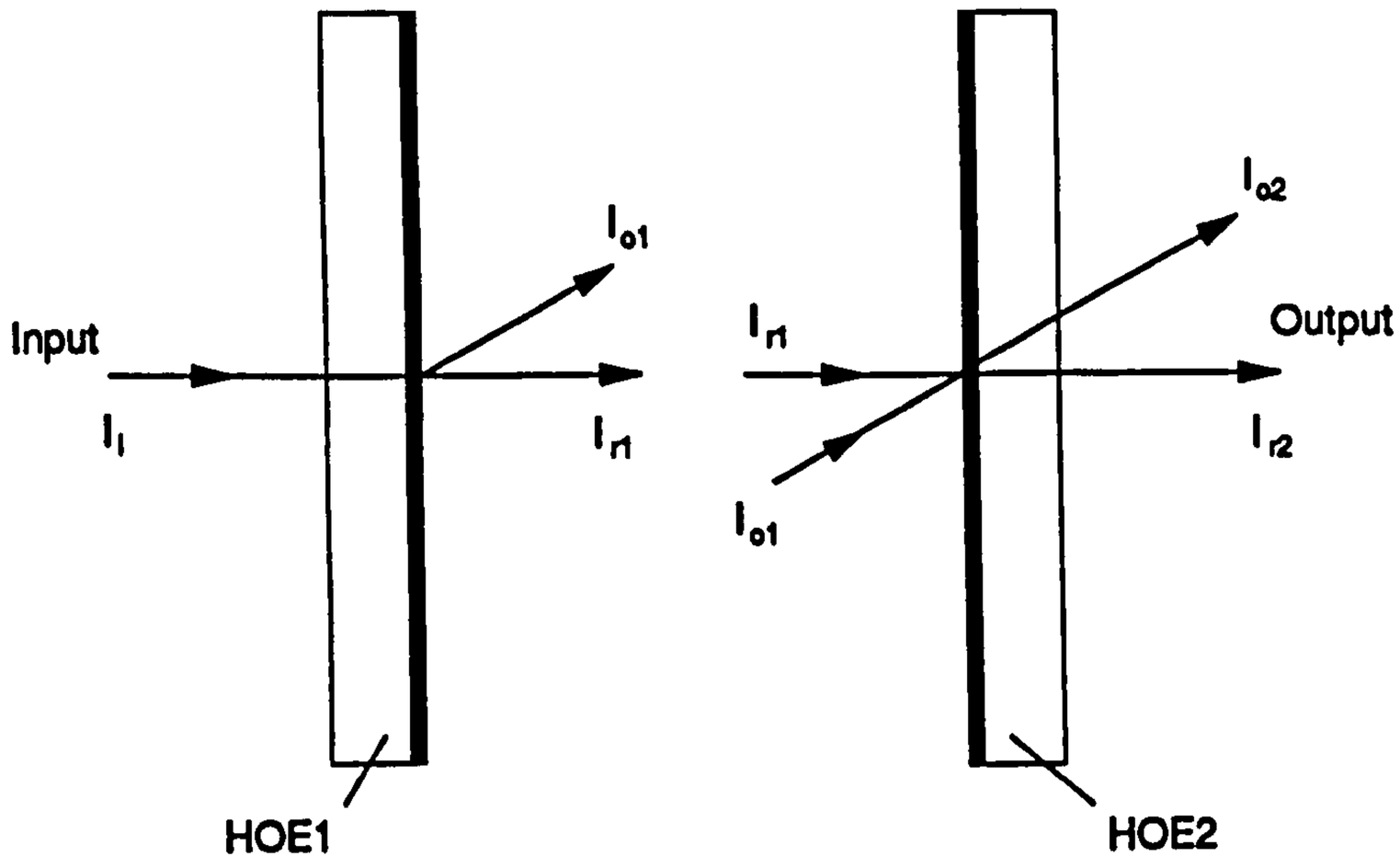

Figure A.1.1 - Holographic doublet geometry.

section 2.6. If the condition $\eta_1 = \eta_2 = \eta$ is met, equation (A.1.3) reduces to

$$I_{r2} = I_i[(1-\eta)^2 + \eta^2 - 2\eta(1-\eta)\sin(\psi)] \qquad (A.1.4)$$

As mentioned in chapters 5 and 6, holographic interconnection schemes require compensator plates to enable them to operate on axis. In the case of plane grating elements, such as the hybrid kinoforms described in chapter 6, coupling between the signal beams undiffracted by the compensator plate and the fanned-out beams produced by the hybrid kinoform may lead to problems if the propagation vectors lie in the same direction. Even if the doublet consists of two 99% efficient gratings this effect will still be noticeable. If ψ is varied between 0 and 2π, the value of I_i will fluctuate by ±2%.

The relative phase difference, ψ, can be changed by shifting the position of HOE2 with respect to HOE1, i.e., by a lateral translation of Δx or a longitudinal translation of Δz. It can be shown that the change in ψ resulting from such a shift, $\Delta\psi$, is given by

$$\Delta\psi = (2\pi/\lambda)(\cos\theta_R - \cos\theta_S)\Delta z \qquad (A.2.4)$$

and

$$\Delta\psi = (2\pi/\lambda)(\sin\theta_R + \sin\theta_S)\Delta x \qquad (A.2.5)$$

where θ_r and θ_o are respectively the angles that the reference and object beams make with respect to the z-axis. Alternatively, ψ may be altered by changing the refractive index of the medium between the two gratings. Such a geometry may be used to realise a compact optical modulator or variable attenuator. By introducing some form of electro-optic material, such as $LiNbO_3$ or a layer of nematic-liquid crystal, between a doublet consisting of two 50% efficient gratings the output signal maybe varied between 0 and I_i. This set-up has the advantage of offering a large angular separation between the signal beam and the noise beam. A similar approach was used by Kuo et. al. [1] to demonstrate a tunable Fabry-Perot étalon based on two reflection gratings.

Experimental Results

To investigate the effect of stacking volume phase holograms in this manner, a number of plane gratings were recorded in dichromated gelatin. The object beam was aligned normal to the holographic plate whilst the reference beam was set at 30° to the normal. Two of these gratings were then arranged in a close cascaded set-up (figure A.2.2) and illuminated with a plane reference beam as shown. Photographs of the resulting zeroth and first diffraction orders were then taken (figure (A.2.3). These show that the output of the holographic doublet consists of a series of circular fringes rather than the uniform irradiance field predicted theoretically. This can be attributed to the hologram being recorded with non-perfectly flat recording beams. In addition, as expected, the first diffraction order is the negative image of the zeroth order beam.

It was observed that as the two gratings were pressed together the fringes shifted radially as the relative phase difference varied between 0 and 2π. Moreover, only by fine adjustment of the holograms positions could a circular fringe pattern be observed. If the holograms were translated laterally with respect to each other this fringe pattern became distorted, eventually tending towards a series of roughly parallel lines. The output pattern was,

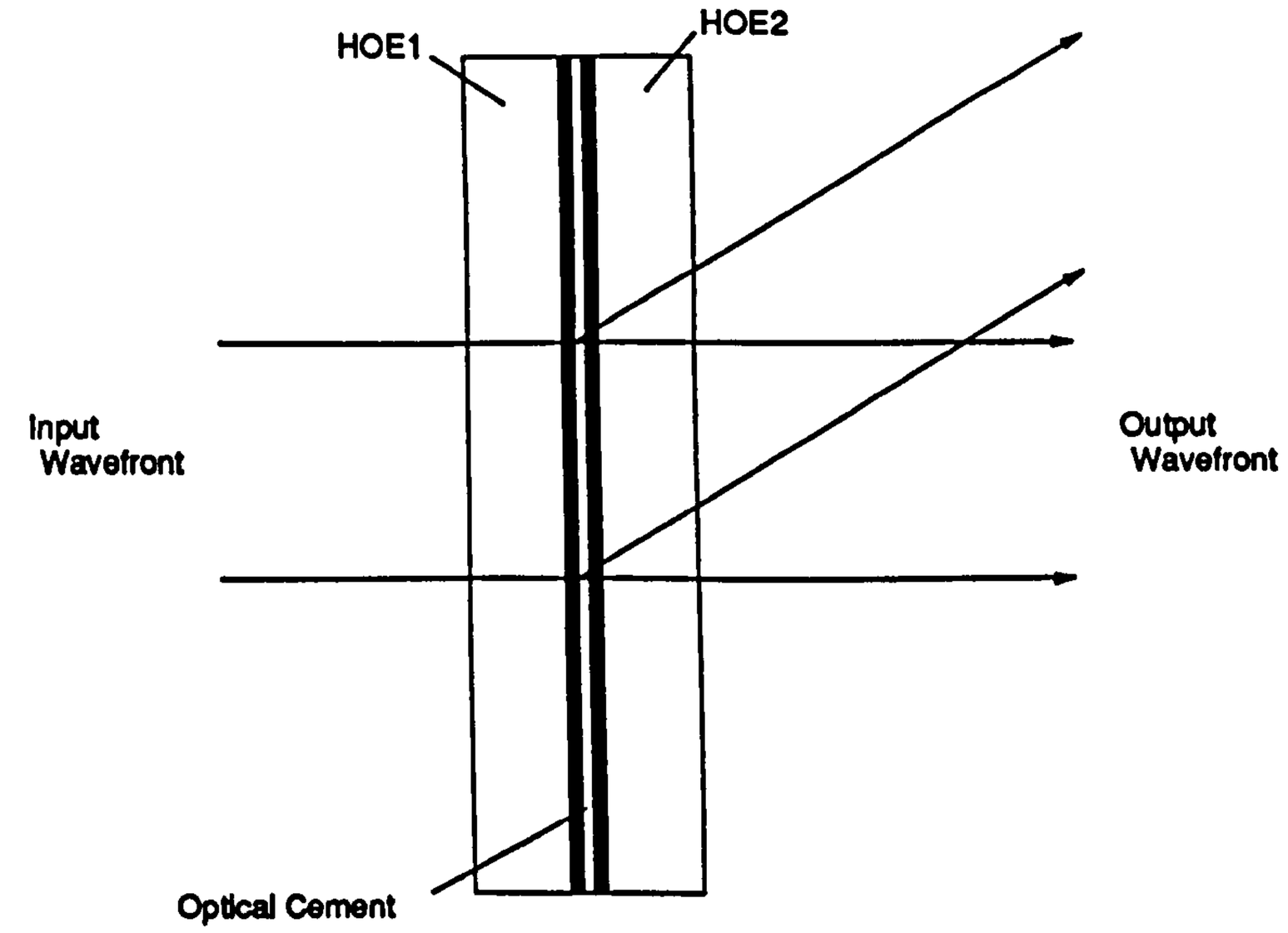

Figure A.1.2 - Experimental set-up.

however, relatively insensitive to changes in the input beam. To check that this effect had nothing to do with multiple interference arising from the air gap between the two gratings, a second pair of HOEs were sealed together using optical cement. The same fringe pattern could still be observed.

As mentioned, the circular fringe pattern can be explained if we assume that the wavefronts used to record the two holograms have a slight curvature to them. Thus, if the doublet is replayed by a perfectly plane wave the object wavefront reconstructed by HOE1 will have the opposite curvature to that required by HOE2. A circularly symmetric phase error will therefore result which, in turn, will lead to the formation of a set of circular fringes, as observed. In order to test this idea, two sensitized plates were index matched together, gelatin surface to gelatin surface, and placed in the recording set-up. Both plates were then simultaneously exposed, which resulted in the formation of closer matched gratings. When properly aligned the output of the doublet consisted of roughly one fringe spread

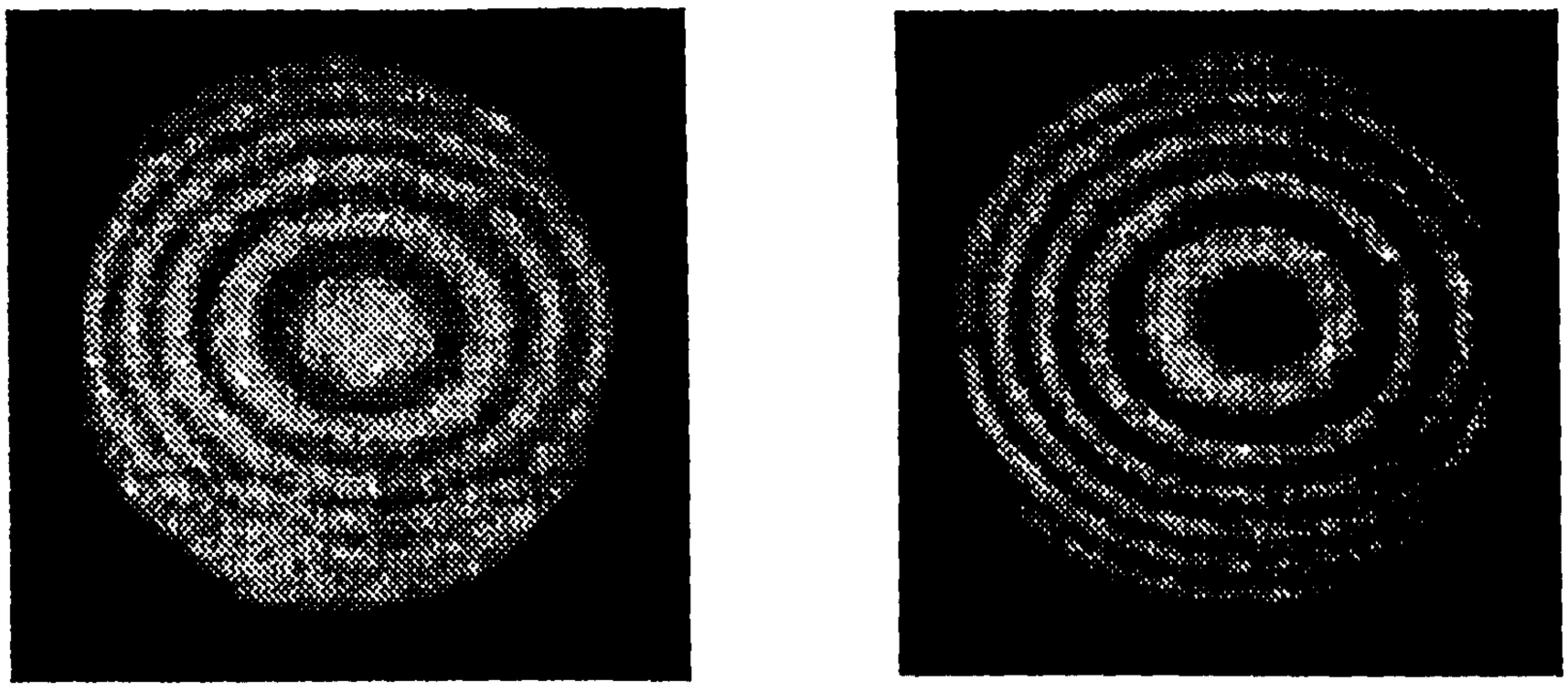

Figure A.1.3 - Output generated by two stacked volume phase holograms. Left-hand side : Zeroth order; Right-hand side : First order.

across a 9mm diameter hologram. This allowed a crude optical attenuator to be demonstrated; the amount of light in the output could be varied by changing the relative separation between the two gratings.

References

1) C. P. Kuo, T. Aye, D. G. Pelka, J. Jannson and T. Jannson, "Tunable holographic Fabry-Perot étalon fabricated from poor-quality glass substrates", Opt. Lett. **15**, 351 (1990).

APPENDIX 2

Temperature Profile Generated by a Gaussian Laser Beam Within a DCG HOE

In the following section, the analysis used by Godslave [1,2] to evaluate the temperature profile generated in a sealed HOE by a Gaussian laser beam will be described. The calculation involves finding the Green's function for the model described in section. 7.5 using a Bessel transform method [2,3]. The Greens function can be thought of as describing the temperature rise, $\Delta T(\underline{r})$, due to a point source. Any heat source can be represented by a continuous distribution of point sources. The steady state temperature distribution within the HOE can therefore be found by summing up these point sources, each source being weighted by the amount of heat energy generated at that point. That is

$$\Delta T(\underline{r}) = \int_V \frac{Q(\underline{r}')}{K_s} G(\underline{r}-\underline{r}')\, d\underline{r}'^3 \qquad (A.2.1)$$

where $\Delta T(\underline{r})$ is the temperature rise, Q the heat energy generated per unit volume per second as a function of position, G the steady state proper Greens function of the system and K_s the thermal conductivity of the substrate and coverplate. The steady state heat equation in cylindrical coordinates is given by

$$\frac{1}{r}\frac{\partial}{\partial r} r \frac{\partial}{\partial r}\Delta T + \frac{1}{r^2}\frac{\partial^2}{\partial \phi^2}\Delta T + \frac{\partial^2}{\partial z^2}\Delta T + \frac{Q}{K_s} = 0 \qquad (A.2.2)$$

The particular solution corresponding to a 'unit' point source can be written in cylindrical coordinates in integral form [5]

$$G_p(r,\phi,z) = \frac{1}{4\pi}\int_0^{\infty} J_0(\zeta R)\exp(-\zeta|z-z'|)\, d\zeta \qquad (A.2.3)$$

where ζ is a dummy variable and the location of the point source is at (r', ϕ', z'). R is given by the Cosine rule.

$$R^2 = r' + r'^2 - 2rr' \cos(\phi - \phi') \qquad (A.2.4)$$

A point source solution valid for the boundary conditions of some region bounded by parallel planes is the sum of this particular solution and the general solution, i.e.

$$G = \frac{1}{4\pi} \int_0^{\infty} W(z)\, J_0(\zeta R)\, d\zeta \qquad (A.2.5)$$

where

$$W = A \exp(\zeta z) + B \exp(-\zeta z) + \exp(-\zeta | z - z' |) \qquad (A.2.6)$$

and the functions, A and B, can be found on application of the relevant boundary conditions. It was assumed for simplicity that only heat loss by radiation was taking place at the outer faces of the substrate and coverplate. Treating the hologram as a black-body radiator then, if the substrate surface is at a temperature T and the surrounding air is at a temperature T_o, the hologram will lose heat at a rate

$$f = \sigma E\, (T^4 - T_o^4) \qquad (A.2.7)$$

where σ is the Stefan-Boltzmann constant, and E is the Emmissivity of the substrate and coverplate. For practical purposes, the temperature rise, $\Delta T = (T - T_o) << T_o$, therefore equation. (A.2.7) will approximate to

$$f|_{z=\pm L} = h\, \Delta T|_{z=\pm L} \quad , \qquad h = 4E\sigma T_o^3 \qquad (A.2.8)$$

In addition, at the substrate surfaces ($z = \pm L$), the outward heat flux will be given by

$$f|_{z=\pm L} = \mp K_z \frac{\partial \Delta T}{\partial z}|_{z=\pm L} \qquad (A.2.9)$$

Combining equations (A.2.8), (A.2.9) and (A.2.5) results in

$$\frac{\partial W}{\partial z}|_{z=+L} = -H\,W|_{z=+L} \qquad (A.2.10(a))$$

$$\frac{\partial W}{\partial z}|_{z=-L} = +H\,W|_{z=-L} \qquad (A.2.10(b))$$

where $H = h/K_z$. These two simultaneous equations (equations A.2.10(a) and A.2.10(b)) can then be used to determine the functions A and B of equation (A.2.7). By appropriate differentiation and manipulation it can be shown that in the case of $z' = 0$

$$W = \frac{2\exp(-\zeta L)}{(\zeta+H)}(\exp(-\zeta L)(\zeta-H))\left(\frac{\zeta\cosh(\zeta L)+H\sinh(\zeta L)}{(\zeta^2+H^2)\sinh(2\zeta L)+2\zeta H\cosh(2\zeta L)}\right)$$

$$\times\{\zeta\cosh(\zeta(L+z))+H\sinh(\zeta(L+z))\}$$

$$+\frac{2\exp(-\zeta(L+z))}{(\zeta+H)}(\zeta\cosh(\zeta L)+H\sinh(\zeta L)) \qquad (A.2.11)$$

This corresponds to heating in the central plane (ie the composite gelatin/optical cement layer), an implicit integration having been performed in equation (A.2.1) with Q being proportional to a delta function in z'.

$$Q(r') = Q_0\exp(-r'^2/s^2) \qquad (A.2.12)$$

where s is 1/e spot radius. Thus,

$$\Delta T = \int_0^{2\pi} \int_0^{\infty} \frac{Q_0}{K_s} \exp(-r'^2/s^2)\, G(\underline{r} - \underline{r}')\, r'\, dr'\, d\phi' \qquad (A.2.13)$$

Q is now defined as the power absorbed per unit area by the gelatin/optical cement layer. Equation (A.2.13) can also be written as

$$\Delta T = \frac{1}{4\pi} \int_0^{2\pi} \int_0^{\infty} \int_0^{\infty} \frac{Q_0}{K_s} \exp(-r'^2/s^2)\, J_0(\zeta R)\, W\, r'\, dr'\, d\zeta\, d\phi' \qquad (15)$$

On using the addition theorem for Bessel functions [5], i.e.

$$J_0(\zeta R) = \Sigma_{m=-\infty}^{\infty} J_m(\zeta r)\, J_m(\zeta r')\cos(m(\phi - \phi')) \qquad (A.2.15)$$

only the m = 0 term survives. As the source term has cylindrical symmetry, then equation (A.2.14) reduces to

$$\Delta T = \frac{Q_0}{2K_s} \int_0^{\infty} \int_0^{\infty} \exp(-r'^2/s^2)\, J_0(\zeta r)\, J_0(\zeta r')\, r'\, dr'\, d\zeta \qquad (A.2.16)$$

On using the result that [5]

$$\int_0^{\infty} \exp(-r^2/s^2)\, J_0(\zeta r')\, r'\, dr' = \frac{s^2}{2} \exp(-\zeta^2 s^2/4) \qquad (A.2.17)$$

The equation governing the steady state temperature rise reduces to a single integral

$$\Delta T = \frac{Q_0 s^2}{4K_s} \int_0^{\infty} W \exp(-\zeta^2 s^2/4)\, J_0(\zeta r)\, d\zeta \qquad (A.2.18)$$

Finally Q_o can be written in terms of the incident power, P_o, and the fraction of the power absorbed by the gelatin/optical cement film, (αl), i.e.

$$Q_0 = \frac{P_0 \alpha l}{\pi s^2} \qquad (A.2.19)$$

and so

$$\Delta T = \frac{P_0 \alpha l}{4\pi K_s} \int_0^\infty W \exp(-\zeta^2 s^2/4)\, J_0(\zeta r)\, d\zeta \qquad (A.2.20)$$

This equation may be used to calculate the temperature profile existing inside the hologram if the restrictions outlined in section 7.5 are met

References

1) E. Abraham, J. M. Halley, "Some Calculations of the temperature profiles in thin films with laser heating", Appl. Phys. A 42, 279 (1987).

2) I. Janossy, M. R. Taghizadeh, J. G. H. Matthew and S. D. Smith, "Thermally induced optical bistability in thin film devices", IEEE J. Quantum Electron. QE-21, 1447 (1985).

3) C. Godsalve, Passive optical bistability in etalons with diffusive nonlinearities with applications to optical computing, Ph.D. Thesis, Physics Department, Heriot-Watt University, Edinburgh, U.K. (1991) and references therein.

4) H. S. Carslaw and J. C. Jaeger, Conduction of heat in solids, 2nd edition, (Claredon Press, Oxford, 1959).

5) Handbook of Mathematical Functions, edited by M. Abramowitz and I. A. Stegun, (Dover Publications, New York, 1970).